Spatio-temporal control of high harmonic generation in semiconductors for attosecond pulse emission

Sven Fröhlich

université PARIS-SACLAY

Spatio-temporal control of high harmonic generation in semiconductors for attosecond pulse emission

Contrôle spatio-temporel de la génération d'harmoniques dans les semiconducteurs pour l'émission d'impulsions attosecondes

Thèse de doctorat de l'université Paris-Saclay

École doctorale n° 572, Ondes et Matière (EDOM)
Spécialité de doctorat : Physique
Graduate School : Physique. Référent : Faculté des sciences d'Orsay

Thèse préparée dans l'unité de recherche **LIDYL (Université Paris-Saclay, CEA, CNRS)**, sous la direction de **Hamed MERDJI**, Directeur de recherche, et le co-encadrement de **David GAUTHIER**, Chercheur

Thèse soutenue à Paris-Saclay, le 20 Octobre 2022, par

Sven FRÖHLICH

Composition du jury

Sophie KAZAMIAS Professeur, Laboratoire Iréne Joliot-Curie, Université Paris-Saclay	Présidente
Amelle ZAÏR Directrice de recherche, King's College London	Rapportrice & Examinatrice
Eric CORMIER Professeur, Laboratoire Photonique, IOGS-CNRS-Université de Bordeaux	Rapporteur & Examinateur
Angela VELLA Professeur, Groupe de Physique des Matériaux, Normandie Université, UNIROUEN	Examinatrice
Milutin KOVACEV Professeur, Institut für Quantenoptik (IQO), Leibniz Universität Hannover	Examinateur
Hamed MERDJI Directeur de recherche, Laboratoire d'optique appliquée, École polytechnique	Directeur de thèse

THESE DE DOCTORAT
NNT : 2022UPASP110

université PARIS-SACLAY

ÉCOLE DOCTORALE
Ondes et matière (EDOM)

Titre : Contrôle spatio-temporel de la génération d'harmoniques dans les semiconducteurs pour l'émission d'impulsions attosecondes

Mots clés : Génération d'harmoniques d'ordre élevé, semi-conducteur, imagerie par diffraction, physique attoseconde, optique non linéaire

Résumé : La génération d'harmoniques d'ordre élevées dans les milieux condensés est un domaine émergent depuis sa première observation en 2011. La forte dépendance des harmoniques à la structure de bande cristalline et aux paramètres laser en fait une excellente observable des mécanismes fondamentaux de génération. De plus, la configuration compacte de la source combinée à la possibilité de structurer le milieu de génération en fait une source prometteuse de rayonnement extrême ultraviolet pour, par exemple, des applications de spectroscopie ou d'imagerie. Dans cette thèse, nous étudions trois caractéristiques de la génération d'harmoniques dans les cristaux. Premièrement, l'effet des changements de structure de bande induits par le dopage sur le processus d'émission. Les deux exemples de systèmes sont l'oxyde de magnésium dopé au chrome et le silicium implanté au gallium, pour lesquels le dopage conduit à une amélioration du rendement de génération. Ensuite, nous montrons qu'en utilisant une technique d'imagerie par diffraction cohérente, il est possible d'imager des nanostructures uniquement en se basant sur les harmoniques émises par la structure elle-même. Parce que la nanostructuration de surface émerge comme un moyen d'induire des propriétés complexes directement dans le faisceau harmonique, comme un moment angulaire orbital, cela ouvre la possibilité d'une caractérisation in-situ de ces structures. Enfin, le concept de porte de polarisation utilisé dans les gaz est adapté pour les solides en utilisant la forte réponse anisotrope des harmoniques. C'est utilisé pour façonner temporellement l'émission et permettre la génération d'impulsions attosecondes isolées.

Title : Spatio-temporal control of high harmonic generation in semiconductors for attosecond pulse emission

Keywords : high harmonic generation, semiconductors, diffraction imaging, attosecond physics, nonlinear optics

Abstract : High harmonic generation in condensed media has been an emerging field since its first observation in 2011. The strong dependency of the harmonics on the crystal band structure and laser parameters make them an excellent observable of the fundamental mechanisms of strong field generation processes. Moreover, the compact configuration of the solid state source combined with the possibility for structuring the generation medium makes it a promising source of extreme ultraviolet radiation for e.g. spectroscopy or imaging applications. In this thesis, we investigate three different aspects of the high harmonic generation in crystals. First, doping that induces changes of the band structure and its effect on the emission process. The two example systems for this are chromium doped magnesium oxide and gallium implanted silicon, for which the doping leads to an enhancement of the harmonic yield. After, we show that by using a coherent diffraction imaging technique, it is possible to image silicon nanostructures solely based on the harmonics emitted by the structure itself. Because surface nanostructuring is emerging as a way of inducing complex properties directly into the harmonic beam, such as an orbital angular momentum, this opens up the possibility of in-situ characterization of these structures. Finally, the concept of polarization gating used in gases is adapted to solids by using the strong anisotropic harmonic response. It is used in order to temporally shape the emission and push towards isolated attosecond pulse generation.

Contents

Acknowledgements

Science is rarely pursued alone. So at this point i would like to take the time to thank all the people that helped me on my path to this thesis with advice, ideas and discussions.

First I would like to thank the Jury *Amelle Zaïr*, *Eric Cormier*, *Sophie Kazamias*, *Angela Vella* and *Milutin Kovacev* for joining my defense and all the insightful comments, discussions and questions. Thank you as well for all the kind words and encouragement after my defense, it has been a pleasure to have you as a Jury!

Going back a couple of years I never could have imagined I would do my PhD in France. However, my supervisor *Hamed Merdji* gave me the incredible opportunity to join his team at the CEA and work on a topic as interesting as HHG from solids. I am extremely grateful not only for the opportunity but also for the constant trust and support he provided throughout the PhD. Thanks for introducing me to this amazing group, countless discussions and all the projects and collaborations that I had the pleasure to be part of!

I'd like to thank *Willem Boutu* who was essential for the every day life at CEA, not only for the experiments but also for all the administrative tasks (of which there were plenty when coming to France). He always had time for a discussion about problems and struggles with the experiments (and extremely valuable ideas to solve them) and also always provided, the sometimes necessary, moral support when facing them.

A special thanks goes to *David Gauthier*, the man who kept the coffee machine alive. During the many hours in the lab he taught me how to handle HHG, was always there when a problem had to be solved and in the end took the time to proof read this manuscript. The endless discussions about HHG pushed my understanding of the topic constantly and made this thesis seem possible. I learned more from him than I ever could've imagined.

I would also like to thank the whole staff of the LIDYL laboratory for the help and support. First the secretaries *Veronique Gereczy* and *Caroline Lebe* who took care of anything related to administration. *Marc Billon* and later *Rodolphe Burtel* who together with *Sylvain Foucquart* and *André Fillon* helped to manufacture all the mechanical components needed for the experiments and around the lab. Without them the set up of the new lab would not have been possible. *Sylvie Jubera*

for managing the IT during my defense and putting up with all my short notice requests over the years. A big thank you also goes to *Catalin Miron*, especially for helping to communicate with the university administration when it seemed impossible.

Science is often not only a team but a community effort, something I experienced through out my PhD in different collaborations. I am grateful for the support and fruitful discussions with *Nicolas Tancogne-Dejean* who in the beginning of my PhD took the time to explain me the theory side of HHG in solids, giving me many valuable insights. I would like to thank *Francisco Navarrete*, *Uwe Thumm* and *Marcelo Ciappina* for the endless discussions about HHG in solids and the role of doping in particular. They not only provided simulations but also brought in crucial ideas for the interpretation of our experimental data. I would also like to thank *Marc Hanna* who kindly provided beamtime at his laser before our own system was delivered. His warm welcome and assistance made the time at the IOGS not only productive but also extremely pleasurable.

I also thank the group at CEA for all the encouragement, help and sometimes distraction. Thank you *Viktoria Nefedova, Shatha Kaassamani, Joana Duarte, Dominik Franz, Marie Froidevaux, Julius Huijts, Lea Krafft, Sara Fernandez, Alric Meunier, Aimrane Hamdou, Sergey Babenkov, Peng Ye, Xu Liu and Vijay Sunuganty*. When I first arrived I knew no one in Paris but everyone in the group gave me a warm and cheerful welcome. You were always there to not only discuss about physics but also about every other topic that came to mind. With all the barbecues, hotpots and parties, you guys made the time in Paris into the amazingly enjoyable time it has been!

And lastly a huge thanks to my family: my parents, my sisters and my brother. Even though moving abroad did put some distance between us they continuously supported and encouraged me during these four years and were always there to cheer me up. Without them this thesis would not have been possible.

Herzlichen Dank!

French Summary

Le but de ce travail de thèse est l'étude de la génération d'harmoniques laser d'ordre élevé dans les cristaux, avec une emphase vers le contrôle spatio-temporel de l'émission harmonique, et une perspective pour des applications techniques telles que de nouvelles sources compactes dans le domaine de l'extrême ultra-violet (XUV) ou le contrôle des courants électroniques petahertz induits. La génération d'harmoniques d'ordre élevé (HHG) est un processus mis en évidence à la fin des années 80, quand les lasers sont devenus capables d'atteindre des éclairements pics de l'ordre de 10^{14} W/cm^2. Lors de l'interaction entre ces champs laser intenses et les gaz, il est possible d'observer les harmoniques impaires du laser, jusque dans le domaine spectral XUV. Grâce aux avancées théoriques et expérimentales du processus physique conduisant à la HHG, il est apparu que la structure spectrale en harmoniques discrètes est en réalité le résultat d'interférences au sein de train d'impulsions attosecondes. Cela a conduit à la génération d'impulsions attosecondes isolées et a permis d'amener les expériences résolues en temps dans le domaine attoseconde. Tous ces développements, mis à l'honneur en 2022 par le prix Wolf, ont poussé le développement de ce domaine de recherche. Les sources HHG sont ainsi rapidement devenues des sources incontournables de rayonnement XUV cohérent dans de nombreux laboratoires.
En 2011 *Ghimire et al.* ont mis en évidence l'émission harmonique à partir d'un cristal de ZnO, étendant l'étude de la HHG aux solides. Cette observation a initié une multitude d'expériences supplémentaires. La HHG a depuis été observée dans d'autres matériaux, tels que l'oxyde de magnésium, l'arsénure de gallium ou le silicium. La description théorique du phénomène a suivi rapidement, fortement inspirée de la HHG dans les gaz. Le processus peut être décrit par trois étapes successives similaires aux gaz. Cependant, l'électron n'évolue pas dans l'espace libre mais au sein de la structure de bandes électroniques du solide. Tout d'abord, un électron est promu vers une bande de conduction par le laser. Il est ensuite accéléré par le champ laser au sein de la bande de conduction. Enfin, il se recombine dans la bande de valence en relâchant l'énergie ainsi gagnée sous forme de photon. Dans le cadre de la HHG dans les solides, ce processus, très similaire au processus électronique lors de la HHG dans les gaz, est appelé processus interbande. Cependant, dans les solides le courant électronique dans la bande de conduction non parabolique conduit à une autre contribution à l'émission harmonique appelée intrabande. Ce double processus de génération et sa dépendance intrinsèque avec la structure de bandes font que la HHG dans les solides se comportent de façon très différente de la HHG dans les gaz. Un exemple est la dépendance de la HHG avec l'angle entre les axes du cristal et la direction de la polarisation du laser, mise en évidence par Ghimire

dans leur première publication en 2011. La réponse harmonique reprend la symétrie de la structure du cristal, certaines directions conduisant à une réponse bien plus efficace que d'autres. Un autre exemple est la réponse à un laser incident polarisé elliptiquement, qui montre une dépendance très non linéaire et non intuitive entre l'état de polarisation du laser et des harmoniques.
Dans la suite de tous ces développements, ce travail de thèse s'est concentré sur le contrôle spatio-temporel de l'émission HHG. Le but est de créer une source HHG flexible et compacte dans le domaine XUV (jusque 30 eV). Les solides sont de bons candidats pour ce type de source car ils peuvent être structurés, ce qui permet par exemple la génération de rayonnement auto-focalisant en utilisant e.g. des lentilles de Fresnel. Ici, le premier point abordé est la génération d'harmoniques dans les semiconducteurs dopés, dans le but d'augmenter l'efficacité de conversion, un effet prédit par plusieurs calculs numériques. Deux systèmes ont été étudiés : des cristaux d'oxyde de magnésium dopés au chrome et du silicium dans lequel est implémenté du gallium. Dans le cas de MgO:Cr, le dopant a une concentration de 5000ppm. Les résultats montrent une augmentation du signal harmonique d'un facteur 2 à 3 par rapport au cristal non dopé. Cependant, ces mesures sont entachées d'une incertitude assez forte, liée à la configuration expérimentale. Les principaux doutes proviennent des différences lors de la propagation du laser incident au travers de l'échantillon avant la génération du rayonnement harmonique détecté en face arrière. Les légères différences des propriétés du laser qui en sont liées, tels que des changements du foyer du laser à cause d'effets non linéaires du troisième ordre, sont susceptibles de modifier les résultats. Le second système, le gallium implanté dans le silicium, est moins sensible à ce type d'effets car les atomes de gallium ne sont présents que sur une fine couche à la surface par un faisceau d'ions focalisé. Ce système montre une augmentation de l'efficacité harmonique en fonction de la dose d'ions reçue. Si les doses faibles de l'ordre de 10^{12} ions/cm^2 ne modifient pas le signal, l'efficacité de la HHG augmente continument jusqu'à un maximum autour de 10^{14} Ions/cm^2. Au-delà, pour des doses supérieures, le rendement harmonique décroit, pour passer sous le niveau du silicium pur. Cette diminution peut être attribuée à un niveau de dommages de la structure cristalline trop important liés au bombardement par les ions. Par rapport à l'expérience dans MgO:Cr, la faible épaisseur de la partie dopée exclut les effets de propagation. Cependant, le bombardement par les ions induit une pléthore de dommages secondaires sur la structure du cristal, qui pourraient expliquer le comportement observé.
Nous utilisons dans un second temps le rayonnement harmonique produit par des nanostructures pour imager cette même nanostructure. Nanostructurer un milieu est un moyen répandu de contrôler les propriétés spatio-temporelles d'un faisceau laser. Générer des harmoniques dans de telles structures permet un transfert efficace de ces propriétés au faisceau harmonique. Cependant, ces nanostructures doivent être caractérisées avant utilisation afin de vérifier leur structure et leurs propriétés optiques. Nous démontrons qu'il est possible de reconstruire l'image des nanostructures en utilisant uniquement les figures de diffraction du champ harmonique lui-même, grâce aux techniques d'imagerie par diffraction cohérente. Nous utilisons l'harmonique 5 d'un laser à 2100 nm, et démontrons une résolution spatiale de 800 nm. Le dispositif expérimental permet la caractérisation de structures

directement dans la ligne de lumière harmonique. Ce concept peut être étendu au domaine XUV, ce qui résultera en une amélioration de la résolution spatiale.
Dans une dernière partie, nous nous intéressons au domaine temporel, avec l'ambition de générer des impulsions attosecondes isolées dans un solide. A l'heure actuelle, l'approche s'est limitée à l'utilisation d'impulsions laser d'un unique cycle optique, alors que de multiples schémas ont été proposés pour la HHG dans les gaz (par exemple, l'utilisation de schémas à deux couleurs ou de la porte de polarisation). Nous proposons et testons un schéma qui adapte la porte de polarisation. Dans les gaz, le faible rendement de conversion observé pour des impulsions lasers polarisées circulairement est utilisé pour limiter l'efficacité de HHG sur une durée plus courte que celle de l'impulsion laser, en lui conférant un état de polarisation complexe qui varie au sein de l'impulsion. Dans les solides, nous proposons d'utiliser la réponse fortement anisotrope à une polarisation rectiligne en fonction de l'orientation des axes cristallins. La porte attoseconde est créée en induisant une polarisation rectiligne qui tourne à la vitesse du cycle optique du laser incident. Les premiers tests, encourageants, sont limités par la durée trop longue des impulsions. Nous avons développé la post compression du laser, diminuant la durée des impulsions à 25 fs, afin d'obtenir des conditions plus favorables. Cependant, les résultats initiaux n'ont pas été reproduits. Des termes de phase du troisième ordre et d'ordres supérieurs propres au schéma d'élargissement spectral sont identifiés comme étant responsables d'une dégradation de la qualité de la porte de polarisation, conduisant à une polarisation elliptique non compatible. Pour l'avenir, des miroirs à dérive de fréquence seront nécessaires pour compenser la phase du troisième ordre, permettant d'obtenir des impulsions de 20 fs utilisables.

Chapter 1

Introduction

Since the beginning of optics, the interaction between light and matter has been observed in the form of linear properties, such as absorption/transmission, dispersion or the angle dependency of reflection. With the invention of the laser [1] this field has become much broader. It enabled higher intensities leading to the first observations of nonlinear effects such as second harmonic generation [2] and two-photon absorption [3]. The discovery of this new class of effects was quickly followed by their theoretical description as pertubative nonlinear effects. Over the following years this new field of nonlinear optics contributed many major advances for spectroscopy and microscopy [4].
After the development of laser based ultrashort pulses and with the invention of *chirped pulse amplification* (CPA) schemes [5], pulses in the femtosecond range with peak powers in the TW regime became widely accessible. High harmonics generation (HHG) in gases was first reported just shortly after [6, 7] using gases as a medium and were exhibiting behaviours that are not explainable in the framework of pertubative nonlinear optics. The most prominent behaviour is the formation of a plateau of equally strong harmonics followed by a cutoff after which the harmonic yield quickly declines. Based on the ionization model of Keldysh [8] a theoretical description of HHG developed in the following years splits the process into three major steps. First the field bends the atomic potential and an electron tunnels through the barrier, after which it is accelerated in the electric field of the laser pulse. Due to the periodic nature of the electric field it recollides with the parent atom releasing its gained kinetic energy into a single photon. HHG are able to generate coherent photons down to the XUV region as a train of attosecond pulses. The shortest HHG pulse ever produced that way was measured to be only 43 attoseconds long [9]. After their initial description, HHG based on gas targets spread widely and is nowadays a prominent source of coherent extreme ultraviolet (XUV/EUV) radiation on the lab scale. This development facilitated a multitude of amazing results and techniques, such as measurements of ionization dynamics [10] or transient absorption spectroscopy [11, 12], that allow new and deep insights into fundamental physical processes and properties. As a consequence the Wolf prize was awarded to *Ferenc Krausz*, *Paul Corkum* and *Anne L'Huillier*, three pioneers in the field of HHG.
While gas has been the dominant generation medium for HHG for the past decades, they have been observed in solids for the first time in 2011 by Ghimire et al [13].

This initial observation sparked the interest of many and the field of high harmonic generation in solid materials, especially semiconducting crystals, experienced a fast growth. It was quickly shown that the harmonics show a close dependency on the crystal structure of the material. A straightforward manifestation is the harmonic yield that varies strongly as a function of the angle between the crystal axis and the linear polarization, reproducing the symmetries of the crystal. In the years following their discovery, harmonics were observed in a multitude of different materials such as bulk ZnSe [13] or GaSe [14] crystals, polycrystalline SiO_2 [15] or 2D materials such as Graphene [16] or MoS_2 [17]. With the first theoretical descriptions of the process, came propositions of characterizing the material properties using HHG as a probe e.g. for the reconstruction of bands [18].
The target of this thesis is advancing towards spatio-temporal control of the harmonics, to enable more compact, simple and versatile HHG sources. Especially when combined with smaller high repetition rate mid infrared laser systems this would result in a simplification of the setup and lead to a broader availability e.g. for spectroscopy applications. A first important aspect is the achieved conversion efficiency of the harmonics. As one of the main limitations of HHG in solids is damaging of the material, the maximal intensities usable for HHG from solids are dictated by the damage threshold of the material. While high bandgap materials have higher damage threshold, which can be further increased by using infrared lasers, the usable intensities are significanlty below those used for HHG from gases. This is also not compensated by the naturally higher efficiency of solids [15]. However, a few recent theoretical studies are proposing doping as a possible way of increasing the efficiency and cutoff for HHG from solids[19]. Some simulations show a strong effect of the doping type, donor or acceptor, on the effect, with the efficiency of donor doping exceeding acceptor doping [20]. Furthermore, an increase of HHG is reported for vacancies [21]. Aside from a pure increase of HHG, the energy states generated by the doping can have more complex characteristics such as spin polarization [22]. In this thesis two example systems are used. The first is chromium doped magnesium oxide, with the advantage that magnesium oxide is a well studied, high bandgap material for HHG from solids. The second system is gallium implanted silicon. Silicon is another material whose HHG response is well studied. Furthermore, the overall characteristics and its response to doping is much better studied due to its wide spread use in semiconductor electronics. In our case we do not doped the silicon homogeneously, as the MgO, but implant the gallium with a focused ion beam as it frequently occurs in the production of nanostructures. Nanostructures are an important difference compared to HHG from gases, as the solid material allows direct structuring of the generation medium. This can be used to impregnate spatial properties into the harmonic beam without the need of further optics. Examples for this reach from the direct focusing of the generated harmonics [23] and grating structures [24] to complex features like generation of beam carrying an orbital angular momentum [25]. However, these nanostructures have to be characterized as well. One approach for this is coherent diffraction imaging, which reconstructs the structure based on its far field diffraction. Relying on the diffraction allows to combine the source of HHG and image sample in one piece. This approach keeps the harmonics as the imaging wavelength and consequently

profits from the increased resolution due to the lower wavelength of the harmonics. Additionally, not only direct phase and amplitude masks can be imaged but any material alteration that changes the harmonic yield. First approaches to this have been shown by *Sivis et al.* [23] and recently by *Roscam Abbing et al.* [26]. However, in their cases the studied structures are regular and highly periodic, leading to a far field picture similar to Bragg diffraction. Here we push for a full imaging of complex structures using ptychography.
Switching to the temporal domain pushes for isolated attosecond pulses from solids are by now limited to the generation with single cycle pulses [27]. However, there are several schemes for their generation used in HHG from gases. One of these approaches, generation with a two-color field, has recently been studied theoretically [28]. They show that isolated attosecond pulses in the range of 300 as can be generated in solids. Another approach used in gases is polarization gating. It utilizes a driving pulse whose polarization state varies over the pulse duration to restrict the generation of harmonics to a single half cycle. For example the field can be circularly polarized at the rising edge, linearly polarized around the center and again circularly polarized at the falling edge of the pulse. This technique is especially appealing for HHG from crystals as the efficiency of the HHG shows a strong anisotropic behaviour. Extending HHG from solids to isolated attosecond pulses could pave a way to integrate the advantages of isolated attosecond pulses have into compact, potentially mobile sources.

This thesis is structured as follow: Chapter 2 is a short introduction into the theory of HHG in gases and solids, followed by an overview of the current state of art in the field of HHG from solids. Chapter 3 studies the effects of crystal doping on the harmonic generation process. The first example, chromium doped magnesium oxide, features a classical doping throughout the whole crystal. The second example however, is a gallium implanted silicon sample as it appears in surface processing with a focused ion beam. The fourth chapter is applying the concept of HHG from solids to perform lensless imaging. Here, we merge the light source with the sample itself, resulting in more compact setups and a unique probe for material properties of the sample. Finally, the fifth chapter studies an approach for the generation of isolated attosecond pulses as they are available from gas based HHG sources. The approach has some similarities with the method of polarization gating for gas HHG but with specificities related to the intrinsic symmetry properties of solid state HHG. This is followed by a conclusion in Chapter 6, that recapitulates the main findings.

Chapter 2

High harmonic generation: Theory and State of the Art

This chapter first introduces notation and optical concepts used throughout the thesis. Secondly, the state of the art for high harmonic generation from solids is summarised, locating the content of this thesis within the framework of the scientific field. This starts with a short historic view into HHG in gases as it arose much earlier and the concepts and ideas developed in it were often transferred to solids. Some with success some without. For example the explanation of one part of the generation mechanism, the *interband harmonics*, has drawn strong inspiration from the semi classical treatment of HHG in gases in the three step model.

2.1 Pulse properties and propagation

As laser-matter interactions are driven by lasers and, in the strong field regime, even by laser pulses in the femtosecond regime, the description and properties of these laser pulses are of central interest for the generation of high harmonics. Even more in solids since the propagation of these pulses can have a strong influence on the shape of the electric field at the point of generation. Here some fundamental properties for the description of the laser pulses as well as their propagation in a medium are described.

2.1.1 Mathematical representation of laser pulses

The propagation of laser pulses is governed by the electromagnetic wave equation derived from Maxwell's equations, which for the case of propagation in a vacuum and a scalar field is called d'Alembert equation and can be written as

$$\left(\frac{1}{c^2}\frac{\partial^2}{\partial t^2} - \nabla^2\right) E(x, y, z, t) = 0, \tag{2.1}$$

with E as the electric field. From there, two possible ways are important for this thesis. The first decomposes the temporal evolution of the electric field into frequency components and derives an equation for the spatial evolution of the field. This results in the Helmholtz equation, which is described further in chapter 4, and

is used to described the numerical basis of diffraction imaging. The second important way is based on restricting the solutions to fields propagating in z direction. In this case the field takes the form

$$E(t, \vec{r}) = A(t, \vec{r}) e^{i\omega_0 t - k_0 z}, \tag{2.2}$$

where E the electric field is separated into an envelope A and a term oscillating at the central wavelength of the corresponding spectrum. The wave vector k_0 and frequency ω_0 are not independent but locked to each other by the phase velocity $v = \omega_0/k_0$. For the case of propagation in a vacuum the phase velocity is equal to the speed of light c.
Taking the field at a fixed position in space and transferring it to the frequency domain via a Fourier transformation yields the electric field in frequency space

$$E(\omega) = a(\omega) e^{i(\omega + \phi(\omega))}, \tag{2.3}$$

with an additional phase term in $\phi(\omega)$. Here $a(\omega)$ connects to the measured spectral density $I(\omega)$ via $a(\omega) \propto \sqrt{I(\omega)}$. $\phi(\omega)$ describes the phase relation between different frequency components and carries important information about the temporal pulse shape. The effects of this phase term on the temporal shape are categorised into the different orders of the Taylor series of the phase term.

$$\phi(\omega - \omega_0) = \underbrace{\phi_0}_{\text{CEP}} + \frac{\phi_1}{1!}(\omega - \omega_0) + \underbrace{\frac{\phi_2}{2!}}_{\text{GDD}} (\omega - \omega_0)^2 + \cdots \tag{2.4}$$

For most laser pulses only the first terms are important, however with increasing complexity and decreasing temporal width of the pulse high order terms can gain significant importance. For laser pulses used in strong field physics, usually the terms up to third order are of interest with the quadratic phase term being the most important. Next the effects of the lowest phase terms and their importance for experiments are shortly described.

Zero order phase: CEP
The zero order phase term, also called *carrier envelope phase* (CEP) describes the position of the carrier wave, oscillating at ω_0, with respect to the envelope of the pulse. This means, that, depending on the CEP the peak of the field oscillation might be shifted compared to the maximum of the envelope. In the worst case the field at the peak of the envelope is zero, resulting in a large drop of peak field strength. For pulses with many cycles the change in the envelope for one cycle is small and the effects of the CEP are generally neglectable. However, when reaching the few cycle or even single cycle regime a shift in CEP has a strong influence on the achieved maximum field.

First order phase
Since the fourier transform of a linear phase corresponds to an absolute shift, a linear spectral phase corresponds to a delayed pulse. A linear phase therefore corresponds to a delay with respect to an arbitrary zero. Since HHG mostly cares

about the pulse structure itself and not about the exact arrival time of the pulse, this phase term is mostly unimportant and, at the same time, can not be measured by common pulse characterization techniques (e.g. FROG or SPIDER).

Second order phase: GDD

In contrast, the *group delay dispersion* (GDD) or linear chirp is of high interest. It describes the delay, and therefore the phase, between the different wavelength of the pulse. A positive GDD corresponds to lower frequencies in the leading part of the pulse and higher frequencies in the trailing part, while a negative GDD corresponds to the opposite behaviour. This dephasing is directly increasing the pulse duration, leading to a loss of peak power. GDD is the primary phase of interest introduced to a pulse that propagates through material. Since the goal for HHG are high fields, the pulses have to be as short as possible, meaning deviations in the GDD have to be compensated as much as possible. Luckily HHG from solids is, for reasons described later, mostly using infrared lasers and materials with negative and positive GDD are available in those wavelength ranges. The GDD can therefore be compensated fairly easy.

Third order phase: TOD

For extremely short pulses the *third order dispersion* (TOD) starts to have a significant influence on the pulse shape as well. A strong TOD leads to the formation of satellite pulses, that lead or trail the main pulse. These satellites pulses can pre-ionize the material before the main pulse arrives and potentially change the interaction of the main pulse. The effect of TOD is normally low but can be hard to correct for.

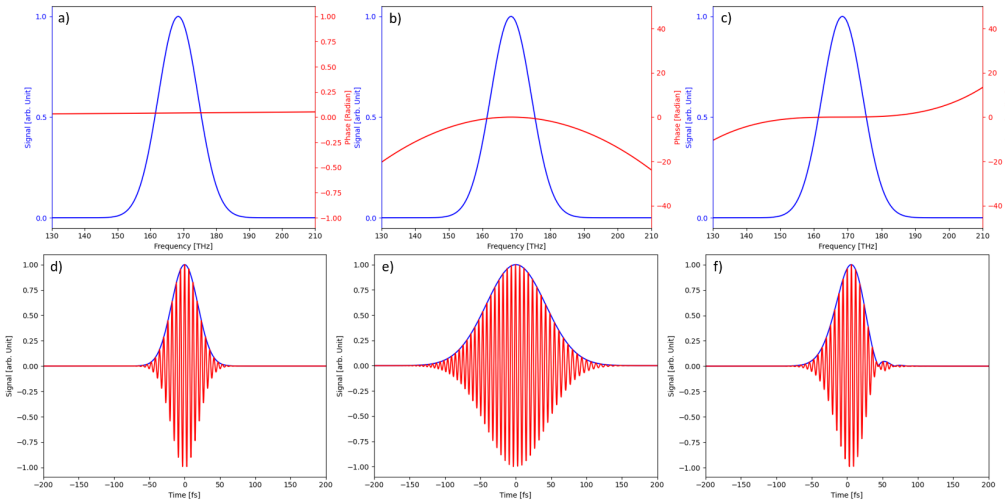

Figure 2.1: Illustration of the changes to the pulse induced by different phase terms in the spectral (a)-(c) and temporal (d)-(e) domain. The base pulse has a temporal width of 30 fs at a center wavelength of 1780 nm. In panel (b) and (e) a GDD of 700 fs^2 is introduced into the pulse while in panels (c) and (f) a TOD of -4500 fs^3 is introduced.

The effects of the different terms are illustrated for a 30 fs pulse at a central

frequency of 1780 nm, a case that is close to the laser parameters used in the experiments, in Figure 2.1. The introduction of GDD doubles the pulse length to 70 fs, while the TOD is leaving it nearly unchanged at 32 fs. However, the TOD shows a clear separation of the pulse into a main peak and a weaker post pulse. Higher order terms, while existing, are usually negligible for the pulses used in this work. However, their importance grows with decreasing pulse duration. To achieve the shortest possible pulse for a given spectrum a uniform flat phase is needed at which point the pulse is called *Fourier transform limited*. Naturally the structure of these pulses needs to be measured. There is a multitude of techniques available for this purpose with *Frequency resolved optical gating* (FROG), *Dispersion scan* (D-Scan) and *Spectral phase interferometry for direct electric-field reconstruction* (SPIDER) being the most prominent ones.

2.1.2 Nonlinear propagation

In condensed matter the propagation equation is not anymore a homogen differential equation. Instead the pertubative response of a material to an incident light wave is driven by the polarization P. It strongly depends on the field strength of the incident light wave and consequently a large part of optics only considering the linear response, an approximation which works well for low intensity laser fields. It is however not sufficient to describe the behaviour at the high intensities reached in HHG experiments. There one needs the whole expansion of the polarization, described as

$$\vec{P}(\omega,\vec{r}) = \varepsilon_0 \left(\chi(\omega)\vec{E}(\omega,\vec{r}) + \chi(\omega)^{(2)}\vec{E}^2(\omega,\vec{r}) + \chi(\omega)^{(3)}\vec{E}^3(\omega,\vec{r}) + \cdots\right). \tag{2.5}$$

Here ε_0 denotes the vacuum permittivity and $\chi^{(n)}$ the n-th order susceptibility tensor. The susceptibility tensor reflects the properties and symmetries of the material. While it can be extremely complex, the symmetries can reduce the amount of independent values greatly. This also leads to the observation that centrosymmetric crystals must have vanishing even order susceptibilities. Consequently, the first nonlinearity in those materials is the third order susceptibility. The third order can then be described by extending the refractive index with an intensity dependent component

$$n(t,x,y) = n_0 + n_2 I(t,x,y). \tag{2.6}$$

The refractive index n_2 is related to the third order susceptibility as

$$n_2 = \frac{3}{4n_0^2\varepsilon_0 c}\chi^{(3)}. \tag{2.7}$$

Here the susceptibility is treated as a scalar, which is valid if considering only one fixed polarization direction with respect to the crystal axis. Notably, the time and space dependency of the intensity is introducing the same terms into the nonlinear refractive index. This means that beams with a non flat top beam profile will have a different propagation properties depending on the local intensity effectively creating a space-time coupling. However, as explained later the effects are commonly

divided into a temporal and spatial effect.

Frequency Conversion

One of the most common applications of nonlinear optics is frequency conversion, particularly second harmonic generation. In this process the central frequency of a portion of the laser pulse is multiplied by a factor n and therefore shifted to the harmonics of the fundamental wavelength. The efficiency of the process is tied to the intensity of the laser pulse and the susceptibility of order n. While this process can be highly efficient in the right conditions, the efficiency drastically decreases with increasing order. The process is more accessible in the framework of the quantum mechanical picture, where the incoming photons excite an electron into a virtual level corresponding to the combined energy of the photons. The electron then drops back to the original stable state and releases a photon of energy $E^{(n)} = n\omega\hbar$, leaving no energy deposition in the material.
Since the efficiency of the process depends on the susceptibility, the emission becomes zero in case it is vanishing. This is notably the case for centrosymmetric material which includes cubic crystals like MgO or silicon, which are quite common crystals in solid state HHG. However, even in those materials even harmonics can arise due to local symmetry breaking e.g. close to the surface [29, 30]. From equation 2.5 it directly follows that the signal S_n of the n^{th} harmonic scales with intensity according to

$$S_n \propto I^n. \tag{2.8}$$

Self focusing

In the spatial domain one consequence of the nonlinear refractive index is *self focusing*. It is based on the spatial dependence of the refractive index in equation 2.6. Due to this, the local refractive index is directly dependent on the beam profile of the laser, which is most commonly a radial symmetric distribution, e.g. a gaussian. The radial decrease of the intensity then leads to a relative change of phase between the center of the beam and the wings of the profile, creating a curved wavefront. The beam is therefore focusing itself, similar to the effect a focusing lens would have in linear optics. For the high peak powers reached in HHG from solids this can lead to a significant shifts of the focal position and focus size with respect to intensity. An estimate for the peak power above which self focusing becomes significant is given by [31]

$$P_{Cr} = \alpha \frac{\lambda^2}{4\pi n_0 n_2} \tag{2.9}$$

Here λ is the wavelength, n_0 the refractive index, n_2 the nonlinear refractive index and α a beam profile dependent constant (e.g. 1.8962 for a gaussian profile).

Self phase modulation

The second consequence of the nonlinear refractive index is called *self phase modulation* (SPM) and is based on the temporal changed of refractive index $n(t) = n_0 + n_2 I(t)$. It results in a phase shift that is accumulated during nonlinear propagation at high intensities. This intensity and therefore time dependence of the phase leads to strong frequency shifts in the spectral domain. If the nonlinearity

is large or the intensity high enough, this can lead to a significant broadening of the spectrum of the pulse, which is often used to reach the broad spectra necessary for ultra short laser pulses. In combination with a compensation of the SPM phase afterwards such a setup is called post compression, as it can shorten the pulse duration of an initial pulse significantly. Additionally, the group velocity is depending on the refractive index and therefore the intensity as well. As a consequence, the pulse peak is propagating slower than its pedestal creating a steep falling edge at the back of the pulse. This effect is called *self-steepening* and adds a strong asymmetric character with an emphasis on a long tail towards higher frequencies to the symmetric SPM broadening of the spectrum. SPM based post compression schemes are extremely popular and have been used to generate single cycle pulses [32, 33]. Due to the development of a multitude of different experimental schemes it is possible to post compress pulses for a large range of lasers, with different average powers, initial pulse durations and peak powers.

2.2 High Harmonic Generation in solids

After first propositions of the concept [34, 35, 36], high harmonics from solids were first demonstrated by *Ghimire et al* in 2011 [13]. This first demonstration using a ZnO crystal irradiated with a 3.25 µm laser already showed several fundamental differences between HHG from gases and solids. First of the generation is no longer isotropic as in atomic gases but shows a clear rotation symmetry that reflects the symmetries of the crystal structure. This shows itself even more when using elliptically polarized driving fields, that produce a harmonic signal even with a completely circularly polarized driving pulse. This stands in contrast to HHG from gases where circular polarization leads to electron trajectories that do not lead to a recombination and photons emission. Furthermore, the scaling of the cutoff and conversion efficiencies were found to be different. For harmonics from solids the cutoff scales linear with the electric field, as opposed to the quadratic scaling in gases, while the efficiency is reported to be higher for HHG from solids [15]. Indeed, high harmonics generated in solids can be expected to behave completely different compared to harmonics created in gases, since the electron never leaves the solid. The free space propagation of the electron in a low density gas is therefore replaced by a propagation inside a condensed material. The electrons energy dispersion is consequently ruled by the band structure of the respective material. As a consequence, solid state HHG mechanisms have fundamental differences compared to the three step model in gases, leading to complex behaviour of the harmonic emission. However, this also offers new possibilities not only for novel light sources but also for the characterization of material properties.
This section gives a short introduction into HHG from semiconductors or insulators (further called solids, while conducting materials are specified). It starts with a short description of HHG from atomic gases as interpretations for HHG from solids take heavy inspiration from this field. Afterwards the fundamental generation mechanism is presented, followed by a summary of the state of the art.

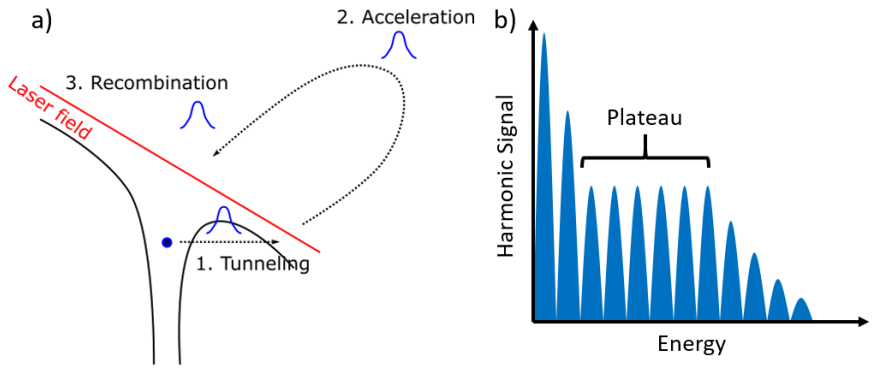

Figure 2.2: (a) Illustration of the high harmonic generation process in gases. (b) Scheme of a typical high harmonic spectrum from gases.

2.2.1 High harmonic generation in gases

The ionization process was described by Keldysh not only for gases but also for solids [8], laying the first ground work for HHG in both materials. However, after laser advanced to sufficient peak intensities, HHG was first demonstrated in gases [6]. Since then harmonics in gases have been studied intensively, leading to a number of astonishing results including the shortest ever produced pulse [9]. By now harmonics have established itself not only as a mean to observe properties of the generating atom itself, but also as a source of XUV radiation for other experiments [37]. While a complete quantum mechanical description of the process is possible [38], it is most commonly described in a semi-classical picture [39] as illustrated in Figure 2.2. It starts with the atomic potential barrier being bend under the influence of the strong electric field, allowing the highest energy bound electrons to tunnel through the potential barrier and leave the atomic potential (1). The electron is then accelerated by the electric field of the laser (2). Due to the oscillating nature of the laser field, the electron has a small chance of recolliding and combining with the atom, releasing the gathered kinetic energy into a photon (3). Consequently, these photons can reach energies many times higher than the original photon energy of the laser. The generation cycle is repeated for every half cycle of the laser pulse, leading to a series of generated pulses that interfere with each other. This interference creates the detected structure with peaks at odd multiples of the driving laser frequency. A scheme of the structure of such a spectrum is shown in Figure 2.2 (b). It can be divided into three parts: the pertubative region, the plateau and the cutoff region. In the pertubative region the harmonics are not generated via the HHG mechanism but rather in a pertubative way as described in section 2.1.2. The plateau region is where the non-pertubative HHG process dominates the generation and gives rise to harmonics with similar spectral power. Towards the highest possible kinetic energies the cutoff sets in and the spectral power of the harmonics steeply decreases. For HHG from gases this cutoff appears at the energy [40]

$$E_{cutoff} = I_p + 3.17U_p, \tag{2.10}$$

where I_p is the ionization potential of the gas and U_p the ponderomotive energy defined as

$$U_p = \frac{e^2 E_0^2}{4m\omega^2}. \tag{2.11}$$

Here e and m are the electron charge and mass, E_0 is the electric field of the laser and ω the wavelength of the laser. The cutoff therefore scales quadratic with the laser field and the inverse of the laser frequency.
To differ between the pertubative and non-pertubative regime and therefore determine whether tunnel ionization occurs or not, the Keldysh parameter defined as

$$\gamma = \frac{\omega\sqrt{2mI_p}}{eE_0} \tag{2.12}$$

was introduced [8]. A value of $\gamma < 1$ signals the regime of tunnel ionization, meaning a high electric field is needed to reach this regime.

The experimental configuration for HHG in gases uses a gas cell or gas jet as a target. This macroscopic size of the interaction region and the interference between harmonics generated at different points within it leads to phase matching conditions [41]. Matching these conditions is necessary to achieve an efficient generation and loose focusing geometries have been identified as favourable to achieve this. However, other parameters such as the gas pressure and the laser intensity have to be adjusted as well [41]. The resulting conversion efficiencies are depending on the wavelength of the driving laser and scale with λ^{-6} [42, 43], resulting in absolute efficiencies of about 10^{-5} [44].
Since the single pulses generated every half cycle have durations in the attosecond regime, there is a natural interest to generate not many but one isolated pulse. This potentially opens up the possibility of experiments with attosecond time resolution and allow precise probing of attosecond dynamics [45]. The most direct ways is to generate harmonics with single cycle pulses and therefore generating only a single attosecond pulse. However, the generation of single cycle pulses with sufficient energies to drive HHG is challenging. Therefore, techniques have been developed to reduce the requirement of a single cycle pulse.
One approach is to break the symmetry of the field by using a two color scheme in which a portion of the laser is frequency doubled. This not only creates even harmonics in the spectrum but also relaxes the limit of acceptable cycles. Another scheme uses the strong extinction of HHG yield when turning the polarization to circular. It is based on creating a pulse whose polarization state varies for different parts of the pulse, going from circular to linear to circular. As a result only the most central part of the pulse has a linear polarization and generates efficient HHG. This additional discrimination of the non-central cycles of the pulse in combination with short pulses can create a situation where only the central cycle generates harmonics efficiently. The resulting pulse is consequently an isolated attosecond pulse.

2.2.2 Basic generation mechanism of solid state HHG

While in atomic gases the electron is accelerated by the laser field with only small influences of the ions potential, in solids the electrons move within a many body

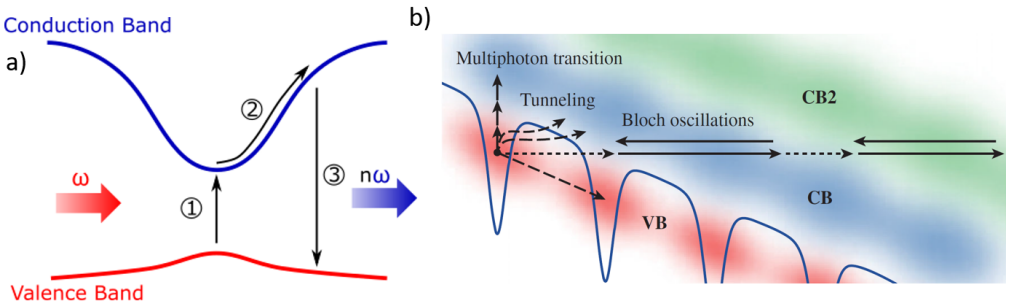

Figure 2.3: Depiction of the HHG process for solids in (a) reciprocal space and (b) real space (real space representation taken from [46]).The step are explained in the main text.

potential. The structure of solids can be described in reciprocal space where it forms a band structure with electron filled valence bands and empty conduction bands. Descriptions of the HHG in solids mostly describe the process in terms of this band structure. However, descriptions in real space are available and describe the direct electron trajectories similarly to gases [22].
The general interaction starts with an electron being promoted into the conduction band where it is subject to interactions with the electric field of the laser. These interactions are classified into two groups. The first are electron motions within one conduction band called intraband, while the second one are excitations between different conduction bands referred to as interband transitions. Both of them can emit harmonics with properties inherently related to their path in the materials electronic bands.
Similar to the atomic case the generation process can be separated into different steps:

1. As illustrated in Figure 2.3 (b) in real space the first step is the electric field bending the potential, allowing an electron to tunnel into the conduction band. In reciprocal space this transition into the conduction band occurs at or close to the direct bandgap. As the indirect bandgap requires the interaction with a phonon it is unlikely to coherently contribute on the sub-cycle ultrafast timescales of the HHG process. The transition of an electron also creates a hole in the valence band that is accelerated in the laser field similar to the electron.

2. As a second step the electron and hole are accelerated in the field. In the reciprocal space the electron gains momentum and propagates along a conduction band. If the crystal momentum exceeds the Brillouin zone the electron starts to perform Bloch oscillations. This step of motion within a conduction band is at the basis for intraband harmonic emission.

3. The electron recombines with the hole and emits a photon whose energy corresponds to the current energy difference between electron and hole. This radiation is called interband harmonics.

This division of the steps and with it especially the interband harmonics closely

resemble the classic three-step model of HHG in gases. However, the intraband contribution is unique to harmonics from solids and is based on the nonlinear dependence of the electron velocity on the electric field inside the band structure. Even in the interband harmonics the resemblance to gas HHG weakens when taking into account multiple conduction bands and the corresponding appearance of multiple plateaus (see Figure 2.5). Additionally, the valence band hole in solids is, despite its heavier effective mass, propagating in the laser field. It therefore could contribute to the phase of harmonics, while the much heavier parent ion in gases stays stationary during the electron excursion.

2.2.3 Theory

For the theoretical description of HHG in solids the full quantum mechanical picture has to be taken into account. Over the past years there have been different approaches by different groups to this problem. The most straight forward one is to solve the *time dependent Schrödinger equation* (TDSE) for a periodic potential [47, 48]. Another approach is the density matrix formalisms [49, 50] and consequently the *semiconductor Bloch equations* (SBE) [36, 51]. Finally the problem can be tackled with a good accuracy in the framework of *time dependent density function theory* (TDDFT) [52, 53, 54, 55]. However, all of these methods are involving time consuming numerical calculations, each one having advantages and disadvantages. For example the TDDFT approach employs the whole band structure without prior assumption, enabling it to include all physical effects, but at the cost of massive required computational power. Meanwhile, the other approaches reduce the numerical calculations by introducing simplifications to the equations. This poses the danger of important effects being cut out of the equations during the simplification.
Following an approach based on the SBE, the two contributions to the laser driven current can be formally described by the interband polarization $P(t)$, describing the electron movements between different bands, and the intraband current $J(t)$, describing the movement of electrons within one specific band. They are linked to the electron occupation and polarization of the bands via [36]

$$P(t) = \sum_k d_k p_k(t) + c.c. \tag{2.13}$$

$$J(t) = \sum_{\lambda,k} e v_k^\lambda n_k^\lambda(t). \tag{2.14}$$

Here d_k is the interband dipole matrix element, v_k^λ the group velocity of the electrons and $n_k^\lambda(t)$ and $p_k(t)$ the occupation and polarization of the bands, while the index λ is counting through the different bands. Calculating the time-dependent contributions $n_k^\lambda(t)$ and $p_k(t)$ requires numerically solving the SBE. The group velocity of the electrons is proportional to the band dispersion $\mathcal{E}$

$$v_k = \frac{1}{\hbar}\nabla\mathcal{E}. \tag{2.15}$$

This reflects material dependent characteristics of the intraband current and the resulting nonlinear behaviour of the current is one way of generating the high harmonic emission. For the interband polarization, since it reflects the transition amplitudes, the current is defined by the time derivative. These two currents are the basis for the emission of high harmonics and the final HHG signal is connected to the total current in the material via the following Fourier transformation

$$I_{HHG}(\omega) \propto |\omega P(\omega) + iJ(\omega)|^2 = \left| \mathcal{F}\left[\frac{\partial}{\partial t} P(t) + J(t) \right] \right|^2 . \tag{2.16}$$

Notably, this includes cross terms between the intra- and interband current.

Under the assumption of adiabatic evolution the acceleration of the electrons in the conduction band can be described by the *acceleration theorem*[52]. It describes the dependence of the electrons *crystal momentum* k on the electrical field E of the laser as

$$\frac{d}{dt} k_e(t) = -\frac{e}{\hbar} E(t), \tag{2.17}$$

with e being the elemental charge and $\hbar$ the reduced Planck constant. By using the corresponding vector potential $E(t) = -\partial A/\partial t$, the evolution of the crystal momentum corresponds to

$$k_e(t) = k_e(t_b) - \frac{e}{\hbar} A(t), \tag{2.18}$$

where t_b is the time at which the electron tunnels into the conduction band. Similar to the relation between linear and nonlinear optics, these changes of the crystal momentum induced by the laser are small compared to the changes due to other effects for most of semi conductor optics. However, in the high intensity regime of HHG it becomes a significant mechanism that can drive electrons to and above the edge of the Brillouin zone. When reaching the end of the Brillouin zone the electron can perform Bloch oscillations with the frequency

$$\omega_B = \frac{ae\,|E|}{\hbar}. \tag{2.19}$$

Here a is the lattice constant of the crystal and E the electric field. The relevance of this mechanism for HHG has been demonstrated by *Schubert et al.* [14] using a THz laser for the generation of harmonics in GaSe. They were not only able to achieve a broadband harmonic spectrum as shown in Figure 2.4 but also to verify the non-pertubative behaviour of the Bloch oscillation driven intraband harmonics.

2.2.4 State of the Art

With a great number of groups taking notice of the first observation of HHG in solids, not only were HHG from solids quickly observed in a multitude of different materials, but the theoretical description saw quick evolution as well. The material selection quickly grew from low band gap materials such as zinc oxide [13], silicon

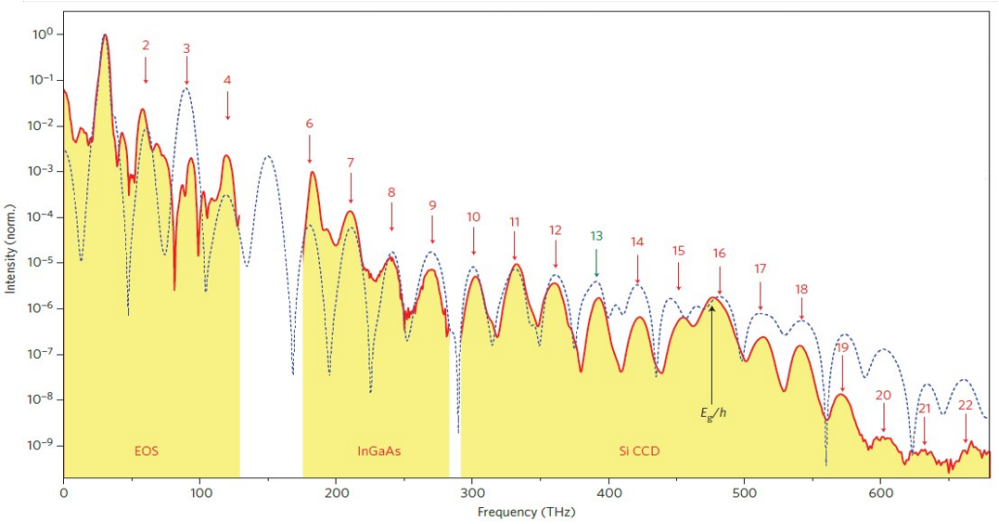

Figure 2.4: a) HHG spectrum in the THz range generated with a 30THz driving pulse taken from [14]

[56], gallium arsenide [57, 58] or gallium selenide[14], to high bandgap materials like magnesium oxide [59], sapphire [60], quartz [15] or noble gas crystals [61]. It also stretched to 2D materials [62, 16, 63, 17, 64] and more exotic materials such as carbon nanotubes [65]. Theoretical studies have predicted HHG in even more exotic materials such as topological insulators [54].
The properties of these materials are naturally influencing the harmonics significantly in a multitude of aspects, which can be used for different applications of HHG from solids. For example looking at HHG as a source for spectroscopy, the harmonic yield has to be maximized which requires a material with a high damage tolerance that is paired with an ultrashort infra to mid-infrared laser. The necessary comprehension of the processes behind HHG in solids requires the study of the individual aspects of it. A few key aspects and their current status of research are described in the following.

2.2.4.1 Cutoff

Unlike gases, solids exhibit a multiplateau structure in the harmonic spectrum. This behaviour can be explained by the band structure dependency, with each plateau corresponding to an accessible conduction band. This can be seen e.g. in measurements of the harmonics is MgO. The band structure (Figure 2.5 (a)) leads to a two plateau structure in the harmonic signal as shown in Figure 2.5 (b). There the first conduction band end after H25 and the harmonic signal pertubatively decreases into the second plateau. In HHG from solids it is important to differ this cutoff like behaviour between the different plateaus from the field based cutoff that shows the limitation of the harmonics due to the maximum field. This leads to a non-intuitive situation where the cutoff seems to change rapidly if a new plateau is accessed. In solids a cutoff in the extreme UV can be achieved with energies of 30 eV in high bandgap materials [15]. Notably, the highest cuttoff is significantly

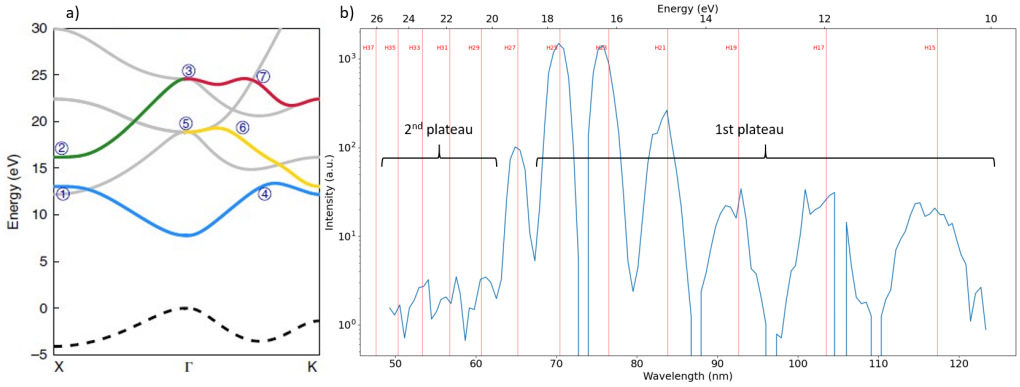

Figure 2.5: a) Bandstructure of MgO showing the multiple bands involved in the HHG process (taken from [74]) b) HHG spectrum from MgO with linearly polarized pulses in the $\Gamma - X$ direction of the crystal showing the two plateaus, with the first plateau stretching up to 18 eV

lower than cutoffs achieved in gas based HHG, which range up to hundreds of eV [66, 67]. The cutoff is shown to have a linear dependence on the electric field [13, 68], which is in strong contrast to gases where the cutoff scales quadratic with the field. Despite this contrast the behaviour can be reasoned, at least in the case of intraband harmonics, by the linear electric field dependence of Bloch oscillations. The dependence of the cutoff on the wavelength is however less clear and is still an object of debate. Some works claim a linear wavelength dependency of the cutoff, attributing it to either just the interband [69] or both inter- and intraband contribution [70, 68, 51]. However, other studies show a wavelength independent cutoff [71, 72, 73], arguing that the wavelength dependence in gas based HHG is due to the electron excursion in *free* space, which is not the case for solids.

2.2.4.2 Dependency on the crystal structure

The harmonics show a strong dependency on the band structure of the crystal. When generating harmonics with a linearly polarized laser, the angle between the crystal axis and the polarization decides which part of the band structure the electron propagates through during its excursion. As a consequence the harmonics show a strong anisotropic behaviour, reflecting the symmetries of the crystal [58]. An example, measured in our lab, is shown in Figure 2.6 (a) with the response of silicon to different directions of linearly polarized pulses. The fourfold symmetry of the silicon crystal is clearly visible in the harmonic response of the crystal. This very early observation [13] reflects the potential HHG has for the characterization of the band structure. A direct way to retrieve the band structure has been proposed by *Vampa et al* [18]. It uses the beating signal an ω-2ω scheme produces and its dependency on the band structure in conjunction with the theoretical description of HHG to retrieve the band structure of the measured material. This approach, however, requires the measurement of harmonics over the whole energy range of the conduction band, which is often limited in experiments. Additionally, only a single conduction band is considered in the theoretical description for the model,

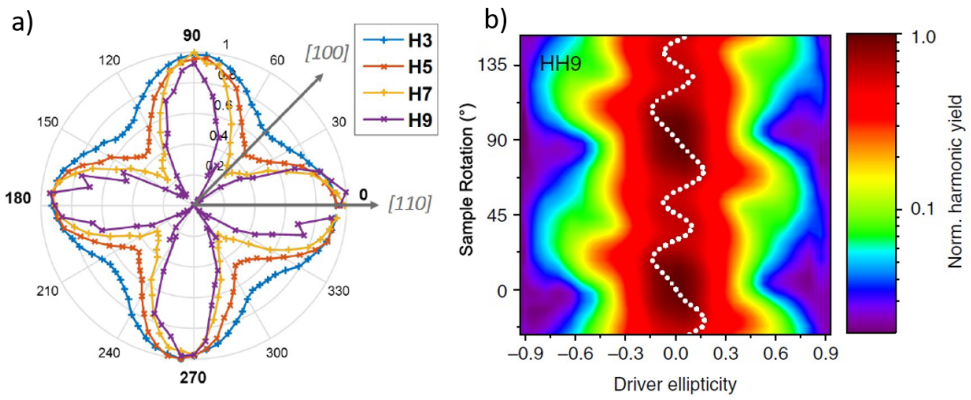

Figure 2.6: a) Angle dependence of multiple harmonics in silicon taken from [58] b) Ellipticity dependence of the harmonic yield as measured by Klemke et al [56]

while the effect and contributions of multiple conduction bands are, depending on the experimental parameters, rather frequent.
A frequent question in the field has been whether intra- or interband harmonics is the dominant process in HHG. However, the dominant process can change based on the material or wavelength region of the harmonic spectrum. Nevertheless, it has been pointed out that the band structure allows a good guess on where interband harmonics can not take place [52], namely when no transitions exist that lead to the observed photon energy. The first, obvious, situation where this applies are below bandgap harmonics. As the bandgap is the lowest possible energy difference between valence and conduction band, any recombination of an electron with a hole needs to emit a photon with an energy higher or equal to it. A second possibility to identify energy regions where no transitions exist is calculating the *joint density of states* (JDOS). This allows identification of additional regions with low or vanishing transitions, meaning harmonics at these energies originate from intraband dynamics [71].

2.2.4.3 Generation with elliptical driving pulses

After studying the HHG response with respect to different directions of linear polarization, the next step is to change the polarization of the incident laser towards elliptical polarization states. In gases an elliptical polarization alters the electron trajectories in a way that prevents recollisions with the atom, consequently leading to quickly vanishing harmonics with increasing ellipticity. However, in solids the picture is more complex and depending on the material, elliptical polarizations can indeed generate high harmonics. Nevertheless, the efficiency of these elliptically, or even circularly, driven harmonics is usually lower than for linear polarizations [62, 13] yet it can be still significant [56]. Due to the complex structure of solids, elliptical driving polarizations in solids can lead to rather unintuitive behaviour of the harmonic yield. An example are the measurements of *You et al* showing a shift of the point of maximal efficiency for tilted crystals towards slightly elliptical pulses

[59]. Their measurements also showed an unexpected asymmetric behaviour for left and right hand circular polarized light. However, this observation was later contested by other authors [56, 75]. An example for the dependency of the harmonic yield of H9 on the ellipticity for silicon is shown in Figure 2.6 (b). The pattern of the harmonic yield repeats with the crystal symmetry but has a strongly nonlinear dependency on the driving ellipticity.
Notably, elliptical and circular polarized driving pulses are generating elliptical harmonics as well. The ellipticity of the harmonics, despite following symmetry patterns corresponding to the crystal structure, is reported to exhibit 'islands' of high ellipticity for specific combinations of crystal rotation and driving ellipticity [56]. For near circular polarization of the laser the polarization of the harmonics becomes circular. In addition, the generation of circularly polarized harmonics is reported to obey selection rules [76], following the scheme

$$n_{HH} = \sigma + \mathrm{N}j, \tag{2.20}$$

with $j \in \mathbb{N}$, $\sigma = \pm 1$ the direction of rotation of the laser and N the order of rotational symmetry e.g. N = 4 for MgO since it has a four fold symmetry.

2.2.4.4 Spectral Phase

As the electron trajectories in solids allow a range of paths that lead to the emission of harmonics, not all wavelength are generated at the same point in time. This leads to a spectral phase of the harmonic spectrum that connects it to the temporal shape of the attosecond pulse structure. This is visible in equation 2.16 that directly connects the harmonic spectrum with the underlying electron current. The phase consequently reflects the mechanisms, involved in the generation of each frequency component. Meaning a full knowledge of it would allow a deep insight into the materials band structure and the ultrafast process of harmonic generation in solids. Phase measurements can therefore also solve the question whether one of the two mechanisms, intra- or interband, is dominating the generation process. Based on theoretical studies a flat phase is predicted for intraband contributions as they are generated throughout the whole interaction. Meanwhile, interband harmonics are predicted to exhibit an attochirp similar to gas harmonics [77, 68].
Reports of experimental estimates of the phase have been given by *Garg et al.* [27] by using attosecond streaking. They analysed harmonics generated in a polycrystalline SiO_2 nanofilm using single cycle pulses and found a nearly flat phase response. Consequently, they conclude that the harmonic generation is dominated by the intraband contribution. In contrast, *Vampa et al* conclude from ω-2ω measurements in ZnO, using a 3.78 µm laser with a pulse duration of 95 fs, that the observed sideband oscillations can only be explained if the main contribution originates from the interband mechanism [78]. Recently an approach for the recontruction of the phase based on the response to CEP changes has been proposed, but only shown experimentally for a, compared to the overall HHG spectrum, narrow 4 eV band [79].
Reports on the intensity dependence of the phase give contradicting results as well. First *Garg et al.* reported a flat phase response to intensity changes for a quartz

[80]. In the measurements they generated HHG in a quartz nanofoil using a 1.2 cycle laser centered at 1.7 eV. The EUV harmonics were then guided into an Argon gas jet inside a *time of flight spectrometer* (TOF) together with the driving laser. Interferences between the *above threshold ionization* (ATI) signal and the ionization signal of the EUV harmonics were then studied for different intensities and CEP values. On the other hand, the intensity dependency of the harmonic phase has been studied by *Lu et al* in MgO and SiO_2 [81], using an interferometric setup with two generating beams, and been found to exhibit a significant shift with increasing intensities. Similar to HHG from gases they attribute the change to a variation of the dipole phase with intensity.
As the harmonic signal from solids is highly sensitive to the band structure, the contradictions in the reports can very well be due to different material choices. A difference in distribution between intra- and interband contributions to the harmonics might also play a role as the driving laser pulses are in vastly different regimes, one a 40 fs pulse centered at 1320 nm and the other a 2.8 fs pulse at 730 nm.

2.2.4.5 Damage threshold

One of the initial expectations for HHG from solids were high conversion efficiencies due to the dense material. In reality the yield is limited due to the physical limitations of the target materials. One of the major limitations is their damage threshold. An intensity or flux that is too high can create irreversable damage on the material leading to a sharp drop in the harmonic yield [82]. The damaging can occur as a direct damage to the crystal structure due to the high fields or as a cumulative damage due to accumulated heat in the sample. While lasers in the kHz repetition rate range leave the material plenty of time to thermalise, MHz repetition rate lasers are however reducing the time available for thermalization greatly and are consequently prone to causing heat accumulation and irreversible damages. This is especially important since one of the major advantages of HHG in solids is the, compared with gases, low needed laser field strength. This incentives the use of high repetition rate lower peak power lasers, leading to more compact and cost efficient setups. Therefore, other ways of limiting the damaging of the target material are necessary.
One other way of mitigating possible damage is the use of longer wavelength lasers. It reduces the absorption of the fundamental laser, due to the photon energy being much lower than the bandgap, allowing for a higher driving flux. This argumentation is conceptually transferable to the material side, selecting only materials with high bandgaps. However, there is a multitude of low bandgap materials with interesting physical properties e.g. monolayer materials such as MoS_2 or graphene.

2.2.4.6 HHG from Nanostructured crystals

One of the biggest advantages of HHG in solids is the possibility to structure the surface of the material and tailor the properties of the generated harmonics. Due to the advent of semiconductor technology in the past decades the techniques required for this nanostructuring are readily available and allow the production of nearly

arbitrary complex patterns with high precision. The inspection of these nanostructures is a well explored question as well, however it often requires complex setups. A proposition on how to simplify these setups is discussed in chapter 4.
Nanostructures have been used in conjunction with HHG from solids with respect to different applications. This concept was first demonstrated in solids with an increase of harmonic yield of one to two orders of magnitude [83, 84, 85, 86], making it an technologically interesting option to integrate such source using only a femtosecond laser oscillator.
Aside from an increase in harmonic yield, a major interest of HHG from nanostructures is the possibility to influence the spatial structure of the generated harmonics. This allows for beam manipulation using diffractive masks as they are common in regular optics, without inserting an additional optic into the beam. An example is direct focusing of the generated harmonics using a patterned *fresnel zone plate* [23]. This has huge advantages over conventional focusing of EUV beams since the used optics are large power losses. In fact even complex beam shapes like laser beam carrying an *orbital angular momentum* can be realized using this approach as demonstrated by *Gauthier et al* [25] using a 2.1 µm fiber laser to generate in a spiral zone plate patterned in ZnO.

2.2.4.7 Propagation effects in solid state HHG

In the experimental realization of HHG from solids the most common geometry is a transmission geometry, in which the generating laser beam goes through the full sample before generating the observed harmonics at the back surface of the sample. This means that besides the strong field interactions leading to the generation of HHG one has to consider the changes to the laser pulse properties (spatial and spectral phases especially) induced by the propagation through the bulk material.
The first consideration is consequently effects raised from linear optics, of which there are two major ones: absorption through out the crystal and reflection on the entry surface. The first one, absorption of the crystal, leads to a reduction of the power at the exit surface and therefore reduces the reached intensity for the HHG process. Furthermore, high absorption can result in a considerable heat load in the sample increasing the probability of heat induced damages. As described in Section 2.2.4.5 this is avoided by using laser sources in the mid IR. This leads to a photon energy of the laser far below the band gap and therefore far off resonance, ensuring a high transmission. The second point is reflection on the entry surface of the material. For the most common case of a laser beam at normal incidence passing from vacuum into the sample, the polarization dependence of the Fresnel transmission vanishes and the transmission coefficient of the intensity can be written as

$$T = \frac{4n}{(1+n)^2}. \tag{2.21}$$

Here n is the refractive index of the sample material. While the power reflected like this is lost for the generation of high harmonics, it is also not contributing to the damage of the crystal.
Since the intensity of the driving field is sufficient to drive HHG, it is naturally

also sufficiently high to drive nonlinear propagation effects (see Section 2.1.2). Out of all nonlinear effects the main concern are SPM and self focusing, since they are present in all centrosymmetric materials and can alter the beam significantly before it reaches the back surface of the sample. With the tight focusing often used in geometries for HHG from solids, self focusing can alter the size and position of the focal spot drastically. The reduction in size of the focal spot can lead to an underestimation of the field strength present at the back surface of the sample and is therefore especially important when measurements of materials with different optical properties are compared. The SPM on the other hand is altering the spectrum of the driving laser pulse and can cause, due to self steepening, a significant blue shift of the fundamental spectrum that is transferred to the harmonics.
One option to avoid these propagation effects is the generation of harmonics in a reflection geometry as presented e.g. by *Vampa et al* [87]. They generate harmonics in magnesium oxide (MgO) and silicon (Si) using a 1.32 µm and 2.1 µm driving laser respectively and observe an even stronger signal from the reflected harmonics than for a transmission geometry. The absence of nonlinear propagation in the reflection geometry is also highlighted by *Xia et al* [57], contrasting measurements in transmission and reflection. The measurements in transmission show broader harmonic peaks compared to the reflection geometry. It also highlights a more pronounced response to the crystal symmetry for thicker crystals.

2.3 Conclusion

In conclusion, HHG from bandgap solids, semiconductors and dielectrics, has emerged as a new way to gain insight into strong field dynamics in solids. Due to the influence of the band structure the generation mechanism is more complicated than for atomic gases but posses the perspective of introducing new tools for the study of material properties and band structure measurements and also to tailor the harmonic emission spatially and temporally. However, conclusions on the band structure are highly dependent on advancements in the understanding of the fundamental generation mechanisms. While in the framework of TDDFT calculations fairly accurate predictions are possible, large scale computational effort makes iterative reconstructions not feasible. Simpler models, e.g. based on the SBE, are able to explain isolated effects and reach qualitative agreement for a variety of cases.
Experimentally harmonics have been generated in a wide variety of materials and with a broad spectrum of laser parameters. They pose several advantages over gas based harmonics e.g. by having a distinct response to elliptical driving lasers with a non zero contribution even at circular polarization states or the possibility to structure the medium at a nanoscale to tailor the harmonic emission.

Chapter 3

HHG from doped crystals

Looking at the intrinsic generating mechanism of high harmonics in solids (see chapter 2) it gets clear that they are highly sensitive to the bandstructure of the material they are generated in. In fact, methods to retrieve the bandstructure solely based on the harmonics have been proposed [18]. At the same time, doping is a technologically well established technique in the semiconductor industry to tailor the bandstructure of semiconductors to match technological needs. Combining these two approaches has the potential to reach more favourable conditions for HHG in technologically relevant semiconductors or further increase the efficiency of established HHG materials such as e.g. MgO or ZnO. However, descriptions related to its effects on HHG are sparse, counting only a few studies. Nevertheless, these studies predict a significant effect of the doping. Here we attempt a first experimental approach to the topic using chromium doped MgO and gallium implanted silicon, to evaluate the potential of this technology in the context of HHG from solids. The experimental study is supported by simulations performed by *Francisco Navarrete* and *Uwe Thumm* and the results are presented in this chapter as well as in [88].

The first section of the chapter treats measurements on MgO and MgO:Cr done at the laboratoire Charles Fabry from the institut d'optique graduate scholar (IOGS). The second section is based on measurements performed at CEA Saclay with an improved version of the XUV spectrometer using the new mid-infrared OPCPA system of the group. This is followed by a discussion of the two results. Finally, a different system, gallium implanted silicon, is presented.

3.1 Structure and theory of doped crystals

This section first briefly discusses structural changes occurring in crystal when foreign atoms are introduced, mainly focusing on the cases related to our experiments. As a second step the state-of-the-art for HHG in doped materials is discussed, which has been studied almost exclusively by numerical means. This is followed by a description of the model used by *Francisco Navarette et al* to simulate our experiments.

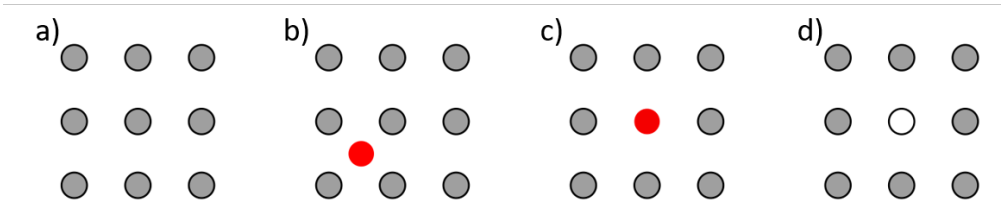

Figure 3.1: Illustration of different crystal defects alongside a perfect crystal. A grey dot symbolizes the native atom while a red one symbolizes an atom foreign to the crystal. The illustrations describe the pristine crystal(a), interstitial defects (b), substitutional defects (c) and vacancy (d).

3.1.1 Structure of doped crystals

Before going into the experiments it is necessary to clarify what a doped crystal is, which practical limitations have to be taken into account and what conclusions can be drawn from the theoretical studies. The starting point for these experiments is naturally the material and the changes made to it by the introduction of foreign atoms into the crystal structure. Since the main experiments are done on *magnesium oxide* (MgO), it will be used as an example through out the chapter.
In general, crystals can occur as single crystals or in polycrystalline form. However, since HHG is highly sensitive to the orientation of the crystal axis, experiments regarding HHG have been performed in single crystals in the vast majority of cases. These single crystals naturally have some crystal defects, the amount of which strongly depending on the material and the production process. Here mainly point defects are of interest which include (as illustrated in Figure 3.1) e.g.:

- *Interstitial defects*, meaning atoms placed at positions in the crystal where normally no atom would be present.
- *Substitutional defect*, where one atom of the crystal is replaced by another atom species, which is normally not present in the crystal.
- *Vacancy defects*, describing an empty site in the crystal structure that should normally be occupied by an atom.

Under normal circumstances the concentration of these defects in the crystal is low, with e.g typical doping concentrations for semiconductor electronics in silicon ranging from about 10^{-6}% to 0.1%. As a consequence the defects are distributed relatively sparsely.
Since the dopants are already included in the growing process of the crystal the distribution is in principal even throughout the crystal. However, clustering of defect sites can occur and is even necessary for some defects. One example for the necessity to build clusters is charge neutrality. Taking the later used chromium doped magnesium oxide as an example, a replacement of a Mg^{2+} site by a Cr^{3+} site is introducing an additional positive charge into the crystal. This is compensated by Mg^{2+} vacancies close to the Cr^{3+} defect, building a defect complex. However, in case the clustering of defects leads to an energetically better state, much larger

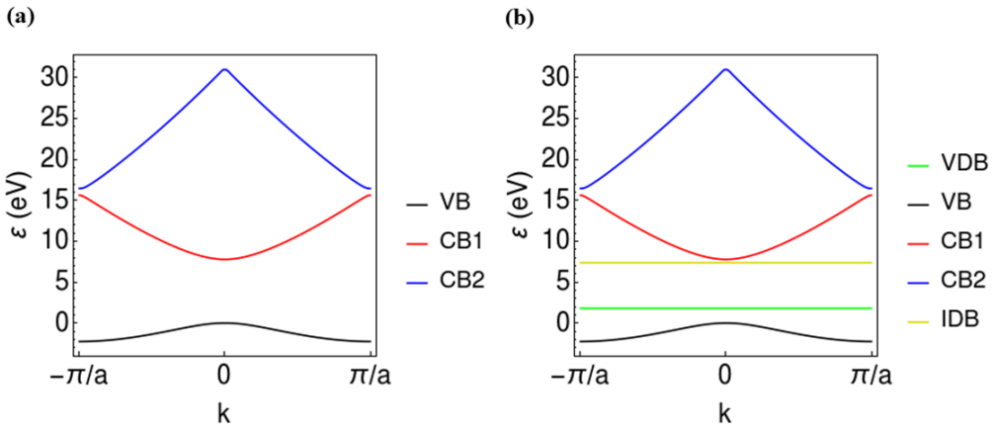

Figure 3.2: Example band structure for MgO and chromium doped MgO (MgO:Cr). Valence (VB) and two conduction bands (CB1 and CB2) of the (a) pristine MgO and (b) MgO:Cr crystal. Panel (b) includes the vacancy defect (VDB) and impurity defect (IDB) bands of MgO:Cr. Taken from the supplementary of [88]

defect clusters can build, e.g. vacancy clusters in silicon [89, 90, 91, 92]. Similar to liquids solids have a maximal amount of dopants that can be inserted in it. If the doping concentration grows above the material specific threshold it starts to form *precipitates*. These are small regions of nearly pure dopant material.
Depending on the concentration, the defects can have unique effects on the band structure of the solid, introducing so called defect states. These are flat bands that can be located inside the band gap [93], as illustrated in Figure 3.2. They can be categorized into two groups, depending on their ability to transfer electrons between the defect state and the unperturbed bands. In the first case the ambient temperature is high enough to allow electron transfer between the defect level and unperturbed bands. For the case of possible transfer donor doping creates a state close to the conduction band basically injecting an electron into the conduction band, while an acceptor doping is doing the same with a hole and the valence band. This is typically the case for n- and p-doping in semiconductors for electronics. If the defect band is far from any other band it acts as a single energy level, which an electron can be excited to. Deep defects are often connected to a large change of the crystal structure by the dopant.

The change in the overall band structure caused by defects plays a minor role due to the low concentration. Increasing the concentration to levels where it has a significant impact on the shape of the undisturbed crystal bands results in practical problems, due to the formation of precipitates. In this case the HHG can be considered to take place in two different materials: One being the precipitate and the other the bare crystal. For even higher doping concentrations the crystal structure can then be considered to have changed completely. As an example one can consider a pristine silicon crystal with each silicon atom having 20 diagonal and 6 direct neighbours. Consequently, if the doping concentration reaches about 5%, a defect site has on average one defect in its direct vicinity. The defects can therefore not be considered as isolated any more. This can even result in the crystal structure

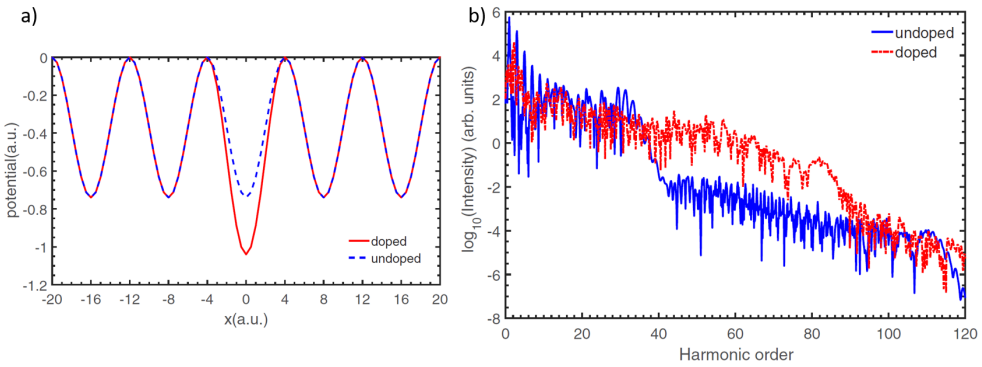

Figure 3.3: (a) Mathieu type potential used for the TDSE simulations of the harmonics. (b) High harmonic spectrum for the undoped and doped material at an concentration of 0.2. Images are taken from [19].

being lost completely and a transition into an amorphous structure. High doping concentrations as used in simulations regarding HHG from crystals are therefore often not realizable in experiments. Nevertheless, they can serve as an example to elaborate whether an effect is possible or not.

3.1.2 State of the art of HHG from doped crystals

The theoretical studies on HHG from doped crystals can be roughly divided into categories as described in section 2.2.3. The easiest approach is using a 1D TDSE model for the calculations, modelling the doping as a change in the local potential at one crystal site. The potential is chosen to be a Mathieu type cosine potential with a reduced or increased depth at the site of the defect. This also implies that the studied defects are substitutional defect, exchanging one atom with another. Due to the periodic boundary condition, the concentration can be controlled by the length of the linear chain. An initial study using this method [19] came to the conclusion that doping drastically enhances harmonics in the second plateau of the model system as visible in Figure 3.3. The doping concentration for these simulations ranges from 5% to 33%, showing a significant effect for all values. However, all these values range far above achievable doping levels for most crystals. As it will be important for later comparisons, the doping in this study appears to be a donor doping as it is a reduction of the local potential. They attribute this enhancement to a reduction of the Brillouin zone and the consequently higher transition rate to the second and third conduction band. Furthermore, the modification of the potential leads to a clear reduction of the bandgap.

Subsequent studies took a closer look at the effect in more detail, studying the type of doping necessary for the enhancement as well. While most studies show a strong enhancement for donor type doping [94, 20], the effect of acceptor type doping is more controversial. *Pan et al.* find an enhancement of the second plateau for changes of the potential according to donor and acceptor doping [94], also noticing a complete splitting of the valence band for high doping concentrations. The complete

splitting of the bands can however, be seen as practically irrelevant for practical cases since, as explained before, the material would undergo massive structural changes before reaching the necessary doping concentrations. In contrast *Yu et al* [20] find an enhancement exclusively for donor type doping.

3.1.3 Theoretical calculations for HHG from doped crystals

To explain our experimental results, theoretical calculations of our experimental case were performed by *Francisco Navarrete et al* [95, 96]. The basic assumption for the explanation is that the defect bands produced by the doping are, as they are close to the original bands, effectively reducing the band gap. This leads to an increased ionization rate and consequently a higher amount of electrons that can produce harmonics. Within the Keldysh approximation the ionization rate is then proportional to the harmonic yield resulting in a semi-quantitative approximation of the shape [95, 96]

$$\mathrm{Y}_{MgO}(E) \propto \exp\left(-\frac{\sqrt{8m^*_{vb-cb1}}\mathcal{E}_g^{3/2}}{eE\hbar}\right), \tag{3.1}$$

with E being the peak electric field and $\mathcal{E}_g$ the minimum bandgap between the valence band (VB) and the first conduction band (CB1). $m^*_{vb-cb1} = \left(\left|\frac{1}{m^*_{vb}}\right| + \left|\frac{1}{m^*_{cb1}}\right|\right)^{-1}$ denotes the reduced mass between VB and CB1, where m^*_{vb} and m^*_{cb1} are the respective effective masses of the valence and first conduction bands (compare Figure 3.2 (a)). This obviously reproduces the known behaviour of HHG from solids that a stronger electric field results in a higher harmonic yield. However more importantly importantly, it couples the harmonic yield to the band gap, as well as the reduced mass. A decrease of either one leading to an increase of the harmonic yield of the material.
To get a first estimate of the behaviour of doped materials equation 3.1 can then be modified to accommodate the defect bands. As mentioned before, in doped materials the modification is manifested in the band structure as flat bands within the band gap that couple to the valence and conduction bands along the entire Brillouin zone [97]. These bands are dispersion free [88], implying that the effective mass of associated electrons is large. Figure 3.2 (b) shows an illustration of these impurity band for the case of chromium doped MgO. The impurity band induced by the chrome atoms appears close to the first conduction band, while the simultaneously appearing magnesium vacancies are inducing an impurity band close to the valence band. Introducing the new structure into equation 3.1 by looking at transitions from the vacancy defect band to CB1 leads to [88]

$$\mathrm{Y}_{MgO}(E) \propto \exp\left(-\frac{\sqrt{8m^*_{vdb-cb1}}(\mathcal{E}_{cb1} - \mathcal{E}_{cdb})^{3/2}}{eE\hbar}\right). \tag{3.2}$$

As in equation 3.1 $m^*_{vdb-cb1}$ is the reduced mass, however in this case between the vacancy defect band and CB1. Consequently, the bandgap is changed as well now denoting the energy difference between the VDB and CB1. Since the effective mass

of the defect band is very large, the reduced mass can be approximated by just the reduced effective mass of the first conduction band. It is consequently larger than the reduced mass in pristine MgO, leading to a decrease in the harmonic yield. However, the reduction in the band gap has the opposite effect, increasing the harmonic yield. The change in the harmonic yield could therefore be strongly dependent on the change in bandgap caused by the introduction of defects into the material.

To directly support the experiments, simulations specifically for our case of chromium doped magnesium oxide have been done by *Francisco Navarrete et al.* The approach is based on numerically solving the SBE for an approximation of the MgO crystal structure. As a basis a cosine potential

$$V_j(x) = V_0 \cos(a r_j) \tag{3.3}$$

is used to represent the crystal structure of MgO. For the study of the polarization dependence the cosine potential is extended in both x and y direction to form a 2D grid. The band structure calculated from this approach reproduces the band width of the lowest conduction bands in the Γ-X direction of MgO accurately, however the calculated bandgap is only 4.2 eV. The valence bands are therefore shifted down to match the experimentally observed bandgap in MgO of 7.8 eV. One additional drawback of the SBE approach is their inclusion of a rather phenomenological dephasing time T_2. It accounts for damping effects of the occupation polarization caused by e.g. many body interactions, electron-electron scattering and phonon interactions. For the simulations the dephasing time is set to the length of a quarter cycle of the driving laser wavelength. For the used laser system with a central wavelength of 1500 nm this means a dephasing time of 1.3 fs.
To incorporate the doping into the model, single minima of the potential are modified by increasing or decreasing their depth. The two effects taken into account for this are the replacement of Mg^{2+} sites with Cr^{3+} atoms and the introduction of vacancies. For vacancies the oscillation amplitude is increased, while for substitutions the amplitude at neighbouring lattice positions is decreased. This results in a new potential of the structure

$$V_j(x) = V_0 \cos(a r_j) + \begin{cases} V_{vac} \cos(a r_j), & n_{vac} a \leq x \leq (n_{vac}+1)a \\ V_{imp} \cos(a r_j), & n_{imp} a \leq x \leq (n_{imp}+1)a \end{cases}, \tag{3.4}$$

with n_{vac} and n_{imp} being the positions of the vacancy and impurity, as well as V_0, V_{imp} and V_{vac} being the potentials of the pristine solid, the impurity and the vacancy respectively. It has to be mentioned that different modelling of the harmonics and the parameters used within the model of the potential can have dramatic effects on the harmonic emission [98]. The values for the impurity and vacancy potential are chosen in order to match the bandgap change of 1.8 eV observed in the used samples, as described in section 3.2.2. An example for the results of these simulations can be seen in Figure 3.4. The polarization is chosen to be along the Γ-X axis of the crystal with a laser wavelength of 1.55 µm (0.80 eV). The spectra show an increase of yield for all harmonics from the MgO:Cr. The appearance of weak even harmonics can be attributed to numerical noise.

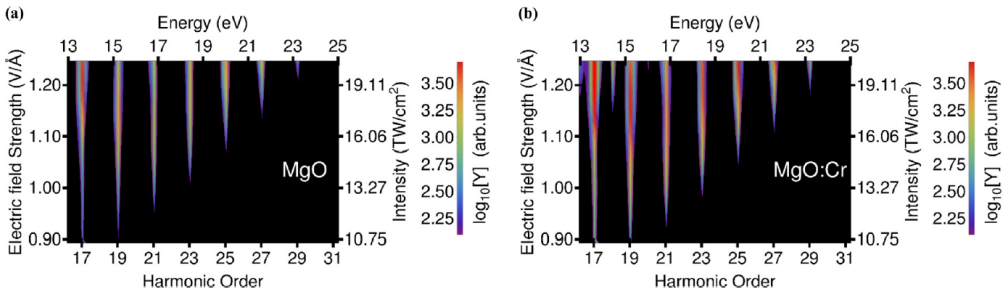

Figure 3.4: Calculated spectra for MgO (a) and MgO:Cr with a 0.5% doping concentration (b). Reprint from [88].

3.2 First measurements on MgO:Cr using a 1.55 µm laser

The first measurements were performed at the *Institut d'Optique* using a mid IR laser system. The original goals were the final build and test of the XUV spectrometer and the study of MgO and chromium doped MgO (MgO:Cr). Here MgO:Cr is taken as an example of a doped semiconductor crystal, to have a first look at the effect of doping. Since the base material, MgO, with its high bandgap is well suited for the generation of high harmonics up to 25-30 eV, at least similar behaviour is expected for MgO:Cr. This makes the material a good candidate for the study of spectral signatures of the doping in the 10-25 eV range.

3.2.1 Setup

The laser system used for these experiments is a two stage OPCPA pumped by a Ytterbium:YAG fiber laser from *Amplitude Systems*, followed by a multipass bulk material based post compression stage. The OPCPA is driven by a pump laser providing 400 fs, 400 µJ pulses centred at 1020 nm at 125 kHz. Inside the OPCPA a portion of these is driving a white light stage to generate a seed for the OPA stages, while the other part is used as a pump for the OPA stages. The resulting pulses are then compressed using 210 mm of bulk SiO_2, leading to 19 µJ, 63 fs pulses centred around 1550 nm. This bulk compression scheme is possible at 1550 nm as SiO_2 introduces negative GDD, with the zero dispersion point located around 1270 nm. These pulses are then fed into a multipass compression cell, where 10 passes through a 2 mm silica plate are done in a soliton compression scheme. As a result the pulses are compressed to 22 fs, with a slight pre- or post pulse. The beam profile has a slightly oval shape with a core diameter of about 4 mm and an M^2 below 1.5. A full description of the laser system and its parameters can be found in [99].

The laser is guided towards a vacuum chamber that contains the HHG generation stage and a home build XUV spectrometer, as depicted in Figure 3.5. Right before the chamber the beam passes a half wave plate and a polarizer, used to regulate the power of the beam, as well as an iris to regulate the beam diameter and cut artifacts around the beam. The experiments are generally carried out using a vertical

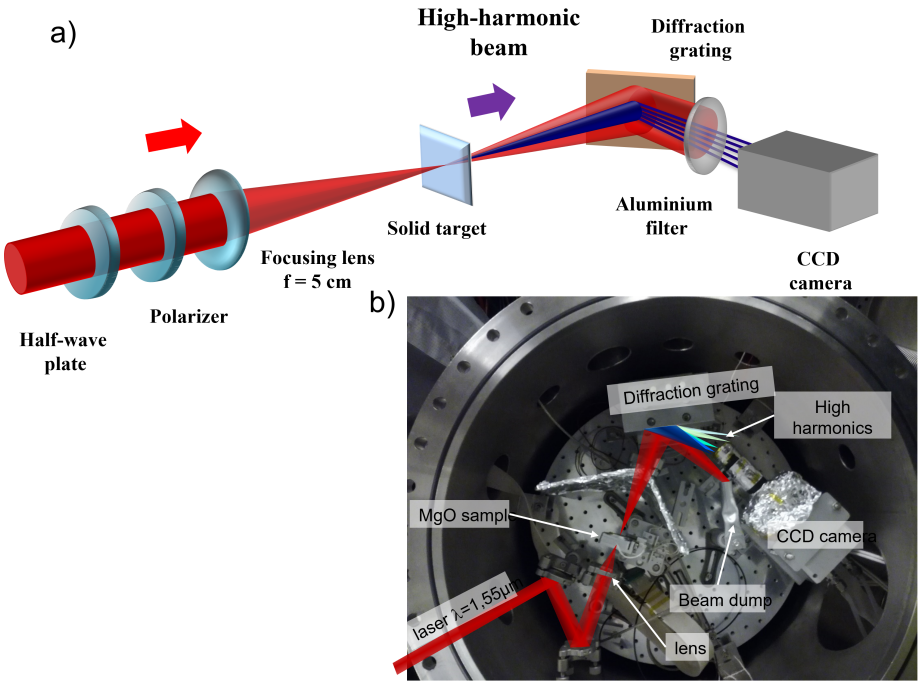

Figure 3.5: (a) Scheme of the beamline used for the experiments at IOGS (b) Image of the HHG generation stage and XUV spectrometer. The half wave plate and polarizer are located outside the vacuum chamber.

polarization of the laser. Inside the chamber the beam is focused into the sample using a 50 mm CaF_2 focusing lens with an anti reflective coating. The sample itself is mounted on a 4D stage, allowing the exact placement of the sample in XYZ and θ. Here θ is the rotation angle of the sample, defining the direction of the crystal axis with respect to the polarization of the laser pulse. A rotation of the sample is preferable compared to a change of the polarization direction of the laser, due to the polarization dependent reflectivity of the optics, especially the grating.
After generation, the EUV beam passes another iris and enters the home build spectrometer, consisting of a grating and a CCD camera. The grating is a toroidal platinum coated grating with 2400gr/mm from a *MCPherson model 302 monochromator*. The spectral lines are therefore imaged on the Rowland circle, where the spectrum is recorded using a *Princeton Instruments* MTE CCD camera with 2048x2048 pixels and pixels size of 13 µm . As visible in Figure 3.5 (b), the camera needs careful shielding of the stray light coming from the HHG generation stage. This is due to the high sensitivity of the CCD to wavelength in the green spectrum, which overlaps with the third harmonic of the laser. The CCD camera is shielded using a thin 150 nm aluminium filter. However, the use of an aluminium filter restricts the detectable energy range to energies above approximately 15 eV. This is far from the band gap of the mainly studied material, magnesium oxide, and therefore cuts part of the regions of interest. Nevertheless, the step from the first to the second plateau in the harmonic spectrum is well within the detectable region.

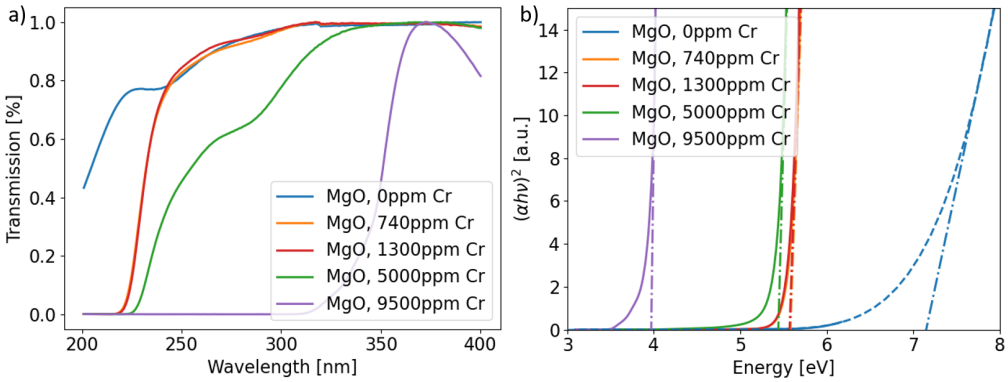

Figure 3.6: (a) absorption spectra for MgO doped with a variety of chromium concentrations. (b) Tauc plots based on the absorption spectra. The dashed line shows the fitted extension for the pristine MgO case, while the dash dotted lines show the linear fits to estimate the bandgap. Same data as in [88].

3.2.2 Sample properties

The samples used in the experiments are magnesium oxide (MgO) samples doped with chromium at 5000ppm (0.5% Cr) and 9500ppm (0.95% Cr), corresponding to doping concentrations of $2.6 \cdot 10^{20}$ and $5 \cdot 10^{20}$. A pure MgO crystal from the same supplier (*SurfaceNet*) is used as a reference. All crystals are 5x5 mm in size, 200 µm thick and cut in the [001]-direction. The samples have been used in experiments before and as a result only the pure MgO and 5000ppm MgO:Cr samples are in a good state, while the 9500ppm MgO:Cr sample shows a slightly milky surface. The color ranges from completely transparent for the pristine MgO to a darker greenish color for the sample doped at 9500ppm. As visible in Figure 3.8, the color change is barely noticeable for the sample doped at 5000ppm, while it is clearly present for the sample at 9500ppm. This visual discrepancy between the different doping levels is partially supported by transmission measurements shown in Figure 3.6 (a). They show a shift of the absorption edge of the material towards higher wavelength, indicating a reduction in the bandgap of the material. Notably, the difference between the lower doping concentrations from 740ppm up to 5000ppm is low, while the absorption edge of the 9500ppm sample is shifted much further. Focusing on the two most used materials in the experiments, MgO:Cr 5000ppm and pristine MgO, Tauc plots are used to estimate the bandgap of the materials (see Figure 3.6 (b)). For the MgO:Cr 5000ppm sample this results in a bandgap of 5.44 eV. Since the detector for the absorption measurements only covers a range down to 200 nm, the absorption edge of MgO is partially outside the detection window. To estimate the bandgap of our sample despite this, the missing part of the Tauc plot is approximated by a fifth order polynomal fit. This results in a bandgap of 7.15 eV for the pristine MgO giving a bandgap reduction by 1.7 eV. For pristine MgO bandgap values of 7.8 eV have been reported before [100], indicating that the difference in bandgap could be

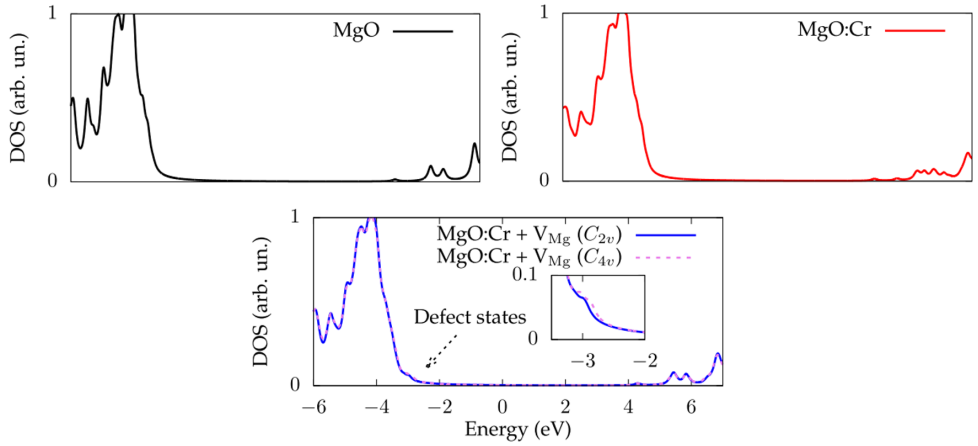

Figure 3.7: Density of states for pristine MgO, MgO:Cr with a chromium concentration of 0.46% and MgO:Cr in the same concentration but including neighbouring vacancies. Rearranged from [88].

even higher. The difference to the literature value can be attributed largely to the incomplete absorption spectrum.

This large change in the bandgap energy is sort of surprising and is not reproduced by the supporting *ab initio* DFT based theoretical calculations of the density of states (DOS), done in parallel by *Nicolas Tancogne-Dejean*. The simulations are done using a 6x6x6 supercell, which yields a defect concentration of 0.46% when replacing one magnesium atom with chromium. Details about the used DFT parameter can be found in the supplementary material of [88]. As visible in Figure 3.7 (a), the literature bandgap of pristine MgO of 7.8 eV is well reproduced by the DOS. Introducing chromium as a substitutional defect into the MgO leads to the formation of a defect band close to the first conduction band. While these defect bands can act as a transitional energy state for the harmonic generation, they are hardly enough to explain the sharp change in the bandgap. However, the introduction of chromium into the material enforces the creation of additional crystal defects. The most important one of those is the creation of magnesium vacancies to compensate for the additional charge introduced into the material by replacing Mg^{2+} with Cr^{3+}. These vacancies have to be generally located close to the substituted Mg^{2+} atom [101]. This leads to two main configurations of the vacancy with respect to the chromium atom: along the [001] or [110]-axis, meaning either directly or diagonally besides the Cr^{3+} atom. Notably, these vacancies, as they compensate for two positive charges, can form complexes of two Cr^{3+} and one vacancy [102]. Figure 3.7 shows the change of the band structure including the single vacancies into the picture. In this case the change is larger with not only the creation of additional defect states close to the top of the valence band, but also a change in the top parts of the valence band ultimately leading to a reduction of the bandgap by 0.6 eV. Compared to the experimentally observed reduction of 1.6 eV this is still small, however it is a significant change of the structure. The remaining differences can for example originate from underestimating the doping concentration or further

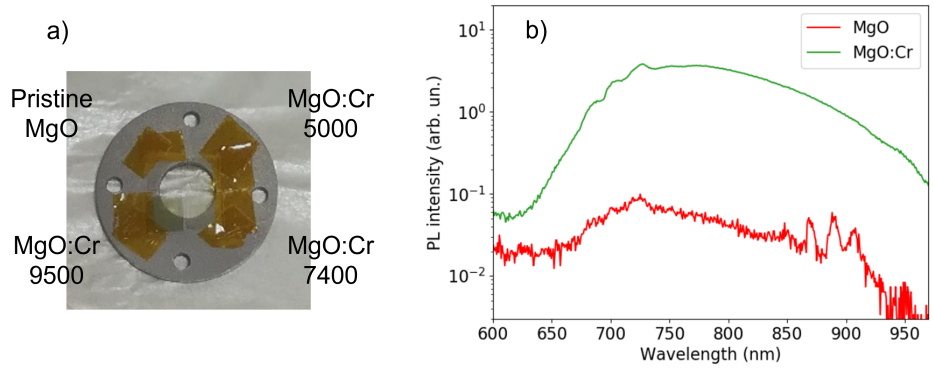

Figure 3.8: (a) Picture of the chromium doped MgO samples on a typical holder. (b) Emission measurements of the pristine MgO and MgO:Cr 5000ppm samples after excitation with a 365 nm diode laser.

changes in the crystal structure that the theoretical model does not account for. Notably, different configurations of the vacancy-chromium complexes yield similar results for the band structure. This indicates the viability of simpler representations including only defect bands, as it is used in simulation of the HHG process.

One way of verifying the presence of chromium and vacancies in the material experimentally are luminescence measurements. For these the pristine MgO sample and MgO:Cr 5000ppm have been excited with a 365 nm diode laser and the luminescence is recorded using an *Ocean Optics QE Pro* spectrometer. The fundamental is rejected by passing a long pass filter with a a cutoff at 514 nm. The resulting luminescence is shown in Figure 3.8. The signal shows three distinct features. The first is the broad luminescence ranging from 700 nm up to nearly 900 nm. This type of signal is reported for ${}^4T_2 \rightarrow {}^4A_2$ transitions of Cr^{3+} atoms in an orthorhombic site, meaning with a vacancy nearby [103, 102, 104]. The second feature are the three peaks around 720 nm and can be attributed to the pure Cr^{3+} atoms [102, 105, 106, 107]. Since chromium is a common contamination even for pristine MgO samples, theses peaks are visible in the spectrum from the pristine MgO sample as well. Lastly the peaks between 850 nm and 900 nm can be attributed to $Mg(OH)_2$ contamination of the sample [107].

A major problem for the study of optical effects in doped materials is that optical constants for those materials are rarely available. This also means the change of these constants for doped materials compared to the pristine ones is unknown, aside of some very common material combinations (e.g. boron doped silicon as it is used for electronics). This prevents an accurate estimation of propagation effects and especially the difference between pristine and doped materials. However, changes to the temporal and spatial shapes of the pulse have been shown to have a huge impact on the HHG spectrum. The first experiments at the IOGS were done under the assumption that the change in optical properties between MgO and MgO:Cr 5000ppm are negligible due to the low doping concentration. There are studies showing this for different materials, e.g. Nd:CaF_2 [108], however no such study is currently present for MgO:Cr. Since the temporal shape of the generating pulse

and the reached intensities, have a huge impact on the harmonic yield, this is a reoccurring source of uncertainty throughout the measurements. Measurements to estimate the effects of propagation were done after it was identified as a critical issue and are presented in section 3.3.

3.2.3 Results

The MgO and MgO:Cr samples can be compared with respect to different facets of HHG in solids. The starting point is a comparison of the direct CCD images, using the additional information to obtain a first gauge of possible propagation effects. Afterwards, the two samples are compared with respect to the scaling of the HHG yield as well as the cutoff with intensity. This is followed by a comparison of the anisotropic behaviour of the two materials.

3.2.3.1 Calibration and spatial effects

Since high harmonics with energies well above the bandgap face strong reabsorption, the observed harmonics are generated only in the last nanometers of the sample. As mentioned before this means the pulse shape of the generating pulse can be changed by the nonlinear propagation through the sample, prior to generation. Due to the high sensitivity of the generation process to the pulse shape this can lead to unexpected behaviours of the harmonics, especially for thicker samples. The signal detection of the home build XUV spectrometer offers the possibility to partially evaluate these by relying on the information in the dimension perpendicular to the grooves of the grating. This can help to identify effects that influence the spatial evolution of the beam such as SPM. With a stronger SPM in the sample the size of the focal spot at the back surface shrinks and higher intensities are reached, leading to a similar effect as expected from the doping. However, this change in the generation spot can lead to a larger spatial extension of the harmonic signal. Additionally, shifts in the divergence of the harmonics e.g. due to plasma generation at the surface can show in the images.
Figure 3.9 shows the CCD images at different powers and therefore different driving intensities for pristine MgO and MgO:Cr 5000ppm. For the measurements the power was varied between 200 mW and 500 mW, corresponding to a vacuum intensity range from 9.6 $\mathrm{TW/cm^2}$ to 24 $\mathrm{TW/cm^2}$. The intensities are calculated based on the powers measured in front of the vacuum chamber and therefore do not take reflection or transmission losses into account. The beam size is regulated by an iris in front of the chamber, which is set to 4 mm. The harmonic signal is optimized by placing the sample before the focus and then gradually move it towards the focus until a maximum for the harmonic signal is reached. This places the actual focal spot at the back surface of the sample, independently of any propagation effect. The acquisition time of the CCD is 30 s after which the beam is blocked by a shutter to avoid artefacts due to the long readout time of the CCD. To reduce the readout noise of the CCD and gain a reasonable signal to noise ratio, the CCD images are acquired using a 16x16 binning. This reduces the original 2048x2048 pixels

of the camera down to only 128x128 pixels. Before the acquisition a background image with a blocked laser beam is taken and is subtracted from each measured spectra. This is necessary since the background images show a faint stray light signal that follows the outline of the aluminium filter and some hot pixels on the camera, making the background non homogenous. The sample is slightly moved perpendicular to the beam after each measurement to refresh the used spot and avoid measurements on pre damaged spots. The full image shows the spectrum in the center with lower wavelength at the right. Since the aluminium filter is cutting the signal below 15 eV, the visible strongest harmonics can be identified as H21, whose energy is located close the top of the first conduction band. Consequently, the following, much weaker, harmonics are originating from the second conduction band. The images in Figure 3.9 are shifted to the same noise background by using a region far from the signal.

The images show a drastic evolution with increasing intensity for both materials. At lower powers the harmonics appear as uniform gaussian like peaks with the harmonics at the upper edge of the first conduction band being clearly visible. With increasing power the harmonic signal transfers into a "half moon" shape (e.g. at 450 mW). This change in shape is due to beam profile, where the highest intensities are only reached near the center of the beam. Consequently, the nonlinear propagation effects are significantly stronger for the central part of the beam than for the outskirts and only the center is blue shifted. Above a power threshold of about 450 mW for the pristine MgO and 425 mW for the MgO:Cr the signal starts to degrade. At first only the overall signal strength is reduced, while at even higher powers the spatial structure of the beam starts to break apart. This is a clear sign of the laser starting to damage the sample. As the damage develops over time the most likely damaging mechanism is thermal damage due to heat accumulation. The apparent cut of the spectral signal in the vertical direction is caused by the iris after the generation stage. Since this iris is an integral part of the shielding that protects the CCD of fluorescence from the crystal it can not be removed without a major loss in the signal to noise ratio.

The damaging of the sample visible in the images is a gradual process. Therefore, short acquisition times, capturing the state before significant damage, would result in accurate measurements even at higher powers. However, the photon flux of this experiment is not high enough to reach sufficiently short acquisition times. One way around this is to continuously move the sample in the focus plane. The constant refreshing of the used spot avoids local heat accumulation in the sample and prevents the damage. The resulting images are shown in Figure 3.10. The measurements are done under the same conditions as the previous static measurements. The spatial effects visible in the static measurements are stronger, with a clear blueshift of the signal with increasing power. For the MgO:Cr the breaking of the spatial structure is especially pronounced for powers of 400 mW and more, where the H21 peak starts to split. However, the constant moving comes at the benefit of increased signal from the second conduction band, which was barely present in the static measurements.

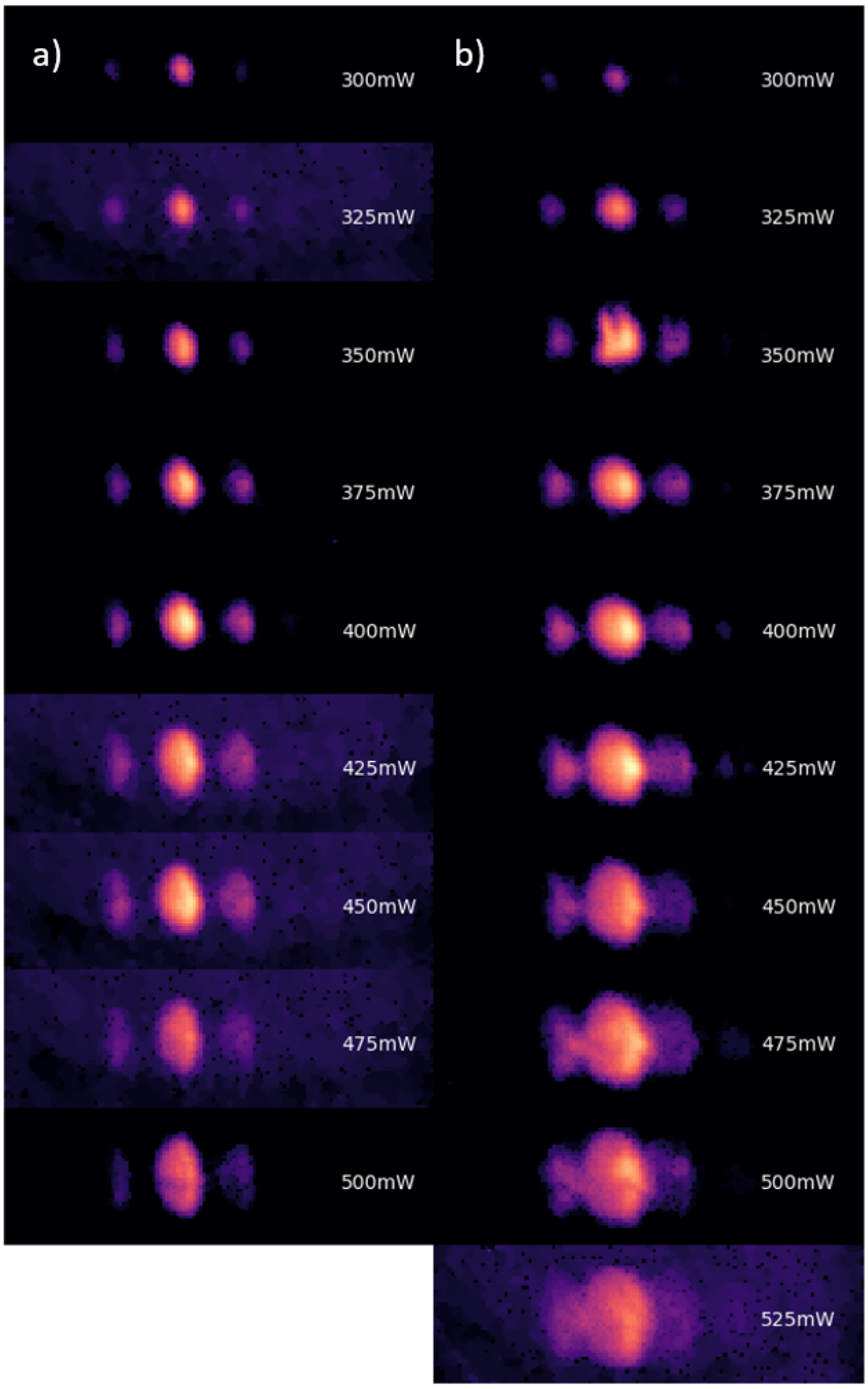

Figure 3.9: Evolution of the CCD signal with increasing intensities in logarithmic scale for MgO (a) and MgO:Cr 5000ppm (b).

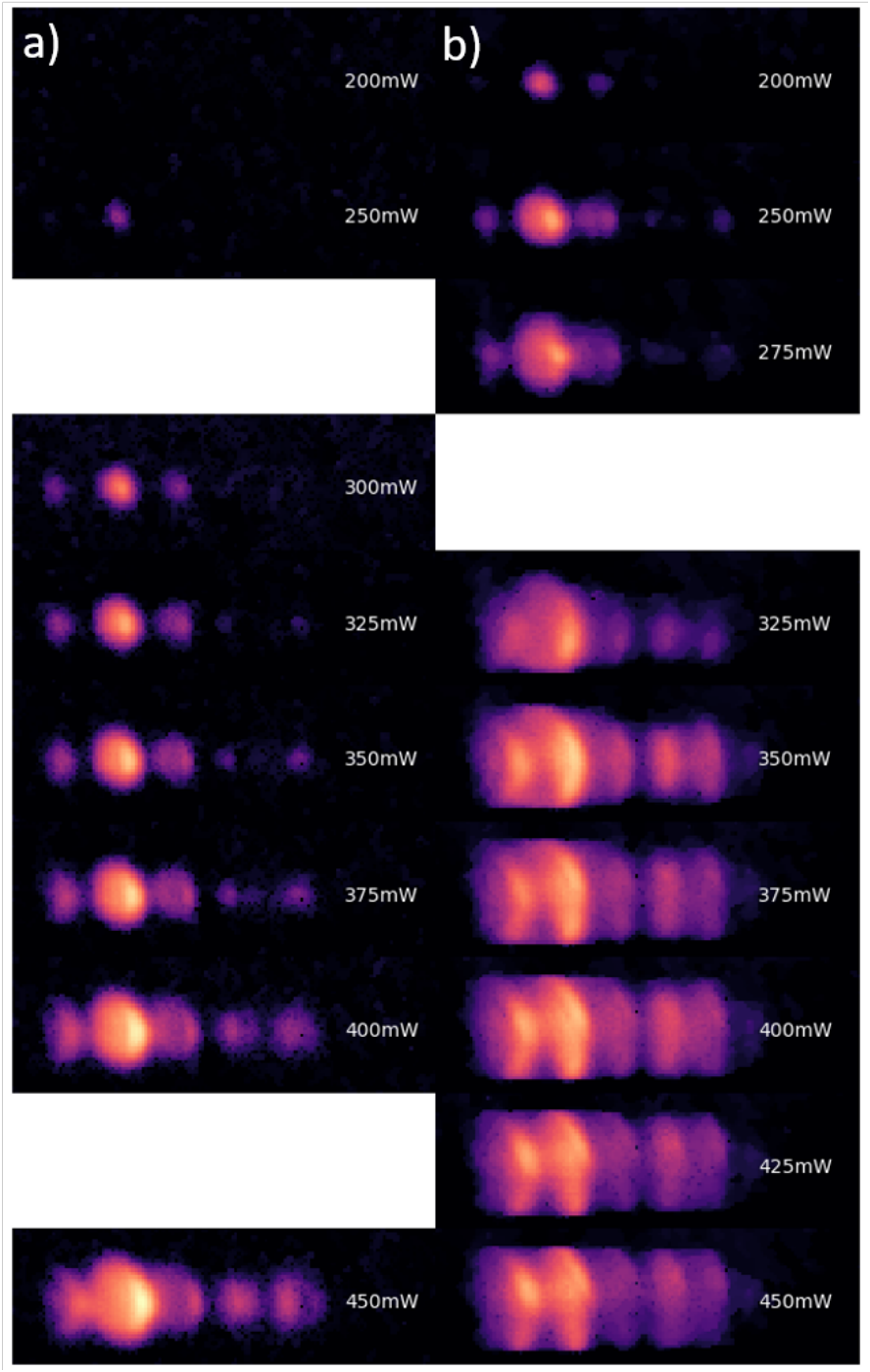

Figure 3.10: CCD images of the spectrum for pristine MgO (a) and MgO:Cr (b) in logarithmic scale, acquired while continuously moving the sample in the focal plane. For the case of MgO:Cr scanning was started only after a power was reached that showed signal decrease due to damaging (325 mW).

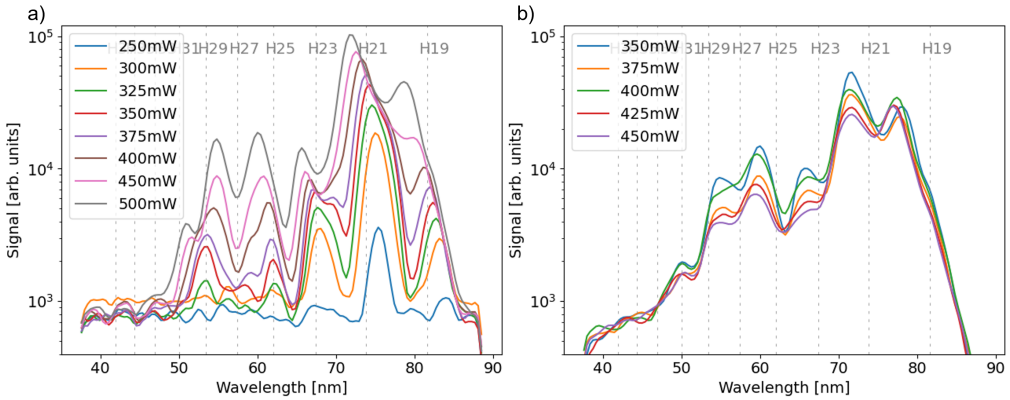

Figure 3.11: Spectra from MgO (a) and MgO:Cr 5000ppm (b) extracted from the CCD images shown in Figure 3.10. For MgO:Cr 5000ppm the spectra utilizing the scanning mode are shown.

3.2.3.2 Power scaling of the harmonics

As a next step spectra are extracted from the images as described in Appendix A. The spectra corresponding to the MgO case in Figure 3.10 are shown in Figure 3.11. Towards longer wavelengths the cut of the aluminium filter is apparent as a sharp drop in signal. This allows to verify that the first visible harmonic is the 19th harmonic. The drop in signal after harmonic 23 is the border between the first and second conduction band. Due to the decreased signal of H23 compared to H21, it is likely that H23 is located within the bandgap between the first and second conduction band. The signal then continues to stretch over the second conduction band and drops below the noise level at its end. This structure of the spectrum is in good agreement with other measurements on MgO [77]. One very notable effect in the spectrum is a blue shift with increasing power, which is especially pronounced for the harmonics in the first conduction band. An increase in power means an increase of intensity, which in turn increases the SPM during the propagation through the MgO. The self steepening then causes a shift of the central frequency of the laser spectrum towards the blue, shifting all harmonics as well. However, the situation in the second conduction band is more complex, as the evolution is not a pure blue or red shift. At low intensities H25 is centred at 62 nm and shifts towards the blue with increasing intensity. Meanwhile, H29 is initially located at 54 nm and shifts towards the red. However, H27 gradually disappears towards higher intensities seemingly by merging with H25, as H29 shifts towards its position. This behaviour can not be explained by changes in the driving pulse alone as this would lead to a pure blue shift.

Especially the spectra at higher power are showing a gradual merging of the harmonics. To still access the power of individual harmonics, each harmonic peak is approximated assuming a gaussian shape of each single harmonic.

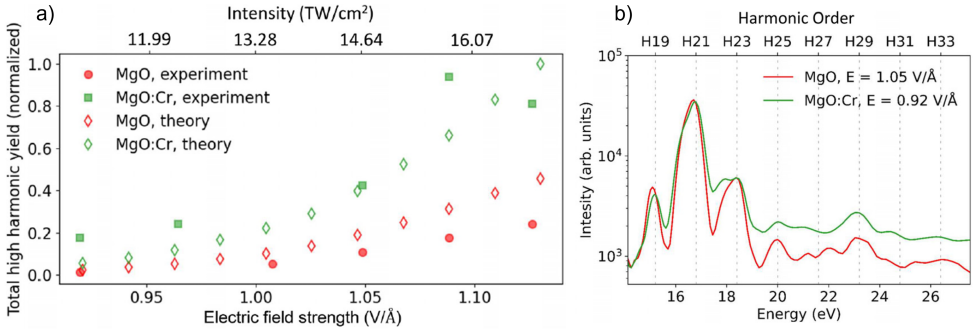

Figure 3.12: Comparison of (a) the integrated harmonic yield for MgO and MgO:Cr and (b) two spectra one from MgO and one from MgO:Cr 5000ppm at different intensities. Reprint from [88]

3.2.3.3 Comparison of pristine and chromium doped MgO

As a starting point for the comparison of the two samples, two spectra at different intensities are shown in Figure 3.12 (b). The spectra are based on the data shown in Figure 3.10 and are taken at 11.2 TW/cm^2 (0.92 V/Å, 250 mW) for the MgO:Cr and 14.6 TW/cm^2 (1.05 V/Å, 325 mW) for MgO. The intensities are calculated as vacuum intensities assuming a gaussian beam shape, based on the power measured in front of the chamber. Consequently, they do not account for losses due to optics before the sample, reflection on the samples surface and absorption inside the sample itself. The experimental spectra of MgO and MgO:Cr are matching for the harmonics originating from the first conduction band, while harmonics from the second conduction band are yielding a higher signal for MgO:Cr. However, the signal from the second conduction band has to be taken with care since it is low and with variation of noise levels between the measurements could therefore have a serious impact. Nevertheless, this shows that the harmonic generation in MgO:Cr is more efficient than in pristine MgO.

In order to further compare the experiments with the simulation, which are based on the field strength, the field strength in the simulations has to be matched with the experimentally observed intensity. To achieve this the appearance of H29 is used as a reference point for a field strength of 1.23 V/Å in vacuum. This leads to a factor of 4.2 between the fields used for the theoretical calculations and the vacuum intensities calculated from the experimental data. With this the total harmonic yield can be calculated and compared between the simulation and experiment (see Figure 3.12 (a)). This has the additional advantage that spectral resolution is irrelevant and therefore even hard to distinguish harmonic peaks are not disturbing the picture. Here the experimental total harmonic yield is calculated by integrating the spectral signal between 14.4 eV and 25.6 eV, covering a range from the beginning of the spectrum at the aluminium filter cut up to the harmonics emitted from the top of the second conduction band. It is visible that the total harmonic yield from MgO:Cr is higher than from the pure MgO by a factor of 2-3 up to an intensity of 20 TW/cm^2. In order to compare these results to the theoretical calculations the same total harmonic yield is calculated for the respective cases. However, the

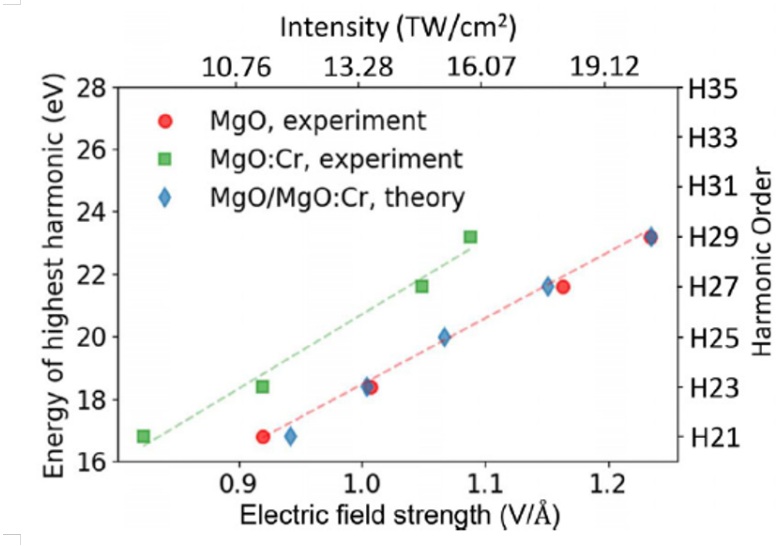

Figure 3.13: Scaling of the highest detectable harmonic with increasing field strength.

signal appearing at the position of even harmonics in the calculated spectra are not counted into the total harmonic yield, since they are a like due to computational noise in the simulation and no even harmonic signal was present in the experiments. The theory predicts an efficiency that starts at about the same signal for low intensities, but quickly diverges due to the steeper increase of the signal for MgO:Cr. Comparing this to the experimental data, the increase of signal predicted for the MgO is not completely matched by the experiment, with the experiment producing less signal than expected. However, the qualitative agreement is good, showing a slightly increasing slope for the experimental data as well. For the MgO:Cr the agreement is less pronounced. The overall slope matches the prediction of the theory, but the variance of the single points is high. For intensities higher than $20\,\mathrm{TW/cm^2}$ the signal starts to saturate. The onset of saturation for MgO:Cr is at lower intensities compared to the MgO, likely due to the lower bandgap and consequently higher electron transition rate. Since the theory does not account for the mechanisms that lead to a damage of the crystal structure, the saturation is not reproduced by the calculated spectra based on the SBEs.

Another aspect of HHG and its applications is the highest photon energy available in the spectrum, the cutoff energy. A comparison of the highest observable harmonic from both samples is shown in Figure 3.13 and reveals an increase of 2 eV for MgO:Cr with respect to the MgO. In both cases the highest detected energy scales linearly with the driving field. However, due to the increased efficiency of the harmonic generation this increase has to be taken with care and is not equivalent with an increase of the cutoff energy. The cutoff marks the end of the plateau region of the harmonic signal, while in our case the signal of higher harmonics is increased above our experimental noise level due to the increase in harmonic signal. This is further supported by the spectra calculated from the SBEs that show no increase between MgO and MgO:Cr.

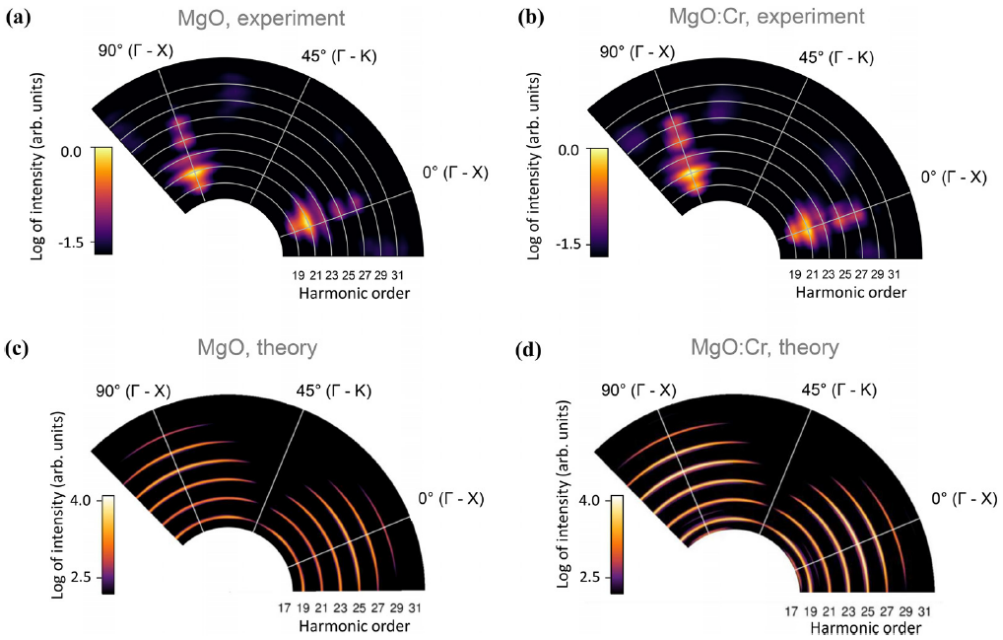

Figure 3.14: Harmonic yield for different orientations of the crystal axis for MgO (a) and MgO:Cr 5000ppm (b). Calculated harmonic yield for both cases respectively (c)-(d). Reprint from [88].

3.2.3.4 Anisotropy scans

Besides the dependency on the intensity, the harmonics are sensitive to the orientation of the crystal as well. The measurement was carried using a 4 mm iris opening and a laser power of 450 mW for the pristine MgO, while the MgO:Cr 5000ppm sample was only driven by 350 mW. This corresponds to a field strength of $20\,TW/cm^2$ (1.23 V/Å) for the pristine MgO and $15.7\,TW/cm^2$ (1.09 V/Å) for the MgO:Cr 5000ppm. The power was in both cases chosen to be close to the damage threshold of the sample to maximize the signal. To avoid differences due to different reflectivities of optical components, the polarization was kept vertical and the sample was rotated covering a range of 130° in 3° steps. Based on the four fold symmetry of MgO this means that two full Γ-X maxima of the harmonic yield are covered. The results are shown in Figure 3.14. The measurements on pristine MgO show the expected four fold symmetry corresponding to the face-centered cubic crystal of MgO. Here the Γ-X direction leads to efficient generation and the Γ-K direction has a comparatively low harmonic yield. This behaviour is shown by the chromium doped MgO as well. However, as already seen for the intensity dependence, the harmonic yield of MgO:Cr is comparable to pristine MgO despite the lower power of the driving field. Notably, the measurement system is not sensitive enough to record the harmonic signal in the Γ-K direction, which is for this wavelength region 2-3 order of magnitude weaker than the Γ-X signal. However, based on literature and later measurements (see e.g. section 5.4) there are harmonics emitted in this direction as well.

As a comparison the angle dependent spectra have been calculated by *Francisco*

Navarette based on a 2D potential. An intensity of 1.23 V/Å is used to match the regime of the experimental results. The calculations (Figure 3.14 (c-d)) generally fit the experimental results, however the decline of the harmonics with increasing angle is slower than the one observed in the experiments. Additionally, the simulated single harmonics are spectrally much more narrow than in the measured harmonic spectra. This is likely a result of using a flat top pulse profile containing five field cycles for the simulation. While the amount of cycles matches the experimental conditions, the flat top profile is reducing the spectral bandwidth of the driving pulse resulting in narrow harmonic peaks.
One distinct notable feature in Figure 3.14 (a-b) is the emergence of a small high energy signal around the 23° that repeats with the crystal symmetry. Due to this symmetry following behaviour it is unlikely that this signal can be attributed to a reflection of stray light onto the CCD. The origin of this is hard to explain since it is not clear if it originates from the HHG process or can be attributed to fluorescence. However, there are studies showing a pronounced harmonic response for a similar energy and angle [74].

3.3 Effects of nonlinear propagation

To further characterize the propagation effects in the samples and possible differences in the propagation between MgO and MgO:Cr, the optical properties of the samples in the intensity regime necessary for HHG have been studied. The study is focused on linear and third order $\chi^{(3)}$ effects, as they represent the most prominent possible nonlinear effects that may occur in our interaction regime. Consequently, three possible effects are studied: SPM, self focussing and absorption. The measurements are done using the 1.8 µm signal of the OPCPA described in section 3.4.1. The setup consists of a 5 cm focusing lens to tightly focus the beam into the sample. Afterwards, the beam is imaged onto a CCD camera using a microscope objective to obtain images of the focal plane. For the spectra and FROG measurements the beam is collimated using another 5 cm focusing lens and guided either into a home build FROG or into a spectrometer (*Fastlite Mozza*).

Absorption
Table 3.1 shows the power loss in the pristine MgO, MgO:Cr 5000ppm and 9500ppm samples. The power is measured in two positions for each sample: one with the samples back surface in the focus and one with the sample far from the focus. This allows to estimate the effect of nonlinear absorption. For the position far from the focus all samples show a similar absorption of 30 mW. Bringing the sample in focus increases the absorption by 25 mW to a total of 55 mW. This clearly shows that nonlinear effects inside the sample play a significant role. For the MgO:Cr 5000ppm the absorption is slightly higher reaching 63 mW. However, the higher doped MgO:Cr 9500ppm shows a lower absorption at the same level as pristine MgO, with the higher doped sample being in worse condition than the MgO:Cr 5000ppm. While this difference is a hint that the MgO:Cr 5000ppm sample is different, this is close to the fluctuation range of the power measurement.

	without sample	MgO	MgO:Cr 5000ppm	MgO:Cr 9500ppm
in focus	225 mW	170 mW	163 mW	170 mW
out of focus		195 mW	195 mW	195 mW

Table 3.1: Transmission of the two doped samples used at the IOGS in an in air setup with the focal spot set at the back surface ("in focus") and inside the crystal ("out of focus").

Self focusing

Self focusing can change the size of the focal spot at the back surface of the sample, which is at the same time the critical area for the generation of the harmonics. For MgO with a refractive index of 1.7355 and a nonlinear refractive index of $39 \cdot 10^{-17} \frac{\text{cm}^2}{\text{W}}$ the critical power for self focusing (see equation 2.9) is around 7 MW, much lower than the 235 MW peak power of the laser. However, the doping is only a small change of the material and the nonlinear refractive index of MgO:Cr is unclear. Therefore, a possible change is studied experimentally by imaging the focal spot onto a CCD with a microscope objective to characterize its size. For each sample the position of the sample has to be readjusted to maintain the focal spot at the back surface. Consequently, also the position of the microscope objective has to be shifted to achieve proper imaging conditions. The sample rotation is chosen to align the polarization of the laser with the [100] crystal axis. This leads to a lower yield of the below bandgap harmonics in the visible [58], but maximizes the yield for the XUV harmonics and matches the conditions used for the previous measurements at the IOGS. The intensities reached in the experiments are about $21\,\text{TW/cm}^2$.

Examples of the recorded images can be seen in Figure 3.15. As can be seen, the spatial modes for the case of MgO:Cr 5000ppm are slightly smaller than their MgO counter parts. However, the difference is small and the profiles show a slightly elliptical shape. This can be either due to the alignment of the lens used for focusing or due to the alignment of the microscope objective used for the imaging. In the second case this would have a major impact on the results of the measurements. Due to the necessary change of the microscope objectives position between each measurement, the error marging for these measurements is quite large. To achieve a quantitative comparison of the different cases, the width of the profiles is calculated. To account for the slightly elliptical shape of the spatial modes a horizontal and vertical profile through the maximum point of the mode are taken. Next each profile is fitted by a gaussian profile of the shape $f(x) = A \cdot \frac{1}{\sigma\sqrt{2\pi}} \exp\left(-\frac{1}{2}\left(\frac{x-\mu}{\sigma}\right)^2\right)$, giving access to the gaussian beam width. The fitting avoids any contributions of the slight pedestals present especially in the low signal measurements of the harmonics. Intensities are then calculated based on the mode area and the power of the beam, where the mode area is based on the elliptical shape of the mode as $A_{Mode} = \sigma_{vertical}\sigma_{horizontal}\pi$. The results for this are summarized in Table 3.2 giving the mode areas for each harmonic and the relative change. It reveals that especially H5 and the fundamental show a large change in the mode size, while H3 remains nearly identical. The largely different behaviour of H3 can be attributed to the huge variance of the measurements, which is further increased by the calcula-

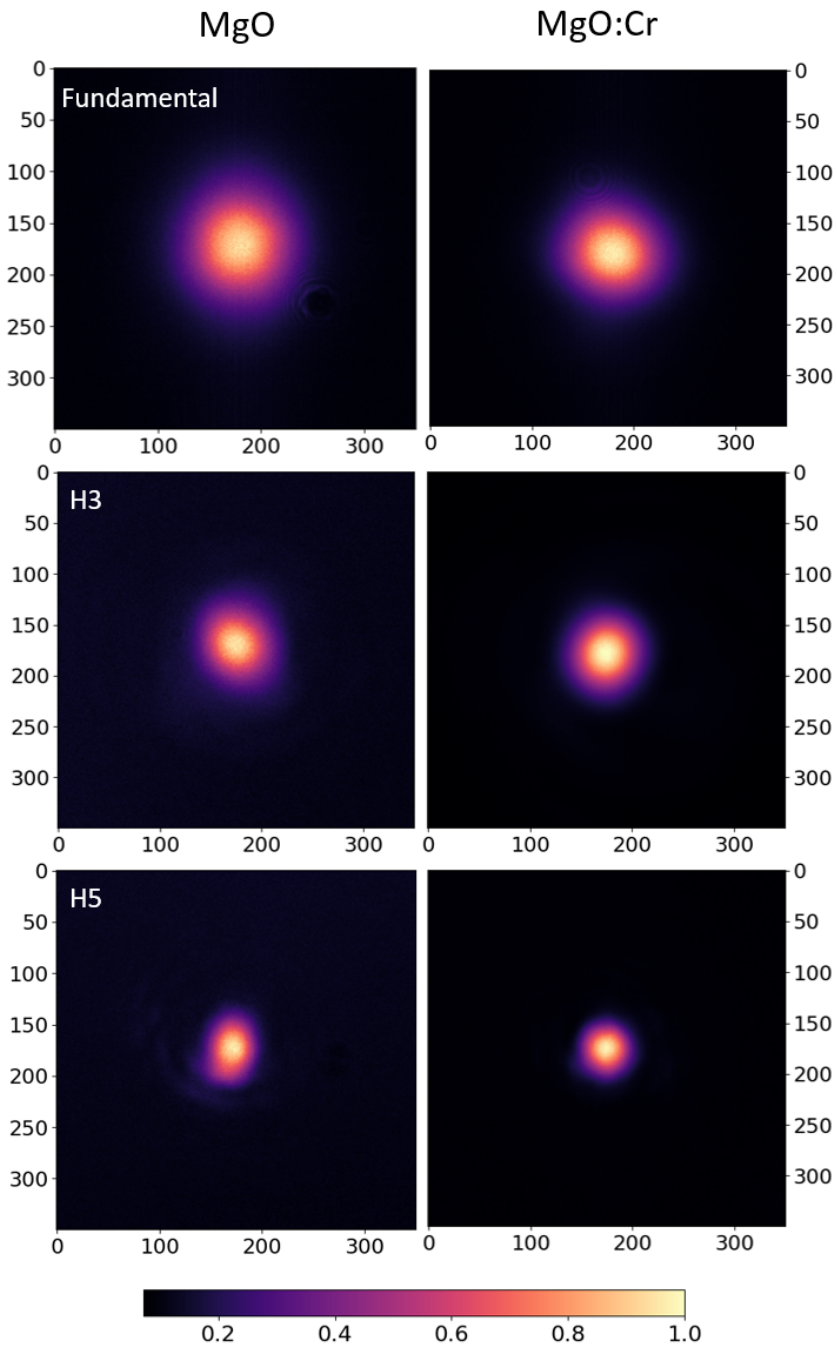

Figure 3.15: Normalized spatial modes from MgO and MgO:Cr 5000ppm.

	MgO	MgO:Cr 5000ppm	Difference (absolute)	Difference (relative)
Fundamental	4065	2989	1076	0.265
H3	1740	1732	8	0.004
H5	875	828	47	0.053

Table 3.2: Area and area difference for the size of the spatial modes between MgO and MgO:Cr in camera pixels. The relative difference is calculated taking the pristine MgO as a reference.

tion of the mode area. Nevertheless, multiple remeasurements yield similar results. While the results still have to be taken with care and do not completely prove a significant difference in the nonlinear behaviour between MgO and MgO:Cr, they can be seen as a indication in that direction.
Notably, comparing the size of the focal spot after propagation through MgO or MgO:Cr to the focal spot without any material in the beam path shows a clear and significant reduction of the mode area. Self focusing as a nonlinear propagation effect is therefore indeed playing an important role for the generation of HHG from solids in a transmission geometry. It can alter the intensity at the back surface, the point of generation, significantly. As it depends on the beam curvature and intensity, as well as the sample thickness and nonlinear refractive index, the effect is strongly depending on the exact experimental geometry.

Self phase modulation

As a last step the amount of SPM and temporal effects introduced into the beam during propagation have to be estimated. The first step for this are spectral measurements of the IR beam after the sample, to reveal any new frequency components in the pulse. These spectra then can also serve as an evaluation of the reconstruction quality of the FROG measurements. Figure 3.16 shows the spectrum of the direct laser together with the spectra after pristine MgO, MgO 5000ppm and MgO 9500ppm. For the measurements the samples are all placed at the focus, to reach conditions similar to the prior measurements (see section 3.2.3). The spectra from all samples, with or without doping, show signs of nonlinear effects. This is visible first in the formation of side peak at both sides of the spectrum, a characteristic change for SPM, and secondly in the smaller overall width of the spectrum. However, while there are differences between the differently doped MgO crystals and the pristine MgO, these differences remain small. The only change is a slightly higher side peak of the MgO:Cr 5000ppm sample around 1650 nm. Nevertheless, the spectra indicate that the effects of SPM accumulated during the propagation through pristine MgO and MgO:Cr are of similar strength. Based on the spectra there is therefore no large difference between the propagation through one or the other sample, however the MgO:Cr 5000ppm sample shows slight signs of change.
To have a closer look at potential nonlinear propagation effects in the sample the IR beam, after passing the sample, is characterized using the FROG technique. This allows access to the full temporal structure of the pulse and therefore reveals any nonlinear effect in the temporal domain. Figure 3.17 shows the reconstructed

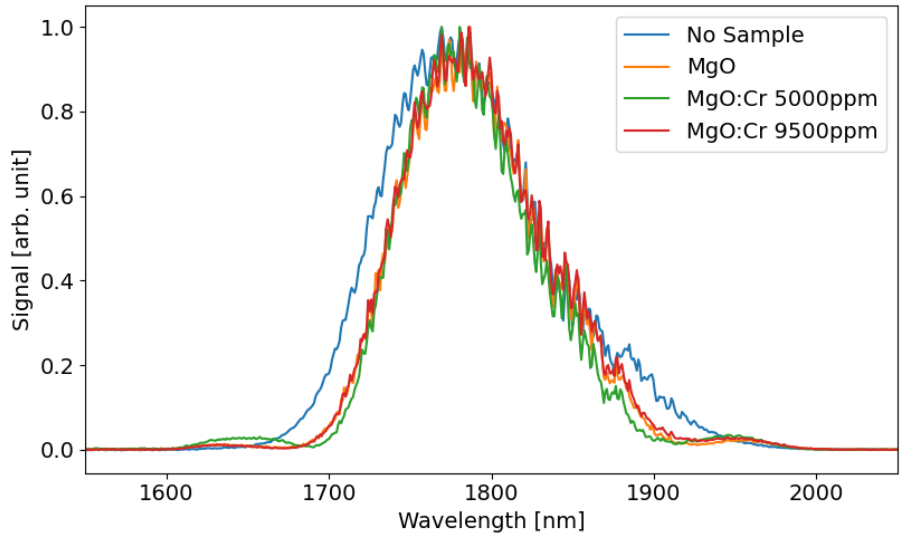

Figure 3.16: Spectra of the IR beam with and without the different samples. The samples are placed in the focus reaching intensities of 21 TW/cm².

FROG trace together with the resulting temporal and spectral shape of the pulse. The undisturbed beam has a spectral width of 153 nm and reaches a temporal FWHM of 45 fs. Notably, there is still a significant negative GDD present in the initial pulse, suggesting that the pulse could be compressed further. After passing the pristine MgO, the spectral and temporal shapes of the pulse change dramatically. First in the spectral domain the bandwidth is narrowed to 100 nm with small side peaks appearing on both sides of the main peak. This matches spectra observed before and confirmes the validity of the FROG reconstruction. In the temporal domain the FWHM is increased to 72 fs with the SPM phase being visible in the shape of an inversion of curvature around the center of the pulse. The increased duration and especially reduction in spectral bandwidth is a combination of the SPM effect and the negative pre-chirp on the pulse. In this case instead of broadening the pulse, the initial wavelengths are shifted towards the central wavelength leading to an effective narrowing of the spectrum. For the MgO:Cr 5000ppm sample the reconstructed phase is extremely similar to the one of pristine MgO, having a spectral bandwidth of 98 nm and a FWHM of 77 fs. There are therefore, no differences between the pristine and doped MgO visible in the temporal structure of the pulse.

3.4 Remeasurements of MgO:Cr using a 1.78 µm laser

The goal for the experiments performed at the CEA was to limit the influence of propagation effects in the measurement, as it turned out to be one of the main uncertainty factors in the former measurements. Additionally, the detection setup for the home build spectrometer was changed from a CCD to a photomultiplier.
One major way to limit the propagation effects are thinner samples. Since the samples used in the experiments before have degraded over time and are, except the

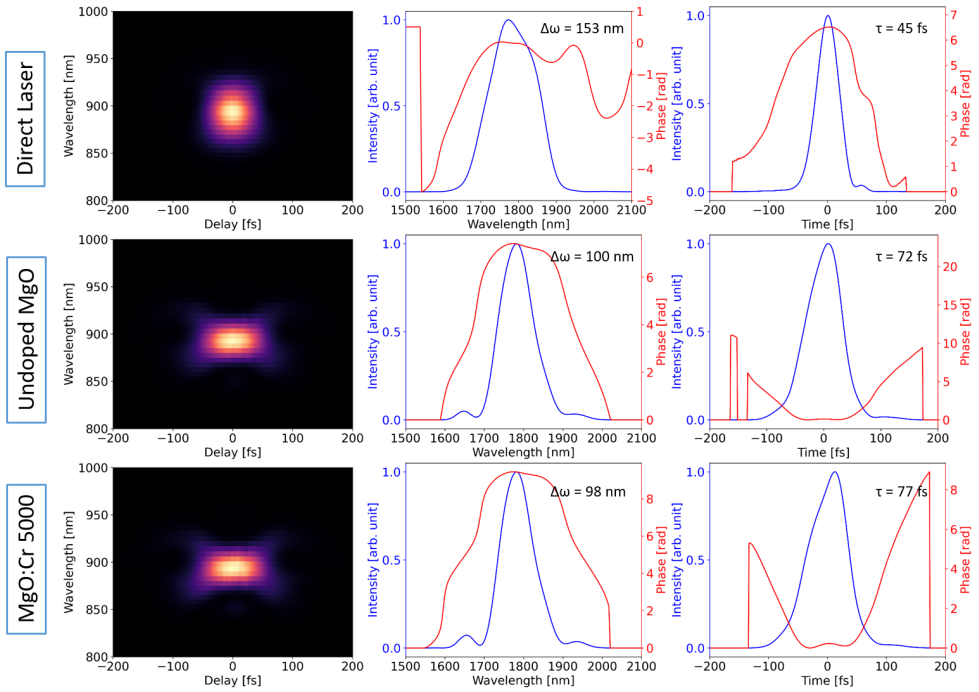

Figure 3.17: FROG reconstructions of the driving laser before and after propagation through the MgO and MgO:Cr 5000 sample. The first column shows the reconstructed temporal shape while the second column shows the reconstructed spectrum with the spectral phase and the third column shows the temporal shape.

MgO:Cr 5000ppm, in rather poor condition, new thinner samples ordered from the same supplier *SurfaceNet* have been used for the experiments. The new samples are only a 100 µm thick compared to the 200 µm thick samples used in the experiments before. A further reduction of the sample thickness below about 60 µm was not possible for the supplier due to the stability of the material and would require e.g. a metallic supporting mesh. These the new samples are then combined with a longer focal length, resulting in a larger focal spot. This further limits nonlinear propagation effects.

3.4.1 Setup

The experiments at the CEA are based on a 100 kHz OPCPA system from *FastLight* with a central wavelength of 1780 nm, 40 fs FWHM and 1.5 W at 100 kHz (see section 5.3). The laser beam is directly guided to the vacuum chamber with the generation stage and the XUV spectrometer. The detection of the XUV spectrometer has been changed from a CCD to a photomultiplier (PM). This change allows not only for higher sensitivity but also has the advantage that the photomultiplier is insensitive to wavelength in the visible range. Since stray light of the third harmonic was one of the biggest contributions to the noise for the previous setup, this can be expected to increase the signal to noise ratio significantly. Addition-

Iris	Power	MgO	MgO:Cr 5000	MgO:Cr 7400	MgO:Cr 9500
6 mm	627 mW	510 mW (0.81)	520 mW (0.83)	520 mW (0.83)	492 mW (0.78)
6 mm	535 mW	447 mW (0.84)	453 mW (0.85)	455 mW (0.85)	440 mW (0.82)
6 mm	450 mW	390 mW (0.87)	393 mW (0.87)	392 mW (0.87)	382 mW (0.85)

Table 3.3: Transmission of the new MgO:Cr samples inside the XUV spectrometer. Transmitted percentage of the input beam is given in brackets.

ally, the range of detectable harmonics can be extended towards longer wavelength, capturing a significant picture of the 1st conduction band as well. In front of the photomultiplier the signal is passing a slit located in the focal plane of the grating to compensate for the big aperture of the photomultiplier. One big disadvantage of this setup is the loss of the spatial information present in the CCD images. Instead the slit is conceptuality averaging the signal over one line of the CCD image and as a consequence spatial effects are now convoluted into the spectrum. The PM is operated in a photon counting mode using an oscilloscope as a readout. The signal is referenced to a trigger from the laser system. This reduces the number of dark counts significantly, reaching a nearly zero background noise.
In the setup the beam is focused by an anti-reflective coated CaF_2 lens with 10 cm focal length. Using a longer focal length leads to a larger foal spot and consequently a higher flux. However, it requires higher average powers to reach the same intensities as in the experiments done at the IOGS. The crystal is mounted on the same XYZΘ stage as for the previous iteration of the setup. Additionally, a moveable mirror is mounted between the crystal holder and the grating, to pick the beam and guide it outside the vacuum chamber. This allows an inspection of the visible harmonics and for potential damages on the crystal.

3.4.2 Results

Since new samples are used for the experiments the transmission of these samples is measured for different doping concentrations and powers to characterize eventual nonlinear absorption effects. The results are summarized in Table 3.3. It shows that for the highest doping of 9500ppm the absorption is stronger than for the lower doping concentrations, resulting in a lower intensity available for the generation of HHG at the back surface of the crystal. Consequently, harmonics generated in this sample can be expected to have a lower yield compared to the other concentrations. Additionally, the transmission becomes worse with higher driving intensities, showing the influence of nonlinear absorption effects. However, all doping concentrations show a similar behaviour and therefore no difference in the nonlinear properties of the samples is expected.

Next, the XUV spectra are recorded for each of the doping concentrations. Since the acquisition of one spectrum takes, depending on the spectral range and resolution, about one to five minutes with this setup, only the harmonics from the top of the first conduction band are measured. This limits the possibility of damage

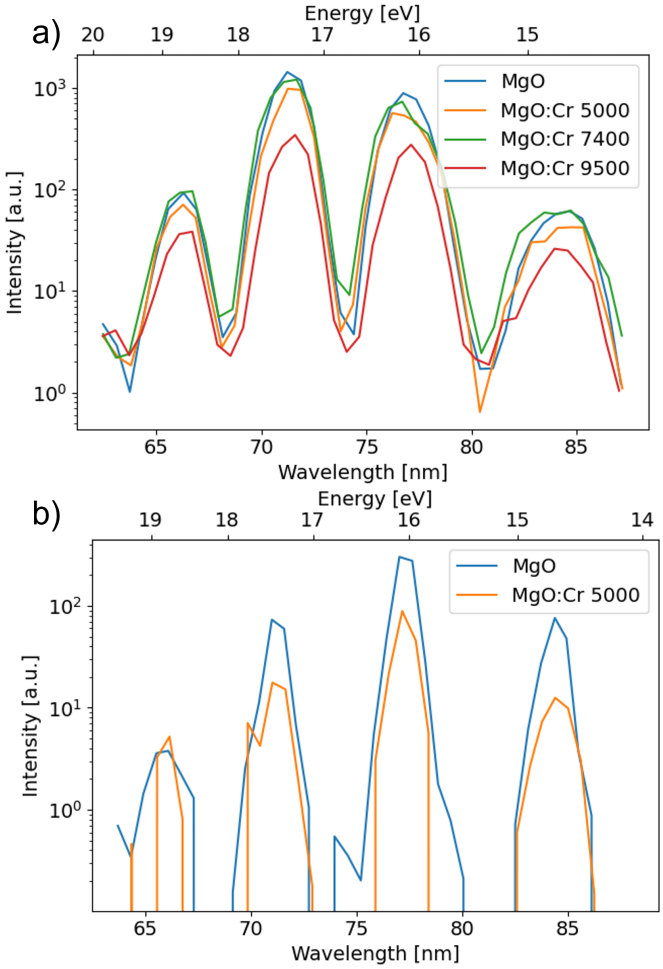

Figure 3.18: Spectra from MgO doped with a variety of chromium concentrations. a) For a high intensity of 9.4 TW/cm^2 and b) an intensity of 3.1 TW/cm^2, marking the lower end of the sensitivity of the setup.

building up during the measurements, which would introduce a significant error margin. Figure 3.18 shows spectra for each doping concentration at two different intensities. The harmonic orders are H21 to H27, with H25 marking the highest harmonic from the first conduction band and H27 showing the beginning decline of harmonic signal towards the second conduction band. At higher intensity the harmonics show a similar signal for all concentrations, however MgO:Cr 9500ppm has a slightly lower yield over all harmonics. The reason for this is likely the increased absorption in the sample observed before. Nevertheless, there is no enhancement of the harmonics. Since our pulses for these experiments are much longer than for the previous measurements, one possibility is the high population of the conduction band with electrons increasing dynamically during the pulse, counter acting the effect induced by the doping. To limit this effect, spectra at lower intensities have been taken on MgO and MgO:Cr 5000ppm. The main limitation for the used in-

tensities in this case is the sensitivity of the measurement setup, allowing to reduce the intensity only by half before the signal vanishes. The resulting spectra (shown in Figure 3.18 (b)) still show no sign of enhancement. In fact the signal from the doped crystal is, in tendency, slightly lower than the one from pristine MgO.
Next, the focus is set on optimizing harmonics from the second conduction band. By the nature of HHG, these measurements can only be carried out with intensities high enough to drive electrons into the high energy ranges of the second conduction band. Because of these high intensities damage to the sample becomes extremely critical and the sample is constantly moved laterally during the measurement to avoid heat accumulation and subsequent damage. The effects of this are clearly visible in the spectra in Figure 3.19. Indeed, harmonics 21-27 are now much broader reaching a point where they start to merge. This is a clear trace of nonlinear effects reshaping the driving pulse during its propagation through the material. Notably, lower harmonics are slightly blue shifted compared to the calculated positions, while higher harmonics are shifted towards the red. This is behaviour that is not explainable by only a shift in the driving wavelength.
The second conduction band appears as a plateau containing H29-H33 with a cutoff around 25 eV. Again the different doping concentrations show very similar spectra with the exception of the MgO:Cr 9500ppm showing a lower signal. One peculiar feature of the second conduction band is H29 (62 nm), which is remarkably pronounced compared to the other harmonics in the second conduction band. In fact only the first and last harmonic in the second conduction band are clearly identifiable, while H31 is only visible as a small peak for pristine MgO. This behaviour was observed by *Uzan et al* [74] as well. They link this feature to points where the relative velocity between the electron in the conduction band and the corresponding hole in the valence band vanishes, leading to an increased recombination rate around these points. Alternatively, this peak could be a fluorescence from the bottom edge of the second conduction band to the valence band. As this peak appears especially pronounced for the MgO:Cr 5000ppm and MgO:Cr 7400ppm, it can indicate an increased transfer rate of electrons into the second conduction band. However, a fluorescence would indicate those electrons loose coherence and are not taking part in the HHG process. A similar observation was made for a pre-population of the conduction band using optical pumping [73]. To determine whether the peak is due to fluorescence or a harmonic would require coherence measurements, which are out of scope for this setup.

Since the follow up experiments using the laser system at the CEA were not able to reproduce the results achieved at the IOGS, another try was performed using the same 5cm lens as used at the IOGS. This achieves similar intensities but induces damage to the crystal at lower energies, while creating a lower flux of HHG photons. However, the nonlinear effects can be expected to play an even more prominent role. The measurements are consequently suffering from low signal but are generally showing the same results as the later measurements performed at CEA Saclay (Figure 3.19).

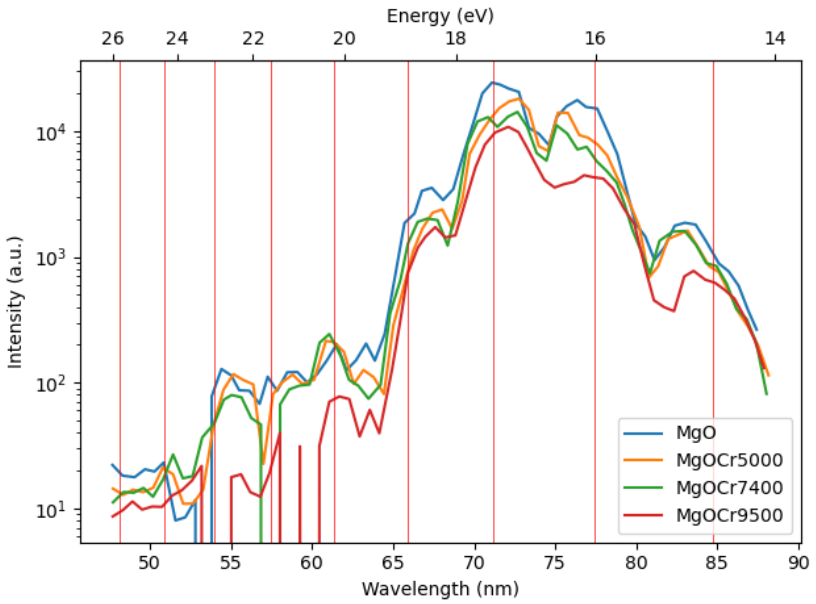

Figure 3.19: Harmonic spectra from MgO doped with different concentrations of chromium. The sample is constantly moved during the measurement to avoid damage.

3.5 Discussion of chromium doping in magnesium oxide

The measurements regarding chromium doped MgO are overall contradictory, with the two measurement sets giving opposing results. It is therefore key to identify the differences between the two measurements.
The first obvious difference is the laser source used for the experiments. However, the driving wavelengths of the two lasers are reasonably close and both far from the bandgap energy of MgO, so that no major difference can be expected. Also the driving intensities are of similar magnitude for both experiments. The largest difference between the two systems is the temporal shape of the pulse, which is a around 20 fs soliton for the experiments at the IOGS while the system at the CEA only achieves about 40 fs pulses. This means an increase from a 4 cycles pulse to a 6-7 cycles pulse. A possible result could be e.g. that the increased ionization rate of the doped samples leads to an saturation of electrons in the conduction band and preventing effective HHG due to electron-electron interactions and a loss of coherence. This is an effect that has been demonstrated for pre-excitation of the material [73, 109]. As the simulations assume a coherent process and the dephasing time is chosen rather arbitrary they might not accurately represent this effect, effectively overestimating the harmonic yield.
The next important point are propagation effects inside the sample, introducing differences between the pristine MgO and the doped samples. In the experiments no clear effect of a difference in these propagation effects was visible in the temporal domain. However, for self focusing the experiments do show a tendency towards stronger nonlinear effects in the doped samples. In general, a misjudgement on the intensity present at the point of generation, at the back surface of the crystal, can

lead to a lateral shift of the experimental points in Figure 3.12 (a), which could lead to a significant overlap of the curves.
The last point is connected to the samples itself. While MgO is normally stable against erosion effects under air, the samples used at the IOGS were already aging for about 2 years. While the bulk material of the sample is unlikely to change significantly, the observed harmonics are generated extremely close to the surface of the material. A number of samples doped with different chromium concentrations than 5000ppm showed a milky degradation of the surface, an indication of the material surface oxidation. The difference compared to the other samples would then be the concentration of this additional impurity, not yet leading to a significant change in the visual appearance of the sample. As a comparison the samples we used for the second experiments were vacuum sealed until the transfer into the vacuum chamber of the XUV spectrometer.

3.6 Gallium implantation in Silicon

During the ptychography experiments discussed in Section 4.2.1 another case of enhanced harmonic yield has been observed that can be attributed to a structural change of the material, similar to doping. The silicon samples used in these experiments require the etching of nanostructures into the silicon substrate, which has been done using a *focused ion beam* (FIB) setup. In this scheme the material is bombarded with a high flux gallium ion beam in order to gradually ablate material from the surface of the substrate. However, this heavy bombardment is naturally changing the material structure close to the surface. Since the observed harmonics are mainly generated in the last tens of nanometers of the substrate, this area of modified material is overlapping with the origin area of the harmonics and can have a strong influence on the process itself.

3.6.1 Structure of the samples

For an understanding of the effect it is important to notice that this way of implementing foreign atoms into the substrate is completely different from the doping process used for the MgO:Cr samples. For the MgO:Cr the dopant, chromium, was already included in the crystal growing, allowing the chromium to occupy magnesium sites in the whole crystal. In contrast for the FIB processing ions are forcefully pushed into the crystal structure using high acceleration energies. This leads to multiple key differences between the two cases. First, to achieve the same occupation of crystal sites as in the MgO, the gallium has to kinetically remove a silicon atom from a crystal side and then occupy it. However, this combination of events is rather unlikely. The much more frequently appearing option is gallium forming an interstitial defect, with the atom resting in between lattice sides. In fact the high kinetic energies are triggering a cascade of events in which one gallium atom can kinetically remove multiple silicon atoms from their lattice sides, forming silicon interstitials and vacancies. Second, the concentration of gallium is not even throughout the

crystal but sharply decreases with increasing distance from the surface. Third, it is possible to introduce more gallium atoms into the crystal lattice than the crystal structure can normally incorporate. As a consequence, the structure gradually starts to break and, above a certain threshold, transfers from a crystalline into an amorphous phase. This amorphous phase can have a porous structure [110, 111] and has a lower density than crystalline silicon. At these high concentrations also gallium precipitates might form [112, 113]. Precipitates are nanoscopic conglomerates of pure gallium encapsulated within the host material, here silicon. Further bombardment with ions is leading to parts of the amorphous layer breaking away resulting in the material ablation. Overall, the transformation of the near surface structure induced by the FIB can be broadly divided into three different zones. The first is the layer closest to the surface, where amorphization takes place and at high ion doses precipitates can form. Below that is a defect rich layer, which contains not only gallium but also silicon vacancies and interstitial silicon atoms produced by the gallium implementation. Beyond that is the unperturbed silicon crystal.
The depth distribution of these defects and the gallium atoms is depending on the kinetic energy of the ions and can be calculated with dedicated simulation tools e.g. *Stopping and Range of Ions in Matter* (SRIM) [114]. SRIM calculations for the case of 30 keV gallium ions and a silicon substrate are shown in Figure 3.20. It simulates the path of each individual ion in the unperturbed material. Repeating this process many times over gives a depth distribution of not only the gallium but also the defects created by it. The resulting distribution shows a peak of gallium atoms at a depth of 25 nm. Further inside the material, the gallium concentration fades until only pure silicon is left. This distribution matches experimental results [111] for low doses, while at higher ion doses the gallium concentration near the surface reaches a plateau. Since the simulation is calculating the penetration of a gallium ion into a pristine material multiple times instead of a gallium slow accumulation of gallium inside the material, it is not capable of reproducing this plateau. However, the simulation allows access to further properties such as the distribution of silicon interstitials and vacancies inside the material. It shows that the amount of silicon interstitials and silicon vacancies is much higher than the amount of gallium ions. As shown in Figure 3.20 (e), the vacancies dominate close to the surface, while interstitials form the majority of the defects in deeper layers. Experimental studies report the amorphous top layer to be about 30-50 nm thick [110, 111], with low concentrations of gallium spreading as far as 150 nm into the material.

This unique structure after the FIB has the advantage that the studied material change is located solely close to the exit surface of the sample. Since the bulk material is unchanged also propagation effects, marking one of the biggest uncertainty factors of the experiments in continuously doped MgO, are only differing in the modified layers. These are, however, to thin to have a meaningful impact on the propagation. Nevertheless, the FIB approach also comes with disadvantages. A first disadvantage has its origin in the depth distribution of the material alteration. Due to the different absorption of the harmonics, each harmonic is generated at a different depth and therefore "sees" a different material composition. Another disadvantage are secondary interactions with the laser such as heating of the sam-

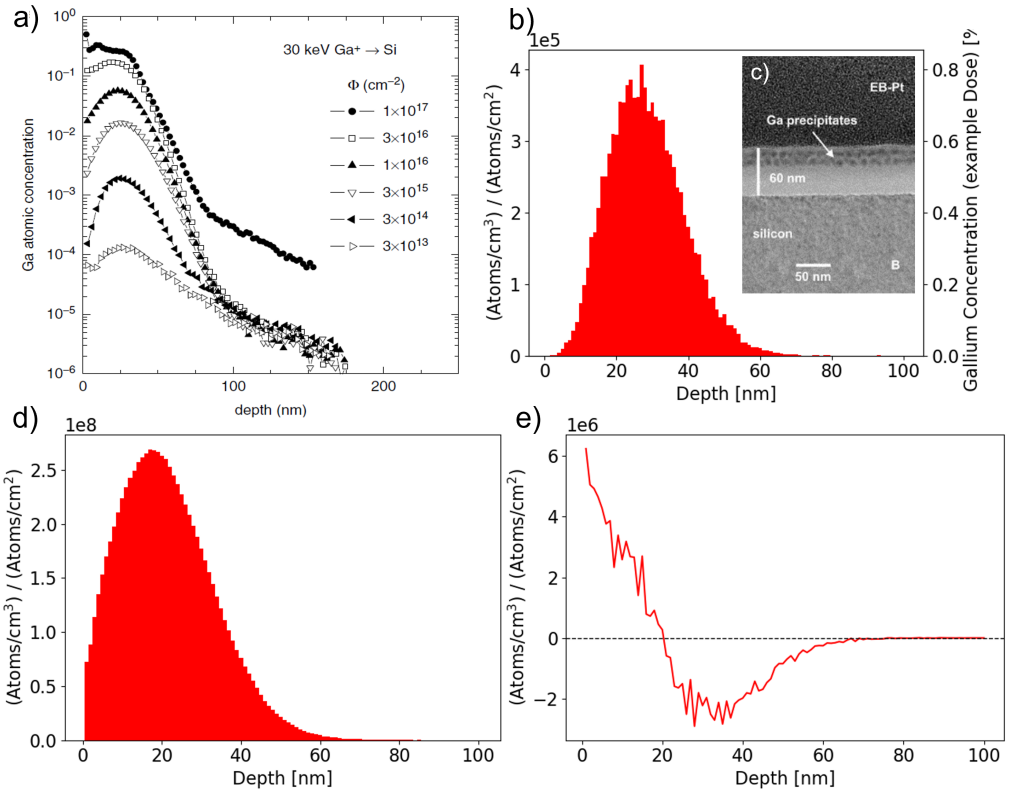

Figure 3.20: (a) Atomic concentration of gallium at different ion doses and 30 keV, measured by *Gnaser et al.* [111]. (b) Theoretical gallium distribution calculated using SRIM [114]. (c) Cross section after FIB etching at an ion dose of 10^{17} $\frac{\text{Ion}}{\text{cm}^2}$ showing the amorphous layer with precipitates (taken from [112]). (d) Calculated distribution of silicon interstitials created by the gallium ions. (e) Difference between vacancies and interstitials in the interaction region.

ple. This heating can anneal the amorphous layer leading to a recrystallization and reforming of defects into larger complexes. Since the effect persists over longer exposure times the heating seems not to remove the origin of the enhancement, but might still change the crystal structure.

3.6.2 Measurement of ion dose dependent HHG signal

While the signal increase was first observed from the ptychography samples (see section 4.2.1), field confinement effects in the patterned structure can have an effect on the signal. Furthermore, the signal is a mixture of modified and unmodified areas adding another layer of complexity to the problem. In order to separate these effects and to quantify the effect of the gallium implantation itself, a set of test areas with different gallium ion doses was produced using the FIB. The single areas are 10x10 µm squares organized in four 2x4 arrays. The doses for theses test areas were chosen to range over a large variety of doses, up to the threshold of material removal. After material removal starts the layer structure of the implanted area is

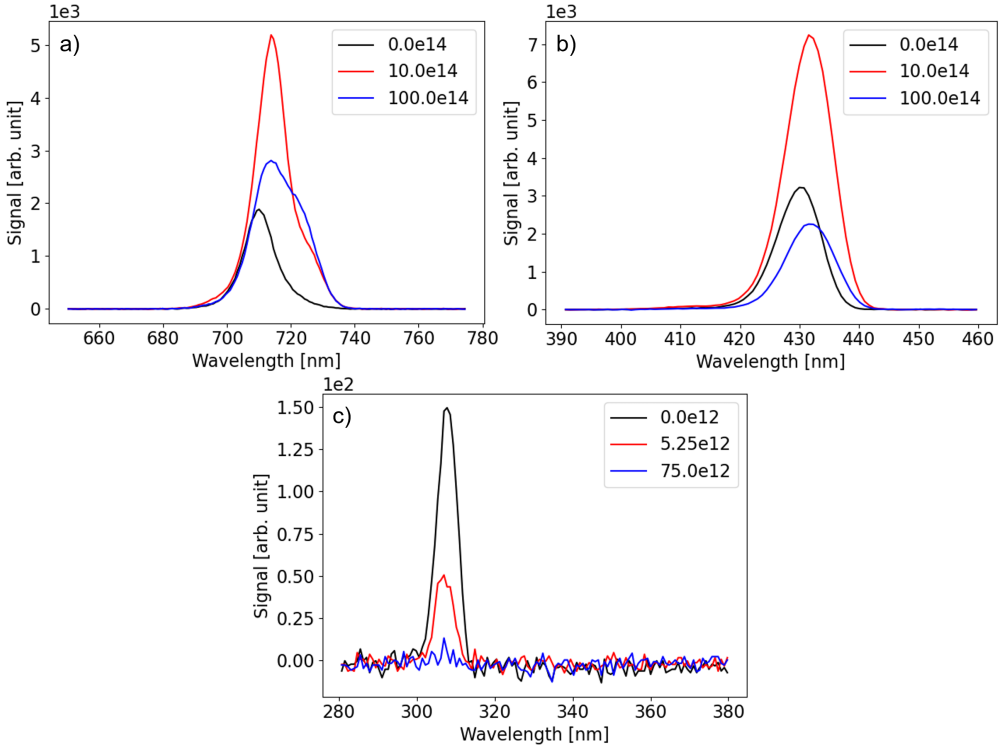

Figure 3.21: Spectra of H3 (a), H5 (b) and H7 (c) for different doses of gallium implantation.

assumed to reach a stable state with a balance of material removal and extension of the modified material layers beneath. For the first array of squares the dose starts at $4 \cdot 10^{12}$ and increases in steps of $1.25 \cdot 10^{13}$ up to a maximum of $12.75 \cdot 10^{14}$. The other arrays of squares cover doses from 10^{13} to 10^{16}, again in steps of $1.25 \cdot 10^{n}$. Here n is the magnitude of the respective dose. The harmonics are generated using the NOVAE laser and setup as described in sections 4.2.2 and 4.2.3. Spectra are recorded for each harmonic separately, with a systematic optimization of the coupling into the spectrometer for each harmonic order.
An example for the resulting spectra is shown in Figure 3.21. H3 and H5 show a signal increase by a factor 2-3 for the lower gallium dose, compared to the unmodified bulk material. The higher gallium dose still lead to an increase of the 3rd harmonic emission, while H5 already shows a slightly decreased signal. Complementing to that earlier measurements on a different, but similar, sample with even higher gallium doses (see Appendix F) show that the highest gallium doses lead to a drastically reduced signal compared to the bulk for both H3 and H5. Initial measurements on the ptychography samples also showed a much stronger increase of H5 above one order of magnitude as well as a visible signal for H7 (see Appendix F). However, while the FIB conditions for the ptychography samples are known (around 10^{14}), one measurement is done on an area where the FIB malfunction. On this area the ion dose is not known but expected to be on the lower end of the ion doses that are technically possible for the FIB (around 10^{12} - 10^{13}). The area

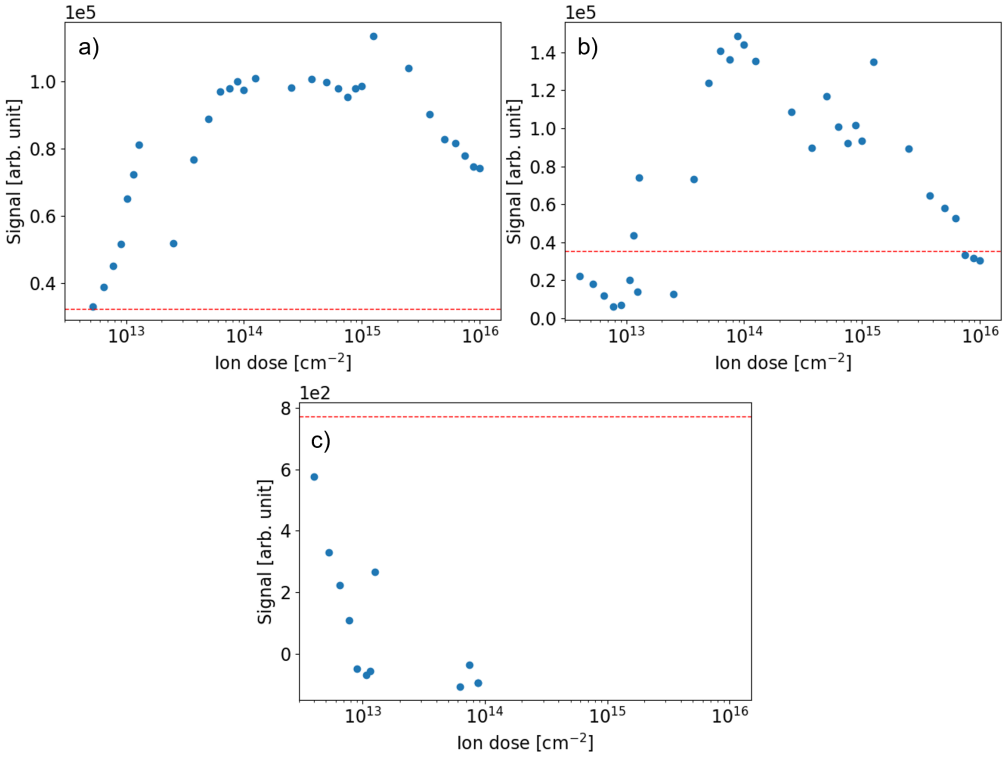

Figure 3.22: Ion dose dependency of the integrated yield for H3 (a), H5 (b) and H7 (c). The dashed red line marks the harmonic yield from an unmodified silicon surface.

produces the highest observed enhancement of H5 reaching nearly two orders of magnitude, which is much higher than any enhancement observed in the controlled samples studied here. This indicates that there might be factors beyond the ion dose that play a role in the observed effect but resolving these would require more extensive studies of the HHG yield in dependence of the FIB parameters.

Compared to pure silicon, for H3 the spectrum exhibits a pronounced red shift with increasing ion dose. One possibility for this is the emergence of a fluorescence close to H3 in the doped material. One possible origin for a fluorescence could be a shift of the indirect bandgap induced by the gallium implantation. The indirect bandgap is located around 1.1 eV (1127 nm) for pristine silicon and therefore outside the range of the spectrometer. A fluorescence based on the gallium implementation into crystalline silicon would make a shift of 0.6 eV necessary to cause a fluorescence close to the third harmonic. Another origin for the fluorescence could be the amorphous silicon. The bandgap of amorphous silicon depends on several factors including the temperature of during formation, but is generally located in the 1.6 eV (775 nm) to 2 eV (620 nm) range [115, 116]. Notably, since CDI measurements were done at H5 (see chapter 4) the increased harmonic signal for H5 has to be coherent and can therefore not be caused by a fluorescence. For H7, the first above bandgap harmonic, no increase of the signal is observed. Instead the signal decreases for even the lowest possible ion doses and vanishes for a higher ion dose. Note that

the threshold for a vanishing signal is reached even before the peak of the increased signal for H5 and H3. Also no fluorescence of the direct bandgap, which should be located between H5 and H7, was detected for this sample. However, as shown in Appendix F, measurements on an earlier sample show a weak broad fluorescence close to H7 at 3.6 eV, which is close to the direct bandgap of silicon. It increases for low ion doses and decreases for the highest ion doses and might be an indication of a changing bandgap structure depending on the used ion dose. Due to the different divergence of each harmonic, the coupling into the spectrometer is depending strongly on the distance between it and the sample. Besides the emergence of a fluorescence signal this could be another reason for the difference in spectral shapes between the measurements on different samples.
To analyse the dependence of the harmonic signal on the ion dose further, the yield of each harmonic is calculated from the spectra by integrating over the respective harmonic. The result is shown in Figure 3.22. Notably, the same measurements have been done using a camera as a detector and filters to separate the individual harmonics, giving a similar dependency. Therefore, the result in Figure 3.22 is not influenced by the coupling of the spectrometer. The red line in the graphs marks the signal from pure silicon, which was measured multiple times at different positions and remains similar over the whole length of sample positions. For H3 and H5 the integrated harmonic signal increases with increasing ion dose, reaching a maximum around 10^{14}, before decreasing again. For H3 the signal is not going down to the bulk signal within the measured range of ion doses, while this is the case for H5. For higher doses the process of material removal starts and the structure can be expected to reach a dynamic equilibrium. As a consequence the curves can be expected to flatten and stabilize when reaching even higher ion doses. Notably, there are some discontinuities in the graph, with each one corresponding to a change between the sets of squares. Since each change of set is also a change in the settings of the FIB, necessary in order to change the possible range of ion doses, this is most likely due to some fluctuations in the FIB itself. Fluctuations like this might be an explanation for the observed differences between these samples and the initial ptychography samples. Nevertheless, the general trend of the signal persists. For H7 the signal is consistently below the unmodified bulk, dropping to zero at an ion dose of about 10^{13}.

3.6.3 Origin of the increased HHG yield

Identifying the mechanisms behind the enhancement is rather complicated due to the nature of the material alteration as a combination of multiple crystal defect types and concentrations. The first important question is therefore, in which layer the single observed harmonics are generated. For this it is important to recognize that already in the unperturbed bulk Si the observed harmonics are generated in different depth. This is due to reabsorption of the generated harmonics by the crystal itself. Naturally, the absorption is strong for harmonics above the direct bandgap of the silicon at 3.4 eV. As a consequence, at room temperature H7 experiences a strong absorption with an absorption length of only 11 nm [117], meaning basically all H7 recorded is generated in the last tens of nanometers of the material.

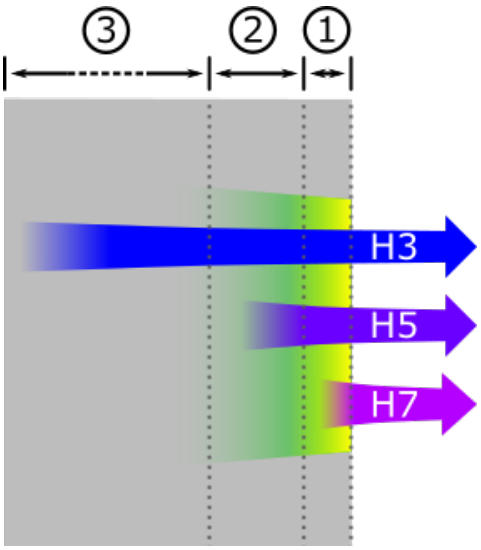

Figure 3.23: Illustration of the different defect layers and the generation depth of the low order harmonics.

For H5 the absorption length is 188 nm and for H3 5 µm. As illustrated in Figure 3.23 this leads to a situation where H7 is generated only in the amorphous layer. H5 is generated mostly throughout the defect rich layer but still has to pass the amorphous layer at the end, while the majority of H3 is generated in the unchanged bulk before. Since the H3 yield from the unchanged area is identical to the completely unmodified silicon, this also implies that the enhancement factor of H3 in the modified area is much stronger than that emitted from the pure silicon. While this is also the case for H5 the effect is not as strong in that case as the generation is much more limited to the defect rich area.
With this picture in mind the first aspect for the interpretation of the observed effects is to divide the effects of the FIB induced material alterations into the different layers present in the sample. Starting with H7, the sharp decline can be explained by the onset of amorphization at the material surface. The amorphous structure is reported to have a lower HHG efficiency than a crystalline structure [118, 119], which in combination with the generation of H7 in only the last nanometers of the sample, leads to a drastic reduction of the H7 signal. This can be amplified by other effects than further decrease the harmonic yield. These effects can e.g. include a degraded surface structure or even porous structure due to material ablation. Since in the measurements filters have to be used in front of the spectrometer to reduce the IR signal, another possibility is a lack of sensitivity of the measurement, ultimately reducing the harmonic signal below the noise threshold. For H5 the area of generation extends over the amorphous layer into the defect rich area of the crystal. Since this area is only preceeded by the pure silicon crystal and the amorphous layer shows a reduction of signal, this layer has to be responsible for the enhancement of the H5 (and H3) signal. Due to the low generation in the amorphous layer such effect can be reduced to a changed transmission. H3 follows the same behaviour with the only difference that the effect of the defect rich area is limited due to the

long absorption length.
While the increase of the harmonic signal can be tracked to the defect rich area, the decrease at higher ion doses can be interpreted as a pure degradation of the surface due to the ion bombardment. As a consequence precipitate formation, extension of the amorphous layer and irregularities of the surface due to removed material become the dominant effects overbearing the enhancement in the defect layer. A second option is an optimal defect concentration in the defect layer which is passed. However, to identify whether there is an optimal defect concentration, one would need to experimentally isolate the defect rich layer. However, due to the thin layer thicknesses, this is an extremely challenging task.

This leaves the physical effects responsible for the increased HHG signal from the defect rich area. There are theoretical studies showing that an increase of only below bandgap harmonics is possible [21], based on introducing a doping into the material. This would imply that the defect bands are taking part in the interaction but do not significantly increase the ionization rate and therefore do not increase the electron density in the conduction band [120]. Indeed, in our experiments only H3 and H5 show a strong enhancement, while H7, the first above bandgap harmonic, shows a steady decline. In contrast, the model used here for the case of chromium doped magnesium oxide predicts an increase even for above bandgap harmonics, based on an overall increased ionisation rate.
Due to the unavoidability of the amorphous layer in the FIB scheme these experiments fail to identify directly which of these two models is valid. The first option is coherent with the complete absence of any enhancement for H7, even for low doping doses where the restructuration of the silicon is still weak. Meanwhile, if H7 was strongly enhanced the absorption of amorphous silicon would still allow for a small 0.6% transmission even through a 40 nm layer [121]. With the pure silicon signal as a reference this is close to the detection limit of the setup and has not been detected even with longer integration times than used in the final measurements. However, the H7 signal is showing a steady decrease without any enhancement even for the lowest ion concentrations.
The two possible options left are therefore that only below bandgap harmonics are enhanced due to the ion implementation, while above bandgap harmonics are not affected or even experience an adverse effect or that the increased signal of H7 is quickly overshadowed by the structural changes of the material and the maximum is outside the range of tested ion doses if it exists.

3.7 Conclusions

Overall, the results from the chromium doped MgO leaves a lot of open questions. The most important one being the reproducibility of the measurements and therefore the difference between the first measurements at the IOGS and the later ones at the CEA as described in section 3.5. The most important points to clarify are the propagation effects inside the sample and especially the possible changes induced by the defects, as well as a much more detailed characterization of the sample with a focus on the structure close to the surface. Experiments using a reflection geometry for the harmonic generation can, despite being more complex and less efficient, help to clarify the contribution of the doping by effectively eliminating the propagation inside the material. As the later experiments on silicon show, defects and doping of the material can have a strong impact on the harmonic emission. Pushing the understanding further would provide not only technological possibilities regarding the use of harmonics from solids as an EUV source but would also allow harmonics to be used to characterize the distribution of defects.
The second part studies the change in harmonic yield from gallium implanted silicon or more precisely, crystal defects induced by gallium implantation by a FIB. The material changes are therefore constrained to a thin layer below the surface of the crystal. It is shown that the defects induced by the implantation process can give rise to an increase in the harmonic signal, with a strong dependency on the amount of implanted ions. This dependency first shows an increase of signal with increasing ion dose, followed by a maximum and a decrease of signal for the highest ion dosages. However, this behaviour is only present for the below bandgap harmonics. Above bandgap harmonics show a decreased signal even for the lowest ion doses used, with a further decrease with increasing ion dose. This behaviour of decreasing signal at the highest ion doses is attributed to the ion dosage dependent transformation of the near surface areas into an amorphous structure.
The obvious goal for further experiments is consequently, the separation of the different effects induced by the gallium implantation with FIB. One possibility for this is using homogeneously doped samples, which will suffer from the same problems described for the chromium doped MgO, but avoid the negative effects of the increasing amorphization of the sample. The mitigation of propagation effects would then require measurements in a reflection geometry. One option to differentiate between the effect of gallium and the defects induced by the implantation process, is to use silicon as a source for the FIB. This would induce defects into the crystal without introducing a foreign atom species into the material. Furthermore, there is the option of a controlled recrystallization of the amorphous layer in the existing samples. A possible way to achieve this is e.g. a controlled heating of the sample.

Chapter 4

Self probed Ptychography

Technological advances have pushed the limits of classical image over and over again, leading to a point where the physical limits related to the use of imaging optics are reached. However, especially with the advent of the semiconductor industry the need for even higher resolutions is present not only in science but also in industry. Due to the direct wavelength dependency of the resolution the most direct way to achieve this is using smaller wavelength for imaging applications. However, with decreasing wavelength the production of suitable imaging optics becomes extremely challenging. One way around these problems is the use of lensless imaging techniques that require only measurements of the scattered electric field, simplifying the setup to the point where only a detector is needed. Unfortunately, the information about the object to be measured is mostly encoded in the phase of the wave, which can not be measured with a pure camera. However, the information is not lost but, as the diffraction pattern directly depends on the shape of the diffracting object, contained within the intensity distribution of the diffraction pattern. Based on this insight iterative algorithms have been developed that are capable of reconstructing the phase based on the recorded diffraction pattern and the experimental geometry[122]. This gave rise to the broad field of lensless imaging, including *coherent diffraction imaging* (CDI)[123] and later ptychography[124]. They enable high resolution measurements using XUV and X-ray sources such as synchrotrons or HHG from gases. Moreover, the reconstructions give access not only to the transmission of an object but also to the phase profile of the object.
Despite being driven largely by the XUV community, the concepts of CDI and ptychography are applicable to a broad wavelength range, given the wavelength has significant diffraction on the object that has to be imaged. Moreover, phase contrast imaging for instance gives the phase properties of a sample with spatial resolution. In this context the combination with HHG from nanostructured solids is especially interesting. In a normal CDI setup the XUV is generated first as an auxiliary probe source and then used to illuminate the object. However, when using a solid target the object can be irradiated with a driving laser e.g. in the IR, generating harmonics directly inside the object itself. These harmonics consecutively diffract coherently in the far field, thus encoding the phase related to the sample spatial arrangement. This leads to a much more compact setup, consisting only of a laser, the sample and a detector, e.g. a CCD. One of the big disadvantages of the combination of CDI and HHG from solids originates from the typical lasers used

to drive the HHG. Under our conditions, since only sub-10nJ laser was available to run the experiment, the laser focal spot was quite sharp to achieve the required intensity for efficient harmonic emission. As a consequence, the field of view remains small. The two major ways to counteract this are, either using a more powerful laser or using ptychography. This thesis concentrates on the use of ptychography since it has several advantages over CDI, e.g. an arbitrarily large field of view and a more robust reconstruction due to the redundant data. Additionally, the spatial distribution of harmonics, in combination with their sensitivity to changes in the band structure opens the possibility of measurements on the spatial distribution of material properties. A concept first presented for pertubative second harmonic generation[125]. Initial concepts of using CDI for this have been tried over the recent years e.g. in [23, 24, 26]. However, the studied structures remain limited to grating like shapes and arrays of nano cones. As a result the diffraction pattern is extremely regular to the point where phase retrieval algorithms are not necessary to calculate the parameters of the structure. Here the approach is tested using harmonics in the visible range but using complex samples in combination with ptychography. The approach can conceptually be scaled to the EUV range but in that case would require refined multiplex or broadband reconstruction algorithms.

4.1 Theoretical background of coherent diffraction imaging

4.1.1 The Diffraction Integral

The mathematical description of diffraction has been treated by a large number of authors and can be found in a variety of textbooks[126, 127, 128]. As mentioned in section 2.1.1 the starting point for the description is the Helmholtz equation:

$$(\nabla^2 + k^2)\psi_\omega(x, y, z) = 0, \tag{4.1}$$

with $k = \frac{\omega}{c}$. It arises from the D'Alembert wave equation as a description for the propagation of monochromatic time independent waves ψ_ω with a frequency $\omega = \frac{2\pi c}{\lambda}$ in free space. A simple solution for the Helmholtz equation are plane waves:

$$\psi_\omega^{PW}(x, y, z) = e^{i\vec{k}\vec{r}}, \tag{4.2}$$

where $\vec{k}$ denotes the wave vector and $\vec{r}$ the propagation direction. Arbitrary choosing the propagation direction to be the z-direction justifies splitting the vectors into their components parallel and perpendicular to the propagation direction

$$\psi_\omega^{PW}(x, y, z) = e^{i(k_x x + k_y y)} e^{ik_z z} = \underbrace{e^{i(k_x x + k_y y)}}_{\psi_\omega^{PW}(x,y,z_0)} \cdot \underbrace{e^{i\sqrt{k^2 - k_x^2 - k_y^2} z}}_{\text{Free space propagator}} \tag{4.3}$$

by using the definitions for $k = (k_x, k_y, k_z)$ where $|\vec{k}| = k = \sqrt{k_x^2 + k_y^2 + k_z^2}$ and $\vec{r} = (x, y, z)$. The equation can be divided further into a z independent part $\psi_\omega(x, y, z_0)$, denoting the wave in the $z = 0$ plane, and a z dependent part, the free space

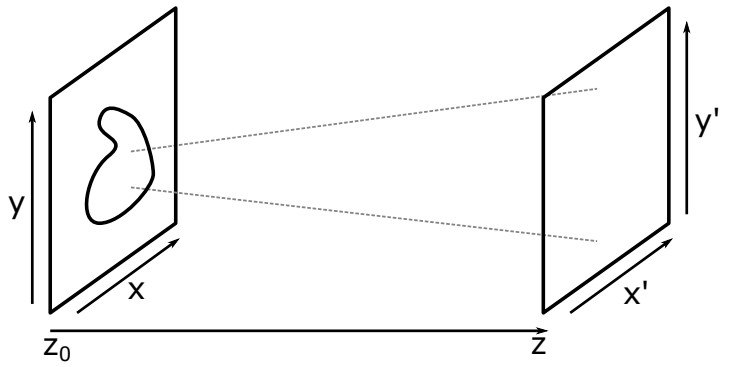

Figure 4.1: Illustration of diffraction on an object.

propagator. However, every wave can be constructed using plane waves as described by the fourier transformation

$$\psi_\omega(x, y, z_0) = \frac{1}{\sqrt{2\pi}} \iint \tilde{\psi}_\omega(k_x, k_y, z_0) e^{i(k_x x + k_y y)} dk_x dk_y, \tag{4.4}$$

where $\tilde{\psi}_\omega(k_x, k_y, z_0)$ describes the 2 dimensional Fourier transformation of $\psi_\omega(x, y, z_0)$. The propagation of an arbitrary wave can therefore be described by

$$\psi_\omega(x, y, z) = \mathcal{F}^{-1}\left[\mathcal{F}\left[\psi_\omega(x, y, z_0)\right] e^{i\sqrt{k^2 - k_x^2 - k_y^2} z}\right] \tag{4.5}$$

with $\mathcal{F}$ denotes the fourier transformation.
The free space propagator can be further simplified for a broad field of cases using the paraxial approximation. It assumes that the field is propagating under small angles deviating only slightly from the z axis. Therefore, k_x and k_y are small compared to k and the square root in the exponent can be approximated by expanding the square root

$$\sqrt{k^2 - k_x^2 - k_y^2} = k - \frac{k_x^2 + k_y^2}{2k}. \tag{4.6}$$

Substituting into equation 4.5 leads to

$$\psi_\omega(x, y, z) = e^{ikz} \mathcal{F}^{-1}\left[\mathcal{F}\left[\psi_\omega(x, y, z_0)\right] e^{i\frac{k_x^2 + k_y^2}{2k} z}\right]. \tag{4.7}$$

Transferring the equation into real space by applying the convolution theorem for Fourier transformations (as described e.g. in [129]) results in the Fresnel diffraction integral

$$\psi(\frac{x'}{\lambda z}, \frac{y'}{\lambda z}, z) = \frac{e^{ikz}}{i\lambda z} e^{\frac{ik}{2z}(x'^2 + y'^2)} \iint \psi(x, y, z_0) e^{\frac{-ik}{2z}\left(x^2 + y^2\right)} e^{\frac{-i2\pi}{\lambda z}(xx' + yy')} dx' dy'. \tag{4.8}$$

By definition the convolution generates two sets of coordinates (x, y) and (x', y'). Due to the dependency of ψ the first set (x', y') can be identified as the coordinates in the diffraction plane, while (x, y) denote the coordinates in the object plane at

$z = 0$, as illustrated in Figure 4.1. Compared to the original Fourier pair ($x \rightarrow k_x$), the spatial frequency k_x is mapped to the corresponding positions in the Fourier plane, via the relation $k_x = \frac{2\pi x'}{\lambda z}$. The integral again takes the shape of a Fourier transformation, now with respect to (x, y). This way the field in the diffraction plane is proportional to the Fourier transformation of the field in the object plane decorated by a phase term $e^{\frac{-ik}{2z}(x^2+y^2)}$, the Fresnel phase.
The last simplification is the "far field" or Fraunhofer approximation in which the object is assumed to be much smaller than the the product propagation distance time the wavelength and therefore $\left(x^2 + y^2\right) \ll z\lambda$. With this, the Fresnel phase can be neglected and the diffraction becomes a pure fourier transformation

$$\psi(x, y, z) = \frac{e^{ikz}}{i\lambda z} e^{\frac{ik}{2z}(x'^2+y'^2)} \mathcal{F}\left[\psi(x, y, z_0)\right]. \tag{4.9}$$

This result has given rise to the field of fourier optics and is the basis for lensless imaging techniques such as *fourier transform holography* and CDI. Nowadays the combination of equation 4.9 and the possibilities for efficient computation of the fourier transformation allows for the fast calculation of far field distributions of nearly arbitrary fields and enables powerful iterative approaches as seen in CDI and ptychography.
In experimental settings it is important to judge if the Fraunhofer approximation is applicable and one tool for this is the *Fresnel number*. The Fresnel phase has three main components: the wave vector k which is directly connected to the wavelength, the propagation distance z and the coordinates x and y in the object plane. To estimate the highest possible value for the term x^2+y^2, it is replaced by an aperture of radius a. a is therefore describing the maximal extend of the diffracting object. With this the exponent of the Fresnel phase can be written as

$$\frac{k(x^2 + y^2)}{2z} \approx \frac{a^2}{\lambda z} = \mathrm{F}, \tag{4.10}$$

where F denotes the *Fresnel number*. This transfers the exponent of the Fresnel phase into a shape consisting of experimentally quantifiable terms. If now $F \ll 1$ the Fresnel phase becomes negligible and equation 4.9 can be applied. However, if $F \approx 1$ equation 4.8 has to be used.

To gain access to the structure of the scattering object its relation to the exit field has to be defined. A usual way for this is in the framework of the *projection approximation*. The scattering object impregnates an amplitude and phase change onto the incoming field. The phase and amplitude changes are gradually applied over the pass through the scattering object depending on its local structure. To simplify this situation the *projection approximation* projects all changes on the exit plane of the object where they are applied to the incoming field in the form of a complex mask. Formally this means the incoming field and the transmission of the object are separable and the transmission t_{object} does not depend on z

$$E_{out}(x, y, \lambda) = E_{in}(x, y, \lambda) \cdot t_{object}(x, y, \lambda). \tag{4.11}$$

Again it is necessary to estimate the conditions for which the approximation is acceptable. For a given diffraction pattern, this is expressed by the *Depth of Focus*

(DOF) which is given in terms of the maximal observed angle θ_{max} as [130]:

$$T \leq \frac{2\lambda}{\theta_{max}^2} \quad \text{or} \quad T \leq \frac{2\delta_r^2}{\lambda} \tag{4.12}$$

where δ_r denotes the resolution and T the sample thickness. The maximal angle of diffraction is the angle between the propagation axis and the highest spatial frequency k of the diffraction pattern. Via the correspondence to the highest spatial frequency the DOF is also coupled to the resolution and can be expressed in its terms as shown in the second part of equation 4.12. Similar but not identical estimates have been derived in [131, 132, 133]. For T smaller than the depth of field the object can be projected to the exit plane. However, if the DOF is smaller than the object this is not the case and the reconstruction algorithm can lock onto multiple object planes, leading to ill conditioned solutions.

4.1.2 Coherent diffraction imaging

4.1.2.1 Concept of coherent diffraction imaging

In most imaging applications a lens or even multiple lenses are used to create an image in the plane of the detector. This allows a direct measurement of the image either using a camera or a directly by eye (see Figure 4.2). The concept of *coherent diffraction imaging* (CDI) takes a fundamentally different route. It skips the imaging optics all together and records the far-field diffraction pattern of the light scattered by the object. If the full field is recorded the image could be restored by a simple fourier transformation. However, most detectors can't record the phase of the light field, which carries a major part of the image information. In CDI this phase is recovered by an iterative reconstruction algorithm as illustrated in Figure 4.2. This concept first proposed by Fienup [122] and later demonstrated experimentally by *Miao et al* [123] allows the reduction of necessary optics to a minimum. This makes it especially but not only suited for the X-ray range, where optics are expensive, hard to produce and have a multitude of technical limitations. Consequently, CDI established itself quickly as an imaging technique at synchrotron facilities and FELs but has also been used with HHG as an XUV source. In these contexts it was used to achieve a number of astonishing results e.g. for biological imaging [134] or high resolution imaging of semiconductors [135]. However, CDI has its drawbacks as well. The phase retrieval algorithms are slow compared to traditional imaging and require an isolated object, meaning an object that is embedded in a region of zero signal (a limitation that was later overcome by ptychography).

4.1.2.2 Reconstruction algorithms in CDI

The original phase reconstruction algorithm has been proposed by Fienup in 1978[122] and is a modified version of a Gerchberg-Saxton algorithm[136]. It uses constraints given by the measurement and the physical geometry of the experiment to retrieve the phase of the diffracted field. To do so the algorithm alternates between the diffraction and image planes, using their connection via the fourier transformation,

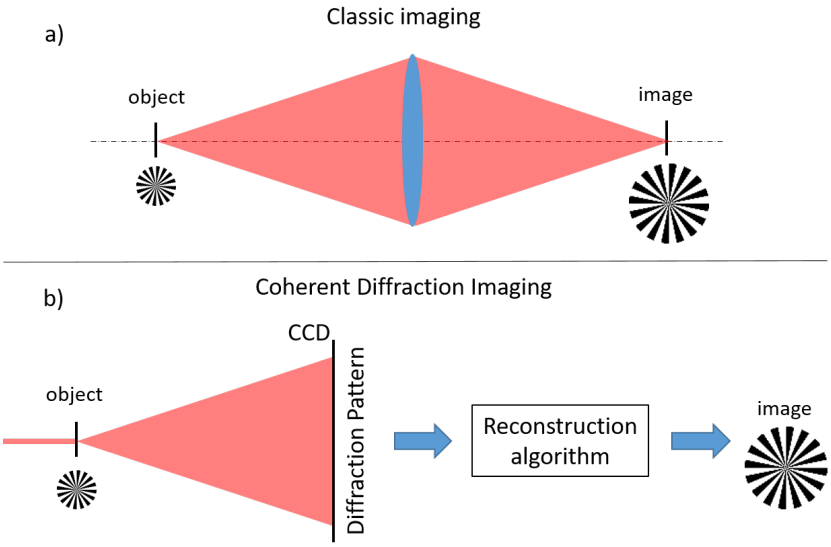

Figure 4.2: (a) Illustration of a classical imaging setup. The lens recreates the image, either in its original size or magnified, in the detector plane where it is recorded. (b) Illustration of a basic CDI setup. The incoming coherent beam illuminates the object, scatters and the resulting far field diffraction pattern is recorded by a detector. The phase corresponding to the diffraction patterns is then calculated by an iterative algorithm, recovering the original image.

to apply a constraint to the solution in both spaces. The constraints used by Gerchberg and Saxton are two intensity measurements, one in the diffraction plane and one in the near field. However, the measurement in the near field is not available for the case of CDI and has to be replaced by a different constraint. The constraint most often used as a replacement is the finite support in the imaging plane, which in a physical view corresponds to the size of the object. Figure 4.3 shows a visualisation of the whole algorithm. After starting with an initial guess for the amplitude and phase of the object, the procedure can be roughly divided into four steps:

1. The fourier transformation is applied to the current guess $\psi^{(i)}$.
2. The first constraint is applied. Generally the measured intensities are used as a constraint in the diffraction plane. Therefore, the current amplitude $|\Psi|$ of the guess is separated from the phase ϕ and replaced by the measured amplitudes $|M|$.
3. The reassembled updated diffraction pattern is fourier transformed to go back to the imaging plane.
4. The second constraint is applied. For the Gerchberg-Saxton algorithm this would be a second measured intensity. For Fienups implementation the support constraint is applied. In its easiest form this consists of replacing all points outside the support with zero. This new image is the new guess ψ^{i+1}.

The new guess ψ^{i+1} then takes the place of ψ^i and the cycle is repeated again until convergence is reached. In his paper Fienup also proposed the *Input-Output-*

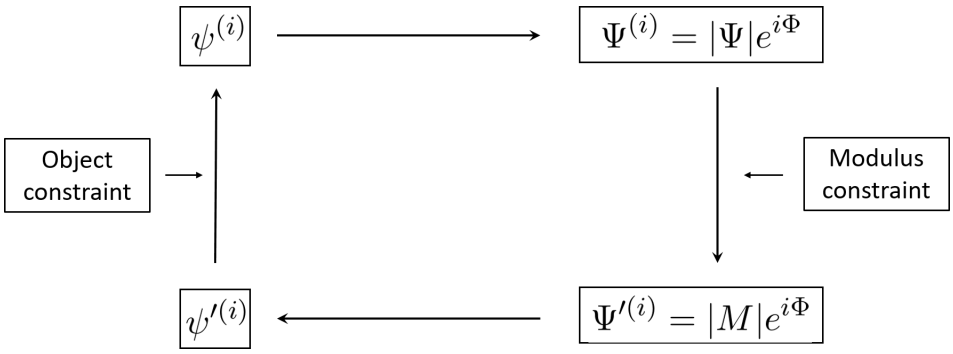

Figure 4.3: Illustration of the iterative phase retrieval algorithm proposed by Fienup. The two constraints are applied in an alternating fashion, one in the object plane and one in the fourier plane.

Algorithm, a modified version of the algorithm that does not replace the points outside the support with zero but with the weighted difference between the new and current guess $(\psi^{(i)} - \beta\psi^{(i+1)})$. This approach of Fienup was later generalized in the *Difference Map algorithm*[137].

In order to estimate the convergence of the phase retrieval algorithms a mathematical description is necessary. This description has been developed since the initial algorithm of Fienup and looks at the algorithms in terms of projections in a Hilbert space. More exhaustive descriptions can be found e.g. in [138, 139, 140, 141, 142]. The phase reconstruction algorithms can be interpreted as a series of projections onto constraint subspaces of the Hilbertspace of possible complex diffraction patterns. So let A and B be subsets, with states in A fulfilling the amplitude constraint and states in B fulfilling the support constraint. The goal then is to find the intersection $A \cap B$. The application of the constraints is a projection onto one of these subspaces defined as

$$P_A(x) := \left\{ \bar{x} \in A | \quad ||x - \bar{x}|| = \inf_{y \in A} ||x - y|| \right\}. \tag{4.13}$$

Meaning the projection $P_A(x)$ returns the value $\bar{x}$ in A that is closest to x. Since only one projection can be done at a time, the two projections corresponding to the constraints can be applied in an alternating fashion until the intersection of A and B is reached. This is called alternating projections and corresponds directly to the first algorithms of Gerchberg-Saxton and Fienup. Following this notation *Difference map algorithm* looks as follows

$$DM := I_d + \beta(P_A r P_B - P_B r P_A) \tag{4.14}$$

where rP_A is a relaxed projection

$$rP_A := (1 + \gamma)P_A - \gamma I_d. \tag{4.15}$$

The *Difference map algorithm* together with *alternating projections* are nowadays the most prominent algorithms and gave rise to a number of derivates. The most

frequently used projections in CDI are the *modulus constraint* P_M in the diffraction plane and the *support constraint* P_S. The modulus constraint is defined as

$$P_M(\psi^{(i)}) = \mathcal{F}^{-1}\left[\frac{\mathcal{F}\left[\psi^{(i)}\right]}{|\mathcal{F}\left[\psi^{(i)}\right]|}\cdot\sqrt{I}\right] \tag{4.16}$$

where I is the measured intensity. It replaces the amplitudes in the diffraction plane with the measured intensities, enforcing the new wave function $P_M(\psi^{(i)})$ to match the measured pattern.
The support constraint is based on the finite area of the object. It assumes that points outside the object are completely non transparent to the light and consequently sets them to zero

$$P_S(\psi^{(i)}(x,y)) = \begin{cases} \psi^{(i)}(x,y) & \text{if}(x,y)\in S \\ 0 & \text{else} \end{cases} \tag{4.17}$$

with S being the set of points within the object. Depending on the experimental conditions other projections can be used, especially with more specific knowledge about the object. Examples include e.g. pure phase or amplitude masks.
Over the past two decades the different algorithms and projections have been implemented for the case of CDI or, as later explained, ptychography in a number of open libraries such as PyNX[143]. The performance of the algorithms is generally evaluated by calculating an error value. There are multiple variations of this, however the experimentally most accessible one is a direct comparison between the reconstructed and measured diffraction pattern by calculating the difference for every point and taking the *root mean square* of them.

4.1.3 Ptychography

Over the last decade a variation of lensless imaging called ptychography has become increasingly popular. It allows the measurement of extended objects. It not only overcomes the need of CDI for isolated objects but generates redundant information that allows more stable reconstructions, less trivial ambiguities of the solution and the retrieval of additional parameters [144]. The basis of ptychography is a merge of the concepts of CDI and scanning microscopy techniques such as *scanning transmission X-ray microscopy*, both in heavy usage in synchrotron facilities, into a single technique. The concept is consequently the recording of an array of diffraction patterns, each at a different position of the sample. Choosing the positions in a way that guarantees a large overlap of the respective probe beams, creates the necessary redundant information the image reconstruction. As in CDI the phase information, and therefore the image, is reconstructed in an iterative fashion. The algorithms of CDI and ptychography are structurally similar and new algorithms for ptychography often emerged on the basis of CDI algorithms.
The first algorithm for ptychography was proposed by Rodenburg and Faulkner in 2004 [145] and is called *ptychographical iterative engine* (PIE). It is based on the error minimization algorithm of Fienup and follows the updating step

$$o^{n+1} = o^n + \beta\frac{|p^{(i)}|}{|\max(p^{(i)})|}\frac{(p^{(i)})^*}{|p^{(i)}|^2+\alpha}\left[P_M\left(\psi^{(i),n}\right) - \psi^{(i),n}\right], \tag{4.18}$$

$$o^{i+1} = o^i + \beta \frac{|p^{(n)}|}{|\max(p^{(n)})|} \frac{(p^{(n)})^*}{|p^{(n)}|^2 + \alpha} \left[P_M \left(\psi^{(n),i} \right) - \psi^{(n),i} \right], \tag{4.19}$$

where β is a relaxation parameter and α prevents zero division. The exit wave function is defined as

$$\psi^{(n),i} = o^i p^{(n)} \tag{4.20}$$

with i noting the iteration and n the probe position. The functions o^i and $p^{(n)}$ denote the object function and the probe illumination. The algorithm calculates and updates the object function for one position at a time until all positions have been visited. At that point one cycle is complete and the next cycle starts, meaning the algorithms works strictly sequential.
This first algorithm was consequently used to reconstruct the first ptychography measurement at a synchrotron [146]. However, shortly after *Guisard et al* proposed a version of his *hybrid input output algorithm* (HIO) adapted for ptychography[144] and then *Thibault et al*[132] proposed a version of the more general *difference map algorithm* adapted to ptychography. The major improvement of the difference map algorithms was the capability of reconstructing object and probe at the same time. The algorithm follows a fundamentally different approach, in that it does not work sequentially but calculates all positions in parallel. Later the PIE algorithm was extended with the option for probe reconstruction as well [147], then called the *extended ptychographical iterative engine* (ePIE).
While Ptychography faces unique challenges such as probe position fluctuations[144, 148, 149, 150], it quickly found broad successful usage in the X-ray community [124]. However, the technique as it is not strictly limited to the X-ray range and can be used in the visible [151] or even in combination with electron scattering[152, 153].

4.1.4 Sampling and resolution in CDI and Ptychography

One of the most important parameters in every imaging technique is the achievable resolution of the image, since it defines the amount of knowledge that can be gained in the studied structure. The resolution in CDI and ptychography can be broken down into three main topics: the diffraction limited resolution, the sampling rate and the achieved resolution based on experimental data. The diffraction limit r gives the theoretical limit for the resolution achievable with an experimental geometry. The possible sharpness of an edge is limited by the fastest variation of amplitude in $\psi(x, y, z_0)$ (see equation 4.9) and therefore by the highest spatial frequency $\sigma_{max} = \frac{k_{max}}{2\pi}$ collected in the diffraction pattern. r is then defined by the half period of the highest collected spatial frequency σ_{max}

$$r = \frac{1}{\sigma_{max}} = \frac{\pi}{k_{max}}. \tag{4.21}$$

In the paraxial approximation k_{max} is linked to a spatial position in the diffraction pattern via $k_{max} = \frac{2\pi x_{max}}{\lambda z}$. x_{max} denotes the point of the diffraction pattern that is furthest from the optical axis and still distinguishable from the noise background. Inserting this into equation 4.21 leads to

$$r = \frac{\lambda z}{2x_{max}} = \frac{\lambda}{2\mathrm{NA}}, \tag{4.22}$$

with NA denoting the numerical aperture of the system. The last part of equation 4.22 is commonly know as Abbe limit [154]. This means the main limitations to the resolution in lensless imaging are the wavelength and the collected diffraction angle. To reach high resolutions it is therefore crucial to collect the diffraction up to large angles.
The second important notion concerning the resolution is the sampling rate, since in reality images are recorded and processed in digital form. This means they are divided into discrete steps, with the distance between those steps defining the sampling rate δ. Naturally the sampling rate of the diffraction image and the object are connected via the fourier transform. A comparison of the continuous and discrete fourier transform (see Appendix B) leads to the relation

$$\delta_x \delta_q = \frac{2\pi}{N}, \tag{4.23}$$

where δ_x and δ_q are the sampling rates in the respective fourier planes and N the number of pixels. As a next step the general fourier transformation can be compared to the diffraction integral (equation 4.8), revealing an additional scaling factor of $2\pi/(\lambda z)$ in the plane wave term. This together with equation 4.23 results in the relation

$$\delta_x = \frac{\lambda z}{\delta_\mathrm{q} N}, \tag{4.24}$$

connecting the sampling rates of the two planes. This connection between the sampling rates, does however leave the question of how the sampling rate has to be chosen. A lower limit for the sampling rate can be derived from the Nyquist theorem, which states that at least two sampling points per period are needed to properly define the respective frequency. In a diffraction pattern the finest fringes in the diffraction are originating from the largest distances in the object and are given by $\lambda z/a$ [155]. Here a is the characteristic size of the object as defined for the Fresnel number (equation 4.10). The sampling then calculates as

$$\delta_q = \frac{\lambda z}{Oa}. \tag{4.25}$$

Here O is a factor called *oversampling ratio* and gives the amount of sampling points per fringe. Experimentally it can be calculated as the ratio between the total points N of the image and the non-zero points of the object N_o. Since the sampling has to fulfil the *Nyquist theorem*, the oversampling ratio needs to be at least 2. However, usually much higher oversampling ratios are used to optimize the convergence of CDI phase retrievals[156]. As an example for such an estimation of the needed sampling one can use the case of a spiral zone plate with a 10 µm diameter at a wavelength of 420 nm. There the needed sampling in the diffraction plane estimates to at least $\delta_q = \frac{420\,\mathrm{nm}\cdot 200\,\mu\mathrm{m}}{2\cdot 10\,\mu\mathrm{m}} = 4.2\,\mu\mathrm{m}$.
From an experimentalist point of view not only the theoretically possible, but also the experimentally achieved resolution for a specific reconstruction is of key interest. For this first a limit has to be defined that determines when two points are separable and therefore still resolved. The most common and accepted limit for this case is the *Rayleigh criterion*, which states that the points are distinguishable if their distance

is greater than half their width. This corresponds to the difference between the 90% and 10% level of an edge. The resolution is therefore defined by

$$R_{Rayleigh} = N_{10\%-90\%}\delta_{obj} \tag{4.26}$$

where $N_{10\%-90\%}$ denotes the number of pixels between the 90% and 10% level. There are however other options, such as fitting the edge with an error function based on a gaussian integral and consequently calculating the width [138].

4.2 Experimental geometry

4.2.1 Sample considerations and production

For the demonstration of the concept of unifying generation and object in the same piece of material it is useful to choose a material with known HHG properties and structures. For these experiments two materials have been chosen: Silicon and ZnO. The harmonic response of both materials is well studied, especially for ZnO as one of the earliest materials used for HHG from solids. Both materials feature bandgaps in the near UV range, ZnO at 3.4 eV and silicon at 3.3 eV. However, silicon has an additional indirect bandgap at 1.1 eV. Silicon shows a strong angle dependent harmonic response with a fourfold symmetry, mirroring the crystal structure, making it necessary to align the polarization accordingly. ZnO on the other hand shows, for low order harmonics (i.e; H3, H5, H7) an isotropic behaviour with respect to the direction of polarization. This is not reflecting the hexagonal crystal structure of the [0001]-cut but is observed multiple times (e.g. [157, 13, 58]) and can be explained by a near isotropic structure of the first conduction band up to 6 eV[158]. The ZnO crystal for the experiments is 500 µm thick. Meanwhile, the silicon sample is 300 µm thick and notably has some damaged surface areas (see Figure 4.4 (a)) but has enough clean surface area for the patterns. It is cut in the [001]-direction with the most efficient direction for HHG being along the [110]-axis. To etch the patterns into the crystal surfaces a *focused ion beam*(FIB) is used. In this type of setup the surface is bombarded with highly energetic ions in normal incidence to either deposit them on the surface or remove material. Which process occurs depends on the energy and type of ions as well as on the ion dose. A full description of the FIB technique is given in Appendix G. For the production of the samples for these experiments Ga^+-ions have been used at an energy of 30 keV. The FIB current was set to 50pA resulting in an ion dose of about $6.24{\cdot}10^{14}$ per pass over the sample. To avoid secondary sputtering of removed material onto the walls of the patterned structure[159] and to gain a better control over the depth, the samples were patterned using multiple passes over the structure, removing a smaller amount of material each time. This also allows to control the overall dose of the sample by the number of passes. For the whole process the FIB was set at a time of 0.05 ns per spot, after which the beam position is changed to the next spot. In between spots the ion stream is closed.
As described in section 3.6 this implementation is inducing a strong enhancement of the harmonic signal from the sample. This effect was not considered during the

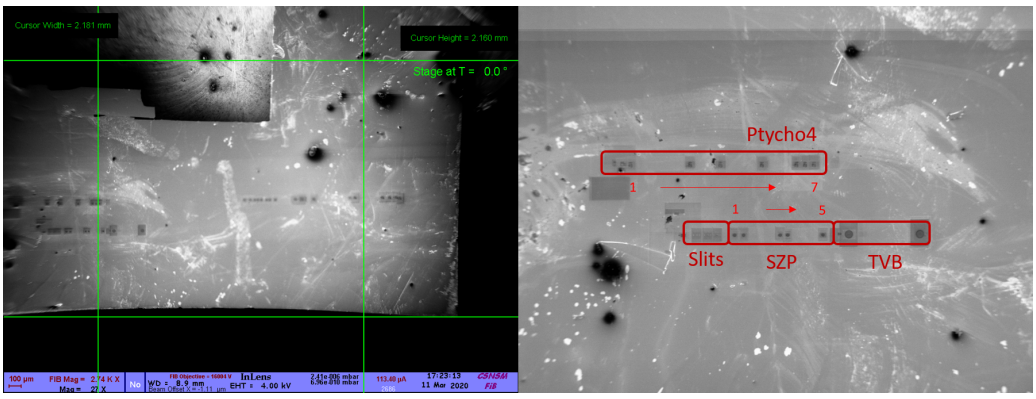

Figure 4.4: (a) Overview over the silicon substrate. (b) Closed up of the area with structures used in the experiments. The 7 Ptycho4 structures are numbered from left to right. Visible in the bottom left is an array of slits used for calibration.

design of the sample and, as it becomes clear later on from the measurements, acts as a pseudo amplitude mask for the purpose of diffractive imaging. Additionally, the doping could have an influence on the intrinsic phase of the emitted harmonics as mentioned in [23]. This effect would need to be considered as an additional term in equation 4.27 to calculate the phase mask of the used patterns. Notably, opposed to silicon, ZnO is reported to have a higher resistance against these changes and mostly maintains its initial crystal structure [160].

Two types of patterns are studied: a *spiral zone plate* (SZP) and a mixture of geometric features, resembling components of an electric circuit (Ptycho4). This two structures have been chosen to represent an application in optics for the case of the SZP, namely generating a beam carrying an *orbital angular momentum*((OAM), and an application in industry in the form of the circuit like sample. The goal for the patterns was initially to achieve a pure phase map with a phase contrast of π. However, this was planned without consideration of the altered mediums physical and optical properties due to the FIB process. The patterning depth of the samples was therefore calculated based on the phase difference between propagation in the material and air according to

$$d = \frac{\lambda \phi_{total}}{2\pi(n-1)}. \tag{4.27}$$

Here n denotes the refractive index of the wavelength that propagates inside the patterned structure, λ the wavelength of interest that propagates outside the structure and ϕ_{total} the desired phase difference. It is important to notice that for the case of HHG the wavelength that propagates inside the structure and outside the structure can be different. In the case of above bandgap harmonics for example, the harmonics are only generated at the end of the structure. Therefore, λ is the wavelength of the harmonic but the refractive index of the fundamental wavelength has to be used. Since H5 was assumed to be generated mostly in the bulk material in front of the pattern, the depth has been calculated with the refractive index of H5 for the pristine material (neglecting any change due to the FIB).

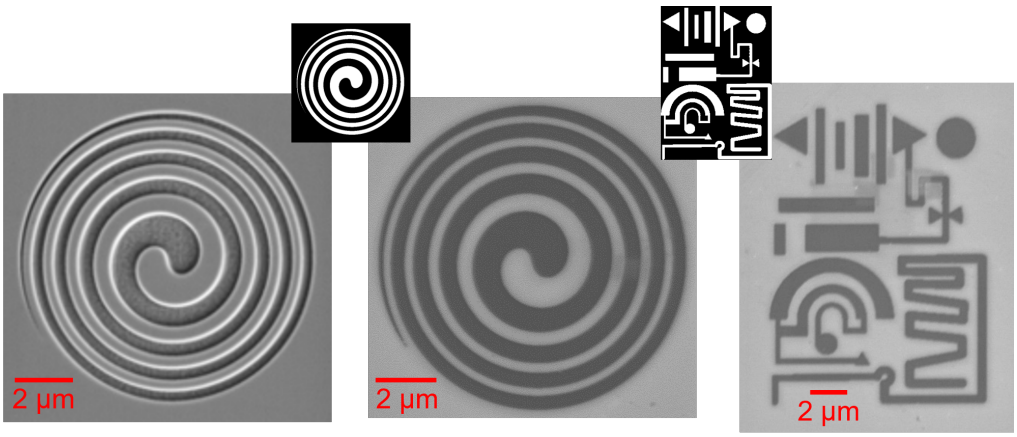

Figure 4.5: SEM images of the studied patterns. (a) the SZP on ZnO, (b) SZP on silicon and (c) the Ptycho4 structure on silicon. The insets at the top show the binary masks used for the patterns.

The SZP profile is the combination of a helical and spherical waves given by

$$\phi_{total} = \exp\left(-il\phi\right) \exp\left(i2\pi\sqrt{R^2 - r^2}/\lambda\right) \tag{4.28}$$

with λ being the wavelength, r the radial coordinate, l the topological charge of the generated OAM and R the radius of curvature of the spherical wave. The radius is chosen to create a focal spot 6 µm after the structure and the angular momentum is $l = 1$. *Scanning electron microscope* (SEM) images of the structures are taken after production, which is conveniently possible within the FIB setup. Examples of the structures are shown in Figure 4.5. Prior to the ptychography our group used the SZP on ZnO in an experiment to generate auto focusing harmonics with a controlled OAM [25]. This allows for a comparison of the ptychography reconstructions with actual experimental measurements of the OAM. The ZnO SZP itself is 210 nm deep, while the structures in silicon have varying depth around 50 nm (see section 4.3.3). This is an important difference for two reasons. The first is whether the depth of the structure is conform with the projection approximation, i.e. if its thickness is below the DOF. For our measurement setup the DOF is 800 nm which is higher than the thickness of either sample. The second reason is the shape of the probe. In the reconstruction algorithm it is assumed that the probe is identical for all positions of the sample. Due to local field enhancement caused by the propagation in the structure, the shape of the probe can be distorted differently for each spot on the sample. This effect is used in some instances [86, 84, 85, 161] to e.g. enhance the driving field locally but in the context of ptychography it might introduce distortions that prevent the reconstruction algorithms either from converging or propagate the distortions into the final image. For that reason, despite the more challenging production process, the silicon samples have been chosen to be significantly less deep than the ZnO sample, matching a phase difference of exactly π. To get a clearer picture of the effects of the propagation inside the sample it is accessed using *finite difference time domain* (FDTD) simulations in the framework

of the *Lumerical* software which are detailed further on.

4.2.2 The Laser system

The laser used for the experiments is a *NOVAE Brevity* [162]. It is an all fiber femtosecond laser centred at 2100 nm, delivering linearly polarized ≈80 fs pulses at 18,66 MHz. It has an output power of ≈200 mW resulting in a pulse energy of about 9,5 nJ. The wavelength of 2100nm corresponds to an energy of 0,59 eV which is well below the bandgap energies of the studied materials.
The optical setup for the experiments is illustrated in Figure 4.6. The beam first passes a half wave plate to turn the polarization vertical. Afterwards the beam diameter is expanded to 6,14 mm using a telescope consisting of two convex lenses, to enable smaller focal spots. This is vital to reach the intensities necessary for HHG in solids, despite the low power of the laser. The losses introduced by the telescope are reducing the maximal available power in front of the iris to 160 mW, but the advantages of tighter focusing are overall out weighting the losses.
After passing an iris the beam is focused into the sample using a 3 cm aspheric lens corrected for spherical aberrations. This allows for focal spot sizes around 4 µm and intensities of about 0,3 TW/cm^2. To avoid the power loss of the polarizer, the power and focal spot size are regulated with the iris in front of the lens. This leads to a coupling of the focal spot size and the power of the beam, resulting in a nonlinear behaviour of the intensity evolution that is further described in section 4.3.1.
Towards the end of the experiments it got clear that the laser was not in optimal condition, most likely as a result of temperature fluctuations in the lab. This resulted in pulse to pulse polarization fluctuations that were likely present during the whole measurements. The measured power after a wire grid polariser was 83 mW for vertical polarization and 60 mW for horizontal polarization. The main axis of the polarization therefore remains vertical. Assuming an elliptical polarization instead would lead to an ellipticity of

$$|\epsilon| = \sqrt{\frac{60\,\mathrm{mW}}{83\,\mathrm{mW}}} = 0.85 \tag{4.29}$$

which is found by *Klemke et al*[75, 56] to have a significantly lower harmonic yield. This low yield has however not been observed in the experiments here, leading to the conclusion that the polarization is indeed linear but varying on a pulse to pulse basis.
The sample is mounted on a motorized xyz-stage and a manual θ-stage, allowing full control over the relative position between sample and focal spot. With a Rayleigh range of 11 µm, well above the absorption length of the harmonics, the focal spot can be positioned at the rear surface of the sample by maximizing the harmonic yield.

4.2.3 Detection scheme

The detection scheme has been used in two configurations: the main one to detect diffraction patterns and another one for spectroscopic measurements. Due to me-

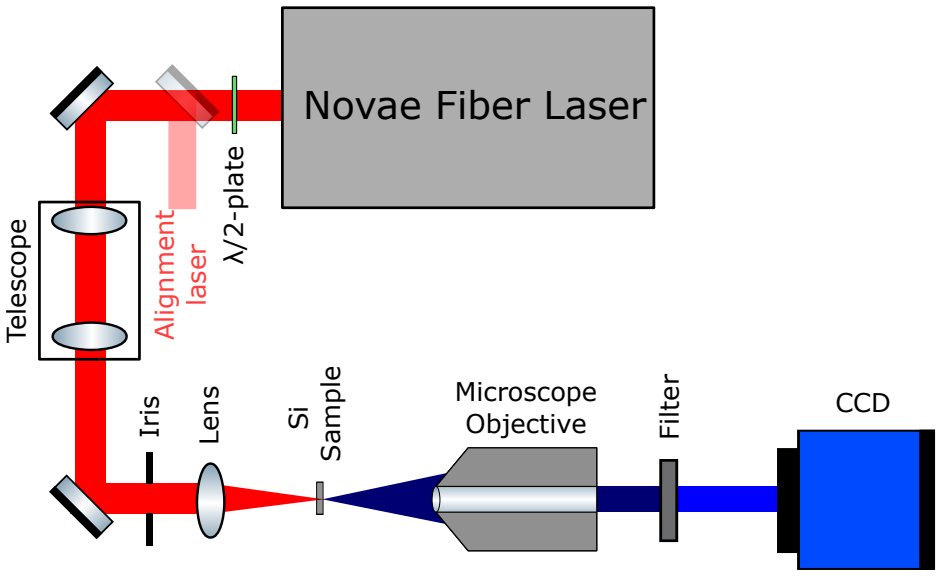

Figure 4.6: Scheme of the ptychography setup.

chanical limitations it is not possible to collect the diffraction patterns directly with the camera. Instead they were imaged onto the camera using a microscope objective (*Nikon N40X-PF -40X*) with an NA of 0.75. The harmonic is then selected with a bandpass filter and guided on the CCD (*PCO.Edge*).
The microscope objective is coupled to the camera to guarantee a fixed distance and the whole combinations can be moved with respect to the sample. This is necessary to switch between the two imaging modes: imaging the samples rear surface and imaging the diffraction pattern, usually about ≈200 µm behind the sample. The possibility to switch between the two is necessary to determine the distance between the two planes, which is a critical parameter in the phase reconstruction algorithm. In the second detection setup a lens is used after the sample to collect the harmonic signal and guide it into a spectrometer. This change is needed since the transmission of the microscope objective rapidly decreases below 400 nm. Thus, H7 located around 300 nm is not transmitted. However, as a drawback of this solution the different divergence of each harmonic leads to differences in the focus position between the harmonics. Therefore, the coupling into the spectrometer has to be adjusted for all harmonics by shifting the lens along the propagation axis.

4.2.4 Data treatment procedure

The diffraction patterns recorded by the camera are normally not perfect but have a couple of shortcomings, like e.g. noise backgrounds or a non centred beam. These shortcomings can become prominent enough to prevent the phase retrieval algorithm from converging. However, some of these issues can be addressed with appropriate post processing methods. The procedure followed for the experiments in the next sections and its motivations are discussed in the following, by sequentially going through the different steps of the applied post-processing.

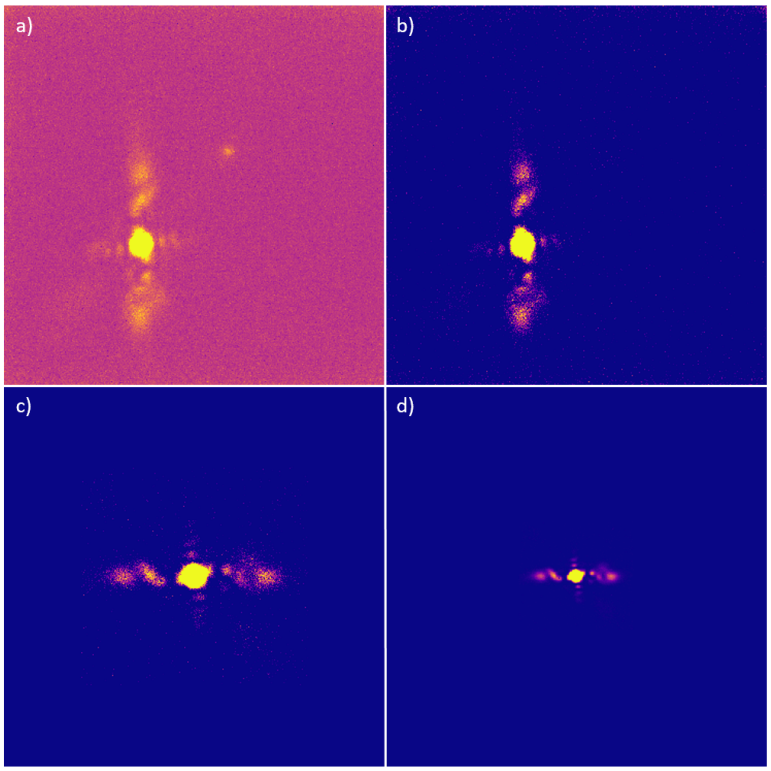

Figure 4.7: Evolution of the diffraction pattern over the different data treatment steps. (a) Image as captured by the CCD. (b) Correction of the range, masking of reflections and noise background subtraction. (c) Centering and rotation of the diffraction pattern. (d) Binning and zero padding

i As a first step an actual error in the labview program that runs the measurements has to be corrected. The diffraction patterns were saved as *png* files and while saving, the measurements were multiplied by 2^n to fill the whole available 2^{16} bit range. The change and relative multiplier between the images can be derived from the noise level of the images and corrected for. This problem had gone unnoticed during the experiment for some time and while not completely preventing reconstruction still lower the image quality.

ii As a second step general background noise in the image has to be addressed. While the phase retrieval algorithms inherently have some stability against background noise and, as a result of continuous work of the CDI and ptychography community, have become more stable against noise over time, noise still is a major reason for stagnation in the algorithm. The level of background noise is calculated from an image region far from the diffraction pattern. Additionally, pixels close to the image border are avoided due to increased noise levels. The average background noise and an additional three standard deviations of it are subtracted to achieve a near zero signal in the outskirts of the images. Negative pixel values are set to zero afterwards.

iii Unwanted reflections that made it onto the CCD are masked. An example of such a reflection can be seen in Figure 4.7 (a) at the upper right of the diffraction pattern. Not all reflections can be masked this way. If the reflection is to close to either the center of the diffraction pattern or overlaps with significant features of the diffraction it is left untouched and consequently acts as an artificial spatial frequencies introducing diffraction lines overlapping the reconstructed image. An example of this can be seen in the measurements in section 4.3.4.

iv The high *numerical aperture* of the imaging system and the consequently large collection angle for the diffraction pattern are not within the paraxial approximation anymore. This artificially increases the pixel size towards the edge of the image in a nonlinear fashion and has to be corrected (see Appendix C).

v Next, as a requirement of the phase retrieval algorithm, the diffraction pattern has to be centred in the image. This is achieved by cutting the diffraction pattern from the image using a square mask. The cut area is chosen to be as large as the camera chips size allows, normally ranging around 1000x1000 pixels out of the overall 2048x2048 pixels available. The image is then padded back to its original size.

vi To compensate for the experimental setup, in which the camera is rotated sideways, the images have to be rotated 90° counter-clockwise in order to match with the recorded coordinates.

vii The last step is binning of the images, normally by a factor of 8 or 10. This comes at the cost of sampling, therefore reducing the oversampling rate, but reduces the computation time and memory needed for the phase reconstruction severely. Importantly despite being reduced the oversampling is still high enough to guarantee convergence of the algorithm. Since the binning is averaging over a small area of pixels it also reduces the standard deviation of the noise background. After binning the images are zero padded up to 512x512 pixels to reach higher sampling rates in the object plane.

4.3 Results

The experiments start with verifying that the setup and samples are capable of achieving the non pertubative regime of HHG. Next, the necessary calibration experiments are conducted to gain access to all the parameters needed for the reconstructions. Finally first images are reconstructed showing the capabilities of this technique and possible applications.

4.3.1 Pertubative and non pertubative harmonics

When generating high harmonics in solids it is important to make sure the harmonics are generated in a non-pertubative way, opposed to the pertubative generation normally described in the framework of an electron cloud oscillating in an anharmonic fashion. This is especially true for studies of lower order harmonics. The

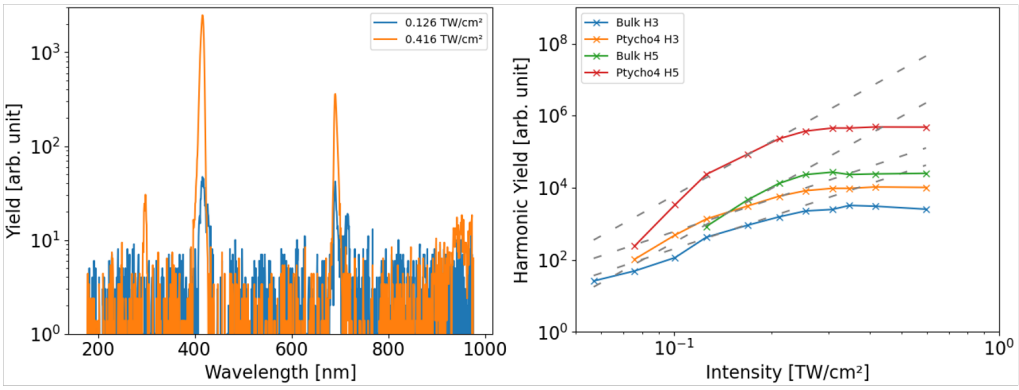

Figure 4.8: (a) Example spectra for two different intensities. (b) Intensity scaling for harmonic 3 and 5. The dashed lines denote a scaling of I^3 and I^5, which are adjusted to the best matching part of each harmonic to guide the eye.

easiest ways of confirming the regime is to record a scan of driving field intensity and compare the behaviour of the harmonic signal to the expected behaviour for pertubative generation. The pertubative harmonics are expected to follow $I_n \propto I^n$, where n is the harmonic order. Experimentally the spectra have been recorded for different driving intensities. Since the losses introduced by a polarizer are too high to maintain the intensities necessary for HHG, the intensity is regulated using an iris before focusing into the sample to cut a part of the beam. The problem with this approach is that beamsize, and therefore the focal spot size, and power are changed at the same time. However, the consequently necessary power measurement after the iris allows calculating the initial beam size. Using this beamsize the in vacuum focal spot sizes for different iris openings can be calculated. This was done via convolution with the iris pattern and subsequent propagation of the beam into the focal plane.

There are multiple reasons why these intensity values have to be taken with care. First the calculation assumes a perfect Gaussian beam and pulse as an input, which the experiment is close to but likely not perfect. Especially when taking the propagation inside the sample into account. This propagation is the second big source of error. As mentioned in section 3.3 and in literature [87] propagation effects are present and change the pulse as well as the beam profile. Since the propagation effects are scaling nonlinear with intensity the difference between reality and calculated values is growing with intensity. Therefore, the higher intensity values are most likely underestimated. As a consequence the measurement is overestimating the extend of the pertubative regime. To calculate the harmonic yield, the spectra are first corrected for integration time and filter transmission and then integrated over the width of the respective harmonic. Example spectra are shown in 4.8 (a). The measurement is repeated for positions on the pure silicon substrate and the Ptycho4_7 sample.

Figure 4.8 (b) shows the intensity vs. harmonic yield plots. Both H3 and H5 are starting to diverge from the pertubative behaviour around 0.2 TW/cm². After diverging from the pertubative behaviour the harmonics seem to saturate. While,

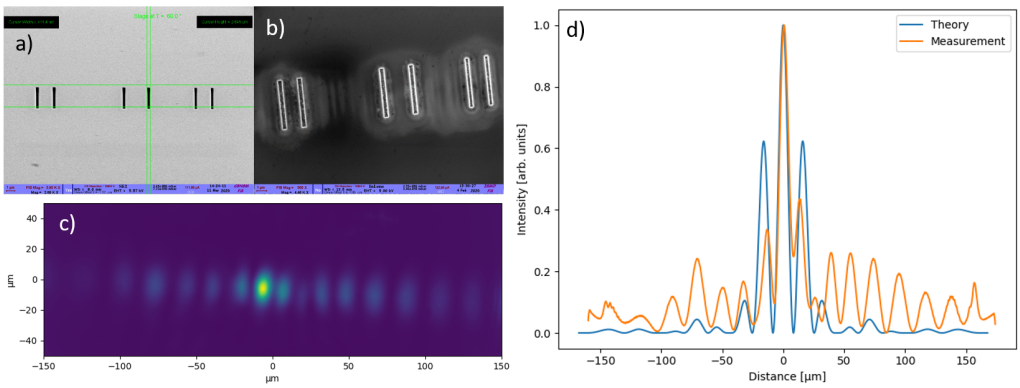

Figure 4.9: SEM images of the etched slits before (a) and after (b) the experiments. (c) shows an example of a diffraction pattern obtained from the structures. (d) compares the profile along the horizontal direction in (c) with a perfect double slit pattern.

due to limitations in the achievable driving intensity, the saturation is only barely visible here, the saturation behaviour is in cohesion with previous observations[75]. In the further experiments the driving intensity was chosen to be 0.21TW/cm^2 to avoid damage on the nanostructure. Therefore, the measurements are located just at the threshold of the non-pertubative regime.

4.3.2 The effective pixel size

Since the microscope objective was not used in conjunction with an ocular, the nominal magnification is not reached. However, since the sampling size of the CCD is an important parameter for the phase retrieval algorithm, the magnification is needed to calculate the effective pixel size in the plane imaged by the microscope objective. At the beginning of the experiment there were three distinct ideas on how to measure or calculate the magnification:

i Directly imaging the slit pattern on the sample and calculate the magnification based on the width of the slits from the SEM images and the pixel size of the camera.

ii Record a far field diffraction pattern of either a single or two slits and compare it to the expected diffraction pattern for that case.

iii Simulate the diffraction in the sample using the experimental parameters and the mask of the sample as a basis and consequently match the simulation to the respective scan position.

Option (i) proved to be impractical due to the small focus and consequently low field of view in combination with low imaging resolution. The signal from one slit pattern extends over just 4-5 pixels and is therefore not resolving clear edges that limit the slit. Calculating the pixel size based on this is consequently connected to huge error margins. Nevertheless, with a single slit being 400 nm wide this results in an effective pixel size of 80-100 nm. As the amount of pixels for one slit is

overestimated due to the low resolution, this underestimates the real effective pixel size.
The concept of option (ii) proved itself to be more suitable but the slits patterned onto the sample were suffering from a couple of drawbacks. First they were etched rather deep making them prone to field confinement effects around them. Changes introduced by this make a comparison with the diffraction expected from a slit much more complicated, since it requires to include not only the diffraction but also the propagation inside the structure into the calculation. When examined with an SEM after the experiments the slits do not show a breakdown of the structure. However, there are signs of local melting and reformation of the material. Deep patterning means that the slits themself are not emitting harmonics but rather the areas around them. Figure 4.9 (c) shows an example of a diffraction from the slits. The pattern is not showing the expected symmetric line diffraction but an asymmetric behaviour with deviations from a perfect line. The pattern itself is much closer to a 2 or 3 slit diffraction pattern than a single slit pattern. Matching this diffraction pattern with a simulation is rather difficult since it is not clear whether the diffraction is happening on a single pair of slits or on multiple slits. Overall, no clear estimate of the effective pixel size could be gained from this. However, after determining the effective pixel size via option (iii) to be close to 300 nm, the pattern could be compared with a theoretical double slit. Using the parameters for two illuminated slit pairs with a distance of 5 µm and a width of 1.9 µm, yields the best similarities to the experimental pattern. The comparison in Figure 4.9 (d) shows a reasonable overlap for the left half of the pattern while the right side is severely distorted, a behaviour that was prevalent for every position of the beam relative to the slits. Nevertheless, this confirms that indeed at least two slits were illuminated during the experiments.
The third option combines the approach of option (ii) with the actual samples by comparing simulated diffraction patterns with the measured data. Especially the Ptycho4 samples are "well behaved", giving a clear and clean diffraction pattern, and therefore allow for accurate matching with the simulation. This comparison results in an effective pixel size of 300 nm. Together with the original pixel size of the CCD (6,5 µm) a magnification of $M = 21,67$ is calculated for the imaging system. However, the reconstructions allow for a further refinement of the effective pixel size, as the algorithm does not converge for pixel sizes far from reality. By gradually changing and optimizing the effective pixel size, an optimum for the algorithm performance was achieved with an effective pixel size of 340 nm. For effective pixel sizes far off this value a successful reconstruction was not possible. This optimized effective pixel size corresponds to a magnification factor of $M = 19,12$ for the imaging system which appears to be reasonable.

4.3.3 Reconstruction of the Ptycho4 sample

The samples chosen for the experiments are on the far left of the row of samples in Figure 4.4, namely Ptycho4_5 and Ptycho4_7. Overall, the row of Ptycho4 samples features a variation of different etching depth of the structure, with Ptycho4_5 and Ptycho4_7 located at the lower end. For the FIB a time of 0.05 ms per point was

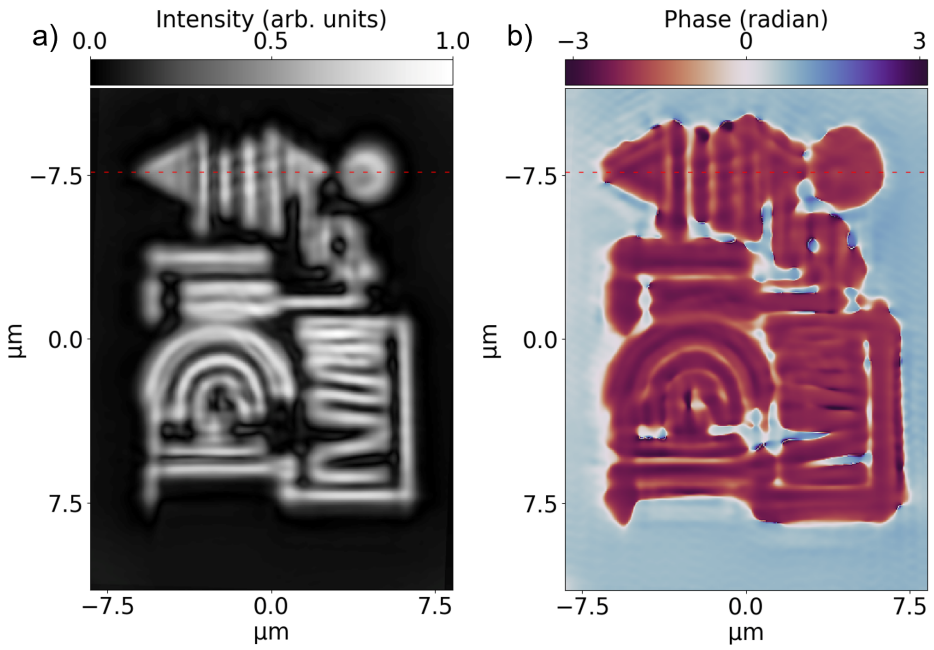

Figure 4.10: Reconstructed Amplitude (a) and phase (b) of the Ptycho4_7 structure. Adapted from [163].

used, making multiple passes over the structure to reach the designated depth. Using multiple passes instead of longer etching times per point improves the quality of the structure by avoiding redeposition of sputtered material on the walls of the structure [159]. For Ptycho4_5, 5 passes are done, while for Ptycho4_7 only 2 passes over the structure are done. The final assessment of the depth of the structures is done based on SEM images taken at a 60° angle, therefore showing the edges of the structure. However, with a target etching depth of 55 nm the etching remains shallow and this method of verifying the depth has large margin of errors. This method leads to a depth of 64 nm for the Ptycho4_5 sample, while for Ptycho4_7 the edges were to vague for an estimate. Nevertheless, due to the lower amount of passes it can be assumed that the etching depth of Ptycho4_7 is lower than the estimate for Ptycho4_5.

For the ptychography scans 2000 measurement points were taken in a spiral pattern, starting in the center of the sample and reaching a diameter of 25 µm. The average step size along the spiral was 0.5 µm. Together with the estimated in vacuum focus size of 6.5 µm FWHM this leads to an overlap of 87% between the scanning positions. However, since the size of the harmonic probe can be expected to be smaller due to self focusing and the nonlinear behaviour of the harmonic this overlapping value is a best case scenario. In the reconstructions the real probe size was later estimated to about 2-2,5 µm based on the reconstructed probe and convergence of the algorithms for different fixed probe sizes, leading to an overlap of 61%. This is rather low compared to usual values in the community but nevertheless this leads to successful reconstructions. Assuming that a larger portion of the beam up to the $1/e^2$ width has enough photons to contribute to the signal, the overlap grows

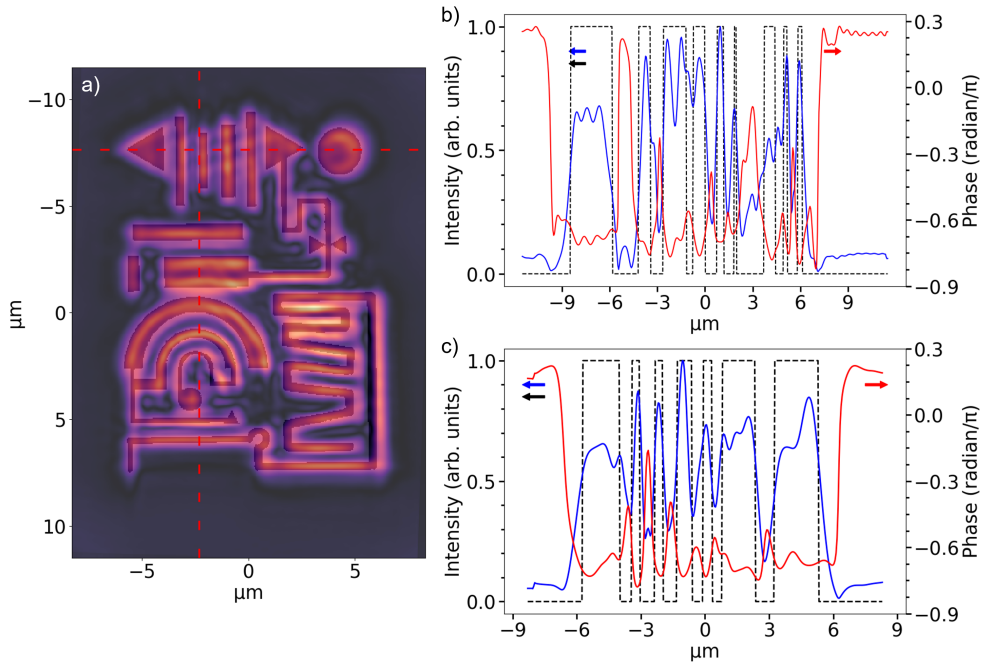

Figure 4.11: (a) Reconstructed amplitude overlayed with a mask of the original structure. Vertical (b) and horizontal (c) cut through the reconstructed structure. The position of the cuts are marked by dashed red lines in (a). The blue line marks the amplitude profile, the red line the phase profile and the dashed black line the profile the mask used to produce the structures.

to 77% (based on the 2.5 µm FWHM). The integration time for the measurements is 3 s, leading to a theoretical total acquisition time of 100 minutes. However, the real total acquisition time was about 2,5 hours as it was extended by delays in the information processing and saving, as well as delays for moving the sample.
Reconstructions have been performed using both the GPU and CPU version of the PyNX ptychography module[143]. For the GPU the probe was reconstructed simultaneously, while it was fixed at a 2 µm width with a Gaussian beam profile for the reconstructions using the CPU version. The main reason for this was the lack of convergence of the CPU version when not fixing the probe. For the CPU version only the *alternating projections* (AP) algorithm converged. For the GPU version all algorithms converged, in even less cycles than for the CPU version, a behaviour that is surprising given that the algorithms should be conceptually identical for both versions. The reconstructions in Figure 4.10 were obtained after only 80 cycles of the *difference map algorithm* (DM) with subsequent summing over multiple reconstructions. To align the different reconstructions properly a subpixel registration algorithm[164] has been used, however the mismatch between the images was far below one pixel making the step obsolete.

The obtained reconstructions are similar for the two samples. An example of the Ptycho4_7 reconstructions can be seen in Figure 4.10. The structure can be

clearly identified in the amplitude and phase pictures, with the amplitude showing a better contrast compared to the phase. For the amplitude it is possible to separate structures down to sizes of about 500 nm, which corresponds to the size of the ridges of the 'zigzag' pattern at the lower right or the distance between the half moons on the left. Complex structures below 500 nm are however, not resolved any more. An example for this is e.g. the top of the 'zigzag' pattern, where the ridges are getting too close to each other or right above that the small triangles (compare with Figure 4.5) that are not identifiable in the reconstructions. The phase image shows a lower contrast compared to the amplitude image but nevertheless contains the same information and reaches the same resolution. Since the original object was designed as a pure phase object this good contrast in the amplitude picture at first comes at a surprise. In fact, this originates from the enhancement of the harmonics, in particular H5, due to the material alterations induced by the FIB doping (see section 4.2.1 and 3.6). By only enhancing the signal from etched areas the enhancement acts as a pseudo amplitude mask for the probe, enabling the well contrasted reconstruction of the amplitude.
The amplitude picture shows some further discrepancies with the original structure, as can be seen in Figure 4.11 (a). First the overall size of the reconstruction is not absolutely matching the initial pattern. While an overall size mismatch can be caused by the uncertainty in the effective pixel size, the reconstruction shows a varying mismatch, with the top parts of the pattern being slightly less wide than the bottom part. This can be seen as artefacts from the microscope objective and systematic image errors introduced by e.g. a slight misalignment. Alternatively it is possible that the reconstruction algorithm is locking into different solutions depending on the position. A second important discrepancy is the emergence of a splitting in larger structures of the reconstruction. This is particularly visible in the large central rectangle and half moon, both showing a stronger signal towards their edges with a dip of signal in the center. This effect is even more clear when taking profiles through the reconstruction, comparing it to the original mask.
A first possible origin of these structures are artefacts in the reconstruction. Since the structure persist over multiple reconstructions, random fluctuations of the algorithm are an unlikely cause. It can however, be a Fourier artefact of the reconstruction caused e.g. by the limited detector size or S/N ratio. At the same time reflections that reach the CCD, e.g. from internal surfaces of the microscope objective are causing regular patterns over the whole image as it is the case in the SZP reconstructions in section 4.3.4. As for physical effects, there are two that can cause a behaviour like this: field enhancement and wave guiding in the structure. The first one, field enhancement, describes an increase in the driving laser field around edges when propagating through a nanostructure, consequently enhancing the harmonic signal. However, this process is polarization dependent and consequently would show a directional behaviour. In the reconstructions the half moon structure covers angles from 0° to 90°, showing a more intense HHG signal at its outlines over the whole range. Additionally, the etching depth of the structures is extremely small compared to the laser wavelength, limiting the effects from field confinement. The other option is waveguiding similar to the case described in [165] for the XUV. The structure matches the observed pattern, being less directional.

The effect could be enhanced by the change in refractive index due to the FIB induced material alterations. The depth of the modifications and their location beneath the etched area could serve as an extension of the waveguide. A big problem is the lacking lateral resolution achieved in the experiments that prevents a clearer picture of these structures. Nevertheless, Fourier artefacts are at this point the most likely explanation.
Using the profiles through the reconstruction in Figure 4.11 (b) and (c), the contrast and resolution can be further accessed. It gets immediately clear that the contrast varies strongly depending on the position in the sample and the size of the surrounding features, with smaller features leading to a locally much worse contrast. In general, the contrast for the amplitude reaches around a value of 0.5, while the phase contrast has regions of much lower contrast. The resolution is estimated by calculating the distance between the 90% and 10% level of an edge. To attribute for the local variances in resolution and reconstruction quality two edges with sufficient contrast are chosen for each profile. One edge of which is close to the best case scenario while the other is closer to the worst case. The respective edges are marked in the profiles in Figure 4.11. This results in an upper and lower limit for the resolution of 800 nm and 375 nm. Considering the wavelength of 420 nm and NA of 0.5, the theoretical resolution of the system is $d = \frac{\lambda}{2NA} = 420\,nm$. Meaning the achieved resolution is about twice the theoretical limit at maximum.

The patterns were originally designed and etched as pure phase masks with a phase difference of Pi. Nevertheless, in their studies *Sivis et al* showed, by comparing the focus position of their etched Fresnel zone plate to theory based predictions, that the process of HHG is adding an additional phase term to the harmonics[23]. They estimate this phase to be $3/\pi$ for the fifth harmonic of their 2-2.3 µm laser system. Since this term was not accounted for during the design of the sample used here and ptychography is highly sensitive to the phase, the question arises whether ptychography is able to retrieve this phase term as well. Especially in the light of recent results showing the reconstruction of the depth of grating like nanostructures using the harmonics generated in those nanostructures [26]. However, the case of a grating like structure is arguably simpler than a full images as the depth has a direct dependency on the position of the diffraction orders in the far field. Nevertheless, for a full ptychography reconstruction this question gets much more complicated. While the structure is clearly visible an extraction of the phase profits from much higher spatial resolutions to extract the phase reliably without interference of edge effects. Additionally, the SEM based depth measurements of the structures that serve as a reference to discern between the structure induced and gallium induced phase are showing a high variance.

As a first step to extract depth information out of the image, the phase difference between pattern and unpatterned areas has to be extracted from the sample. Due to the high phase variation inside the structure and the spatial resolution that, for some parts of the sample is just enough to image the structure, the phase difference between the outside of the structure and the first etched feature inside is used for the phase difference. For the Ptycho4_7 sample depicted in Figure 4.10 this results in a phase difference of 1-1.1π, matching the design value exactly. The other studied sample, Ptycho4_5, the phase difference is 1.1-1.2π.

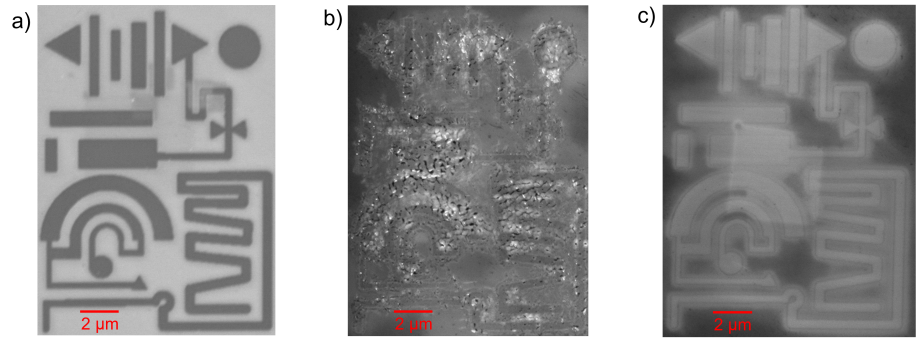

Figure 4.12: SEM images of the Ptycho4_6 sample before (a) and after (b) the experiments. In contrast the Ptycho4_7 sample (c) shows no damage after the measurements.

To judge the information in these phase values, they need to be compared to the expected phase difference. For this calculation the real depth of the structure is needed. However, during the FIB etching the depth of the lowest dose structures, Ptycho4_5 and Ptycho4_7, could not be determined by the SEM pictures due to the low depth. An estimate of the depth can be made assuming the etching depth changes close to linear with the ion dose. This results in 12 nm for the Ptycho4_7 and 30 nm for the Ptycho4_5 sample (see Appendix E.1). The phase difference additionally depends on the generation point of the harmonic, for a generation far in front of the structure the index of refraction of the harmonic is used in equation 4.28, while for a generation inside the structure the index of the fundamental is used. For the Ptycho4_5 and Ptycho4_7 sample this results in phase values of 0.35π and 0.14π for the generation before the structure and 0.59π and 0.23π when generated at the end of the structure. None of these are matching the difference of π the structures were designed for.
This means the phase difference between the reconstruction and the theoretical value based on sample depth is at least 0.6π for the Ptycho4_5 and 0.8π for Ptycho4_7. Both of which are above the additional phase term estimated by *Sivis et al.* As the phase extraction from the image and the calculation of depth of the structure are connected to high tolerances this can very well be due to measurement errors. It seems however that the phase profile of the image is, for the reconstructions here, not or only with additional terms connected to the depth of the structure.
It is however noteworthy that the origin of the additional phase is not necessarily due to the process of harmonic generation itself. It can also be a result of the propagation through the material layers modified by the FIB. Based on the refractive index of amorphous silicon[121] a 30 nm layer could for example change the phase difference by 0.1π. For other material changes, as the implementation of gallium into the crystal, data regarding the optical properties is not available. Together with the remaining uncertainties regarding the exact depth of the material alterations this makes a final judgement on the phase information difficult.

To drive the HHG in a solid extremely high intensities are needed which, as a

consequence, are often pushed close to the damage threshold of the material. This can naturally lead to the destruction of the sample, especially if the field enhancement in the sample is locally amplifying the field even further. Nevertheless, the signal in the performed experiment was low, making integration times of multiple seconds for each spot a necessity. At the same time laser induced damage of the samples have been observed. It is visible in the measurements as a gradual loss of the diffraction pattern, until only the central Gaussian beam profile of the harmonic is left. For some samples this process took a few seconds while other samples were damaged basically instantaneously. Notably, patterns using a low etching depth (like the used samples Ptycho4_5 and Ptycho4_7) seem to be much more stable against damage than patterns with a deeper etching. An example for a damage is shown in Figure 4.12. It shows SEM images of the sample before and after the experiments in (a) and (b), clearly demonstrating the possible damage to the sample. (c) shows an image of the Ptycho4_7 sample which was used for measurements. There, no clear damage of the structure is visible. Regarding the damaging it has to be noted that additionally to direct thermal damages, there is the possibility of the implanted gallium drifting to the surface and building clusters on it due to the heat introduced into the material.

4.3.4 Reconstruction of the ZnO SZP

As a next step, data taken by *Dr. Mukhtar Hussain* on the same setup but using ZnO as a base substrate for the patterns have been analysed. Here spiral zone plate patterns, as described in section 4.2.1, that can be used to generate a focused OAM are imaged. Measurements studying the capabilities of this SZPs for OAM generation have been studied by *Gauthier et al*[25], including experimental observation of the generated in focus intensity distribution. The SZP was patterned with the same mask used to produce the silicon SZP. However, due to lower refractive index of H5 in ZnO the patterning needs to be 210 nm deep to reach the target phase difference of π. With a bandgap of 3.3 eV, ZnO is similar to silicon but it lacks the indirect bandgap present in silicon. This lowers the absorption of the below bandgap harmonics significantly, resulting in the observed harmonics being generated much deeper inside the material than for the case of silicon. Especially H5, which is used for these measurements as well, is therefore generated before the layers that are potentially altered by the FIB. Additionally, ZnO is much more stable against implantation of ions and surface amorphization during the FIB process [160]. In contrast to silicon, an alteration of the harmonics due to changed material properties is therefore not expected for the ZnO sample. On the other hand, the higher etching depth of 210 nm introduces propagation effects in the ZnO sample that are no longer negligible. This includes both field confinement of the fundamental driving laser, as well as waveguiding of the harmonics inside the structure.

For the measurement, 457 positions were scanned following a grid pattern with an average stepsize of 400 nm. Each spot is illuminated with a 6.5 µm FWHM beam waist of the driving laser, which can be expected to result in an H5 probe smaller than this, similar to the silicon. Using the driving laser as a base this again corresponds to an overleap of 87%. The diffraction patterns are imaged onto

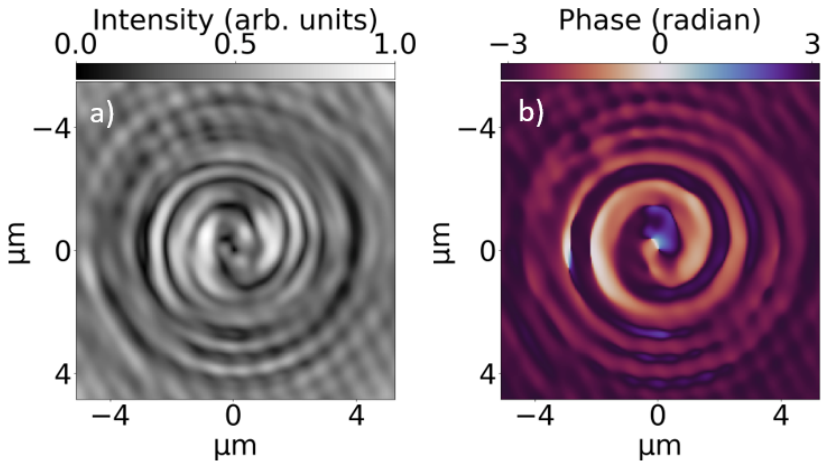

Figure 4.13: Amplitude (a) and phase (b) of the reconstructed SZP. Adapted from [163].

the camera from a plane 120 µm after the sample using an integration time of 5 s. Image treatment prior to the reconstruction follows the same procedure as for the silicon sample (see section 4.2.4), using a binning factor of 10 and zero padding up to an image size of 512x512 pixels. This results in an effective pixel size of 2 µm after the binning, which corresponds to a pixel size of 50 nm in the object plane. The diffraction patterns were reconstructed using 210 iterations of *alternating projections* (AP) and 10 iterations of *difference map* (DM). The probe was not reconstructed but fixed at 2 µm gaussian beam width. Notably, AP was the only algorithm that reached consistent convergence. The 10 iterations of DM were used periodically after every 40 iterations of AP to counteract stagnation. The width of the fixed Gaussian probe and the pixel size of the CCD could be varied slightly without breaking convergence, however doing so yielded worse results. The result is displayed in Figure 4.13.

The first thing visible in the reconstructions is a diagonal modulation structure overlaying the whole image. We attribute this to a reflection from the microscope objective, located close to the center of the diffraction pattern. Since the far field diffraction pattern corresponds to the spatial frequencies present in the object plane, a reflection like this artificially introduces spatial frequency components into the reconstructed object. These are then visible as the observed modulations. As the reflection is present in every diffraction pattern the modulation is stretching over the entire image. A removal of this reflection prior to reconstruction is not possible without loss of information due to its position too close to the diffraction pattern. The SZP structure itself is clearly visible in the phase map, extending outwards for about 1.5 turns along the spiral before merging with adjacent features due to lacking information in the ptychography scan. Outside this well reconstructed area, extends a region where the circular aspect of the structure is still captured but the amount of available information is so low that the spiral arms start to merge. In contrast to the silicon nanostructures the target phase contrast of π of the sample is reproduced well. In the amplitude the picture is less clear. As a first observation

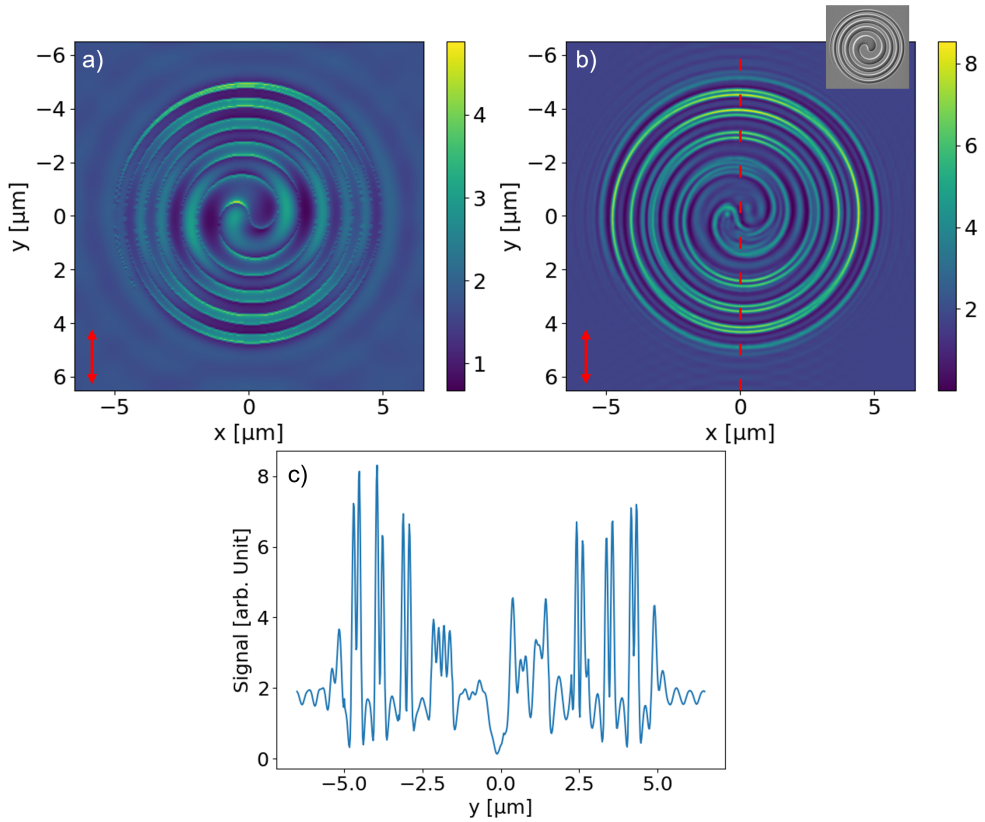

Figure 4.14: (a) Simulation of the electric field propagation of a plane wave at the fundamental wavelength through the ZnO SZP and (b) propagation of the fifth harmonic through the SZP with an SEM image of the SZP as an inset. The small red arrow is indicating the direction of polarization. (c) shows a profile along the dashed red line in (b).

here not only the etched areas are emitting harmonics but the non etched areas as well. The amplitude reconstruction therefore suffers from low contrast and only edges locally lower the harmonic yield. As a consequence a double spiral pattern arises in the reconstruction, with one spiral for each etched and non etched area. Furthermore, the amplitude shows a much stronger signal along the horizontal direction than for the vertical extend. This can be a sign of propagation effects of the laser inside the sample.

To get a more precise view on this aspect the propagation inside the structure is simulated using FDTD simulations (*Lumerical*). The results for the fundamental and the fifth harmonic are shown in Figure 4.14. At the fundamental wavelength strong traces of the electric field confinement are present around the center in vertical direction on the unpatterned area. Moving further outside a strong confinement in the horizontal direction is visible for the etched areas, increasing with lower line widths. However, as this part is the etched area the confinement does not take place inside the material and therefore does not generate harmonics. The field enhancement inside the material reaches values of about 2.5 times the incident field. This confinement inside the material in the vertical direction is similar to the behaviour

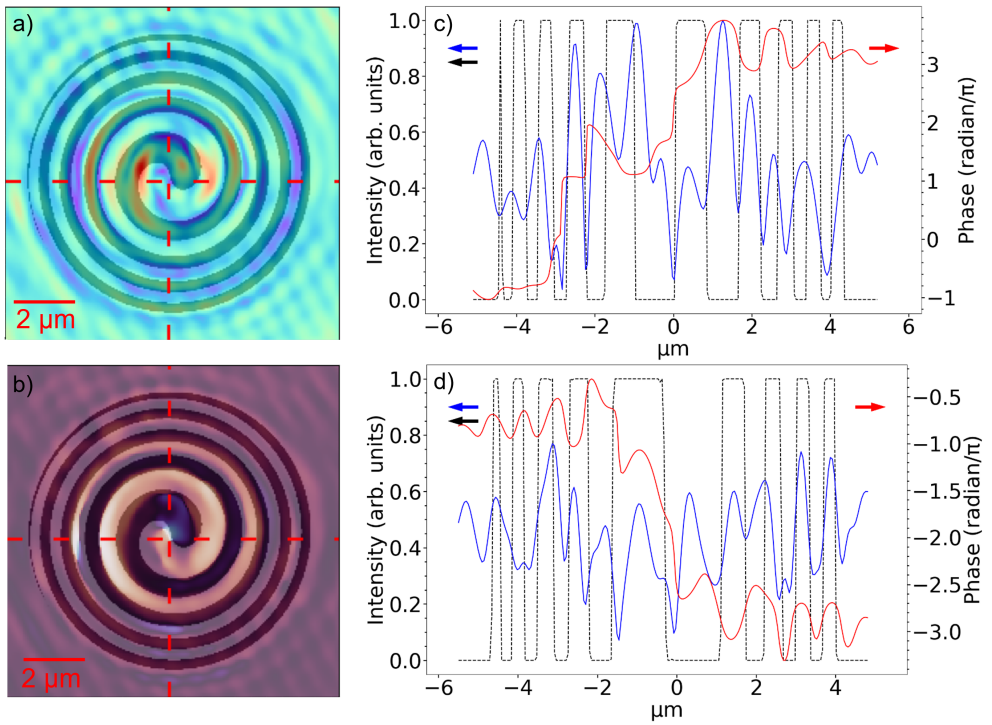

Figure 4.15: Overlays of the mask and the reconstructed structure for amplitude (a) and phase (b). Shaded area are marking the area the sample was etched in. The dashed red lines are marking the position of a horizontal (c) and vertical (d) cut through the structure. The dashed black line is representing the mask, while amplitude and phase are shown in blue and red respectively.

visible in the reconstructed amplitude, with a stronger signal in the horizontal direction. However, the resolution in the amplitude picture is not high enough to discern the any waveguiding of H5.
For H5 the propagation shows waveguiding within the etched areas of the structure, leading to the development of propagation modes visible at large line widths in the center of the structure. This creates the picture of an outline around the etched areas of the structure. This is clearly visible in a profile through the structure (Figure 4.14 (c)).

To assess the differences of the reconstruction compared to the mask in more detail, Figure 4.15 shows the overlap of the reconstructions and the mask used to produce the structures. To achieve a proper comparison the initial mask is scaled to fit with the reconstruction as well as possible. Similar to the Ptycho4 samples this reveals an overall distortion of the reconstructed structure. While the inner parts of the mask are slightly too large to fit with the reconstruction, the outer spiral arms have a much narrower spacing than the mask. In the amplitude picture the overlap is even worse due to the low contrast between etched and non-etched areas. Nevertheless, it emphasises the double spiral structure in the reconstruction. The resolution of the reconstructions is calculated with an identical approach used for the Ptycho4 samples, relying on a profile through the reconstruction (see Figure

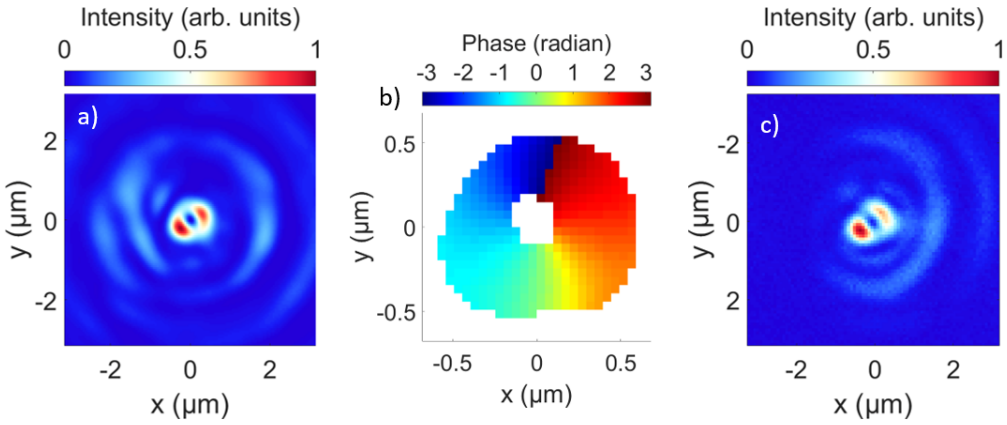

Figure 4.16: (a) Gaussian beam propagated through the reconstruction in the focal plane of the OAM. (b) Phase of the central lobe of the OAM. Adapted from [163]. (c) Previous experimental measurements of the intensity distribution of the OAM[25].

4.15 (c) and (d)). A resolution of 700 nm for the central area of the reconstruction is calculated this way, which is in line with the previous results. Notably, the profiles show no signs of the waveguiding of H5 inside the structure. This is likely due to a lack of resolution compared to the size of even the largest edged areas on this sample.

Since SZPs are used to generate OAM beams an obvious application of this type of ptychography would be a quality assessment of the etched structures. Following the approach of *Vila Comamala et al* [166], a gaussian beam is propagated through the reconstructed complex pattern to retrieve the generated OAM. This allows a comparison with the experimental measurements of the OAM mode by *Gauthier et al*[25] that are generated using the same sample. The Gaussian mode simulating a theoretical harmonic wavefront propagating through the sample is set to have a width of 4 µm, covering basically the whole SZP structure, and a flat phase. Figure 4.16 shows the intensity and phase of the OAM at the focal plane of the SZP 6 µm behind the sample. The intensity distribution of the OAM deviates from a perfect ring shaped OAM mode by splitting into two half lobes. This is the result of the combination of a binary SZP and illumination of only the inner most parts by the gaussian mode. Since the size of the illuminated area has to be limited to the well reconstructed inner part of the reconstruction, a simple increase of the gaussian mode is not possible. To achieve a better reconstruction a measurement with a larger scanning area is needed. Nevertheless, the retrieved intensity distribution matches the experimentally recorded one, that shows a similar half lobe structure. In the experiment the incomplete illumination of the SZP arises purely due to the size of the used focal spot of about 3 µm FWHM, covering only a fraction of the 10x10 µm sized SZP. The good match shows the capabilities of the technique for in-situ characterization of nanostructures in the framework of HHG experiments.

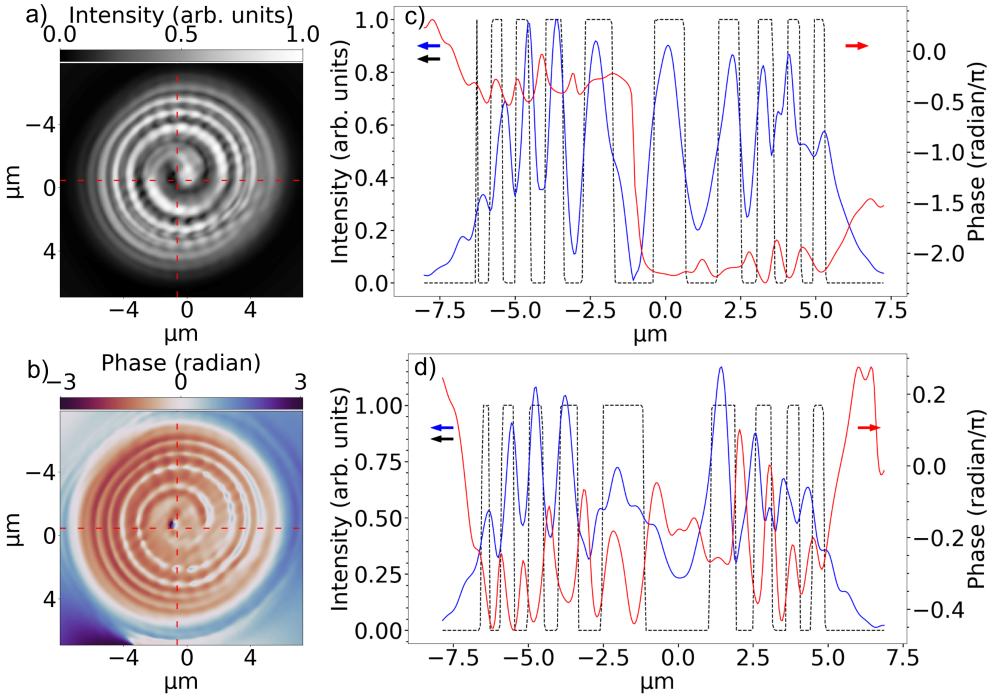

Figure 4.17: Amplitude (a) and phase (b) of the reconstructed SZP. Vertical (c) and horizontal (d) cut through the silicon SZP reconstruction. The cut is taken along the dashed red lines in (a) and (b). The phase is shown in red, the amplitude in blue and an overlay of the original mask as a dashed black line.

4.3.5 Reconstruction of Silicon SZP

As a last test for the technique and to achieve a reconstruction with a sufficient number of measurement points to cover the whole SZP, the same SZP structure as for ZnO is etched into silicon. Measurements were taken in the same experimental conditions as for the Ptycho4 samples, again scanning in a spiral pattern. Reconstruction of the pattern is done using 210 iterations of AP and 10 iterations of DM, resulting in the reconstructions shown in Figure 4.17. The SZP is clearly visible in amplitude and phase, with the spiral extending outwards 2-3 turns before breaking. As for the Ptycho4 samples the phase image shows less contrast than the amplitude. In contrast to the ZnO SZP here only one spiral arm is visible along the etched part of the sample and the amplitude shows good contrast between the etched and non etched areas. The phase image shows the SZP well defined and with even less disturbances. Calculating the phase contrast similar to the Ptycho4 samples results in 0.6π, which is slightly less than for the Ptycho4 samples.

4.4 Conclusion

In this chapter an approach for the combination of ptychography and HHG from solids was presented. It uses the harmonics generated in the sample itself as an intrinsic source for the lensless imaging, achieving an extremely compact setup. This approach allows the characterization of nanostructured samples, as they are more and more used in the context of HHG in solids, within the experimental setup itself. For the measurements here the fifth harmonic of our laser was used. Using the open PyNX library to reconstruct the images, a resolution of about 700 nm was achieved. This is about two times the theoretical limit for the resolution in our setup. The capabilities of the technique are demonstrated on a ZnO spiral zone plate. Here, the emerging OAM beam structure could be retrieved based on the reconstructed amplitude and phase of the structure, showing that the spatial distribution of optical properties is reconstructed well.
During the measurements it got apparent that the sensitivity of HHG to material properties allows this approach to image the distribution of these. This was studied using the gallium induced changes in silicon, which give rise to a stronger H5 signal compared to the pure bulk silicon. As a consequence the silicon nanostructure changes its behaviour from a pure phase mask into an amplitude mask. This change can be seen clearly on the ptychography reconstructions of the structure.

After the demonstration of the concept using a harmonic situated in the visible range, the next step is to push towards higher harmonics. The main reason for this is the direct coupling of the wavelength to the resolution in ptychography. Currently, cutoff energies around 25 eV, corresponding to 50 nm, have been achieved here and by a variety of groups, making resolutions below 100 nm feasible. At the same time higher harmonic orders are more susceptible to distortions of the material, which can increase the sensitivity of ptychography measurements to those distortions even further. One technical challenge when going for near cutoff harmonics is the separation of a single harmonic. CDI and ptychography experiments commonly select the wavelength prior to the sample. However, in our approach the harmonics are generated directly in the sample and a monochromator would therefore need to include an imaging to maintain the information in the beam. While this is not impossible it would result in an extremely complicated setup. Broadband and multi-wavelength CDI and ptychography algorithms presented recently [167, 168, 169] can nevertheless overcome this problem and open up the opportunity to even achieve attosecond temporal resolution, suitable to follow terahertz electron dynamics in the semiconductor nanostructure.

Chapter 5

Routes towards attosecond pulse using anisotropy polarization gating

In HHG the driving laser is creating an attosecond burst of radiation every half optical cycle, meaning for each peak of the field. Due to the distance of one half cycle between these bursts the interference is then taking the shape of odd harmonics in the spectral domain, which are known as high harmonics. However, for many experiments, e.g. *attosecond transient absorption spectroscopy* the isolation of one of these pulses is necessary or beneficial [45, 170, 171]. Since the harmonic peaks only arise due to the interference of multiple pulses, for an isolated attosecond pulse the harmonic peaks vanish, leaving a steady spectrum. To generate isolated attosecond pulses the emission of the HHG process has to be limited to only one half cycle of the driving field. Most techniques used to achieve this can be understood as a gating of the driving laser. The goal of the gate is to limit the field cycles that are available for efficient HHG.
The most intuitive way of restricting the generation to a single half cycle is amplitude gating. It uses single cycle driving pulses, to limit the emission of the highest harmonics, which are generated at the highest peak fields of the driving pulse, to one half cycle. By spectrally selecting only the near cutoff harmonics one attosecond pulse is isolated [172, 173]. However, while the generation and handling of single cycle laser pulses becomes more and more common, it is still an extremely challenging task often requiring extensive post compression of the laser pulses and accurate CEP stabilization. Therefore, other techniques have been developed within the HHG community. One example of this is polarization gating [174, 175]. It uses the strong polarization dependency of HHG in gases, with maximal efficiency at linear polarization and minimal efficiency at circular polarization, to create a sharp time gate. This is achieved by creating a pulse with an optical cycle dependent polarization structure that changes from circular polarization at the pulse front, to linear polarization at the center and back to circular at the trailing edge. The polarization structure acts as an additional 'gate' for the HHG. This gate effectively limits efficient HHG to the central portion of the pulse, optimally achieving efficient generation only in a single half cycle. The concept allows the generation of isolated attosecond pulses down to 53 as using two cycle NIR pulses as an input driver [176].
In the following chapter I describe our try to adapt this concept to HHG in solids. As described in section 2.2.4.2 the dependency of harmonics on the polarization

in solids is much more complex than in gases. Two important aspects of this are that not for all materials the efficiency of harmonic generation is going to zero for circular light [56] and that solids show a pronounced and asymmetric response to elliptical driving fields [75]. Both of these aspect complicate the time gate imposed by the polarization gating scheme used for gases from reaching the necessary half cycle width. This makes polarization gating more challenging in solids. The scheme used in gases can work for some materials, however the rich response to polarization of HHG in solids opens up paths to further polarization gating geometries. One example of this is the strong anisotropic response with regard to the angle between the linear polarization and the crystal axis, found in most well studied materials (e.g. MgO, ZnO). This opens the possibility for a gating based on different directions of linear polarization, an approach that is examinated in this chapter.

5.1 Concept of anisotropy gating

The concept of the gating scheme is based on the creation of a pulse with a 'rotating linear' polarization state. An example can be seen in Figure 5.1, with every half optical cycle of the pulse being quasi linear in a slowly varying direction. The gating pulse starts as a horizontally polarized field, to then slowly rotate the polarization to vertical at the tail of the pulse. However, each individual cycle maintains a locally near linear field. The temporal gate is then imposed by the anisotropic response of the material. Choosing an appropriate crystal with a four fold symmetry, the material can be oriented in such a way that only one of the quasi linear field cycles is aligned with the most efficient crystal axis for HHG. Other cycles, which do not align with this axis, have a reduced yield with a minimum for the horizontal and vertical polarized leading and trailing edges of the pulse. This scheme has two big cornerstones: the synthesis of pulses with an internally rotating polarization and the strength of the anisotropy of the material, meaning the speed with which the efficiency decreases when rotating away from the most efficient axis.

5.1.1 The Gating pulse

The gating pulse generation is based on the combination of two replicas of the pulse with perpendicular polarization. If these two replicas are delayed with respect to each other the local polarization state depends on two factors: the phase delay and the relative difference of intensity between the pulses at that point. A $\pi/2$ delay creates circular polarization states while a phase difference of π leads to linear states. However, the delay also creates a time dependent intensity difference due to the shape of the pulse envelope. Using a Gaussian pulse envelope as an example, as illustrated in Figure 5.1, a delay shifts the second pulse so that the tails of the pulses are not overlapping, creating a linear vertical or horizontal polarization at the front and back of the pulse. In between the relative intensity of the horizontal and vertical component is rapidly changing with the evolution of the pulse envelope and create a different linear polarization state for every point in the pulse. This gives rise to a state of a rotating linear polarization, meaning the direction of the linear polarization quickly rotates from horizontal to vertical, or vice versa, over

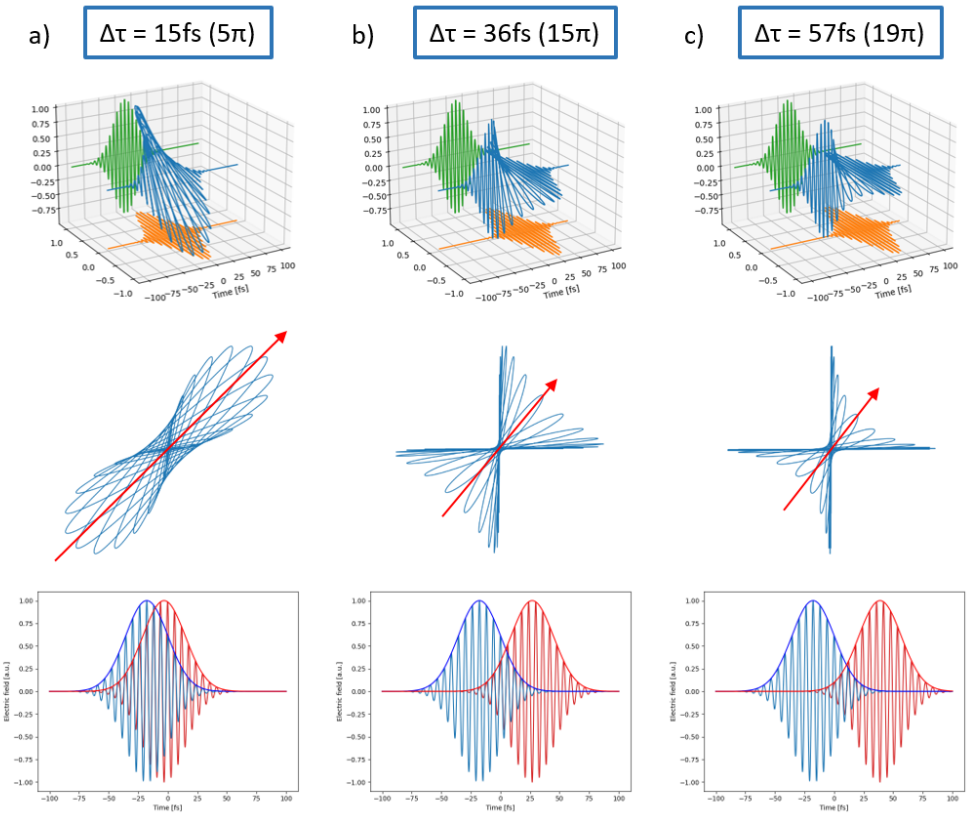

Figure 5.1: Illustration of the pulses electric field structure for decreasing overlaps of an ideal gaussian pulse. The first row shows the 3D polarization structure of the pulse, the second row a projection on the xy plane and the third row the overlap between the pulses. The red arrow in the second row gives the direction of the half cycle used for gating and signals the direction of the most efficient crystal axis.

the duration of the pulse. For simplicity this is referred to as "quasi linear" in the following.

Depending on the steepness of the pulse flank and the amount of cycles in the pulse the angular separation between the maxima of the field can be regulated. As a consequence the delay has to be chosen carefully to have sufficient field strength in the central linear cycle to generate harmonics, while still having enough angular separation between single cycles to achieve a suppression of all other cycles. For example in Figure 5.1 (a) the delay is low and as a result the maxima of the locally linear field are close together with multiple ones being strong enough for efficient HHG. As a consequence many cycles would contribute to the HHG signal, not only preventing isolated attosecond pulses but also introducing multiple overlapping polarization states. In Figure 5.1 (c) a large delay of 57 fs is introduced. As visible in the 2nd and 3rd row of the Figure, the field of the central cycle originates from the far tail of the pulses and does not reach the necessary intensities for HHG. Moving the delay in between these two positions, as shown in Figure 5.1 (b), corresponds to a near optimal case. Here the intensity of the central half cycle is still sufficient for

HHG, while the spacing between the cycles is sufficient to achieve a discrimination of the non central cycles.

The examples so far deal with the case of an optimal pulse, having a flat phase and a Gaussian envelope. In reality this is rarely the case, especially when using post compression schemes based on SPM and subsequent GDD compensation by propagation through material. These phase terms influence the polarization state of the pulse in two ways. The first is due to the more complex envelopes (e.g. asymmetric pulse shapes due to TOD) which directly influence the local relative strength of the horizontal and vertical components. The second is due to the connected shift of frequency components inside the pulse. This overlaps non equal frequencies components of the two replicas, resulting in a 'dephasing' over the length of the pulse. An example of this are pulses with a high GDD. The blue half of the spectrum is located in the leading portion of the pulse and overlaps the red components of the leading pulse. As a result the electric field peaks are not perfectly overlapping and a strong elliptic component is introduced into the final polarization structure of the pulse. An example of an imperfect pulse as it can appear in the experiments can be seen in Figure 5.2 (c). As described in section 5.1.2, the final pulse is then subject to complex HHG yield and polarization behaviours instead of a clear gating for the central, linear, portion. While it is extremely hard to completely prevent this effect in experiments, it has to be minimized. Due to the wavelength range of the used laser the GDD introduced by optical elements inside the vacuum chamber can be pre-compensated by placing appropriate material plates in the beam path before. However, higher order phase terms can not be easily compensated for and have to be avoided as much as possible.
While for the initial pulses delivered by the OPCPA the compensation of the GDD is the main concern, the effect and therefore the challenges are increasing with broader spectra as they are needed for shorter pulses. For example a TOD of up to a few thousand fs^3 as measured for the 12 fs pulses in section 5.6 leads to serious distortions in the polarization structure of the pulse.

Since the goal of the anisotropy gating is to produce an isolated attosecond pulse, an important question for the experiments is how to identify such a pulse without the ability for temporal characterization. Since the spectral structure of high harmonics with distinct peaks at odd harmonics relies on the interference of multiple attosecond pulses, this spectral structure vanishes when isolating one of the pulses. As a result the observed spectrum should show a loss of contrast for the harmonic peaks when approaching the state of an isolated pulse.
Additionally, to achieve a higher sensitivity to this effect, the anisotropy gating can be forcefully broken generating a reference spectrum that is not based on an isolated attosecond pulse. There are three ways of doing this: changing the CEP and by that changes the position of the cycles with respect to the crystal axis, similarly rotating the crystal axis and lastly changing the delay to switch between circular and linear polarization. The most reliable way is a change of CEP. It changes the internal distribution of the field peaks without affecting the orientation of the inefficient Γ-K axis of the MgO with respect to the leading and trailing linear pulse portions. A rotation of the crystal is also changing the position of the crystal

axis with respect to the central linear field peak but also changes the alignment of leading and trailing edge to the Γ-K axis.

5.1.2 High harmonic response to polarization

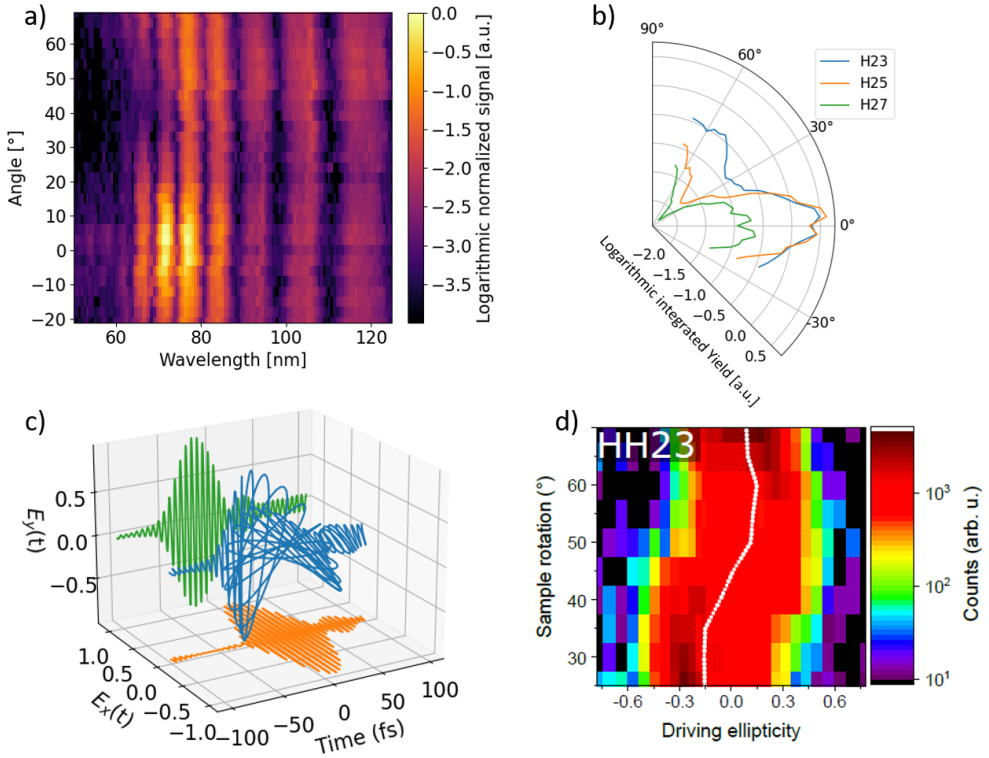

Figure 5.2: (a) Measured HHG response of a 200 µm MgO crystal to different directions of linear polarization. (b) Comparison of the signal from H23, H25 and H27. (c) Structure of a distorted pulse as it appears in the experiments. (d) Response of H23 from a 10 µm thick MgO crystal for different ellipticities of the driving pulse (taken from [75]).

The first point is the response of harmonics from solids to the polarization of the driving pulse. As described before this is strongly dependent on the band structure of the respective solid and has been described for many of the materials commonly used for HHG in solids. To match the previously described pulse structure the perpendicular polarized leading and trailing edges of the pulse should be aligned with minima of the harmonic efficiency. Meanwhile, the central fields half cycle should be aligned with the direction of maximal efficiency. This directly leads to a four fold symmetry of the harmonic efficiency. A two fold symmetry can work as well but since in that case the alignment for the leading and trailing edge is not precisely at the minima it can be expected to be less effective than a four fold symmetry. This directly leads to cubic crystals, as their structure leads to a fourfold symmetry in most cuts. However, also non cubic crystals can be used when cut in an appropriate direction that exhibits a fourfold symmetry.
Since imperfect pulses, as they frequently appear in experiments, lead to elliptical

polarization states, the materials response to these polarizations is important to estimate. Works on the response to elliptical drivers are more sparse with [75] being one of the more extensive studies in that regard. Elliptical driving fields are especially important in this context since (i) the target pulse shape for the anisotropy gating is only quasi-linear and (ii) imperfect input pulses lead to higher ellipticity of the half cycles. The first condition favours a low dependency of the harmonic yield on the ellipticity of the driving laser, while the second one favours the opposite. However, in practice the second condition is much more problematic since ideal pulses are extremely hard to achieve especially in the sub 30 fs regime and after SPM based pulse broadening.
Aside from the efficiency of the elliptically driven HHG it is worth noting that the elliptical pulses do not have a uniform direction of the major axis. This means the ellipticity dependence of the harmonic efficiency for each cycle corresponds to a different vertical position in Figure 5.2 (c). Additionally, as reported by *Klemke et al* the ellipticity of the generated harmonics is not necessarily the same as the driving ellipticity but instead shows an extremely complex and harmonic dependent behaviour [56]. Small contributions from field peaks adjacent to the central one can therefore change the polarization state of the final harmonics in a complicated way.

Since the decline of the harmonic yield as a function of the angle is more pronounced towards higher harmonic orders the material of choice should support harmonics in the EUV range. As one of the best studied materials MgO features a high bandgap and fourfold symmetry with a high damage threshold and bandgap, making it a good candidate for these experiments. Figure 5.2 (a) and (b) shows the measured dependency of the harmonic yield on the linear polarization direction in MgO. The strongest decline appears close to the edge of the first conduction band. Especially H25 shows a dramatic decrease as the first conduction band in the Γ-X direction is extending further than in Γ-K direction. However, the harmonic yield shows a decline for other harmonics as well.

5.2 Experimental realization of the pulse shaping

To create the necessary polarization state of the laser pulses a TWINS interferometer as described by *Oriana et al* [177] is used. It is based on a pair of birefringent wedges which are introducing a phase delay between the portion of the pulse propagating along the ordinary and extraordinary axis. The wedge pair is followed by a flat piece of the same birefringent material with its axis exchanged compared to the wedges, to regulate the point of zero delay.
In total two wedges and a rectangular piece of α-BBO are used in the setup, all AR coated for 1780 nm to achieve maximal transmission for the laser. The wedges have a 20 mm by 10 mm front face, while the thickness is varying due to the 5° angle between a maximum thickness of 3 mm and a minimum thickness of 1.25 mm. Meanwhile, the rectangular piece has a front face of 20 mm by 10 mm but is consistently 4.25 mm thick. The optical axis of the crystal and the wedges is located in the frontal plane, however the optical axis of the wedges is perpendicular to the optical axis of the crystal. As a result the optical axis of the wedges is aligned parallel to the 20 mm side of the front surface (horizontal) and the optical axis of the crystal

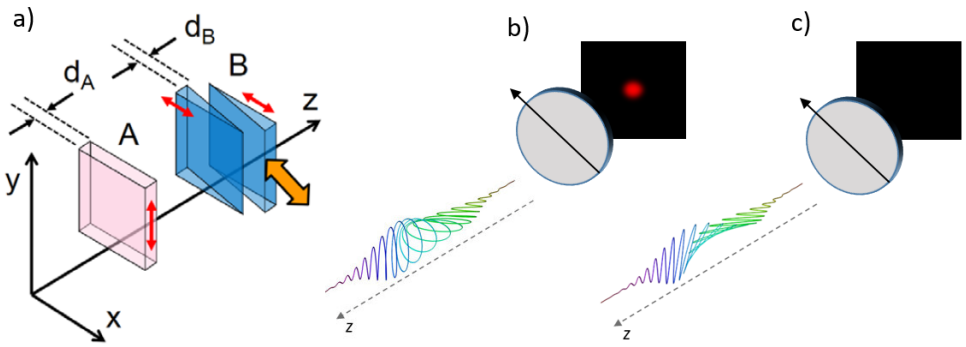

Figure 5.3: (a) setup of the TWINS interferometer as described in by *Oriana et al* (from [177]). (b) and (c) illustration of the phase delay measurement. The black arrow denotes the direction of the polariser (in grey), with a partial interference for the circular polarization state and a destructive interference for the desired gating pulse structure. For high delays a full destructive interference is not achieved anymore.

is aligned parallel to the 10 mm side (vertical). In this configuration the crystal is introducing a fixed amount of delay between the two polarization directions, that is opposed to the delay introduced by the wedges. Consequently, it shifts the point of zero delay to a position where the wedges are partially in the beam. This allows a range of delays that spans not only one direction but both negative and positive delays.

The introduced delay has to be separated into two components: the phase delay and the group delay. The group delay describes the delay between the two pulse envelopes and therefore the relative intensity of the two polarization directions. Meanwhile, the phase velocity describes the phase relation of the two electric fields. This means the phase velocity decides the final polarization state of the pulse, while the group delay decides the angular distance between adjacent quasi-linear cycles of the pulse. For the used interferometer setup both quantities can be calculated with similar equations. For the group velocity this takes the shape of

$$\tau = (d_A - d_B)\left(\frac{1}{v_{go}} - \frac{1}{v_{ge}}\right), \tag{5.1}$$

where d_A and d_B are the thickness of the crystal and the combined wedges respectively. v_{go} and v_{ge} are the group velocities of the ordinary and extraordinary direction. The phase velocity is given by

$$\phi = (d_A - d_B)\left(\frac{1}{v_{po}} - \frac{1}{v_{pe}}\right), \tag{5.2}$$

where v_{po} and v_{pe} are the ordinary and extraordinary phase velocities. In order to regulate the split of the laser onto the ordinary and extraordinary axis, a half wave plate is placed in front of the interferometer, turning the polarization direction. Since the target is a linear polarization of the center portion of the pulse, the polarization is turned to 45°, splitting the energy evenly between the two directions.

One advantage of this geometry is that the beam remains collinear throughout the whole setup. This first removes the need of beam recombination and therefore the need for either beam splitters or spatial separation and secondly achieves an extremely phase stable setup. Since the local polarization state of the generated laser pulse is highly depended on the phase difference of the two pulse replicas, a high level of phase stability is indeed needed for the experiments. The drawback of this setup is the introduction of additional material into the beam path. The introduced GDD can be compensated since materials with positive and negative dispersion are available in the wavelength range between 1.5 µm and 2 µm, however TOD and higher order phase terms cannot. While this is relatively unproblematic for the initial 40 fs pulses or the 30 fs pulses obtained in the first iteration of the pulse compression stage (see section 5.4), 10 fs, 1.5 cycle, pulses as generated from the second iteration of the compression stage see a huge impact. The additional phase can not only result in strong pre- and post-pulses but also increase the pulse duration.

One important aspect for the experiment is the measurement of the generated pulse structure. This includes the temporal shape as well as the polarization state. In the setup this is split into two characterization steps. A first one to determine the phase delay and a second one to determine the temporal structure of the pulse. Both are based on the introduction of a polariser into the beam path that projects the 2D polarization structure of the pulse onto a single axis.
For the phase delay the beam after the polariser is guided onto a camera. Then the polariser is first set to match the polarization direction of the desired gating direction, which is naturally coincident with the initial polarization direction before the TWINS stage. Changing the delay introduced by the TWINS stage is then showing a series of constructive and destructive interferences, with the constructive interference becoming weaker for higher delays. This allows to locate the zero delay position by finding the strongest maximum. After the polariser is turned by 90°. Each desired pulse state, with a quasi linear polarization, then corresponds to a destructive interference. Similar to the case of constructive interference, the destructive interference becomes less pronounced for higher delays. Nevertheless, the contrast against the case of circular polarization is high enough to set the phase delay by counting the cycles of destructive interferences.
To achieve a full characterization of the electric field of the pulse for a given delay, the projected electric field has to be characterized in time for two different projection planes. Since the TWINS stage is introducing a delay between the horizontal and vertical component, those two planes are the planes of choice for the projections as well. Together with the set delay of the interferometer the complete pulse structure can be recovered. The temporal characterization of the projections is done with a FROG.
As the FROG is not able to reconstruct the first order phase, this leaves the determination of the group delay between the pulses. However, it can be calculated based on the phase delay. Knowledge about the introduced phase delay and the group velocities in the medium allow the calculation of the factor $(d_A - d_B)$ in equation 5.2. Together with the materials group velocities this determines equation 5.1 and yields the group delay between the two replicas.

A general problem with the setup is that the characterization is only possible in front or after the vacuum chamber. Crucial for the HHG is however, the pulse shape at the back surface of the HHG medium. To reduce the impact of dispersive elements after the generation medium, the recollimation lens and vacuum chamber window are made out of CaF_2 which has a low GDD in the near IR. Comparing FROG measurements before and after the chamber for vertical polarization and without the generation medium in the beam showed little to no difference in the temporal shape of the pulse. However, the phase delay needs a slight correction corresponding to 0.03 µm wedge insertion per cycle.

5.3 Incorporation into the HHG setup

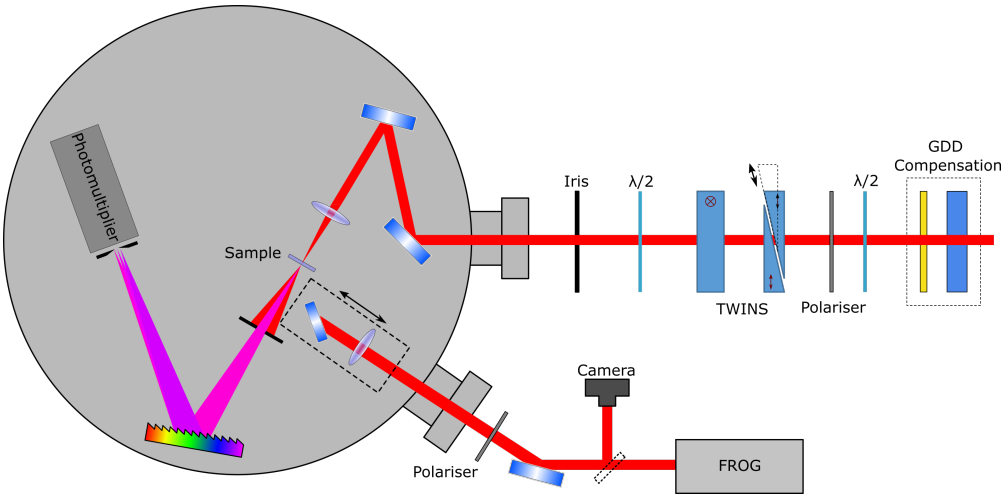

Figure 5.4: Schematic of the setup, starting with the interferometer stage outside the vacuum.

The complete experimental setup for the anisotropy gating is depicted in Figure 5.4. The laser used for the experiments is a CEP stable OPCPA system from *FastLight*. It uses an *Amplitude Tangerine* as a pump for two OPA stages, one collinear and one non-collinear, and the generation of a white light seed. Both the 1780 nm signal and the 2400 nm idler are available as a an output of the system. In addition to the passive CEP stability of the signal the system has the option of additional active CEP stabilization. The necessary CEP measurement for the active stabilization is achieved by an f-2f interferometer first located right after the laser. It uses a small portion of the beam, separated by a beam splitter, to constantly monitor the CEP of the laser. In combination with the *Dazzler* in the OPCPA this allows a precise control of the CEP. However, later in the experiments the beam for the f-2f was picked after the post compression stage described in section 5.4. The output used in these experiments is the signal with a central wavelength of 1780 nm, 40 fs FWHM and 1.5 W at 100 kHz.
The incoming laser beam first passes some material plates for dispersion compensation. After the first half wave plate, used to regulate the input polarization, the

TWINS stage is passed. The TWINS stage is followed by another half wave plate and an iris, before the beam enters the vacuum chamber. Inside the vacuum chamber the generation stage, consisting of the crystal mounted on a xyzθ - stage, is placed. After the generation crystal the beam can take two paths. The first recollimates the driving pulse using a CaF_2 lens and guides it outside the chamber. There the characterization tools for the polarization state and pulse shape are situated. The other path leads into a home build XUV spectrometer consisting of a toroidal grating and a photomultiplier as described in section 3.4.1. The CEP stability of the laser is monitored using a portion of the beam picked from the main beam right in front of the interferometer. This proximity of the CEP measurement to the TWINS stage ensures the CEP stability even after the later implemented post compression stage.
An important factor for the experiments is the polarization state of the laser. The anisotropy polarization gating technique requires a precise control of the polarization state of the incoming IR beam. For this reason initially a polariser and a half wave plate are located in front of the TWINS stage and an additional polariser after the TWINS stage. The polariser was originally used to ensures a clean incoming polarization state, however it was dropped since the polarization state of the compressed laser was sufficient. The first half wave plate is used to turn the polarization by 45° to achieve, since the crystal axis of the TWINS stage are vertical and horizontal, an even split of the pulse. Finally, the second half wave plate is used to turn the polarization state of the central gated pulse part back to vertical for maximal efficiency of the grating. This maximizing of the efficiency is not crucial for the experiments making the second half wave plate optional, however the polarization direction of the central pulse portion then has to be matched by adjusting the rotation of the HHG crystal. Consequently, it has been dropped during the presented measurements to simplify the setup and minimize variables.
It is important to note in this context that, while the grating is discriminating the horizontal polarization by roughly a factor two, the XUV spectrometer generally averages over the polarization. This means harmonics that are generated with elliptical polarization or by quasi linear cycles adjacent to the central cycle can not be separated from the gated signal in these measurements.

First tests of the gating scheme have been conducted in our group with the full setup including both half wave plates and the polarizer by the previous PhD student *Shatha Kaassamani* [58]. For the measurements the TWINS stage was set to a phase delay of 7.5 cycles with the central linear part of the gated pulse being oriented along the vertical axis, matching the efficient direction of the grating. Spectra were acquired at $10\,TW/cm^2$ for H21 to H27, corresponding to energies at the top of the first conduction band. Figure 5.5 shows the result of that measurement in contrast to a measurement at zero delay. As it can be expected the signal is magnitudes lower than for a delay of zero with only a few counts per second. However, it shows the emergence of signal between H25 and H23 as well as between H23 and H21. The positions are corresponding to even harmonics indicating a break of symmetry. The spectrum at zero delay does not show these even harmonics meaning the symmetry break can be attributed to the structure of the gated pulse. This kind of response is not the continuous spectrum expected from isolated attosecond pulses but a first

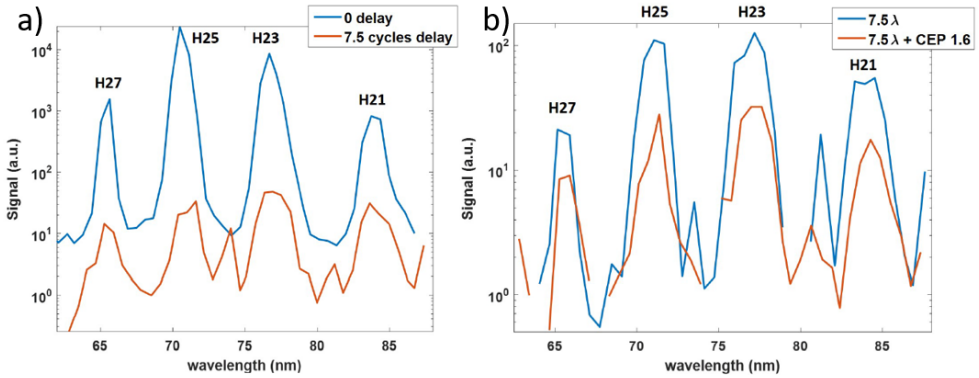

Figure 5.5: (a) Comparison of spectra with zero delay and 7.5 optical cycles delay. (b) Spectra at the 7.5 cycle delay position at two different CEP values. Spectra are taken from [58]

indication that the scheme is having a strong influence on the HHG process.

5.4 Pulse compression: First iteration

The CEP dependency of the signal obtained in the initial tests indicates some gating might take place in the interaction, however it is weak and remains rather unclear. One way to obtain a better gate is to post compress the pulses from the laser prior to the TWINS stage. As a consequence the gated pulse contains less cycles and a steeper envelope. This leads to a larger angular separation of the peak field positions, allowing to i) reduce the delay between the pulse replicas, therefore increasing the peak field of the gated pulse and ii) a better extinction of the harmonic yield from the cycles not oriented along the efficient axis.

There are a few ways to achieve the spectral broadening necessary for shorter pulses, with all of them being based on SPM. Generally the beam is propagated through a medium and is broadened depending on the amount of SPM. This in turn depends on the nonlinear refractive index of the medium, the intensity of the pulse and the propagation length. Two main schemes are currently used to achieve this nonlinear propagation experimentally: fibers, often hollowcore fibers and multipass cells. Due to the good quality of the resulting beam profile and scalability for different average powers hollowcore fibers are the most common option [32, 178, 179]. They use the confinement of the beam in the fiber to reach sufficient intensities and fill the fiber with a noble gas to induce the nonlinear propagation, with the option to control the nonlinear refractive index by changing the pressure. However, they have drawbacks such as the need for high beam pointing stability. Multipass cells on the other hand achieve the necessary propagation length by using Herriott cells. The nonlinear medium is either a gas with which the cell is filled or a solid located in the beam path [33, 180, 181, 182, 183].
One common disadvantage for all of these approaches is the complexity of the alignment and components of the necessary setup. The approach chosen here therefore follows a rather simple compression scheme with a single pass through a solid ma-

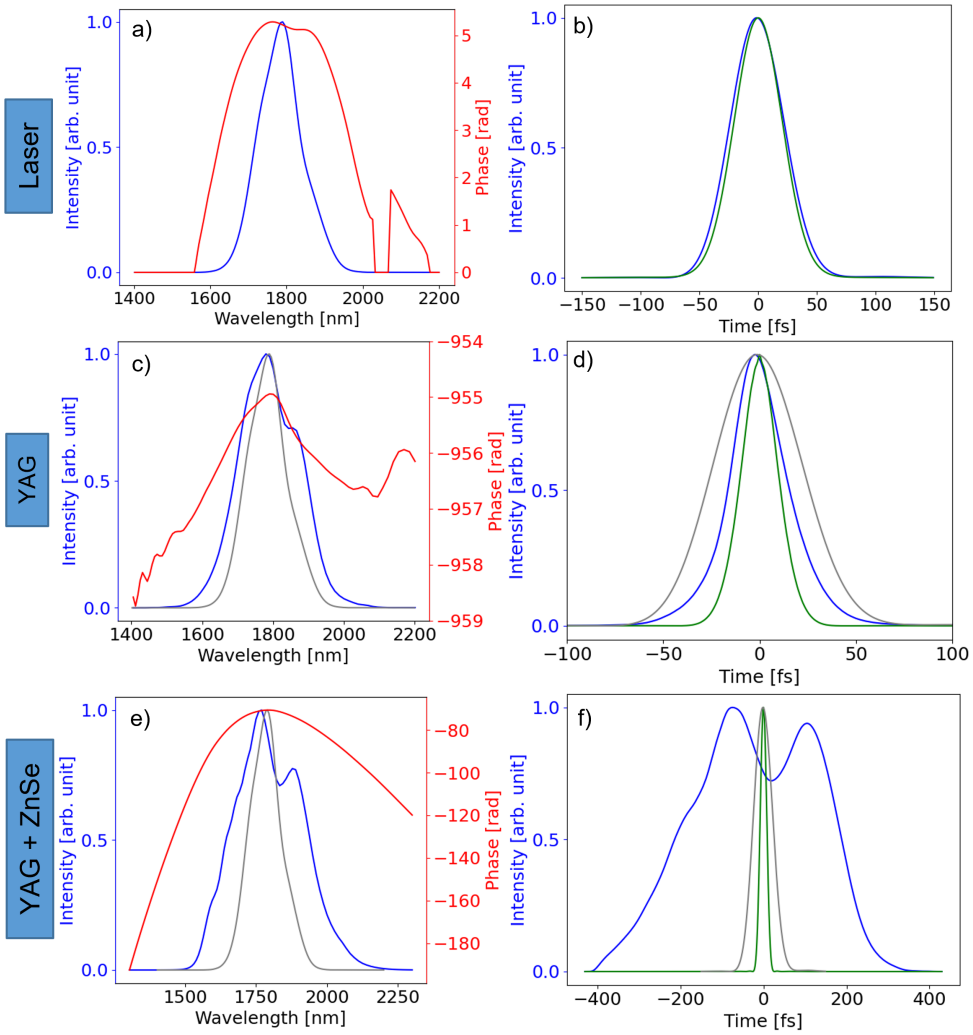

Figure 5.6: Simulated broadening in the YAG crystal compared to the broadening in using YAG and ZnSe. (a) and (b) show the initial laser spectrum and temporal shape. (c) and (d) the spectrum and temporal shape after propagation through a 4 mm YAG crystal and (e) and (f) through the YAG and an additional 5 mm ZnSe crystal placed 10 cm after the YAG. Grey curves in (c) - (f) represent the initial laser properties. The green curve in (d) and (f) illustrates the fourier transform limit of the broadened spectrum, while the blue curve shows the pulse shape after the broadening.

terial as described e.g. in [184, 185, 186]. Compared to the other techniques this is not easily scalable to higher pulse energies and has the disadvantage of possible spatio-temporal couplings due to high electron densities and filamentation. This makes the management of reached peak intensities an important parameter, which has to be regulated by carefully choosing the position of the materials placed in the beam. For our case the scheme has the main advantage that it uses materials that were readily available in the lab and has a flexible geometry. The broadening can directly be controlled by the placement of the nonlinear materials in the beam path making alignment easy compared to the other methods of post compression.

The experimental setup was guided by the materials available at that point in the lab. This led to the use of a 4 mm YAG crystal and a 5 mm ZnSe crystal. The additional ZnSe crystal was added behind the YAG crystal to induce further SPM, only after the YAG alone did not show the desired broadening of the spectra. Since the overall performance of the compression stage was lacking behind the expectations, simulations were performed to better judge the performance. For the sake of the structure in the following, these simulations are described first. However, the simulated cases are chosen to be exactly the experimental cases.
Simulations are based on a 1+1D split-step propagation as described in [187]. It employs a matrix formalism approach for the spatial propagation of a Gaussian beam through the material plates, describing the Kerr lens in an intensity dependent transfer matrix. The spectral response includes SPM, self steepening and Raman contributions to the spectral broadening. The results are presented in Figure 5.6 for two cases. The first describes the initial approach with a single 4 mm YAG crystal located at the focus of the beam, the second one includes an additional 5 mm ZnSe crystal in the beam path. Starting with the single YAG crystal the initial spectrum gets broadened by a factor of 2 to a spectral width of 219 nm, with a fourier transform limit of 22 fs. The crystal not only introduces a phase due to the nonlinear interaction but also due to the linear dispersion of the YAG crystal, which has to be compensated. However, compensating only the GDD the achievable pulse duration is 25 fs, 3 fs above the fourier transform limit. In the wavelength range of the OPCPA (between 1500 nm and 2000 nm) a compensation of the GDD can be realized with just material insertion, as materials with positive as well as negative dispersion are readily available. Here, AR coated ZnSe and Al_2O_3 (sapphire) plates are used to control the dispersion of the input as well as broadened pulse. Since the spectral bandwidth of the pulse after the YAG crystal does not allow for a compression down to about 20 fs, a 5 mm ZnSe crystal is set about 10 cm after the YAG crystal to induce further broadening of the spectrum.
The additional ZnSe crystal increases the spectral bandwidth to 311 nm allowing for pulse durations down to 19 fs. However, the ZnSe also introduces a large GDD into the pulse that has to be compensated after the compression stage. The amount of material in the beam path required to compensate this GDD is, while indeed compensating the GDD, introducing a large TOD into the pulse, which can lead to the formation of post-/pre-pulses. This indeed occurs in the experiments, where a strong post pulse appears (see Figure 5.9).

For the experimental tests the beam is focused by a 750 mm AR coated CaF_2

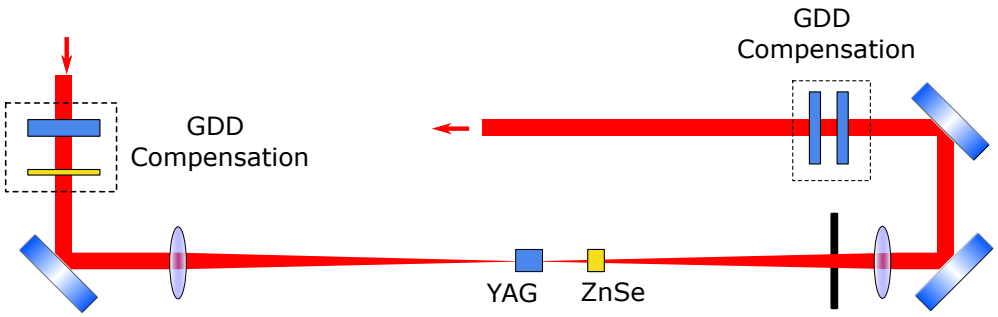

Figure 5.7: Scheme of the compression stage setup.

lens. A 4 cm YAG crystal is placed on a translation stage allowing for a fine control of the position and positioned about 2 cm behind the focus (see Figure 5.7). The additional later introduced 5 mm ZnSe crystal is set about 10 cm behind the focus making the positioning less critical and consequently a fine control of the translation not necessary. The input power into the stage was initially at 1.1 W, corresponding to 11 µJ pulse energy, however the laser was slowly degrading over the course of the experimental campaign and by the end only 950 mW were available just before the post compression stage.
The YAG crystal is positioned as close as possible to the focus while still avoiding the filamentation regime. After the ZnSe crystal the beam passes an iris to select the core part of the beam and is recollimated by another 750 mm AR coated CaF_2 lens. As a last step the pulse has to be compressed by compensating the GDD. For this purpose multiple materials are arranged in the beam path. For case of compression in ZnSe the majority of the compensation is done with a 3 cm long piece of fused silica, while this is removed for the case of just the 4 cm YAG in the compression stage. Afterwards a beam splitter is used to pick a small portion of the beam and guide it into an f-2f interferometer. The final GDD is afterwards regulated with a set of different kinds of plates, including 3 mm and 5 mm sapphire plates, 3 mm BK7, 5 mm fused silica and 3 mm ZnSe. Only some of the plates are inserted in the beam path depending on the desired GDD.
Figure 5.8 presents recorded spectra for the case of only the YAG crystal in the beam path, the YAG and ZnSe crystals in the beam path and a reference without any material. Here it is clearly visible that the YAG is only inducing a slight broadening of the spectrum with small wings forming on both sides. The spectral broadening matches the shape predicted by the simulations and has a spectral width of 196 nm close to the predicted 211 nm. Adding in the ZnSe is then broadening the spectrum further. The characteristic SPM shape of two pronounced side maxima is emerging and the spectral width reaches 300 nm, again close to the calculated value.
The temporal characterization of the broadened pulses is done using a FROG after compensating the GDD and is shown in Figure 5.9. For the case of just the YAG crystal the GDD of the initial and compressed pulse have been managed by a 3 mm ZnSe and a 5 mm sapphire plate in front of the compression stage and a 5 mm BK7 after the stage. This inserts a positive GDD of 522 fs^2 in front of the compression

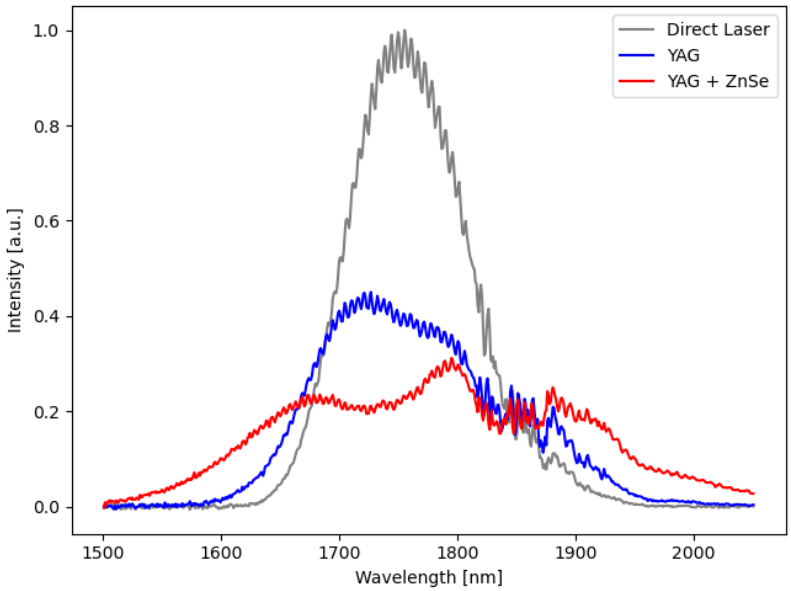

Figure 5.8: Spectra after the compression stage for different configurations.

stage and a negative GDD of -275 fs^2 after the stage, with the YAG crystal itself introducing another -100 fs^2. The GDD in front of the stage is compensating a slight chirp in the incoming laser beam, while the GDD of the YAG and the BK7 are compensating the phase introduced by the nonlinear propagation. Notably, the ZNSe and sapphire in front of the YAG are not compensating the GDD perfectly. This can in fact have strong effects on the resulting SPM [188, 189]. However, the configuration resulted in the best overall performance of the compression stage with only the YAG crystal. It achieves a pulse duration of 34 fs, being about 10 fs longer than the simulated pulses. Multiple other configurations have been tried, aiming at a better compensation of the input pulse and after the stage with neither configuration delivering the predicted 25 fs pulses. This might already be due to a high TOD as the temporal structure shows a slight side peak. Shifting the crystal position relatively to the focus or sharper focussing to achieve higher peak intensities did not lead to shorter pulses or stronger broadening either.
Introducing the additionally ZnSe crystal immediately allows much broader spectra close to the simulated case. However, a total of 40 mm BK7 and 5 mm sapphire are introduced into the beam to compensate the large GDD, accounting for a total of 2575 fs^2 of introduced GDD. The saphhire plate was AR coated, while the 30 mm and 10 mm BK7 pieces are uncoated. This amount of material is introducing a significant amount of TOD into the pulse which shows as a clear side pulse that reaches up to 20% of the main pulses peak intensities. Due to its lower intensity the harmonic generation from the side pulse is low compared to the main pulse. Nevertheless, for the case of a pre-pulse (negative TOD) it can pre ionize the material leading to inefficient HHG [73]. Since all the used materials introduce a positive TOD in our wavelength range, the TOD of the pulse has to be positive. Consequently, the side pulse has to be a post-pulse. While not optimal it is still used for

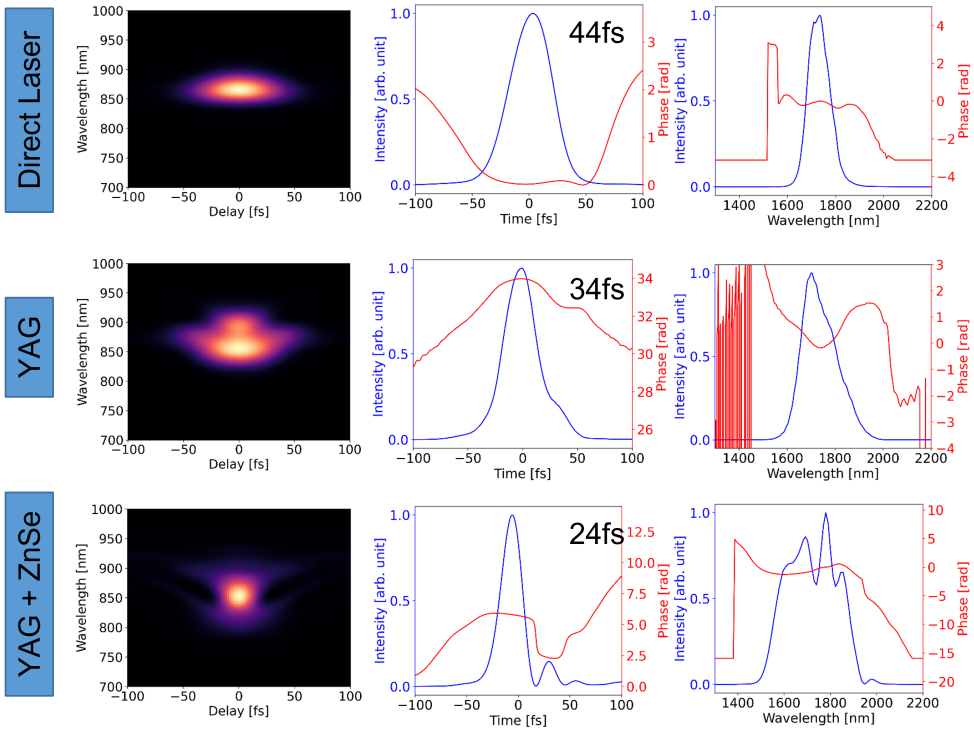

Figure 5.9: FROG traces of the compressed pulse for the direct laser, the YAG crystal and the YAG and ZnSe crystal. The first column shows the reconstructed trace, the second column the temporal pulse shape and the last column the reconstructed spectrum.

the anisotropy experiments in the following.
An important factor in post compression is the efficiency. Before the compression stage the laser reaches a maximal power of 950 mW of which 250 mW are lost in the YAG and ZnSe used for compression, leaving 700 mW after the SPM stage. The beam then passes multiple materials to compensate the GDD, reducing the average power down to around 450 mW. The SPM stage therefore has an efficiency of 73% which is further reduced to 47% after the GDD compensation. These are huge losses in average power, however the damage threshold of MgO for the used experimental configuration is reach around 400 mW. This means the power is sufficient for the purpose of HHG generation.

Before going on with the anisotropy gating the shorter 25 fs pulses are directly used to generate harmonics. An example spectrum can be seen in Figure 5.10. For the experiment a laser power of 320 mW is focused into a 100 µm MgO crystal using a 10 cm focusing lens. The power of the laser is regulated using an iris in front of the vacuum chamber. To avoid strong nonlinear effects in the sample as well as damaging the MgO crystal is placed slightly behind the focus. This allows a higher average power and therefore a higher EUV photon flux, increasing the signal to noise ratio of the spectrum. The spectrum shows the harmonics located at the upper edge of the first conduction band and the decay into HH from the second conduction band. All harmonic peaks are well pronounced and the harmonic spectrum cuts after H33 after which the harmonic signal vanishes in the noise background. Overall,

the spectrum looks similar to the spectra observed with the uncompressed pulses.

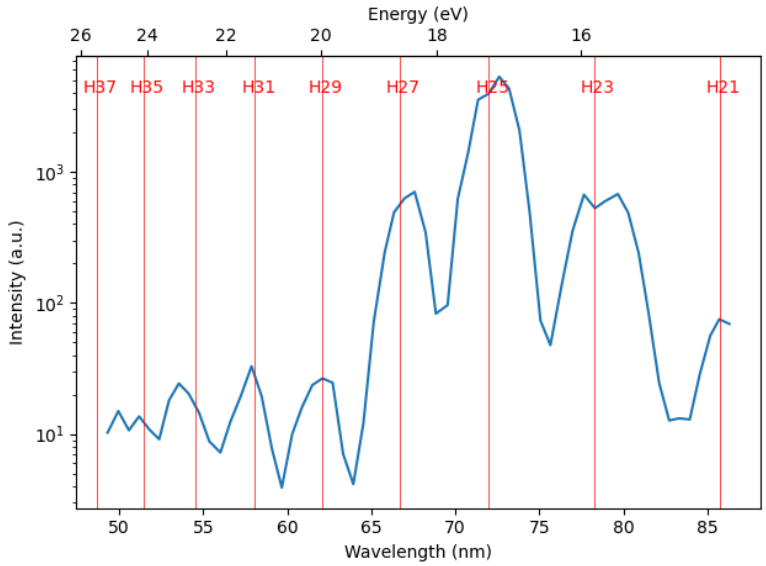

Figure 5.10: HHG spectra in MgO from the post compressed 25 fs pulses.

5.5 Anisotropy gating with 30 fs pulses

For the test of the anisotropy gating the 25 fs pulses could not be used for several reasons. First the laser degraded over the course of the experiments reducing the input power of the compression stage. Second the side pulse had to be reduced, which was done by relaxing the compression stage. However, the results show the limitations of the setup and the need of higher quality pulse profiles.

As a first step after bringing the anisotropy stage into the beam path, the polarization structure of the tailored pulse is characterized. As mentioned before this is achieved by temporally characterizing the projection on the vertical and horizontal axis using a FROG. The structure of the vertical component is shown in Figure 5.11 (a) and (b). With 33 fs the pulse width is longer than the shortest achieved states but shows little post- and pre-pulse. The structure of the gated pulse shows a strong ellipticity in the cycles adjacent to the central cycle. Meanwhile, as visible in Figure 5.11 (d), the central linear cycle is slightly off the 45° axis which has to be compensated in the experiments. Overall, this structure of the gated pulse is not optimal but a further compensation of the TOD was not possible with the available materials. On the positive side the high ellipticity of the adjacent cycles can reduce the harmonic signal as well, leading to a similar effect as an angular displacement of the quasi linear position.

One notable aspect of the setup is that the characterization of the pulse is only possible before and after the vacuum chamber. Because the gate direction is 45°, the optics inside the chamber can introduce a change of the gating pulse, due to different reflectivities of mirrors for s- and p-polarization. This introduces a dif-

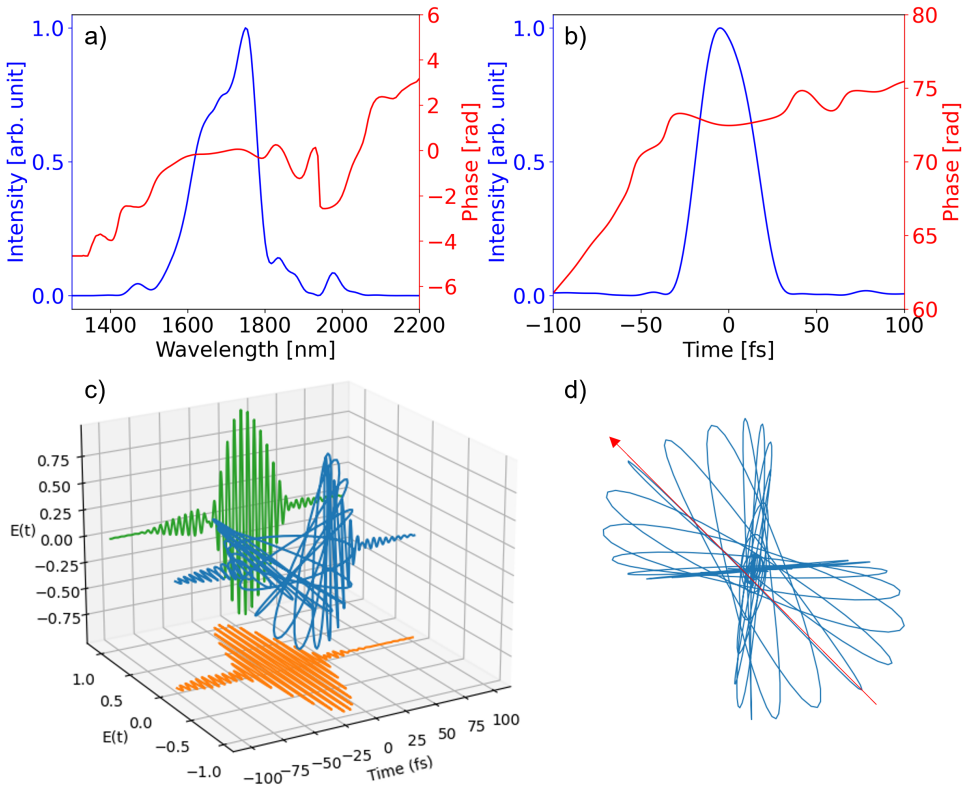

Figure 5.11: Spectral (a) and temporal (b) shape of the vertical projection of the gating pulse. The polarization structure for a delay of 5λ is shown in (c). (d) shows a projection of the polarization structure onto the xy-plane, with the arrow indicating the direction of the gated half cycle.

ference between the horizontal and vertical field amplitude and therefore changes the angular position of the quasi linear cycles. To judge the effect of this on the gating pulse the delay needed to reach 5λ before and after the chamber is measured, leading to wedge insertion values of 0.182 mm and 0.186 mm per 2π delay respectively. The difference of 0.004 mm between the values is small, accounting for only 2% of a cycle and might very well be due to the visual judgement of the destructive interference during the measurements.

Since the signal showed a response to the CEP in the first experiments, it is the first feature to take a look at. For the measurements the TWINS stage is set at a delay of 5λ, corresponding to a position of 2.21 µm of the wedge, with the beam being limited to 270mW by the 4 mm iris opening in front of the chamber. Since the second half wave plate is not present the more efficient Γ-X direction of the MgO crystal is set to 45°, matching the gated portion of the pulse. A spectrum is acquired for H21-H27 whose energies correspond to the top of the first conduction band and are at the same time the strongest observed harmonics. The CEP value is changed by 1.2 radian between the measurements shifting the position of the peak field. Averaging over two measurements for each CEP results in the spectra

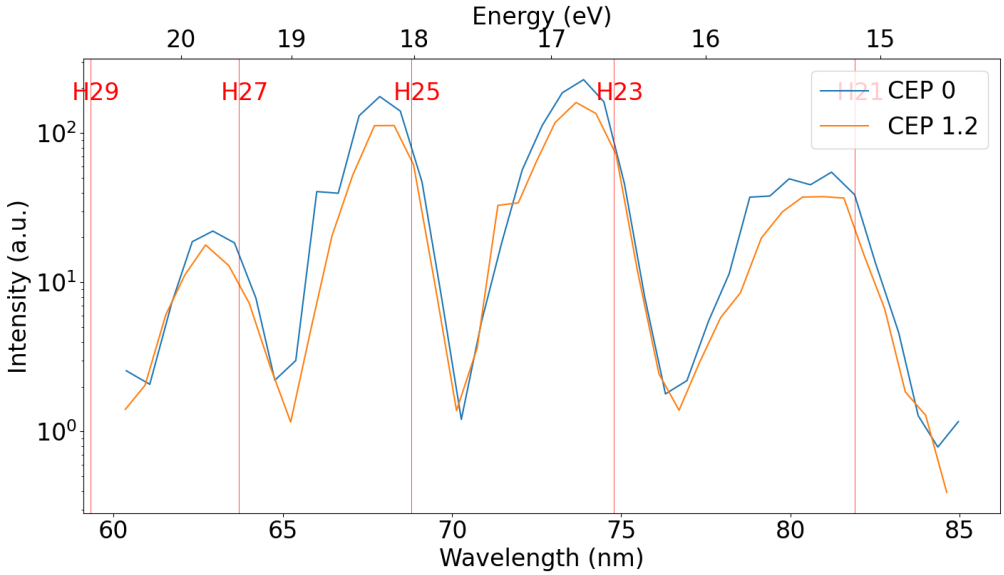

Figure 5.12: High harmonic spectra for two different CEP values at a phase delay of 5λ.

presented in Figure 5.12. There is no significant change of the spectrum with a change in CEP. A rotation of the crystal angle, which similar to the CEP changes the relative position between the crystals Γ-X axis and the peak of the gated pulse, did not show any change in the spectrum either.

Consequently, the next step was targeted at determining whether the gated field has any effect on the HHG or not. To achieve this the signal from a gated pulse is contrasted with a delay at which the horizontal and vertical pulse are completely separated. Since the detection is not able to characterize the polarization of the harmonics, there is always a background of harmonics generated by the linearly horizontal and vertical polarized tailing/leading edge of the pulse. Separating the two pulses is eliminating the "gated" portion of the pulses and shows the harmonics directly generated by them. One concern with this approach was the difference in introduced GDD between the -5λ and -15λ case that could lead to an overall decline of the spectrum. However, this difference turns out to be negligible with a difference of only -12 fs^2 based on the maximum difference in introduced thickness of 0.16 mm [190]. The resulting spectra are shown in Figure 5.13. While H21 is similar for all delays first differences are apparent at H23 and a large difference is visible for H25. So there is indeed a huge difference between the gated pulse and the single horizontal and vertical pulses. The large difference in H25 can be explained with the band structure differences between the Γ-X and Γ-K direction in MgO. In the Γ-X direction the top of the first conduction band is slightly higher than for the Γ-K direction, making the 25th harmonic part of the emission from the first conduction band. In the Γ-K direction the harmonic is in the energy range of the second conduction band leading to the observed sharp reduction in efficiency. As a consequence the main gate for MgO is located between 16 eV and 20 eV, corresponding to H23 to H27, as the contrast between the polarization direction is the highest (see Figure 5.2). This also verifies that within that range a large portion

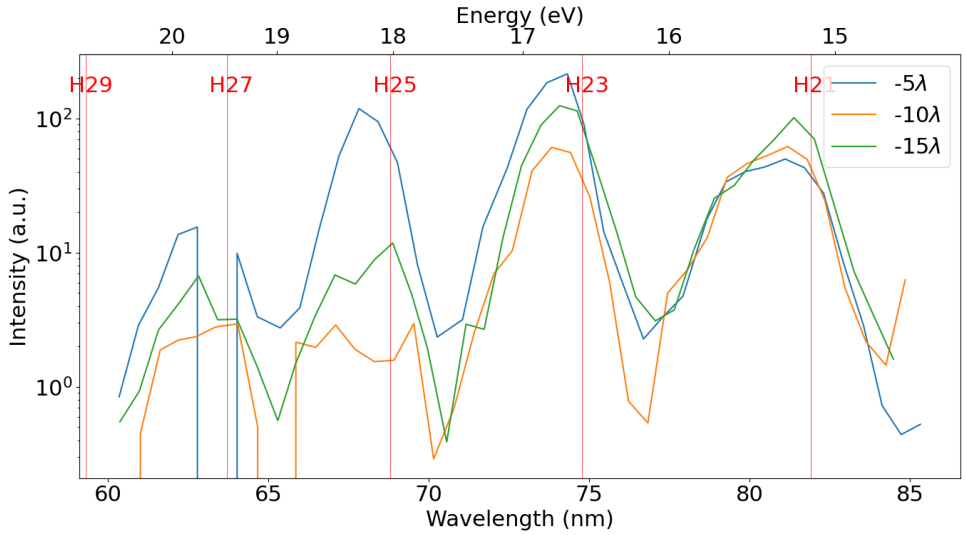

Figure 5.13: Comparison of harmonic spectra from the gated pulse with completely separated horizontal and vertical pulse components.

of the pulse is generated by the diagonal polarization direction, meaning either the central peak of the gating pulse or adjacent more elliptical portions of the pulse.

To study this behaviour further the delay is scanned, in small steps, around a value of 5λ taking spectra in the relevant wavelength range. The scaned wedge positions range from 2.32 mm to 2.16 mm, which corresponds to a calculated delay range from 4.235λ to 5.1λ. This covers the whole range of polarization structures of the pulse, from the "quasi" linear state to a circular polarization. The measurement results are shown in Figure 5.14. As it can be expected all harmonics show an increase in signal with a decreasing delay (corresponding to an increase in the wedge insertion). The evolution shows a pronounced dip at an insertion of 2.24 µm (4.67λ) as well as a rapid decline of H25 for insertions lower than 2.22 µm (4.78λ). The maxima are, taking H23 and H21 as a reference, located at 2.20 µm (4.9λ) and 2.30 µm (4.34λ). From the measurement it is rather clear that the maxima and minima of the signal do not match the expected positions. For example one would expect a minimum of the signal for circularly polarized light with an increase of the signal when approaching a linearly polarized state. One explanation of the discrepancy is a misjudgement in the pulse delay introduced by the TWINS stage. Shifting the observed minima and maxima by 0.1λ would lead to a matching scenario, with the maxima being matched on 5λ and 4.5λ while the minimum sits at 4.77λ. Nevertheless, the broad peaks around the maxima indicate that even elliptical states contribute significantly to the HHG signal. This can be problematic for the linear anisotropy gating scheme since it depends on a steep discrimination not only between different crystal axis directions but also between linearly and elliptically polarization states.

All together the experiments did not show a clear signature of isolated attosecond pulses as a result of the anisotropy gating scheme. There is a clear change in the spectra for the gated pulse structure confirming the influence of the TWINS stage

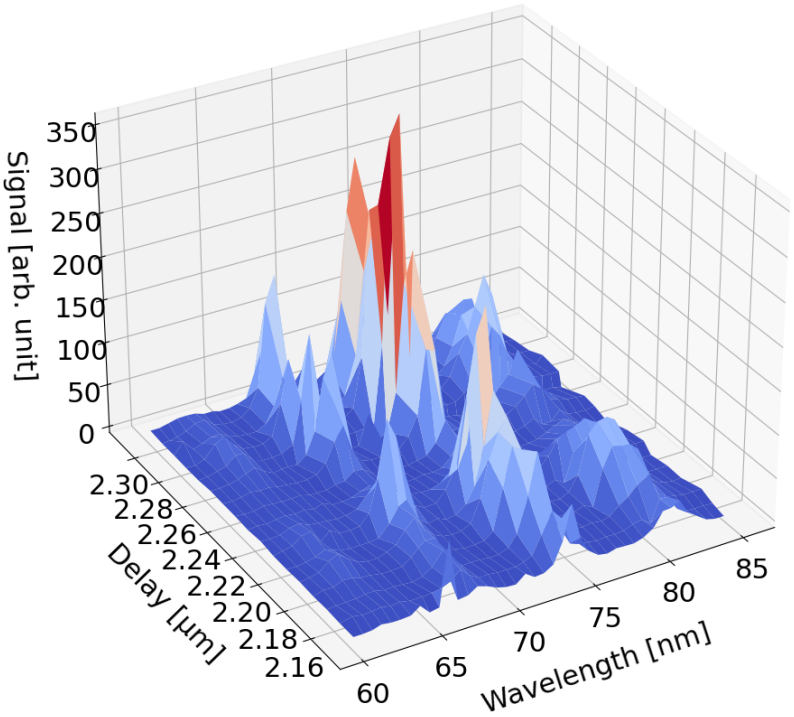

Figure 5.14: Ramp of the phases delay covering the transition between elliptic/circular polarization states and "quasi linear" polarization states.

and the presence of the gating pulse. However, the exact influence of this structure on the HHG needs further investigation. At this point theoretical support to narrow the possible parameters and confirming the potential of the concept would help the experimental effort significantly. It is also worth noting that *Klemke et al*[75] pointed out that for elliptically polarized pulses induced birefringence during the propagation through the material can have strong effects on the polarization state at the back surface of the crystal, where the harmonics are generated. While in our measurements the observed difference between the measurements of the projection of the pulse after and before the chamber were minimal, this might have a strong influence on the possible applications of this anisotropy scheme.

5.6 Pulse compression: Second iteration

The original setup was dismantle due to a move of the laboratory, giving the chance for an improved second iteration. Additionally, the lab move allowed for a change of the damaged compression grating in the pump laser, allowing the OPCPA system to run according to the nominal specifications again. As a consequence the input power for the compression stage could be increased to 1.4 W (14 µJ) which directly translates into a performance increase. Following an approach described by *Lu et al* [191] the formerly used thick pieces of YAG and ZnO are replaced by thin YAG plates. This configuration has been demonstrated to be capable to achieve compressions to the single cycle regime [192]. In total 3 plates of which two are

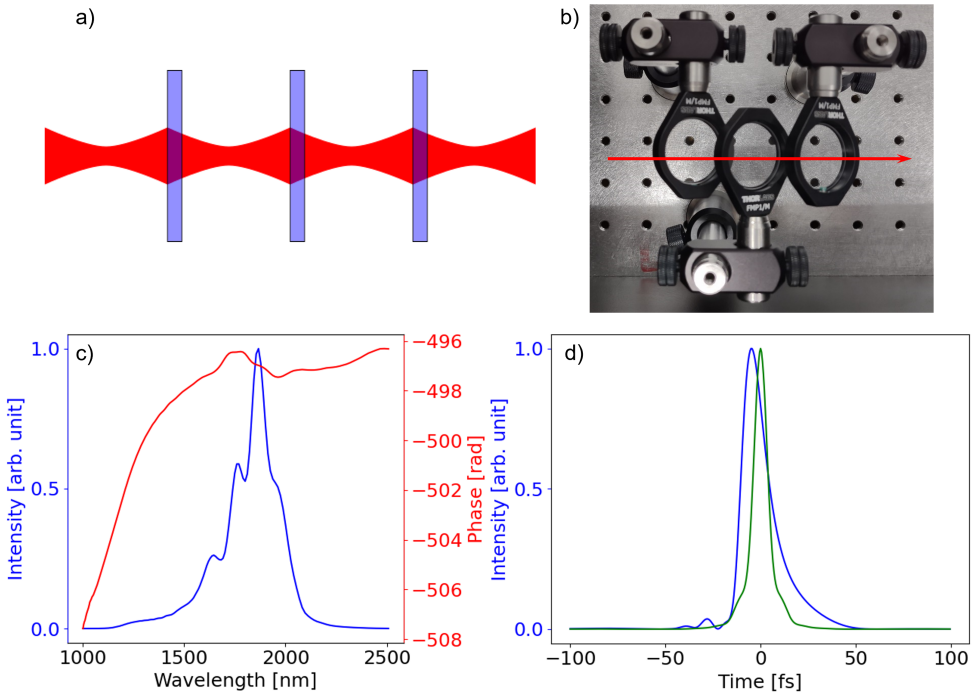

Figure 5.15: Scheme of the optimal focusing conditions for the multiplate compression scheme (a) and an image of the used three YAG plates at brewster angle (b). Spectrum (c) and temporal pulse shape (d) after the simulated propagation through the 3 YAG plates of the new compression stage design. The green curve in (d) shows the fourier transform limited pulse shape.

2 mm thick and one 1 mm thick are aligned in the beam at brewster angle. The total propagation length in the material is then, due to the 61.4° brewster angle, 10.45 mm. The first plate is placed about 15 cm in front of the focus followed by the second and third plate with a spacing of 2.5 cm. In optimal condition this geometry creates a "quasi-filament", where Kerr focusing inside the plates does not reach critical intensities for filamentation and the focus is located after the YAG plate. After the focus the beam enters the next plate and repeats the same cycle (see Figure 5.15 (a) and (b)). This allows powers higher than the critical power for self-focusing in the plates and therefore a stronger broadening of the spectra. Figure 5.15 (c) and (d) present the simulated propagation through the three plates. The spectrum is spanning nearly an octave after the compression stage due to a long tail stretching towards shorter wavelength, as it is characteristic for slef steepening. The spectrum supports 8 fs pulses if compressed to the fourier transform limit, however compensation of only the GDD leads to 10 fs pulses.

For the experimental realization the same setup as for the previous iteration (see section 5.4) is used with the difference that the YAG and ZnSe are replaced by the three YAG plates. Due to the improved state of the laser the compensation of GDD in the incoming laser could be dropped as well. A FROG characterization of the resulting pulses after GDD compensation is shown in Figure 5.16. The spec-

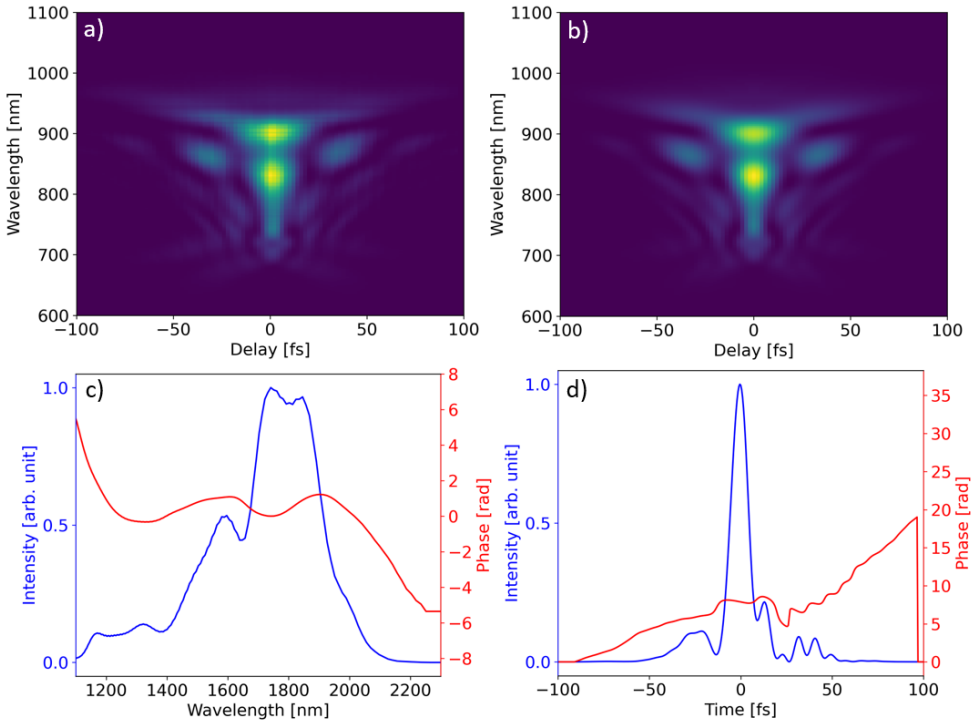

Figure 5.16: FROG measurements of the compressed pulse before the vacuum chamber. The reconstructed and measured FROG traces are shown in (a) and (b) respectively. Panel (c) shows the reconstructed spectrum, while panel (d) shows the reconstructed temporal pulse shape.

trum resembles the simulated case, spanning nearly an octave. The spectral phase reveals the presence of a TOD that leads to a pronounced side pulse in the temporal structure of the pulse. The main peak of the pulse has a FWHM of 11 fs, however the spectrum supports a fourier transform limit of 8 fs. With a cycle length of 5.6 fs (1700 nm) the pulses are spanning 1.5-2 cycles. The GDD compensation after the compression stage consists of only the beam splitter used to create a seed for the f-2f interferometer, which is a coated fused silica substrate.
While the GDD can be compensated using materials as in the first iteration of the setup, at these spectral bandwidth the TOD becomes extremely important. It can easily introduce post and pre-pulses with intensities of 25% of the peak intensity. Since the materials used for GDD compensation are all introducing positive TOD into the pulse, a GDD compensation as before can not be efficiently realized anymore. The solution for this problem are generally double chirped mirrors that introduce a fixed amount of GDD and TOD into the pulse. These mirrors are especially necessary for the anisotropy experiment since the TWINS stage itself is introducing a large phase into the pulse. However, while this is the favourable solution and such mirrors have been ordered they also have a long delivery time and could not be tested during this thesis.
As a first test the dispersion introduced into the beam after the compression stage is minimized by removing the TWINS stage and half wave plates. At the same time

the thickness of the entrance window to the vacuum chamber is reduced to 3 mm. This leaves only the collimation lens, the window and the beam splitter for the f-2f in the beam path. As a result 12 fs pulses (2 cycles) are achieved in front of the HHG crystal, with no significant pre- or post-pulse. Inside the vacuum chamber the beam passes the CaF_2 Ar coated focusing lens with a focal distance of 10 cm. Notably, the chromatic aberration of a lens can increase the expected pulse duration in the focus for sharper focusing.

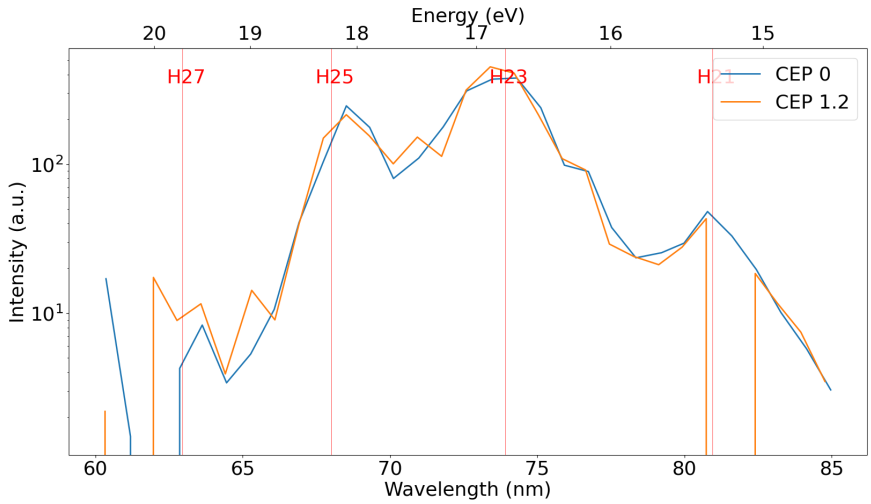

Figure 5.17: HHG spectra in MgO using 12 fs pulses for two different CEP values.

The 12 fs pulses, 2 cycle, pulses are in a regime where the harmonics can show significant CEP dependencies. As described in section 2.1.1, for ultra short pulses the peak field of the pulse depends on its alignment with the peak of the envelope. As a result the harmonic signal can vary with changes in the CEP, with the maximal change being achieved at a phase shift of $\pi/2$ (assuming the field maxima are aligned with the envelopes maxima in the initial state). To test this behaviour, as well as the general behaviour of the setup with shorter pulses, first harmonics are generated with the compressed pulses in a 100 µm MgO crystal. As can be seen in Figure 5.17, the harmonics around the top of the first conduction band are much broader than in previous measurements due to the increased spectral bandwidth of the driving pulses. Comparing spectra with a CEP difference of 1.2 radian, a small peak between H23 and H25 arises. While this peak is small, the change is repeatable and consistent with the CEP response observed in the initial anisotropy measurements. This is a first sign that should become much more present with a proper TOD compensation and fully compressed 1.5 cycle pulses. Reaching the two cycle regime is also a huge improvement for the anisotropy gating, placing the input pulses in a range similar to classical polarization gating schemes for gases.

5.7 Conclusion

In conclusion, the possibility of a polarization based gating scheme targeting the anisotropic harmonic response of solids has been studied to push towards isolated attosecond pulses. The advantage of such a scheme compared to direct generation of isolated pulses using single cycle driving lasers are the relaxed requirements on the driving laser. It would enable the generation of isolated attosecond pulses without cutting edge post compression stages and enable a wider spread of EUV attosecond pulses.
The setup used here is based on an interferometer consisting of a birefringent material to introduce a variable delay between two perpendicular polarized copies of the pulse. This introduces a rotating linear polarization structure that can be used to align single cycles of the field to a specific crystal axis. After promising results in an initial study, the laser was post compressed to about 25 fs using SPM broadening in solids to achieve a more pronounced polarization gate. Using these post compressed mid-IR pulses, different delays, and therefore polarization states, of the gated pulse have been studied for signatures of isolated attosecond pulses. However, it was not possible to reproduce the promising initial results. The reasons for this are likely differences between the ideal gating pulse structure and the experimentally produced pulse structure, namely a large TOD leading to more elliptical polarization states. This TOD could sadly not be compensated before the system needed to be shutdown for repairs and a move of the laboratory. Another concern with the pulse structure is the angular spacing between the "quasi linear" field peaks. A low separation leads to a mixing between the HHG from the desired central peak and the surrounding peaks, preventing an isolated HHG pulse.
After an upgrade, the compression scheme was improved to now reach 12 fs pulses. After limiting the introduced TOD as much as possible first HHG spectra were recorded using these 12 fs. Notably, they show a weak CEP response similar to the one observed in the initial gating experiments.
Going forward with the experiment a further exploration of the parameter space to locate the faint CEP response of the signal is needed. To guide the experiments a collaboration with *Uwe Thumm* and *Francisco Navarrete* has been initialized to provide theoretical guidance [95]. The first goal for this is to verify the theoretical feasibility of the polarization gating approach and study the polarization of the resulting harmonics. On the experimental side the setup needs to be reworked for usage with single cycle pulses. This allows not only tests of the anisotropy scheme with shorter pulse duration, but also a route towards isolated attosecond pulses via generation with single cycle mid IR pulses. The two cycle pulses generated so far already show first signs of CEP dependency, despite the high TOD introduced into the pulse during the transfer into the crystal. Custom designed mirrors to compensate the TOD of the pulse together with an adapted setup would allow the generation with clean two cycle pulses. Additionally, further materials can be explored with the goal of a sharper polarization dependency of the harmonics than in MgO.
Furthermore, there are other techniques that, similar to the polarization gating, target the generation of isolated attosecond pulses from solids. For example a two

color gating scheme has been proposed, achieving pulse durations down to 220 attoseconds in theoretical calculations [28] together with an enhanced harmonic yield [96]. It uses a weak second harmonic field to induce a field asymmetry, effectively limiting the time frame of HHG in the pulse. One possible further approach would be to use the propagation of the pulse inside the material for post compression of the pulse. However, after first tests that showed sufficient compression is possible [58], it became clear that the intensities necessary for the efficient self compression are above the damage threshold for MgO crystals of 100 µm and 200 µm in vacuum. Going forward, approaches with thick crystals could push this scheme towards single cycle pulses in the plane of high harmonic generation. However, this scheme comes with challenges as the possible spatial distortions in the beam due to the strong nonlinear interactions. They can be transferred to the harmonics and might render the beam practically unusable.

Chapter 6

Conclusion

This thesis studied three main topics: the influence of doping on the harmonics from MgO and silicon, imaging of nanostructures based on the harmonics generated in the structure itself and a gating scheme using a tailored driving laser to achieve isolated attosecond pulses.

In the third chapter two different cases of material defects have been studied for their influence on the process of high harmonic generation. The first material is magnesium oxide doped with low concentrations of chromium atoms. The experiments use a 1.55 µm OPCPA based laser with a pulse duration of about 20 fs that is focused into a 200 µm MgO crystal reaching vacuum intensities up to 14 TW/cm^2. The harmonics from the doped crystal show a higher harmonic yield than harmonics from an undoped MgO crystal. However, the results do have a large uncertainty due to possible, doping induced, differences in the optical properties of the two samples. An investigation of the spatial and spectral phase modulation of the driving laser pulse led to mixed results. Compared to the undoped MgO the MgO:Cr shows slight signs of stronger self focussing, indicated by a smaller focal spot at the exit surface under same conditions. The spectral and temporal structures of the transmitted driving pulse are identical with no signs of self phase modulation. Additionally, using a set of new crystals from the same producer, the increased harmonic yield could not be reproduced using a different laser system. There is a sign of an increased ionization rate in the form of fluorescence from the second conduction band, indicating that the theoretical description as a bandgap reduction due to the doping is valid. This would align with the electrons loosing coherence and therefore not contributing towards the harmonics. The overall still existing uncertainties related to propagation effects, could experimentally be solved with a switch to a full reflection geometry [87, 58] as it avoids any propagation inside the material.

The second approach uses a focused ion beam to bombard the surface of a silicon sample with energetic gallium ions. This leads to a forceful implantation of the ions into the silicon crystal structure and, as a consequence, to additional silicon defects and vacancies in the crystal. At high ion doses these effects can even change the crystal structure, transferring it into an amorphous state. At the same time the effect is limited to the last nanometers of the material and therefore does not interfere with the propagation of the driving laser, removing many of the restriction observed in the MgO experiments. The harmonic yield from these crystal modi-

fications has been studied for a variety of different ion doses, showing an increase of signal for ion doses around 10^{14} ions/cm^2. Afterwards the signal dropped even below the signal from pure silicon at doses above $\approx 10^{16}$ ions/cm^2. The increase of signal can be connected to additional flat defect bands generated in the bandgap and a potential decrease of the bandgap itself. However, it is unclear if the increased yield is caused by the gallium atoms introduced into the material or the secondary silicon defects. This has to be clarified in further experiments using e.g. other ions, potentially even silicon itself, for the material modifications.
Overall doping can enhance the harmonic signal but the effect seems highly material and dopant dependent making a technical use in e.g. solid based EUV HHG sources difficult to generalize. However, the effect opens up the possibility to detect and image these structural changes by using the enhancement as a unique probe with structural sensitivity. Furthermore, the concept opens up an additional parameter for the study of fundamental HHG mechanisms.

The fourth chapter demonstrates the possibility to image nanostructures, as they are frequently used to generate spatially structured beams. The basic concept for our lensless imaging approach is ptychography, which belongs to the family of coherent diffraction imaging techniques. A compact fiber laser centred at 2100 nm with a pulse duration of 80 fs was enough to generate harmonics inside the structure itself (near field) and collect the diffraction patterns in the far field. As a test of the concept two different kinds of nanostructures were fabricated using a focused ion beam: one spiral zone plate and one sample imitating electric nano-circuits. Using the fifth harmonic at a wavelength of 420 nm, diffraction patterns were recorded and successfully reconstructed. The reconstructed images achieve a resolution of about 800 nm, which is less than half of the driving laser wavelength. These resolutions have been reached before and can be achieved with classical microscopy as well, however there is a clear path towards sub-100 nm resolutions by using higher harmonic orders. The harmonic spectrum from solids extends up to 30 eV and, while connected to some challenges, using these EUV harmonics would directly improve the resolution of the technique. Additionally, the change in HHG due to structural changes in the material observed in chapter 2 can probe near surface material modifications with nanometer scale spatial resolution.
As a second test a spiral zone plate pattern on ZnO has been studied and successfully reconstructed as well. The calculated propagation of a Gaussian beam through the reconstructed zone plate into the focus of the OAM matches the experimentally observed OAM, further proving that the achieved image quality is enough to accurately predict the spatial shaping of the HHG from the nanostructuration of the sample.
Going forward the next step is to extend the concept to the EUV to achieve higher resolutions. However, this is connected to a couple of challenges. A first major one of these is likely the broadband/multi wavelength nature of the recorded diffraction patterns. As the divergence depends on the wavelength, overlapping the diffraction of broadband lasers leads to a 'smearing' of the diffraction pattern making a reconstruction challenging. One solution for this is filtering a single harmonic, which is the path used in our experiments. However, filtering in the EUV is much more challenging, especially with the geometric constraints connected to the tight

focusing. The second solution are broadband [167] or multi-wavelength reconstruction algorithms [168]. This solution allows a larger variety of applications but adds complexity to the reconstruction. In particular, the multi-wavelength approach with an harmonic comb has the possibility to strengthen the material sensitivity of the technique. An even bigger challenge in the EUV is a much lower flux. Measurements therefore require a lower noise background, possibly even longer integration times and higher sensitivity of the detection. Alternatively, the intensity of the driving laser can be increased, given that it stays below the damage threshold of the material.

The fifth chapter discusses and tests a temporal gating scheme similar to polarization gating in HHG from gases as a possibility to achieve isolated attosecond pulses with HHG from solids. Compared to gases it uses a rotating linear polarization to align only one half optical cycle with the efficient HHG generation axis of an MgO crystal. This limits the HHG emission to this half cycle and consequently has the potential to produce isolated attosecond pulses. After first tests the 40 fs pulses of the laser were identified as to long for reaching harmonic emission from only a single half cycle. To push for shorter pulses a post compression stage based on self phase modulation in a solid has been build reaching 30 fs in a single stage, limited by the immediately available materials at that time. The SPM inducing materials were a 4 mm YAG crystal and a 5 mm ZnSe. The ZnSe has a much higher nonlinearity compared to YAG but also introduces a large GDD that has to be compensated for afterwards. Due to the large amount of material needed for GDD handling, the pulse has a large TOD, which is on the verge of producing significant post pulses.
The compressed pulses have been nevertheless used for another try on the anisotropy scheme. The general behaviour of the harmonic response to the polarization tailored pulses was studied. As first tests did not show a strong dependence on the CEP, the studies focused on the dependence on the delay between the two polarization replica using the 25th harmonic signature. Indeed, since the upper edge of the first conduction band is different for the Γ-X and Γ-K direction of MgO, the 25th harmonic is originating in the first conduction band for the Γ-X direction while it is part of the second conduction band for the Γ-K direction. This difference is used to verify that the pulse is generating harmonics with the desired central part of the polarization tailored pulse. Afterwards the polarization structure is varied in fine steps from the desired rotating linear polarization state to a circular polarization state to verify the sensitivity of the setup. It shows that harmonic emission is indeed maximized at least close to the desired polarization state. However, the observed maximum is much broader and less sensitive than necessary for the generation of isolated attosecond pulse. Again the direct way to improve the gate is the usage of shorter pulses.
Therefore, after a lab move and laser upgrade the compression stage was improved to achieve 12 fs pulses using a similar scheme but a series of 3 YAG plates at brewster angle to introduce the necessary broadening. However, at this point the high TOD is resulting in postpulses reaching up to 25% of the main peak. This can be compensated with specifically designed mirrors, which are ordered but could sadly not be tested during this thesis.

Overall, polarization gating approach to generate isolated attosecond pulses from solids seems feasible. The shorter two cycle pulses generated in the second iteration of the compression scheme achieve durations similar to those used for polarization gating in gases. However, there are further challenges that have to be solved. One of them is the transmission geometry used for the experiments so far. While non linear effects could be at least limited for 'longer' 40 fs pulses, 12 fs pulses are not only reaching much higher peak fields but are also much more sensitive to disturbances by e.g. additional phase. It is furthermore possible that effects such as induced birefringence that appeared to be not relevant for longer pulses become a serious problem for higher peak fields and broader pulses. A the same time a switch to a reflection geometry adds another complexity to the practical implementation of the scheme. Another approach would be a classic polarization gating as it is used in gases. While the extinction for the circularly polarized is not as large and sharp as in gases for most crystals there still is a significant drop of about two orders of magnitude in the harmonic efficiency. Both of these schemes could additionally be connected with a two color generation scheme to further sharpen the selection of a central half cycle of the driving pulse.

With the progress made in HHG from solids over the past decade, the focus starts to shift towards applications of not only these harmonics but also the underlying electron currents. The lower driving powers needed can lead to a compact and mobile EUV sources for e.g. spectroscopy and imaging. This can be further facilitated by nanostructures that allow for easy and effective spatio-temporal manipulations of the EUV beam, for example to separate harmonic orders and/or refocus them without the need for further optics. Additionally, the material sensitivity of HHG can be used as a novel probe for imaging, giving access to band structure changes with nanometer scale spatial resolution. With further studies on the effects of doping on the harmonic emission such a probe also has the potential to allow measurements of nanoscale doping concentration induced amplitude and phase modulation.
The underlying current driving the HHG is directly dependent on the laser field and band structure of the material. This can be used for direct measurements of the field [193], but also opens up the possibility for ultrafast electronic circuits. Indeed, the current is changing at a perahertz rate, outpacing any currently available electronics. In this context materials with local energy minima in the conduction band are an intensively studied candidate [194]. The valley can allow information storage using its inherit properties such as the valley pseudospin, which can be accessed using mid-infrared strong fields.
The goal of petahertz switches makes a precise characterization of the electronic currents necessary. Luckily the direct connection of the HHG to the electron dynamics allows a reconstruction of the coherent current flows based on a full characterization of the harmonics. Retrieving the full amplitude and phase information of the harmonics would consequently allow for a deep insight into the fundamental processes driving the HHG in solids. This could e.g. result in a clear distinction between intra- and interband harmonics. This is not only useful in the context of petahertz electronics but also for doped crystals and other materials that have complex and rare

band structure features. However, while the spectrum can be easily measured, the phase of the harmonics and therefore the exact temporal structure of the attosecond pulses is much harder to characterize. There are two major techniques known from HHG in gases that achieve this: Attosecond streaking and Resolution of Attosecond Beating By Interference of Two-photon transitions (RABBITT). Streaking works in the regime of isolated attosecond pulses while the RABBITT is targeted at harmonic spectra. In our lab the setup of a RABBITT scheme for HHG from solids has been planned in the framework of the ATTOCOM project (in collaboration with groups of the LCPMR, Sorbonne University). In a RABBITT setup, the harmonic beam is overlapped with a weak coherent IR field and focused into a gas target. There the combination of harmonics and IR leads to multiple ionization paths that result in identical energies. The consequence is an interference pattern that contains information about the attosecond phase.
However, while the traditional RABBITT scheme is working for HHG from solids the detection range is limited by the used gas targets. For HHG from noble gases are used with Xenon having the lowest Ionization potential at about 12 eV. This works for the energy ranges of HHG from gases but for solids it is far above the usual bandgap energies and allows for a characterization of only a small portion of the harmonic spectrum. As a solution we plan to use potassium as a target bringing the ionization energy down to 4 eV, capturing the near bandgap dynamics of HHG from solids. Nevertheless, this leads to a technically much more complex experimental setup.

Appendix A

Spectrum extraction from CCD images

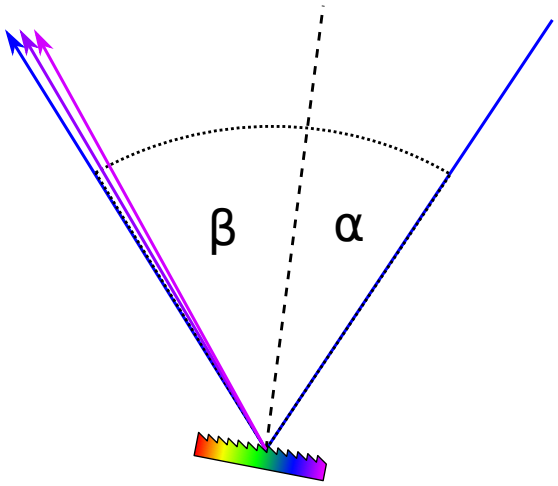

Figure A.1: Illustration of the angles for the monochromator grating used in the XUV spectrometer.

To extract a spectrum from the CCD images in chapter 3 the spectral intensity as well as the wavelength scale have to be calculated. For the spectral intensity the images can be summed in the vertical direction, however due to the spatial structure of the beam this would transfer distortions into the spectra. Instead only a small portion in the center of the spectrum (about 5 pixels wide) is used as a basis for the spectra.
For the wavelength axis the mapping of pixel position to wavelength is needed. The geometry for the used toroidal grating (2400gr/mm, platinum coated) is shown in figure A.1. It is designed for a fixed total angle of $\alpha+\beta = 64$, where α is the incident angle and β the reflection angle. The harmonics are then focused onto a Rowland circle with a distance of 20 cm from the grating in the direction of the reflected beam. For the monochromatiser mode the wavelength of the reflected beam can then be calculated via [195]

$$m\lambda = 2d\cos(K)\sin(\phi). \tag{A.1}$$

The angles K and ϕ are defined as $\frac{\alpha-\beta}{2}$ and $\frac{\alpha+\beta}{2}$ respectively. This equation is

used to calculate the wavelength scale throughout the use in combination with the photomultiplier. For the use with a CCD detector the grating is set to a fixed incident angle. For this the 23rd harmonic is identified using the absorption edge of the aluminum filter and positioned central on the CCD chip. The calculation of the wavelength is then done in two steps. First the angles for each pixel position on the CCD chip are calculated. Second the angles are mapped to wavelength using the standard grating equation

$$d\left(\sin(\alpha) - \sin(\beta)\right) = m\lambda. \tag{A.2}$$

Notably, the grating is only reaching the maximal resolution in the monochromator configuration, meaning the spectral resolution becomes worse with increasing distance to the 23rd harmonic.

Appendix B

The fourier transformation

The fourier transformation is an important tool in optics connecting time and frequency domain, as well as being the cornerstone for the framework of fourier optics. The continuos fourier transformation is defined as:

$$\mathcal{F}\left[f(x)\right] = \frac{1}{\sqrt{2\pi}} \int_{-\infty}^{\infty} f(x) e^{-ik_x x} dx \tag{B.1}$$

$$\mathcal{F}\left[f(k_x)\right] = \frac{1}{\sqrt{2\pi}} \int_{-\infty}^{\infty} f(k_x) e^{-ik_x x} dk_x \tag{B.2}$$

where (x, k_x) is the real space and frequency space coordinate pair and $\mathcal{F}$ denotes the fourier transformation. Notably, the prefactor can vary with the full factor of $1/2\pi$ being either split between the forward and backwards transformation or attributed to one of them.
Nowadays the signal processing is digital. The continuos function is therefore sampled with discrete points $n, p = (1, 2, 3, ..., N-1, N)$, with sampling steps δ_x, δ_q. The discrete fourier transformation (DFT) then takes the form:

$$\mathcal{F}\left[f(n\delta_x)\right] = F(p\delta_q) = \frac{1}{\sqrt{N}} \sum_{n=0}^{N-1} f(n\delta_x) \exp\left(-i\frac{2\pi}{N} pn\right) \tag{B.3}$$

$$\mathcal{F}^{-1}\left[F(p\delta_q)\right] = \frac{1}{\sqrt{N}} \sum_{p=0}^{N-1} F(p\delta_q) \exp\left(-i\frac{2\pi}{N} pn\right). \tag{B.4}$$

This is implemented as the so called *fast fourier transformation* (FFT) and can be calculated in computationally very efficient ways.
The connection between the sampling of the different domains can be calculated by comparing the continuos and discrete transformations. The two phase terms of the two transformations have to represent the same phase, therefore[138, 196, 197]:

$$\exp\left(-ik_x x\right) = \exp -i(p\delta_q)(n\delta_x) = \exp\left(-i\frac{2\pi}{N} pn\right) \implies \delta_q \delta_x = \frac{2\pi}{N}. \tag{B.5}$$

Appendix C

Image distortion at high numerical aperture

At high numerical apertures, i.e. high diffraction angles, the paraxial approximation is breaking and the recorded diffraction pattern becomes distorted. Assuming elastic scattering the momentum is conserved and the wavevectors of the scattered light form a sphere, the Ewald sphere. For low diffraction angles the mapping from the sphere on a plane detector is approximately linear. However, for higher diffraction angles this mapping becomes non linear and has to be compensated for, by remapping the recorded data. FigureC.1 shows an illustration of the geometry of the problem. There are two ways to calculate the re-mapped coordinates r_{real}. For the first one (e.g. [125]) the problem is reduced to two dimensions using the rotational symmetry. The important coordinates are then the initial propagation direction z with the flat detector at z_0 and the radial coordinate $r = \sqrt{x^2 + y^2}$. In this case the angle θ calculates to

$$\theta = \arctan\left(\frac{r_{meas}}{z_0}\right) \tag{C.1}$$

with the radius of a measured position r_{meas} corresponding to the coordinates (x_{meas}, y_{meas}). The radius r_{real} then calculates to

$$r_{real} = z_0 \sin(\theta) = z_0 \sin\left(\arctan\left(\frac{r_{meas}}{z_0}\right)\right) \tag{C.2}$$

This equation can be simplified to

$$r_{real} = z_0 \frac{\frac{r_{meas}}{z_0}}{\sqrt{1 + \left(\frac{r_{meas}}{z_0}\right)^2}} = \frac{r_{meas}}{\sqrt{1 + \left(\frac{r_{meas}}{z_0}\right)^2}}. \tag{C.3}$$

The inverse function is then

$$r_{meas} = z_0 \tan\left(\arcsin\left(\frac{r_{real}}{z_0}\right)\right) = \frac{r_{real}}{\sqrt{1 - \left(\frac{r_{real}}{z_0}\right)^2}}. \tag{C.4}$$

The alternative way (e.g. [198]) calculates the vector $\vec{s}$ to the point on the sphere and projects from there to the detector plane. The vector $\vec{s}$ is just a shorter version

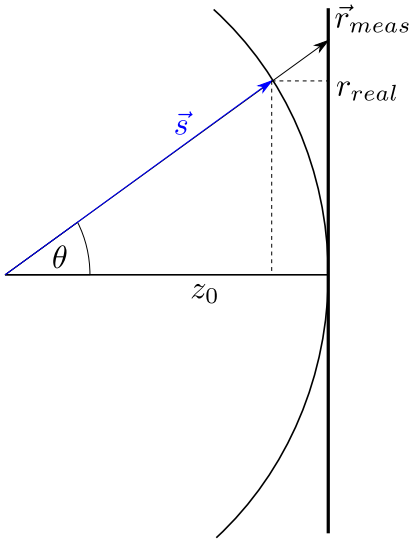

Figure C.1: Illustration of the Ewald sphere and the detector plane.

of the vector to the measured point and can therefore be calculated by rescaling the length to the known radius z_0 off the sphere

$$\vec{s} = \vec{r}_{meas} \cdot \frac{z_0}{|\vec{r}_{meas}|} = \frac{\vec{r}_{meas}}{\sqrt{\frac{x^2+y^2+z_0^2}{z_0^2}}} = \frac{\vec{r}_{meas}}{\sqrt{1+\frac{x^2+y^2}{z_0^2}}}. \tag{C.5}$$

The projection on the detector plane at z_0 can be done by simply replacing the z component of the vector by z_0. With this the solution takes the same shape as before.

Since the light is propagating for an additional distance corresponding to the difference $\vec{r} - \vec{s}$, the intensity has to be rescaled as well, according to

$$I_{scaled}(x,y) = I_{meas}(x,y)\frac{|\vec{r}_{meas}|^2}{|\vec{s}|^2} = I_{meas}(x,y)\left(1+\frac{x^2+y^2}{z_0^2}\right) \tag{C.6}$$

Appendix D

Intensity from an Iris scan

The radial profile of a gaussian beam propagating in z-direction has the shape

$$E(r,t) = E_0 \exp\left(\frac{-r^2}{\omega^2}\right) \exp\left(\frac{-t^2}{\tau^2}\right), \tag{D.1}$$

with ω being the spatial width at the $1/e^2$ level, τ the pulse width at $1/e^2$ level, r the radial coordinate and t the time. The intensity then calculates to

$$I = \frac{1}{2} c_0 \epsilon_0 n |E(r,t)|^2 = I_0 \exp\left(\frac{-2r^2}{\omega^2}\right) \exp\left(\frac{-2t^2}{\tau^2}\right), \tag{D.2}$$

where $I_0 = E_0^2$, c_0 the speed of light in vacuum, ϵ_0 the electric permittivity and n the refractive index of the medium.
The definition of the beam and pulse width as the width at $1/e^2$ level is mathematically natural for gaussian beams but experimentally rather unusual. Instead the *full width half maximum* (FWHM) width is used. For gaussian beams the FWHM can be calculated from the gaussian width as

$$\text{FWHM} = \omega\sqrt{2\ln 2}. \tag{D.3}$$

In normal experimental conditions the intensity can rarely be measured directly. The most accessible experimental parameter related to the intensity is the *average power* P_{avg} of the laser. From there the per pulse energy P_{pulse} can be calculated as

$$P_{pulse} = \frac{P_{avg}}{f_{rep}}. \tag{D.4}$$

The total pulse energy can be calculated by integrating over the whole pulse as well

$$P_{pulse} = \int_{-\infty}^{\infty} \int_0^{2\pi} \int_0^{-\infty} I r dr d\phi dt = \frac{I_0 \omega^2 \pi}{2} \int_{-\infty}^{\infty} \exp\left(\frac{-2t^2}{\tau^2}\right) = \frac{I_0 \omega^2 \tau \pi^{3/2}}{2\sqrt{2}} \tag{D.5}$$

and therefore

$$I_0 = c \cdot \frac{P_{avg}}{f_{rep} \tau \omega^2} \tag{D.6}$$

To calculate the beam diameter of the initial beam based on power measurements

after an iris at different radii, the measurement points have to be fitted to the expected values given by

$$P(r) = P_0 \left(1 - \exp\left(\frac{-r^2}{\omega^2}\right)\right). \tag{D.7}$$

From equationD.7 follows $P_0 - P(r) \propto I(r)$. This gives a fit function for the measurement and allows the calculation of the initial beam width.

Appendix E

Estimation of the ptychography sample depth

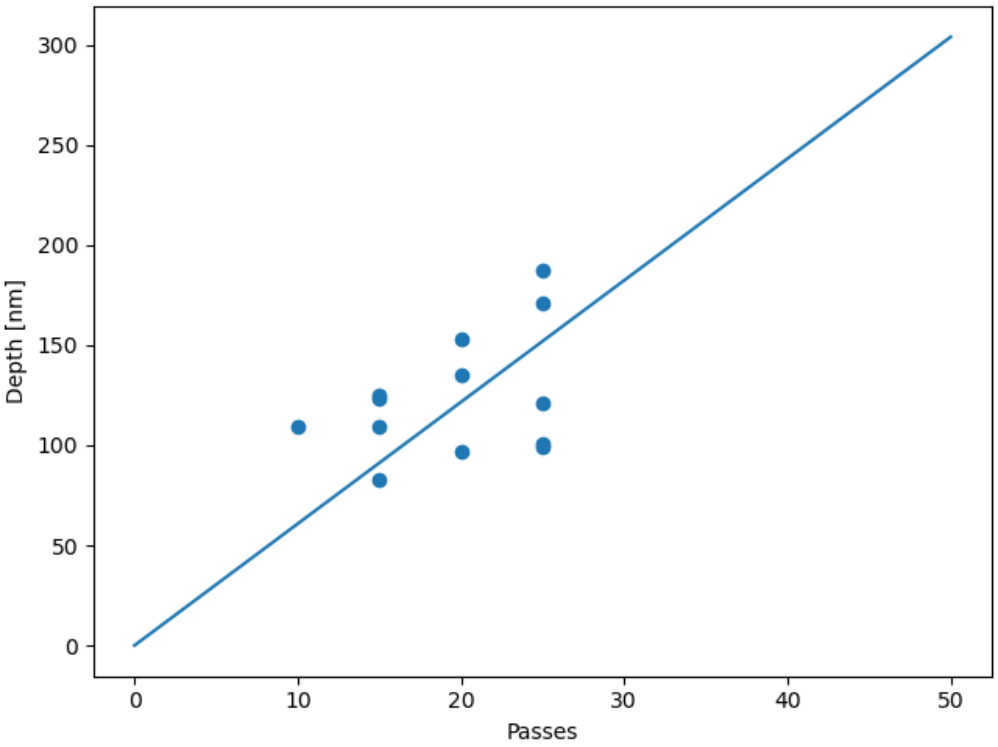

Figure E.1: Measured structural depth of the produced samples using SEM images at an angle of 60°.

During the production of the samples the ion dose was controlled by the number of passes that the FIB does over the sample pattern. This number of passes is therefore directly proportional to the ion dose and serves as a parameter instead. Estimates for the depth of each Ptycho4 sample are extracted from the SEM images that were taken with an angle of 60° between the sample surface and the electron beam. This allows to retrieve an depth estimate from the image since the walls of the structure are visible. However, for the Ptycho4_5 and Ptycho4_7 sample the edge is too small to estimate the depth. Unfortunately these are exactly the samples that produced good diffraction patterns without damage to the structure. In order

to get an estimate of the depth for these samples an extrapolation based on the depth of the deeper structures is done. The base assumption for this is that the etching depth scales linearly with the number of paths during fabrication. This assumption should hold after at least one or two passes as a dynamic equilibrium is formed between removed material and damage to the material below. Since the depth for no passes has to be zero the fitting equation is a simple line that crosses the origin. The depth estimated from the images together with the fit are shown in Figure E.1. The rise of the line is 6nm/pass. This means that Ptycho4_5 is about 30 nm deep, while Ptycho4_7 is only about 12 nm deep. It is important to keep in mind that especially the depth of Ptycho4_7 likely has a large error bar.

Appendix F

First set of dose dependent gallium implanted silicon measurements

The measurements were taken with the same parameters as described in section3.6 but only squares with extremely high doping and a moderate doping, around the peak of the enhancement, were tested. The high dose is at 3.48e16 ions/cm^2, the low dose at 1.9e14 ions/cm^2 and the reference is the pure silicon substrate. The spectra shown in Figure F.1 show a spectral shift of H3 as well but here the high dose is blue shifted while the low dose is red shifted compared to the reference. H5 behaves identical to the later measurements, more continuos measurements in section3.6. For H7 there is a large fluorescence present close to the harmonic, which might be caused by a FIB induced bandgap change. However, the H7 signal is not present even for the lower dose. This is in agreement with the later measurements that show H7 falling off at a doses below 1e13 already. This is below the ion dose used for these first experiments.

The evolution with the dose for these measurements is shown in Figure F.2. H3 and H5 show the increasing tendency here as well, but due to the low number and spread of the ion doses not the full rise and fall of the signal is captured. Notably, the highest doses here reach much higher than for the sample used in section3.6 and show a further decrease of the signal with higher ion doses, far below the signal from pure silicon. Additionally, the signal seems to reach a plateau for the high ion doses, signalling that a stable equilibrium of ablation and structural damage has been reach for the highest doses.

Another earlier set of measurements is from the initial ptychography measurements. They use a spot on the Ptycho4_7 sample, the bulk close to that sample and a spot close to the TVB samples. The spot close to the TVB sample has been passed by the FIB due to a malfunction of the FIB, meaning the ion dose for this area is uncertain. However, it shows an even stronger signal increase than the ptychography samples (see Figure F.3). In fact the increase is even stronger than for the sample spots studied in section 3.6.2. The spectra are taken separately for each harmonic and corrected for the integration time of the spectrometer (hence the different noise background) and filter transmissions. For H5 and H7 a low pass filter is used, while H3 is recorded with a ND filter for the IR of the driving pulse. The contributions of H5 to H3 are insignificant due to the coupling of the spectrometer and much higher signal of H3. Integration times for H7 is 3 s for all measurements,

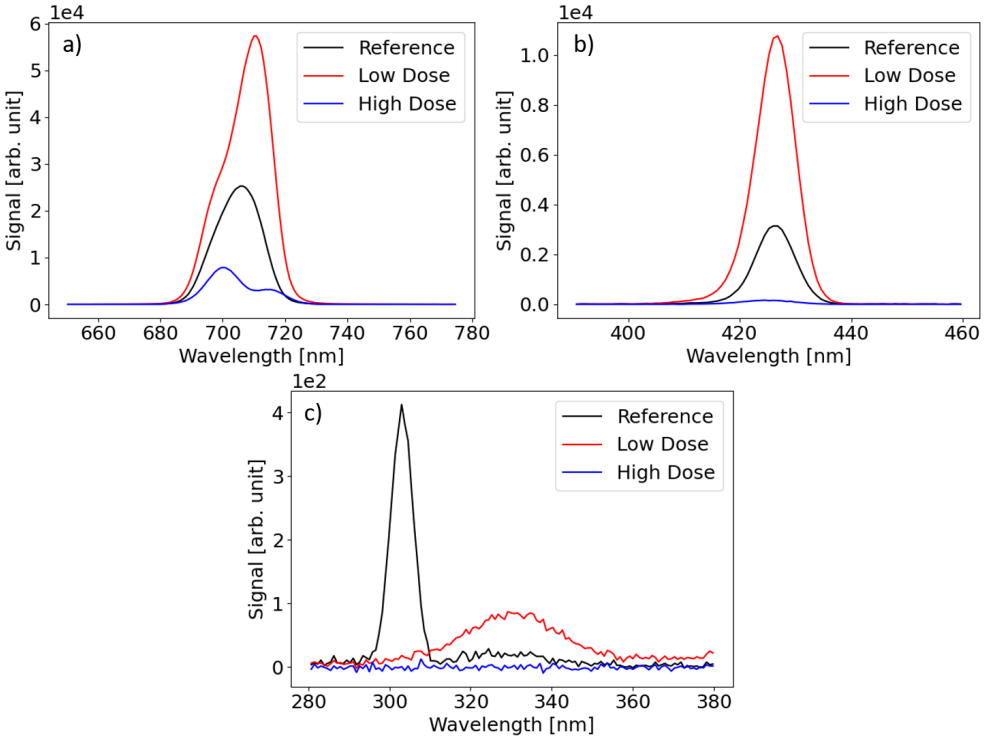

Figure F.1: Spectra of H3, H5 and H7 for different doses of gallium implantation.

while it is 200 ms for H3. For H5 the integration time varies depending on the spot, being 500 ms for the Ptycho4_7 and bulk spot and 100 ms near the TVB. This difference was necessary due to the higher signal close to the TVB.

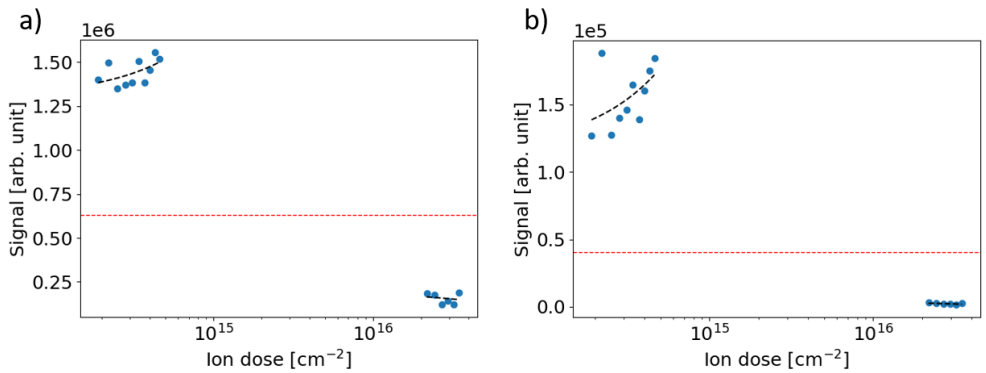

Figure F.2: Ion dose dependency of the integrated yield for H3 (a), H5 (b) and H7 (c). The dashed red line marks the harmonic yield from an unmodified silicon surface.

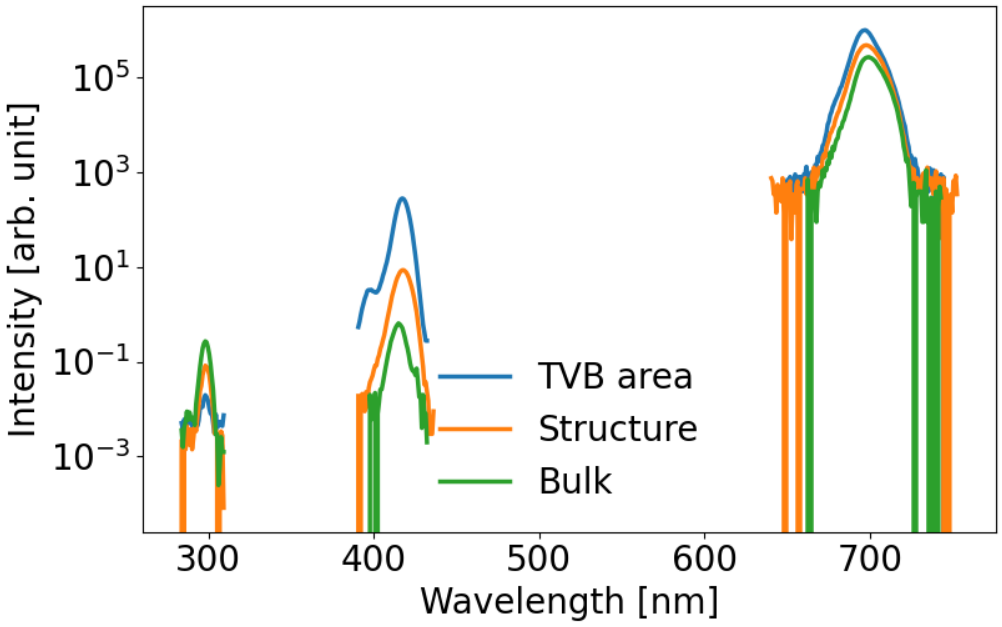

Figure F.3: Spectra from taken on the Ptycho4_7 sample, bulk silicon and close to the TVB sample. Spectra are taken separately for each harmonic and are corrected for the transmission of the used filters as well as the integration time.

Appendix G

Focused Ion Beam

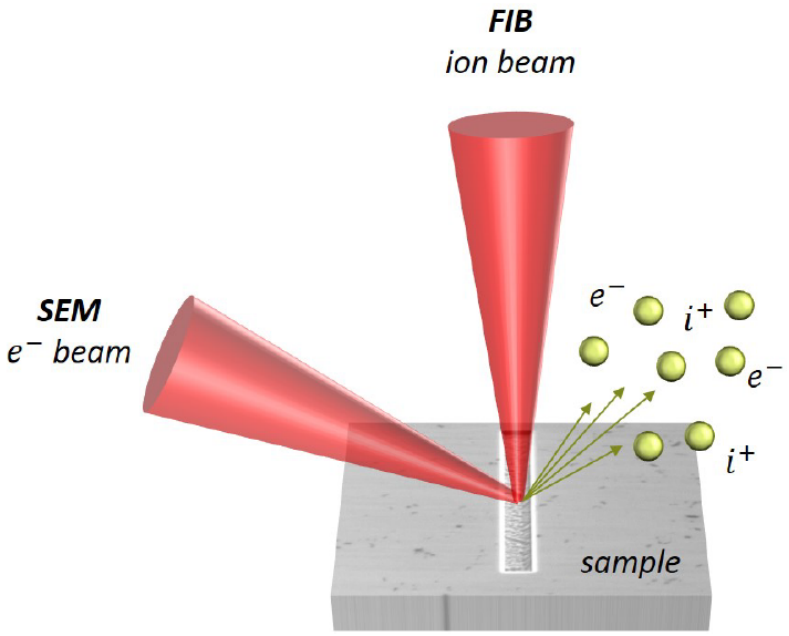

Figure G.1: Schematic of the FIB setup in combination with an SEM (taken from [58]).

The focused ion beam (FIB) technique is a way of milling nanostructures into a variety of materials. As the name suggests it accelerates ions to high kinetic energies and focuses them onto a small spot of the sample. The main goal of the ion beam is to remove material by sputtering atoms from the surface and breaking the crystal structure. Using ions allows focal spot sizes of tens of nanometers. FIB setups are often combined with scanning electron microscopes (SEM) to inspect the etched structures. A schematic of such a setup can be seen in Figure G.1.
Ions can be accelerated to a variety of energies with normal values ranging from 5 keV to 40 keV. Different ion species can be used, however in this work the etching has been done exclusively with gallium ions at 30 keV. Structures are inspected with the SEM after production. To determine the depth of the etched structures SEM images at an angle are taken. The depth is then calculated based on the angle and height of the wells walls.

List of Figures

List of Tables

Bibliography

[1] T. H. Maiman. Stimulated Optical Radiation in Ruby. Nature, 187(4736):493–494, August 1960. Number: 4736 Publisher: Nature Publishing Group.

[2] P. A. Franken, A. E. Hill, C. W. Peters, and G. Weinreich. Generation of Optical Harmonics. Physical Review Letters, 7(4):118–119, August 1961. Publisher: American Physical Society.

[3] W. Kaiser and C. G. B. Garrett. Two-photon excitation in CaF_2:Eu^{2+}. Physical Review Letters, 7(6):229–231, September 1961. Publisher: American Physical Society.

[4] W. R. Zipfel, R. M. Williams, and W. W. Webb. Nonlinear magic: multiphoton microscopy in the biosciences. Nature Biotechnology, 21(11):1369–1377, November 2003. Number: 11 Publisher: Nature Publishing Group.

[5] D. Strickland and G. Mourou. Compression of amplified chirped optical pulses. Optics Communications, 56(3):219–221, December 1985.

[6] A. McPherson, G. Gibson, H. Jara, U. Johann, T. S. Luk, I. A. McIntyre, K. Boyer, and C. K. Rhodes. Studies of multiphoton production of vacuum-ultraviolet radiation in the rare gases. JOSA B, 4(4):595–601, April 1987. Publisher: Optica Publishing Group.

[7] M. Ferray, A. L'Huillier, X. F. Li, L. A. Lompre, G. Mainfray, and C. Manus. Multiple-harmonic conversion of 1064 nm radiation in rare gases. Journal of Physics B: Atomic, Molecular and Optical Physics, 21(3):L31–L35, February 1988. Publisher: IOP Publishing.

[8] L. V. Keldysh. Ionization in the field of a strong electromagnetic wave, 1965.

[9] T. Gaumnitz, A. Jain, Y. Pertot, M. Huppert, I. Jordan, F. Ardana-Lamas, and H. J. Wörner. Streaking of 43-attosecond soft-X-ray pulses generated by a passively CEP-stable mid-infrared driver. Optics Express, 25(22):27506–27518, October 2017. Publisher: Optica Publishing Group.

[10] A. Autuori, D. Platzer, M. Lejman, G. Gallician, L. Maëder, A. Covolo, L. Bosse, M. Dalui, D. Bresteau, J.-F. Hergott, O. Tcherbakoff, H. J. B. Marroux, V. Loriot, F. Lépine, L. Poisson, R. Taïeb, J. Caillat, and P. Salières.

Anisotropic dynamics of two-photon ionization: An attosecond movie of photoemission. Science Advances, 8(12):eabl7594, March 2022. Publisher: American Association for the Advancement of Science.

[11] E. Goulielmakis, Z.-H. Loh, A. Wirth, R. Santra, N. Rohringer, V. S. Yakovlev, S. Zherebtsov, T. Pfeifer, A. M. Azzeer, M. F. Kling, S. R. Leone, and F. Krausz. Real-time observation of valence electron motion. Nature, 466(7307):739–743, August 2010. Number: 7307 Publisher: Nature Publishing Group.

[12] Y. Cheng, M. Chini, X. Wang, A. González-Castrillo, A. Palacios, L. Argenti, F. Martín, and Z. Chang. Reconstruction of an excited-state molecular wave packet with attosecond transient absorption spectroscopy. Physical Review A, 94(2):023403, August 2016. Publisher: American Physical Society.

[13] S. Ghimire, A. D. DiChiara, E. Sistrunk, P. Agostini, L. F. DiMauro, and D. A. Reis. Observation of high-order harmonic generation in a bulk crystal. Nature Physics, 7(2):138–141, February 2011.

[14] O. Schubert, M. Hohenleutner, F. Langer, B. Urbanek, C. Lange, U. Huttner, D. Golde, T. Meier, M. Kira, S. W. Koch, and R. Huber. Sub-cycle control of terahertz high-harmonic generation by dynamical Bloch oscillations. Nature Photonics, 8(2):119–123, February 2014.

[15] T. T. Luu, M. Garg, S. Y. Kruchinin, A. Moulet, M. T. Hassan, and E. Goulielmakis. Extreme ultraviolet high-harmonic spectroscopy of solids. Nature, 521(7553):498–502, May 2015.

[16] N. Yoshikawa, T. Tamaya, and K. Tanaka. High-harmonic generation in graphene enhanced by elliptically polarized light excitation. Science, 356(6339):736–738, May 2017.

[17] H. Liu, Y. Li, Y. S. You, S. Ghimire, T. F. Heinz, and D. A. Reis. High-harmonic generation from an atomically thin semiconductor. Nature Physics, 13(3):262–265, March 2017.

[18] G. Vampa, T. Hammond, N. Thiré, B. Schmidt, F. Légaré, C. McDonald, T. Brabec, D. Klug, and P. Corkum. All-Optical Reconstruction of Crystal Band Structure. Physical Review Letters, 115(19):193603, November 2015.

[19] T. Huang, X. Zhu, L. Li, X. Liu, P. Lan, and P. Lu. High-order-harmonic generation of a doped semiconductor. Physical Review A, 96(4):043425, October 2017. Publisher: American Physical Society.

[20] C. Yu, K. K. Hansen, and L. B. Madsen. Enhanced high-order harmonic generation in donor-doped band-gap materials. Physical Review A, 99(1):013435, January 2019.

[21] A. Pattanayak, M. M. S., and G. Dixit. Influence of vacancy defects in solid high-order harmonic generation. Physical Review A, 101(1):013404, January 2020. Publisher: American Physical Society.

[22] M. M. S., A. Pattanayak, M. Ivanov, and G. Dixit. Direct Numerical Observation of Real-Space Recollision in High-Harmonic Generation from Solids. arXiv:1903.02264 [cond-mat, physics:physics], March 2019. arXiv: 1903.02264.

[23] M. Sivis, M. Taucer, G. Vampa, K. Johnston, A. Staudte, A. Y. Naumov, D. M. Villeneuve, C. Ropers, and P. B. Corkum. Tailored semiconductors for high-harmonic optoelectronics. Science, 357(6348):303–306, July 2017. Publisher: American Association for the Advancement of Science.

[24] A. Korobenko, S. Rashid, C. Heide, A. Y. Naumov, D. A. Reis, P. Berini, P. Berini, P. Berini, P. B. Corkum, and G. Vampa. Generation of structured coherent extreme ultraviolet beams from an MgO crystal. Optics Express, 29(15):24161–24168, July 2021. Publisher: Optical Society of America.

[25] D. Gauthier, S. Kaassamani, D. Franz, R. Nicolas, J.-T. Gomes, L. Lavoute, D. Gaponov, S. Février, G. Jargot, M. Hanna, W. Boutu, and H. Merdji. Orbital angular momentum from semiconductor high-order harmonics. Optics Letters, 44(3):546–549, February 2019. Publisher: Optical Society of America.

[26] S. D. Roscam Abbing, R. Kolkowski, Z.-Y. Zhang, F. Campi, L. Lötgering, A. F. Koenderink, and P. M. Kraus. Extreme-Ultraviolet Shaping and Imaging by High-Harmonic Generation from Nanostructured Silica. Physical Review Letters, 128(22):223902, May 2022. Publisher: American Physical Society.

[27] M. Garg, M. Zhan, T. T. Luu, H. Lakhotia, T. Klostermann, A. Guggenmos, and E. Goulielmakis. Multi-petahertz electronic metrology. Nature, 538(7625):359–363, October 2016. Number: 7625 Publisher: Nature Publishing Group.

[28] Z. Nourbakhsh, N. Tancogne-Dejean, H. Merdji, and A. Rubio. High harmonics and isolated attosecond pulses from mgo. Physical Review Applied, 15(1):014013, January 2021. Publisher: American Physical Society.

[29] P. Guyot-Sionnest, W. Chen, and Y. R. Shen. General considerations on optical second-harmonic generation from surfaces and interfaces. Physical Review B, 33(12):8254–8263, June 1986. Publisher: American Physical Society.

[30] P. Guyot-Sionnest and Y. R. Shen. Local and nonlocal surface nonlinearities for surface optical second-harmonic generation. Physical Review B, 35(9):4420–4426, March 1987. Publisher: American Physical Society.

[31] G. Fibich and A. L. Gaeta. Critical power for self-focusing in bulk media and in hollow waveguides. Optics Letters, 25(5):335–337, March 2000. Publisher: Optical Society of America.

[32] M. Nisoli, S. De Silvestri, and O. Svelto. Generation of high energy 10 fs pulses by a new pulse compression technique. Applied Physics Letters, 68(20):2793–2795, May 1996. Publisher: American Institute of Physics.

[33] J. Schulte, T. Sartorius, J. Weitenberg, A. Vernaleken, and P. Russbueldt. Nonlinear pulse compression in a multi-pass cell. Optics Letters, 41(19):4511–4514, October 2016. Publisher: Optica Publishing Group.

[34] F. H. M. Faisal and J. Z. Kamiński. Floquet-Bloch theory of high-harmonic generation in periodic structures. Physical Review A, 56(1):748–762, July 1997. Publisher: American Physical Society.

[35] A. K. Gupta, O. E. Alon, and N. Moiseyev. Generation and control of high-order harmonics by the interaction of an infrared laser with a thin graphite layer. Physical Review B, 68(20):205101, November 2003. Publisher: American Physical Society.

[36] D. Golde, T. Meier, and S. W. Koch. High harmonics generated in semiconductor nanostructures by the coupled dynamics of optical inter- and intraband excitations. Physical Review B, 77(7):075330, February 2008. Publisher: American Physical Society.

[37] J. Li, J. Lu, A. Chew, S. Han, J. Li, Y. Wu, H. Wang, S. Ghimire, and Z. Chang. Attosecond science based on high harmonic generation from gases and solids. Nature Communications, 11(1):2748, June 2020. Number: 1 Publisher: Nature Publishing Group.

[38] M. Lewenstein, P. Balcou, M. Y. Ivanov, A. L'Huillier, and P. B. Corkum. Theory of high-harmonic generation by low-frequency laser fields. Physical Review A, 49(3):2117–2132, March 1994. Publisher: American Physical Society.

[39] P. B. Corkum. Plasma perspective on strong field multiphoton ionization. Physical Review Letters, 71(13):1994–1997, September 1993. Publisher: American Physical Society.

[40] A. L'Huillier, M. Lewenstein, P. Salières, P. Balcou, M. Y. Ivanov, J. Larsson, and C. G. Wahlström. High-order Harmonic-generation cutoff. Physical Review A, 48(5):R3433–R3436, November 1993. Publisher: American Physical Society.

[41] M. B. Gaarde, J. L. Tate, and K. J. Schafer. Macroscopic aspects of attosecond pulse generation. Journal of Physics B: Atomic, Molecular and Optical Physics, 41(13):132001, June 2008. Publisher: IOP Publishing.

[42] A. D. Shiner, C. Trallero-Herrero, N. Kajumba, H.-C. Bandulet, D. Comtois, F. Légaré, M. Giguère, J.-C. Kieffer, P. B. Corkum, and D. M. Villeneuve. Wavelength Scaling of High Harmonic Generation Efficiency. Physical Review Letters, 103(7):073902, August 2009. Publisher: American Physical Society.

[43] K. Schiessl, K. L. Ishikawa, E. Persson, and J. Burgdörfer. Quantum Path Interference in the Wavelength Dependence of High-Harmonic Generation. Physical Review Letters, 99(25):253903, December 2007. Publisher: American Physical Society.

[44] W. Boutu, M. Ducousso, J.-F. Hergott, and H. Merdji. Overview on HHG High-Flux Sources. In F. Canova and L. Poletto, editors, Optical Technologies for Extreme-Ultraviolet and Soft X-ray Coherent Sources, Springer Series in Optical Sciences, pages 63–78. Springer, Berlin, Heidelberg, 2015.

[45] R. Borrego-Varillas, M. Lucchini, and M. Nisoli. Attosecond spectroscopy for the investigation of ultrafast dynamics in atomic, molecular and solid-state physics. Reports on Progress in Physics, 85(6):066401, May 2022. Publisher: IOP Publishing.

[46] S. Y. Kruchinin, F. Krausz, and V. S. Yakovlev. Colloquium : Strong-field phenomena in periodic systems. Reviews of Modern Physics, 90(2):021002, April 2018.

[47] P. G. Hawkins, M. Y. Ivanov, and V. S. Yakovlev. Effect of multiple conduction bands on high-harmonic emission from dielectrics. Physical Review A, 91(1):013405, January 2015. Publisher: American Physical Society.

[48] M. Wu, D. A. Browne, K. J. Schafer, and M. B. Gaarde. Multilevel perspective on high-order harmonic generation in solids. Physical Review A, 94(6):063403, December 2016. Publisher: American Physical Society.

[49] G. Vampa. Role of Electron-Hole Recollisions in High Harmonic Generation from Bulk Crystals. Thesis, Université d'Ottawa / University of Ottawa, 2016.

[50] G. Vampa, C. McDonald, G. Orlando, D. Klug, P. Corkum, and T. Brabec. Theoretical Analysis of High-Harmonic Generation in Solids. Physical Review Letters, 113(7):073901, August 2014.

[51] G. Vampa, C. R. McDonald, G. Orlando, P. B. Corkum, and T. Brabec. Semiclassical analysis of high harmonic generation in bulk crystals. Physical Review B, 91(6):064302, February 2015. Publisher: American Physical Society.

[52] N. Tancogne-Dejean, O. D. Mücke, F. X. Kärtner, and A. Rubio. Ellipticity dependence of high-harmonic generation in solids originating from coupled intraband and interband dynamics. Nature Communications, 8(1):1–10, September 2017.

[53] T. Otobe. First-principle description for the high-harmonic generation in a diamond by intense short laser pulse. Journal of Applied Physics, 111(9):093112, May 2012. Publisher: American Institute of Physics.

[54] D. Bauer and K. K. Hansen. High-Harmonic Generation in Solids with and without Topological Edge States. Physical Review Letters, 120(17):177401, April 2018. Publisher: American Physical Society.

[55] I. Floss, C. Lemell, G. Wachter, V. Smejkal, S. A. Sato, X.-M. Tong, K. Yabana, and J. Burgdörfer. Ab initio multiscale simulation of high-order harmonic generation in solids. Physical Review A, 97(1):011401, January 2018. Publisher: American Physical Society.

[56] N. Klemke, N. Tancogne-Dejean, G. M. Rossi, Y. Yang, F. Scheiba, R. E. Mainz, G. D. Sciacca, A. Rubio, F. X. Kärtner, and O. D. Mücke. Polarization-state-resolved high-harmonic spectroscopy of solids. Nature Communications, 10(1):1319, March 2019.

[57] P. Xia, C. Kim, F. Lu, T. Kanai, H. Akiyama, J. Itatani, and N. Ishii. Nonlinear propagation effects in high harmonic generation in reflection and transmission from gallium arsenide. Optics Express, 26(22):29393–29400, October 2018. Publisher: Optica Publishing Group.

[58] S. Kaassamani. Polarization Spectroscopy of High Order Harmonic Generation in Semiconductors. PhD thesis, Université Paris Sud - Paris XI, Paris, December 2020.

[59] Y. S. You, D. A. Reis, and S. Ghimire. Anisotropic high-harmonic generation in bulk crystals. Nature Physics, 13(4):345–349, April 2017.

[60] H. Kim, S. Han, Y. W. Kim, S. Kim, and S.-W. Kim. Generation of Coherent Extreme-Ultraviolet Radiation from Bulk Sapphire Crystal. ACS Photonics, 4(7):1627–1632, July 2017. Publisher: American Chemical Society.

[61] G. Ndabashimiye, S. Ghimire, M. Wu, D. A. Browne, K. J. Schafer, M. B. Gaarde, and D. A. Reis. Solid-state harmonics beyond the atomic limit. Nature, 534(7608):520–523, June 2016.

[62] M. Taucer, T. J. Hammond, P. B. Corkum, G. Vampa, C. Couture, N. Thiré, B. E. Schmidt, F. Légaré, H. Selvi, N. Unsuree, B. Hamilton, T. J. Echtermeyer, and M. A. Denecke. Nonperturbative harmonic generation in graphene from intense midinfrared pulsed light. Physical Review B, 96(19):195420, November 2017. Publisher: American Physical Society.

[63] Z.-Y. Chen and R. Qin. High harmonic generation in graphene–boron nitride heterostructures. Journal of Materials Chemistry C, 8(35):12085–12091, September 2020. Publisher: The Royal Society of Chemistry.

[64] G. Le Breton, A. Rubio, and N. Tancogne-Dejean. High-harmonic generation from few-layer hexagonal boron nitride: Evolution from monolayer to bulk response. Physical Review B, 98(16):165308, October 2018. Publisher: American Physical Society.

[65] H. Nishidome, K. Nagai, K. Uchida, Y. Ichinose, Y. Yomogida, Y. Miyata, K. Tanaka, and K. Yanagi. Control of High-Harmonic Generation by Tuning the Electronic Structure and Carrier Injection. Nano Letters, 20(8):6215–6221, August 2020. Publisher: American Chemical Society.

[66] E. A. Gibson, A. Paul, N. Wagner, R. Tobey, S. Backus, I. P. Christov, M. M. Murnane, and H. C. Kapteyn. High-Order Harmonic Generation up to 250 eV from Highly Ionized Argon. Physical Review Letters, 92(3):033001, January 2004. Publisher: American Physical Society.

[67] Y.-L. Liu, J. Wang, J. Wang, J. Wang, H.-h. Chu, and H.-h. Chu. Ion-based high-order harmonic generation from water window to keV region with a transverse disruptive pulse for quasi-phase-matching. Optics Express, 30(2):1365–1380, January 2022. Publisher: Optica Publishing Group.

[68] M. Wu, S. Ghimire, D. A. Reis, K. J. Schafer, and M. B. Gaarde. High-harmonic generation from Bloch electrons in solids. Physical Review A, 91(4):043839, April 2015.

[69] X. Liu, X. Zhu, X. Zhang, D. Wang, P. Lan, and P. Lu. Wavelength scaling of the cutoff energy in the solid high harmonic generation. Optics Express, 25(23):29216–29224, November 2017. Publisher: Optical Society of America.

[70] Z. Guan, X.-X. Zhou, and X.-B. Bian. High-order-harmonic generation from periodic potentials driven by few-cycle laser pulses. Physical Review A, 93(3):033852, March 2016. Publisher: American Physical Society.

[71] N. Tancogne-Dejean, O. D. Mücke, F. X. Kärtner, and A. Rubio. Impact of the Electronic Band Structure in High-Harmonic Generation Spectra of Solids. Physical Review Letters, 118(8):087403, February 2017.

[72] O. D. Mücke. Isolated high-order harmonics pulse from two-color-driven Bloch oscillations in bulk semiconductors. Physical Review B, 84(8):081202, August 2011. Publisher: American Physical Society.

[73] Z. Wang, H. Park, Y. H. Lai, J. Xu, C. I. Blaga, F. Yang, P. Agostini, and L. F. DiMauro. The roles of photo-carrier doping and driving wavelength in high harmonic generation from a semiconductor. Nature Communications, 8(1):1686, November 2017.

[74] A. J. Uzan, G. Orenstein, A. Jiménez-Galán, C. McDonald, R. E. F. Silva, B. D. Bruner, N. D. Klimkin, V. Blanchet, T. Arusi-Parpar, M. Krüger, A. N. Rubtsov, O. Smirnova, M. Ivanov, B. Yan, T. Brabec, and N. Dudovich. Attosecond spectral singularities in solid-state high-harmonic generation. Nature Photonics, pages 1–5, January 2020.

[75] N. Klemke. High harmonic generation from solids with elliptically polarized laser pulses. PhD thesis, Universität Hamburg, Hamburg, December 2020.

[76] N. Saito, P. Xia, F. Lu, T. Kanai, J. Itatani, and N. Ishii. Observation of selection rules for circularly polarized fields in high-harmonic generation from a crystalline solid. Optica, 4(11):1333–1336, November 2017.

[77] Y. S. You, M. Wu, Y. Yin, A. Chew, X. Ren, S. Gholam-Mirzaei, D. A. Browne, M. Chini, Z. Chang, K. J. Schafer, M. B. Gaarde, and S. Ghimire.

Laser waveform control of extreme ultraviolet high harmonics from solids. Optics Letters, 42(9):1816–1819, May 2017.

[78] G. Vampa, T. J. Hammond, N. Thiré, B. E. Schmidt, F. Légaré, C. R. McDonald, T. Brabec, and P. B. Corkum. Linking high harmonics from gases and solids. Nature, 522(7557):462–464, June 2015.

[79] D. H. Ko, G. G. Brown, C. Zhang, and P. B. Corkum. Delay measurement of attosecond emission in solids. 53(12):124001, May 2020. Publisher: IOP Publishing.

[80] M. Garg, H. Y. Kim, and E. Goulielmakis. Ultimate waveform reproducibility of extreme-ultraviolet pulses by high-harmonic generation in quartz. Nature Photonics, 12(5):291, May 2018.

[81] J. Lu, E. F. Cunningham, Y. S. You, D. A. Reis, and S. Ghimire. Interferometry of dipole phase in high harmonics from solids. Nature Photonics, 13(2):96, February 2019.

[82] G. Vampa, S. Vasilyev, H. Liu, M. Mirov, P. H. Bucksbaum, and D. A. Reis. Characterization of high-harmonic emission from ZnO up to 11 eV pumped with a Cr:ZnS high-repetition-rate source. Optics Letters, 44(2):259–262, January 2019.

[83] D. Franz, R. Nicolas, W. Boutu, L. Shi, Q. Ripault, M. Kholodtsova, B. Iwan, U. E. Etxano, M. Kovacev, J. Biegert, and H. Merdji. Amplification of high harmonics in 3D semiconductor waveguides, 2017.

[84] S. Han, H. Kim, Y. W. Kim, Y.-J. Kim, S. Kim, I.-Y. Park, and S.-W. Kim. High-harmonic generation by field enhanced femtosecond pulses in metal-sapphire nanostructure. Nature Communications, 7(1):13105, October 2016.

[85] G. Vampa, B. G. Ghamsari, S. Siadat Mousavi, T. J. Hammond, A. Olivieri, E. Lisicka-Skrek, A. Y. Naumov, D. M. Villeneuve, A. Staudte, P. Berini, and P. B. Corkum. Plasmon-enhanced high-harmonic generation from silicon. Nature Physics, 13(7):659–662, July 2017.

[86] D. Franz, Kaassamani, D. Gauthier, R. Nicolas, M. Kholodtsova, L. Douillard, J.-T. Gomes, L. Lavoute, D. Gaponov, N. Ducros, S. Février, J. Biegert, L. Shi, M. Kovacev, W. Boutu, and H. Merdji. All semiconductor enhanced high-harmonic generation from a single nanostructured cone. Scientific Reports, 9(1):5663, April 2019. Number: 1 Publisher: Nature Publishing Group.

[87] G. Vampa, Y. S. You, H. Liu, S. Ghimire, and D. A. Reis. Observation of backward high-harmonic emission from solids. Optics Express, 26(9):12210–12218, April 2018.

[88] V. E. Nefedova, S. Fröhlich, F. Navarrete, N. Tancogne-Dejean, D. Franz, A. Hamdou, S. Kaassamani, D. Gauthier, R. Nicolas, G. Jargot, M. Hanna,

P. Georges, M. F. Ciappina, U. Thumm, W. Boutu, and H. Merdji. Enhanced extreme ultraviolet high-harmonic generation from chromium-doped magnesium oxide. Applied Physics Letters, 118(20):201103, May 2021. Publisher: American Institute of Physics.

[89] P. K. Giri. Photoluminescence signature of silicon interstitial cluster evolution from compact to extended structures in ion-implanted silicon. Semiconductor Science and Technology, 20(6):638–644, May 2005. Publisher: IOP Publishing.

[90] S. Lee and G. S. Hwang. Growth and shape transition of small silicon self-interstitial clusters. Physical Review B, 78(4):045204, July 2008. Publisher: American Physical Society.

[91] A. Sieck. Structure and physical properties of silicon clusters and of vacancy clusters in bulk silicon, Jul 2000.

[92] T. Staab, A. Sieck, M. Haugk, M. Puska, T. Frauenheim, and H. Leipner. Stability of large vacancy clusters in silicon. Physical Review B, 65(11):115210, March 2002. Publisher: American Physical Society.

[93] C. Freysoldt, B. Grabowski, T. Hickel, J. Neugebauer, G. Kresse, A. Janotti, and C. G. Van de Walle. First-principles calculations for point defects in solids. Reviews of Modern Physics, 86(1):253–305, March 2014. Publisher: American Physical Society.

[94] X.-F. Pan, T. Han, C.-L. Xia, T.-T. Xu, J. Zhang, and X.-S. Liu. Energy band splitting and high-order harmonic generation from a doped semiconductor. 16(11):115301, October 2019. Publisher: IOP Publishing.

[95] F. Navarrete, M. F. Ciappina, and U. Thumm. Crystal-momentum-resolved contributions to high-order harmonic generation in solids. Physical Review A, 100(3):033405, September 2019. Publisher: American Physical Society.

[96] F. Navarrete and U. Thumm. Two-color-driven enhanced high-order harmonic generation in solids. Physical Review A, 102(6):063123, December 2020. Publisher: American Physical Society.

[97] S. Almalki, A. Parks, G. Bart, P. B. Corkum, T. Brabec, and C. R. McDonald. High harmonic generation tomography of impurities in solids: conceptual analysis. Physical Review B, 98(14):144307, October 2018. arXiv: 1805.03806.

[98] V.-H. Hoang and A.-T. Le. Factorization of high-order-harmonic-generation yields in impurity-doped materials. Physical Review A, 102(2):023112, August 2020. Publisher: American Physical Society.

[99] G. Jargot, N. Daher, L. Lavenu, X. Delen, N. Forget, M. Hanna, and P. Georges. Self-compression in a multipass cell. Optics Letters, 43(22):5643–5646, November 2018.

[100] D. M. Roessler and W. C. Walker. Electronic Spectrum and Ultraviolet Optical Properties of Crystalline MgO. Physical Review, 159(3):733–738, July 1967. Publisher: American Physical Society.

[101] M. O. Henry, J. P. Larkin, and G. F. Imbusch. Nature of the broadband luminescence center in MgO:Cr^{3+}. Physical Review B, 13(5):1893–1902, March 1976. Publisher: American Physical Society.

[102] E. Shablonin, A. I. Popov, A. Lushchik, A. Kotlov, and S. Dolgov. Excitation of different chromium centres by synchrotron radiation in MgO:Cr single crystals. Physica B: Condensed Matter, 477:133–136, November 2015.

[103] P. J. Burnett and G. A. D. Briggs. The elastic properties of ion-implanted silicon. Journal of Materials Science, 21(5):1828–1836, May 1986.

[104] A. Boyrivent, E. Duval, and R. Louat. Broad band luminescence in MgO:Cr3+. Solid State Communications, 19(12):1221–1224, September 1976.

[105] C. C. Chao. Charge-transfer luminescence of Cr3+ in magnesium oxide. Journal of Physics and Chemistry of Solids, 32(11):2517–2528, January 1971.

[106] T. Kato, G. Okada, and T. Yanagida. Optical, scintillation and dosimeter properties of MgO transparent ceramic and single crystal. Ceramics International, 42(5):5617–5622, April 2016.

[107] C. A. F. Vaz, C. Moutafis, M. Buzzi, and J. Raabe. X-ray excited optical luminescence of metal oxide single crystals. Journal of Electron Spectroscopy and Related Phenomena, 189:1–4, August 2013.

[108] Y. Guo, S. Lu, L. Su, C. Zhao, H. Zhang, and S. Wen. Z-scan measurement of the nonlinear refractive index of Nd^{3+}, Y^{3+}-codoped CaF_2 and SrF_2 crystals. Applied Optics, 54(4):953–958, February 2015. Publisher: Optica Publishing Group.

[109] C. Heide, C. Heide, Y. Kobayashi, Y. Kobayashi, A. C. Johnson, F. Liu, F. Liu, T. F. Heinz, T. F. Heinz, D. A. Reis, D. A. Reis, and S. Ghimire. Probing electron-hole coherence in strongly driven 2D materials using high-harmonic generation. Optica, 9(5):512–516, May 2022. Publisher: Optica Publishing Group.

[110] L. Bischoff, W. Pilz, and B. Schmidt. Amorphous solid foam structures on germanium by heavy ion irradiation. Applied Physics A, 104(4):1153–1158, September 2011.

[111] H. Gnaser, A. Brodyanski, and B. Reuscher. Focused ion beam implantation of Ga in Si and Ge: fluence-dependent retention and surface morphology. Surface and Interface Analysis, 40(11):1415–1422, 2008. _eprint: https://analyticalsciencejournals.onlinelibrary.wiley.com/doi/pdf/10.1002/sia.2915.

[112] M. Rommel, G. Spoldi, V. Yanev, S. Beuer, B. Amon, J. Jambreck, S. Petersen, A. J. Bauer, and L. Frey. Comprehensive study of focused ion beam induced lateral damage in silicon by scanning probe microscopy techniques. Journal of Vacuum Science & Technology B, 28(3):595–607, May 2010. Publisher: American Vacuum Society.

[113] F. Stumpf, A. A. Abu Quba, P. Singer, M. Rumler, N. Cherkashin, S. Schamm-Chardon, R. Cours, and M. Rommel. Detailed characterisation of focused ion beam induced lateral damage on silicon carbide samples by electrical scanning probe microscopy and transmission electron microscopy. Journal of Applied Physics, 123(12):125104, March 2018. Publisher: American Institute of Physics.

[114] J. F. Ziegler. SRIM-2003. Nuclear Instruments and Methods in Physics Research B, 219:1027–1036, June 2004.

[115] Y. Abdulraheem, I. Gordon, T. Bearda, H. Meddeb, and J. Poortmans. Optical bandgap of ultra-thin amorphous silicon films deposited on crystalline silicon by PECVD. AIP Advances, 4(5):057122, May 2014. Publisher: American Institute of Physics.

[116] J. Steffens, J. Rinder, G. Hahn, and B. Terheiden. Correlation between the optical bandgap and the monohydride bond density of hydrogenated amorphous silicon. Journal of Non-Crystalline Solids: X, 5:100044, March 2020.

[117] C. Schinke, P. Christian Peest, J. Schmidt, R. Brendel, K. Bothe, M. R. Vogt, I. Kröger, S. Winter, A. Schirmacher, S. Lim, H. T. Nguyen, and D. MacDonald. Uncertainty analysis for the coefficient of band-to-band absorption of crystalline silicon. AIP Advances, 5(6):067168, June 2015. Publisher: American Institute of Physics.

[118] G. Orlando, C.-M. Wang, T.-S. Ho, and S.-I. Chu. High-order harmonic generation in disordered semiconductors. JOSA B, 35(4):680–688, April 2018. Publisher: Optical Society of America.

[119] Y. S. You, Y. Yin, Y. Wu, A. Chew, X. Ren, F. Zhuang, S. Gholam-Mirzaei, M. Chini, Z. Chang, and S. Ghimire. High-harmonic generation in amorphous solids. Nature Communications, 8(1):724, September 2017.

[120] M. S. Mrudul, N. Tancogne-Dejean, A. Rubio, and G. Dixit. High-harmonic generation from spin-polarised defects in solids. npj Computational Materials, 6(1):1–9, January 2020.

[121] D. T. Pierce and W. E. Spicer. Electronic Structure of Amorphous Si from Photoemission and Optical Studies. Physical Review B, 5(8):3017–3029, April 1972. Publisher: American Physical Society.

[122] J. R. Fienup. Reconstruction of an object from the modulus of its Fourier transform. Optics Letters, 3(1):27–29, July 1978. Publisher: Optical Society of America.

[123] J. Miao, P. Charalambous, J. Kirz, and D. Sayre. Extending the methodology of X-ray crystallography to allow imaging of micrometre-sized non-crystalline specimens. Nature, 400(6742):342–344, July 1999.

[124] F. Pfeiffer. X-ray ptychography. Nature Photonics, 12(1):9–17, January 2018.

[125] M. Odstrcil. Coherent Diffractive Imaging Using Table-Top Sources. PhD thesis, RWTH Aachen, Aachen, February 2017.

[126] W. Demtröder. Interferenz, Beugung und Streuung. In W. Demtröder, editor, Experimentalphysik 2: Elektrizität und Optik, Springer-Lehrbuch, pages 299–345. Springer, Berlin, Heidelberg, 2013.

[127] J. W. Goodman. Introduction to fourier optics, roberts & co. Publishers, Englewood, Colorado, 2005.

[128] J. D. Jackson. Classical electrodynamics. American Institute of Physics, 15(11):62–62, 2009.

[129] D. Paganin and others. Coherent X-ray optics. Number 6. Oxford University Press on Demand, 2006.

[130] J. M. Rodenburg and R. H. T. Bates. The theory of super-resolution electron microscopy via Wigner-distribution deconvolution. Philosophical Transactions of the Royal Society of London. Series A: Physical and Engineering Sciences, 339(1655):521–553, June 1992. Publisher: Royal Society.

[131] E. H. R. Tsai, I. Usov, A. Diaz, A. Menzel, and M. Guizar-Sicairos. X-ray ptychography with extended depth of field. Optics Express, 24(25):29089–29108, December 2016. Publisher: Optical Society of America.

[132] P. Thibault, M. Dierolf, A. Menzel, O. Bunk, C. David, and F. Pfeiffer. High-Resolution Scanning X-ray Diffraction Microscopy. Science, 321(5887):379–382, July 2008. Publisher: American Association for the Advancement of Science.

[133] H. N. Chapman, A. Barty, S. Marchesini, A. Noy, S. P. Hau-Riege, C. Cui, M. R. Howells, R. Rosen, H. He, J. C. H. Spence, U. Weierstall, T. Beetz, C. Jacobsen, and D. Shapiro. High-resolution ab initio three-dimensional x-ray diffraction microscopy. JOSA A, 23(5):1179–1200, May 2006. Publisher: Optical Society of America.

[134] J. Nelson, X. Huang, J. Steinbrener, D. Shapiro, J. Kirz, S. Marchesini, A. M. Neiman, J. J. Turner, and C. Jacobsen. High-resolution x-ray diffraction microscopy of specifically labeled yeast cells. Proceedings of the National Academy of Sciences, 107(16):7235–7239, April 2010. ISBN: 9780910874106 Publisher: National Academy of Sciences Section: Physical Sciences.

[135] B. Abbey, G. J. Williams, M. A. Pfeifer, J. N. Clark, C. T. Putkunz, A. Torrance, I. McNulty, T. M. Levin, A. G. Peele, and K. A. Nugent. Quantitative coherent diffractive imaging of an integrated circuit at a spatial resolution of 20 nm. Applied Physics Letters, 93(21):214101, November 2008. Publisher: American Institute of Physics.

[136] R. W. Gerchberg. A practical algorithm for the determination of phase from image and diffraction plane pictures. Optik, 35:237–246, 1972.

[137] V. Elser. Phase retrieval by iterated projections. JOSA A, 20(1):40–55, January 2003. Publisher: Optical Society of America.

[138] A.-L. Robisch. Phase retrieval for object and probe in the optical near-field. 2016. Accepted: 2016-02-19T10:48:14Z Artwork Medium: Print ISBN: 9783863952525 Interview Medium: Print.

[139] F. Deutsch. Best Approximation in Inner Product Spaces. CMS Books in Mathematics / Ouvrages de mathématiques de la SMC. Springer, New York, NY, 2001.

[140] C. L. Byrne. Applied Iterative Methods. page 396.

[141] V. Elser, I. Rankenburg, and P. Thibault. Searching with iterated maps. Proceedings of the National Academy of Sciences, 104(2):418–423, January 2007. Publisher: National Academy of Sciences Section: Physical Sciences.

[142] H. H. Bauschke, P. L. Combettes, and D. R. Luke. Phase retrieval, error reduction algorithm, and Fienup variants: a view from convex optimization. JOSA A, 19(7):1334–1345, July 2002. Publisher: Optical Society of America.

[143] V. Favre-Nicolin, G. Girard, S. Leake, J. Carnis, Y. Chushkin, J. Kieffer, P. Paleo, and M.-I. Richard. Pynx: high-performance computing toolkit for coherent x-ray imaging based on operators. Journal of Applied Crystallography, 53(5):1404–1413, October 2020. Number: 5 Publisher: International Union of Crystallography.

[144] M. Guizar-Sicairos and J. R. Fienup. Phase retrieval with transverse translation diversity: a nonlinear optimization approach. Optics Express, 16(10):7264–7278, May 2008. Publisher: Optica Publishing Group.

[145] J. M. Rodenburg and H. M. L. Faulkner. A phase retrieval algorithm for shifting illumination. Applied Physics Letters, 85(20):4795–4797, November 2004. Publisher: American Institute of Physics.

[146] J. M. Rodenburg, A. C. Hurst, A. G. Cullis, B. R. Dobson, F. Pfeiffer, O. Bunk, C. David, K. Jefimovs, and I. Johnson. Hard-X-Ray Lensless Imaging of Extended Objects. Physical Review Letters, 98(3):034801, January 2007. Publisher: American Physical Society.

[147] A. M. Maiden and J. M. Rodenburg. An improved ptychographical phase retrieval algorithm for diffractive imaging. Ultramicroscopy, 109(10):1256–1262, September 2009.

[148] A. Shenfield and J. M. Rodenburg. Evolutionary determination of experimental parameters for ptychographical imaging. Journal of Applied Physics, 109(12):124510, June 2011. Publisher: American Institute of Physics.

[149] Y. Takahashi, A. Suzuki, N. Zettsu, Y. Kohmura, Y. Senba, H. Ohashi, K. Yamauchi, and T. Ishikawa. Towards high-resolution ptychographic x-ray diffraction microscopy. Physical Review B, 83(21):214109, June 2011. Publisher: American Physical Society.

[150] A. M. Maiden, M. J. Humphry, M. C. Sarahan, B. Kraus, and J. M. Rodenburg. An annealing algorithm to correct positioning errors in ptychography. Ultramicroscopy, 120:64–72, September 2012.

[151] A. M. Maiden, J. M. Rodenburg, and M. J. Humphry. Optical ptychography: a practical implementation with useful resolution. Optics Letters, 35(15):2585–2587, August 2010. Publisher: Optica Publishing Group.

[152] C. T. Putkunz, A. J. D'Alfonso, A. J. Morgan, M. Weyland, C. Dwyer, L. Bourgeois, J. Etheridge, A. Roberts, R. E. Scholten, K. A. Nugent, and L. J. Allen. Atom-Scale Ptychographic Electron Diffractive Imaging of Boron Nitride Cones. Physical Review Letters, 108(7):073901, February 2012. Publisher: American Physical Society.

[153] S. Gao, P. Wang, F. Zhang, G. T. Martinez, P. D. Nellist, X. Pan, and A. I. Kirkland. Electron ptychographic microscopy for three-dimensional imaging. Nature Communications, 8(1):163, July 2017. Number: 1 Publisher: Nature Publishing Group.

[154] E. Abbe. Beiträge zur Theorie des Mikroskops und der mikroskopischen Wahrnehmung | SpringerLink. Archiv für Mikroskopische Anatomie, 9:413–468, 1873.

[155] J. C. H. Spence, U. Weierstall, and M. Howells. Coherence and sampling requirements for diffractive imaging. Ultramicroscopy, 101(2):149–152, November 2004.

[156] T. Latychevskaia. Iterative phase retrieval in coherent diffractive imaging: practical issues. Applied Optics, 57(25):7187–7197, September 2018. Publisher: Optica Publishing Group.

[157] S. Gholam-Mirzaei, J. Beetar, and M. Chini. High harmonic generation in ZnO with a high-power mid-IR OPA. Applied Physics Letters, 110(6):061101, February 2017. Publisher: American Institute of Physics.

[158] L. Y. Lim, S. Lany, Y. J. Chang, E. Rotenberg, A. Zunger, and M. F. Toney. Angle-resolved photoemission and quasiparticle calculation of ZnO: The need

for d band shift in oxide semiconductors. Physical Review B, 86(23):235113, December 2012. Publisher: American Physical Society.

[159] O. Wilhelmi, S. Reyntjens, C. Mitterbauer, L. Roussel, D. J. Stokes, and D. H. W. Hubert. Rapid Prototyping of Nanostructured Materials with a Focused Ion Beam. Japanese Journal of Applied Physics, 47(6S):5010, June 2008. Publisher: IOP Publishing.

[160] S. O. Kucheyev, J. S. Williams, C. Jagadish, J. Zou, C. Evans, A. J. Nelson, and A. V. Hamza. Ion-beam-produced structural defects in ZnO. Physical Review B, 67(9):094115, March 2003. Publisher: American Physical Society.

[161] K. Imasaka, T. Kaji, T. Shimura, and S. Ashihara. Antenna-enhanced high harmonic generation in a wide-bandgap semiconductor ZnO. Optics Express, 26(16):21364–21374, August 2018. Publisher: Optica Publishing Group.

[162] NOVAE Brevity. `https://www.novae-laser.com/brevity/`.

[163] S. Fröhlich, X. Liu, A. Hamdou, A. Meunier, M. Hussain, M. Carole, S. Kaassamani, M. Froidevaux, L. Lavoute, D. Gaponov, N. Ducros, S. Février, S. Février, P. Zeitoun, M. Kovacev, M. Fajardo, W. Boutu, D. Gauthier, and H. Merdji. Self-probed ptychography from semiconductor high-harmonic generation. Optics Letters, 47(19):4865–4868, 2022.

[164] M. Guizar-Sicairos, S. T. Thurman, and J. R. Fienup. Efficient subpixel image registration algorithms. Optics Letters, 33(2):156–158, January 2008. Publisher: Optical Society of America.

[165] S. Zayko, E. Mönnich, M. Sivis, D.-D. Mai, T. Salditt, S. Schäfer, and C. Ropers. Coherent diffractive imaging beyond the projection approximation: waveguiding at extreme ultraviolet wavelengths. Optics Express, 23(15):19911–19921, July 2015. Publisher: Optical Society of America.

[166] J. Vila-Comamala, A. Sakdinawat, and M. Guizar-Sicairos. Characterization of x-ray phase vortices by ptychographic coherent diffractive imaging. Optics Letters, 39(18):5281–5284, September 2014. Publisher: Optical Society of America.

[167] J. Huijts, S. Fernandez, D. Gauthier, M. Kholodtsova, A. Maghraoui, K. Medjoubi, A. Somogyi, W. Boutu, and H. Merdji. Broadband coherent diffractive imaging. Nature Photonics, 14(10):618–622, October 2020. Number: 10 Publisher: Nature Publishing Group.

[168] B. Zhang, D. F. Gardner, M. H. Seaberg, E. R. Shanblatt, C. L. Porter, R. Karl, C. A. Mancuso, H. C. Kapteyn, M. M. Murnane, and D. E. Adams. Ptychographic hyperspectral spectromicroscopy with an extreme ultraviolet high harmonic comb. Optics Express, 24(16):18745–18754, August 2016. Publisher: Optica Publishing Group.

[169] A. Rana, J. Zhang, M. Pham, A. Yuan, Y. Lo, H. Jiang, S. J. Osher, and J. Miao. Potential of Attosecond Coherent Diffractive Imaging. Physical Review Letters, 125(8):086101, August 2020. Publisher: American Physical Society.

[170] A. Chew, N. Douguet, C. Cariker, J. Li, E. Lindroth, X. Ren, Y. Yin, L. Argenti, W. T. Hill, and Z. Chang. Attosecond transient absorption spectrum of argon at the $L_{2,3}$ edge. Physical Review A, 97(3):031407, March 2018. Publisher: American Physical Society.

[171] A. L. Cavalieri, N. Müller, T. Uphues, V. S. Yakovlev, A. Baltuška, B. Horvath, B. Schmidt, L. Blümel, R. Holzwarth, S. Hendel, M. Drescher, U. Kleineberg, P. M. Echenique, R. Kienberger, F. Krausz, and U. Heinzmann. Attosecond spectroscopy in condensed matter. Nature, 449(7165):1029–1032, October 2007. Number: 7165 Publisher: Nature Publishing Group.

[172] S. M. Teichmann, F. Silva, S. L. Cousin, M. Hemmer, and J. Biegert. 0.5-keV Soft X-ray attosecond continua. Nature Communications, 7(1):11493, May 2016. Number: 1 Publisher: Nature Publishing Group.

[173] N. Ishii, K. Kaneshima, K. Kitano, T. Kanai, S. Watanabe, and J. Itatani. Carrier-envelope phase-dependent high harmonic generation in the water window using few-cycle infrared pulses. Nature Communications, 5(1):3331, February 2014. Number: 1 Publisher: Nature Publishing Group.

[174] O. Tcherbakoff, E. Mével, D. Descamps, J. Plumridge, and E. Constant. Time-gated high-order harmonic generation. Physical Review A, 68(4):043804, October 2003. Publisher: American Physical Society.

[175] I. J. Sola, E. Mével, L. Elouga, E. Constant, V. Strelkov, L. Poletto, P. Villoresi, E. Benedetti, J.-P. Caumes, S. Stagira, C. Vozzi, G. Sansone, and M. Nisoli. Controlling attosecond electron dynamics by phase-stabilized polarization gating. Nature Physics, 2(5):319–322, May 2006. Number: 5 Publisher: Nature Publishing Group.

[176] J. Li, X. Ren, Y. Yin, K. Zhao, A. Chew, Y. Cheng, E. Cunningham, Y. Wang, S. Hu, Y. Wu, M. Chini, and Z. Chang. 53-attosecond X-ray pulses reach the carbon K-edge. Nature Communications, 8(1):186, August 2017. Number: 1 Publisher: Nature Publishing Group.

[177] A. Oriana, J. Réhault, F. Preda, D. Polli, and G. Cerullo. Scanning Fourier transform spectrometer in the visible range based on birefringent wedges. JOSA A, 33(7):1415–1420, July 2016. Publisher: Optica Publishing Group.

[178] C. Vozzi, M. Nisoli, G. Sansone, S. Stagira, and S. De Silvestri. Optimal spectral broadening in hollow-fiber compressor systems. Applied Physics B, 80(3):285–289, March 2005.

[179] T. Nagy, M. Forster, and P. Simon. Flexible hollow fiber for pulse compressors. Applied Optics, 47(18):3264–3268, June 2008. Publisher: Optica Publishing Group.

[180] K. Fritsch, M. Poetzlberger, V. Pervak, J. Brons, and O. Pronin. All-solid-state multipass spectral broadening to sub-20 fs. Optics Letters, 43(19):4643–4646, October 2018. Publisher: Optica Publishing Group.

[181] L. Lavenu, M. Natile, F. Guichard, Y. Zaouter, X. Delen, M. Hanna, E. Mottay, and P. Georges. Nonlinear pulse compression based on a gas-filled multipass cell. Optics Letters, 43(10):2252–2255, May 2018. Publisher: Optica Publishing Group.

[182] M. Hanna, X. Délen, L. Lavenu, F. Guichard, Y. Zaouter, F. Druon, and P. Georges. Nonlinear temporal compression in multipass cells: theory. J. Opt. Soc. Am. B, 34(7):1340–1347, July 2017.

[183] A.-L. Viotti, A.-L. Viotti, M. Seidel, E. Escoto, S. Rajhans, W. P. Leemans, I. Hartl, C. M. Heyl, C. M. Heyl, and C. M. Heyl. Multi-pass cells for post-compression of ultrashort laser pulses. Optica, 9(2):197–216, February 2022. Publisher: Optica Publishing Group.

[184] M. Hemmer, M. Baudisch, A. Thai, A. Couairon, and J. Biegert. Self-compression to sub-3-cycle duration of mid-infrared optical pulses in dielectrics. Optics Express, 21(23):28095–28102, November 2013. Publisher: Optica Publishing Group.

[185] M. Seidel, G. Arisholm, J. Brons, V. Pervak, and O. Pronin. All solid-state spectral broadening: an average and peak power scalable method for compression of ultrashort pulses. Optics Express, 24(9):9412–9428, May 2016. Publisher: Optica Publishing Group.

[186] V. Shumakova, P. Malevich, S. Ališauskas, A. Voronin, A. M. Zheltikov, D. Faccio, D. Kartashov, A. Baltuška, and A. Pugžlys. Multi-millijoule few-cycle mid-infrared pulses through nonlinear self-compression in bulk. Nature Communications, 7(1):12877, September 2016. Number: 1 Publisher: Nature Publishing Group.

[187] M. Hanna, N. Daher, F. Guichard, X. Délen, and P. Georges. Hybrid pulse propagation model and quasi-phase-matched four-wave mixing in multipass cells. JOSA B, 37(10):2982–2988, October 2020. Publisher: Optica Publishing Group.

[188] M. Seidel, X. Xiao, and A. Hartung. Solid-Core Fiber Spectral Broadening at Its Limits. IEEE Journal of Selected Topics in Quantum Electronics, 24(5):1–8, September 2018. Conference Name: IEEE Journal of Selected Topics in Quantum Electronics.

[189] E. Escoto, A.-L. Viotti, A.-L. Viotti, S. Alisauskas, H. Tünnermann, I. Hartl, C. M. Heyl, C. M. Heyl, and C. M. Heyl. Temporal quality of post-compressed pulses at large compression factors. JOSA B, 39(7):1694–1702, July 2022. Publisher: Optica Publishing Group.

[190] D. Zhang, Y. Kong, and J.-y. Zhang. Optical parametric properties of 532-nm-pumped beta-barium-borate near the infrared absorption edge. Optics Communications, 184(5):485–491, October 2000.

[191] C.-H. Lu, Y.-J. Tsou, H.-Y. Chen, B.-H. Chen, Y.-C. Cheng, S.-D. Yang, M.-C. Chen, C.-C. Hsu, and A. H. Kung. Generation of intense supercontinuum in condensed media. Optica, 1(6):400–406, December 2014. Publisher: Optica Publishing Group.

[192] M. Seo, K. Tsendsuren, S. Mitra, M. Kling, and D. Kim. High-contrast, intense single-cycle pulses from an all thin-solid-plate setup. Optics Letters, 45(2):367–370, January 2020. Publisher: Optica Publishing Group.

[193] S. Sederberg, D. Zimin, S. Keiber, F. Siegrist, M. S. Wismer, V. S. Yakovlev, I. Floss, C. Lemell, J. Burgdörfer, M. Schultze, F. Krausz, and N. Karpowicz. Attosecond optoelectronic field measurement in solids. Nature Communications, 11(1):1–8, January 2020.

[194] F. Langer, C. P. Schmid, S. Schlauderer, M. Gmitra, J. Fabian, P. Nagler, C. Schüller, T. Korn, P. G. Hawkins, J. T. Steiner, U. Huttner, S. W. Koch, M. Kira, and R. Huber. Lightwave valleytronics in a monolayer of tungsten diselenide. Nature, 557(7703):76–80, May 2018.

[195] C. Palmer and E. G. Loewen. Diffraction grating handbook. 2005.

[196] T. Latychevskaia and H.-W. Fink. Practical algorithms for simulation and reconstruction of digital in-line holograms. Applied Optics, 54(9):2424–2434, March 2015. Publisher: Optical Society of America.

[197] D. Gauthier. Imagerie nanométrique ultra-rapide par diffraction cohérente de rayonnement extrême-UV produit par génération d'harmoniques d'ordre élevé. PhD thesis, Université Paris Sud - Paris XI, Paris, July 2012.

[198] D. F. G. Jr. Coherent Diffractive Imaging Near the Spatio-Temporal Limit with High-Harmonic Sources. PhD thesis, University of Colorado, Colorado, 2017.

Publications

The following research articles have been published in the context of this thesis:

Sven Fröhlich, Xu Liu, Aimrane Hamdou, Alric Meunier, Mukhtar Hussain, Mathieu Carole, Shatha Kaassamani, Marie Froidevaux, Laure Lavoute, Dmitry Gaponov, Nicolas Ducros, Sébastien Février, Philippe Zeitoun, Milutin Kovacev, Marta Fajardo, Willem Boutu, David Gauthier, Hamed Merdji. *'Self-Probed Ptychography from Semiconductor High-Harmonic Generation'.* Optics Letters 47, no. 19 (October 2022): 4865–68. https://doi.org/10.1364/OL.471113.

Viktoria E. Nefedova, **Sven Fröhlich**, Francisco Navarrete, Nicolas Tancogne-Dejean, Dominik Franz, Aimrane Hamdou, Shatha Kaassamani, David Gauthier, Rana Nicolas, Gaëtan Jargot, Marc Hanna, Patrick Georges, Marcelo F. Ciappina, Uwe Thumm, Willem Boutu, and Hamed Merdji. *'Enhanced extreme ultraviolet high-harmonic generation from chromium-doped magnesium oxide'.* Applied Physics Letters 118, no. 20 (May 2021): 201103. https://doi.org/10.1063/5.0047421